

NASA Conference Publication 10143, Volume 1

Fourth High Alpha Conference
NASA Dryden Flight Research Center
July 12-14, 1994



(NASA-CP-10143-Vol-1) FOURTH HIGH
ALPHA CONFERENCE, VOLUME 1 (NASA.
Dryden Flight Research Center)
212 p

N95-14229
--THRU--
N95-14238
Unclas



G3/02 0016078

High Alpha Aerodynamics

6 pg

324021

1995107815

NASA Conference Publication 10143, Volume 1

**Fourth High Alpha Conference
NASA Dryden Flight Research Center
Edwards, California
July 12–14, 1994**



National Aeronautics and
Space Administration
Office of Management
Scientific and Technical
Information Program
1994

Foreword

High-angle-of-attack flight research and development has matured in the past 5 years. We have seen four different aircraft investigate the different methods of stability, control, and effectiveness of high-angle-of-attack flight. Of these four vehicles, three use thrust vectoring to achieve their goals. Production aircraft, such as the F-22, are now using thrust vectoring. The use of forebody vortex control has been and is being investigated in flight, as well as in ground facilities. Considerable research, development, and validation of ground predictive tools, including computational fluid dynamics, wind tunnels, and simulations, have taken place to enable better, faster, cheaper development of new aircraft and modification of current aircraft.

The goal of the Fourth High Alpha Conference, held at the NASA Dryden Flight Research Center on July 12–14, 1994, was to focus on the flight validation of high-angle-of-attack technologies and provide an in-depth review of the latest high-angle-of-attack activities. Areas that were covered include high-angle-of-attack aerodynamics, propulsion and inlet dynamics, thrust vectoring, control laws and handling qualities, tactical utility, and forebody controls.

This document is a compilation of presentations given at the Fourth High Alpha Conference. The presentations included in this document are included as supplied by the presenters with no modifications. This conference, along with its predecessors, was sponsored by the NASA High Alpha Technology Program Steering Committee.

Fourth NASA High Alpha Conference
NASA Dryden Flight Research Center
July 12–14, 1994

Table of Contents—Volume 1:

High Alpha Aerodynamics

A Status Report on High Alpha Technology Program (HATP) Ground Test to Flight Comparisons, R. M. Hall, D. W. Banks, F. Ghaffari, and D. G. Murri, NASA Langley Research Center, Hampton, VA, D. F. Fisher, NASA Dryden Flight Research Center, Edwards, CA, and J. C. Ross and W. R. Lanser, NASA Ames Research Center, Moffett Field, CA

Flight and Full-Scale Wind-Tunnel Comparison of F/A-18 Pressure Distributions From an F-18 Aircraft at High Angles of Attack, David F. Fisher, NASA Dryden Flight Research Center, Edwards, CA, and Wendy R. Lanser, NASA Ames Research Center, Moffett Field, CA

Correlation of F/A-18 Tail Buffet Results, Larry Meyn, NASA Ames Research Center, Moffett Field, CA and Kevin D. James, Sterling Federal Systems, Inc., Moffett Field, CA, and Robert Geenan, PRC Inc., Edwards, CA

Numerical Simulation of the Flow About an F-18 Aircraft in the High-Alpha Regime, Scott M. Murman, MCAT Institute, Moffett Field, CA, and Yehia M. Rizk, NASA Ames Research Center, Moffett Field, CA

Hybrid Structured/Unstructured Grid Computations for the F/A-18 at High Angle of Attack, Robert T. Biedron and David L. Whitaker, Analytical Services and Materials, Inc., Hampton, VA

Comparison of X-31 Flight, Wind-Tunnel, and Water-Tunnel Yawing Moment Asymmetries at High Angles of Attack, Brent R. Cobleigh, PRC Inc., Edwards, CA, and Mark A. Croom, NASA Langley Research Center, Hampton, VA, and B. F. Tamrat, Rockwell International, North American Aircraft, Los Angeles, CA

Parameter Identification for X-31A at High Angles of Attack, S. Weiss, DLR Institute of Flight Mechanics, Edwards, CA, and D. Rohlf and E. Plaetschke, Rockwell International North American Aircraft, Los Angeles, CA

Validation of the NASA Dryden X-31 Simulation and Evaluation of Mechanization Techniques, Edward Dickes, Jacob Kay, and John Ralston, Bihrie Applied Research, Inc., Hampton, VA

High Alpha Aerodynamics (cont'd.)

Free-to-Roll Tests of X-31 and F-18 Subscale Models With Correlation to Flight Test Results, David L. Williams II and Robert C. Nelson, Hessert Center for Aerospace Research, University of Notre Dame, Notre Dame, IN, and David F. Fisher, NASA Dryden Flight Research Center, Edwards, CA

Static and Dynamic Force/Moment Measurements in the Eidetics Water Tunnel, Carlos J. Suarez and Gerald N. Malcolm, Eidetics Aircraft, Inc., Torrance, CA

26 pg

1995107816

N95-14230

324022

10079

P. 25

A STATUS REPORT ON HIGH ALPHA TECHNOLOGY PROGRAM (HATP) GROUND TEST TO FLIGHT COMPARISONS

by

**R.M. Hall, D.W. Banks, D.F. Fisher
F. Ghaffari, D.G. Murri, and J.C. Ross**

***Members of HATP
Experimental Aerodynamics Working Group***

and

**W.R. Lanser
NASA Ames Research Center**

**A Status Report on High Alpha Technology Program (HATP)
Ground Test to Flight Comparisons**

In this paper two topics are reviewed. The first is a testing technique, high- α gritting, that promises to significantly improve the correlations between ground test and flight data. The second portion addresses the status of the High Alpha Technology Program (HATP) Experimental Aerodynamics Working Group. One of the key objectives of the Working Group is to make sure that critical comparisons are made of ground test to flight data. The co-authorship of this report reflects the members of both the Working Group and a key researcher from Ames Research Center who is actively involved in the ground test to flight correlations.

A STATUS REPORT ON HIGH ALPHA TECHNOLOGY PROGRAM (HATP) GROUND TEST TO FLIGHT COMPARISONS

- Introduction
- Importance of Reynolds number in simulating forebody pressures
- Improvement of correlations with high- α gritting techniques
- Final tests planned
- Comments on HATP Experimental Aerodynamics Working Group

Abstract

This status paper reviews the experimental ground test program of the High Alpha Technology Program (HATP). The reasons for conducting this ground test program had their origins during the 1970's when several difficulties were experienced during the development programs of both the F-18 and F-16. A careful assessment of ground test to flight correlations appeared to be important for reestablishing a high degree of confidence in our ground test methodology. The current paper will then focus on one aspect of the HATP program that is intended to improve the correlation between ground test and flight, high- α gritting. The importance of this work arises from the sensitivity of configurations with smooth-sided forebodies to Reynolds number. After giving examples of the effects of Reynolds number, the paper will highlight efforts at forebody gritting. Finally, the paper will conclude by summarizing the charter of the HATP Experimental Aerodynamics Working Group and future experimental testing plans.

INTRODUCTION - MOTIVATION FOR HATP TESTING PROGRAM

- Experience since the 1970's on vortex dominated configurations demonstrated need for improving high- α prediction capability of ground test methodology
 - F-16, pitchup and deep stall
 - F-18, lateral / directional departure susceptibility
- Vast majority of high- α aerodynamics configuration development conducted in sub-scale low / moderate Reynolds number wind tunnels

Introduction–Motivation for HATP testing program

During the 1970's, testing programs with both the F-16 and F-18 experienced difficulties, see reference 1. For the F-16, a deep stall was discovered during the flight test program which was not anticipated on the basis of ground test data. This necessitated an enlargement of the horizontal tail. Similarly, the F-18 experienced lateral/directional shortcomings in its flight test program that required a rescheduling of the wing leading-edge flaps. At least one aspect of the incorrect predictions has involved the subscale Reynolds number effects during the model tests.

INTRODUCTION - OBJECTIVES OF HATP EXPERIMENTAL PROGRAM

- Address fundamental understanding of vortical flows about F/A-18 as an example high- α vehicle
 - Reynolds number and Mach number effects
 - Vortex flow physics
 - Lack of prediction of departures
- Provide key correlations between tunnel / flight / CFD
- Support test technique development

Introduction–Objectives of HATP experimental program

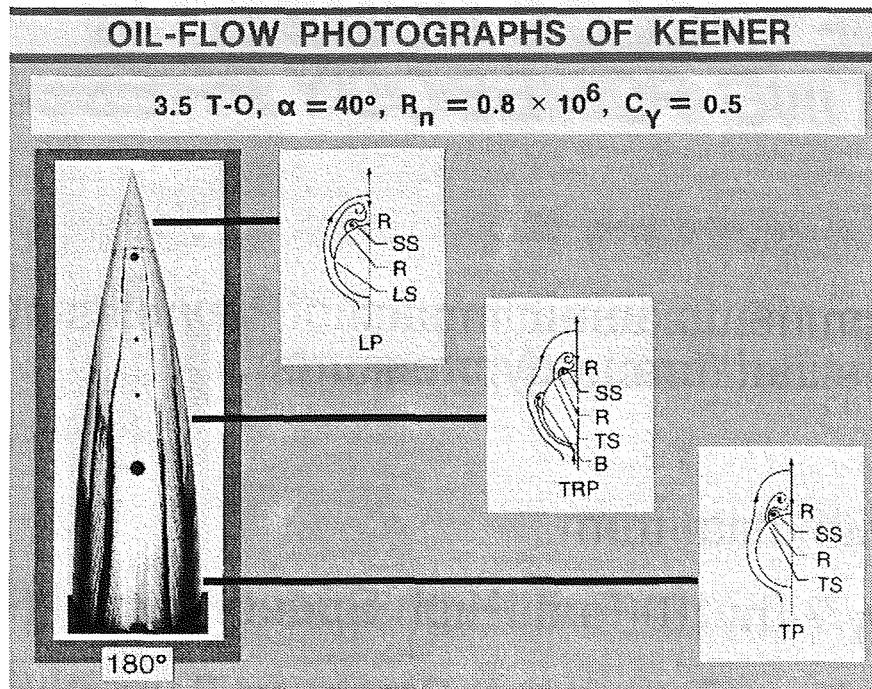
The objectives of the HATP program included (1) detailing Reynolds and Mach number effects, (2) increasing our fundamental understanding of the vortical flows about the F-18, as an example vehicle, and (3) determining if there was a systematic problem that led to the unexpected departures with the F-18. Correlations between tunnel, CFD, and flight are also considered to be an important priority. A final goal was to utilize HATP to foster test technique development.

IMPORTANCE OF REYNOLDS NUMBER IN SIMULATING FOREBODY PRESSURES

- General comments about impact of Reynolds number on smooth-sided forebody pressures
- Illustrate with data from
 - Langley 7- by 10-Foot High Speed Tunnel (HST)
 - Langley Low-Turbulence Pressure Tunnel (LTPT)

Importance of Reynolds number in simulating forebody pressures

The impact of Reynolds numbers on smooth-sided forebodies has been an active subject in the literature, see references 2 to 10. It has often been a source of differences when comparing model-to-model, tunnel-to-tunnel, and tunnel-to-flight data. The magnitude of these effects will be highlighted with data from two Langley experiments—a conventional, moderate Reynolds number test in the Langley 7- by 10-Foot High Speed Tunnel (HST) and a high Reynolds number test in the Langley Low-Turbulence Pressure Tunnel (LTPT).

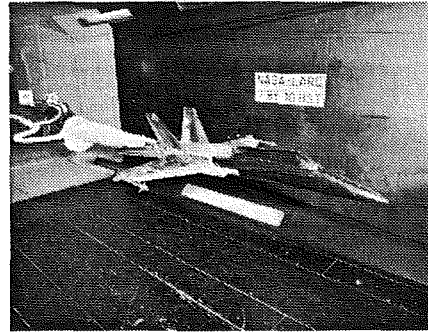


Oil Flows illustrating Reynolds number effects

Earlier research by Keener, see reference 10, contributed to our understanding of Reynolds number effects by interpreting a series of oil flows and sketching the corresponding flow topologies. The three topologies documented by Keener are shown and occur when (1) the boundary layer separates in a laminar fashion, see the sketch LP, (2) the boundary layer separates in a laminar fashion but reattaches before separating a second time as a turbulent boundary layer, see sketch TRP, and (3) the boundary layer transitions to turbulence before it has a chance to separate in a laminar manner, see sketch TP. Each of these topologies has a characteristic pressure signature and results in different separation locations and strengths of vortical suction on the surface.

1992 EXPERIMENT IN LANGLEY 7- by 10-FOOT HIGH SPEED TUNNEL (HST)

- Tested pressure instrumented 6% forebody on NAVAIR / McDonnell Douglas 6% high speed model
- Force and moment as well as pressure data recorded
- Conditions:
 - $M_\infty = 0.08$ and 0.30
 - $p_t = 1$ atm
 - $R_C = 0.4$ and 1.4 million
 - $-2^\circ < \alpha < 40^\circ$
 - $-10^\circ < \beta < 10^\circ$
- Tested 4 different gritting patterns, leading edge flap settings of 25° and 34° , flight test nose boom on and off

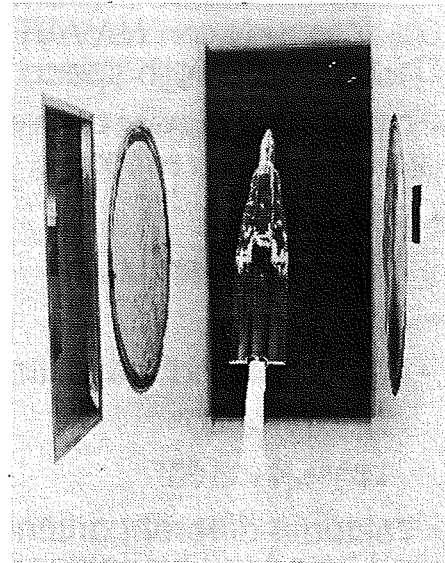


1992 Experiment in the Langley 7- by 10-Foot High Speed Tunnel (HST)

A cooperative experiment with NAVAIR and McDonnell Douglas was designed to gather pressure data with a Langley-manufactured forward fuselage (black component in photograph) mounted on the aft fuselage and wings of the 6% high speed model. The Langley forebody is equipped with a subset of the flight pressures, although not all of the orifices were active during this test. Data were taken at values of Mach number, M_∞ , equal to 0.08 and 0.3 while angle of attack, α , varied from -2° to 40° and angle of sideslip, β , from -10° to 10° . Major objectives of this test included exploring high- α gritting patterns and examining the impact of flight test nose boom on configuration stability and control. Results of this test are also discussed in reference 11.

1994 EXPERIMENT IN LANGLEY LOW-TURBULENCE PRESSURE TUNNEL (LTPT)

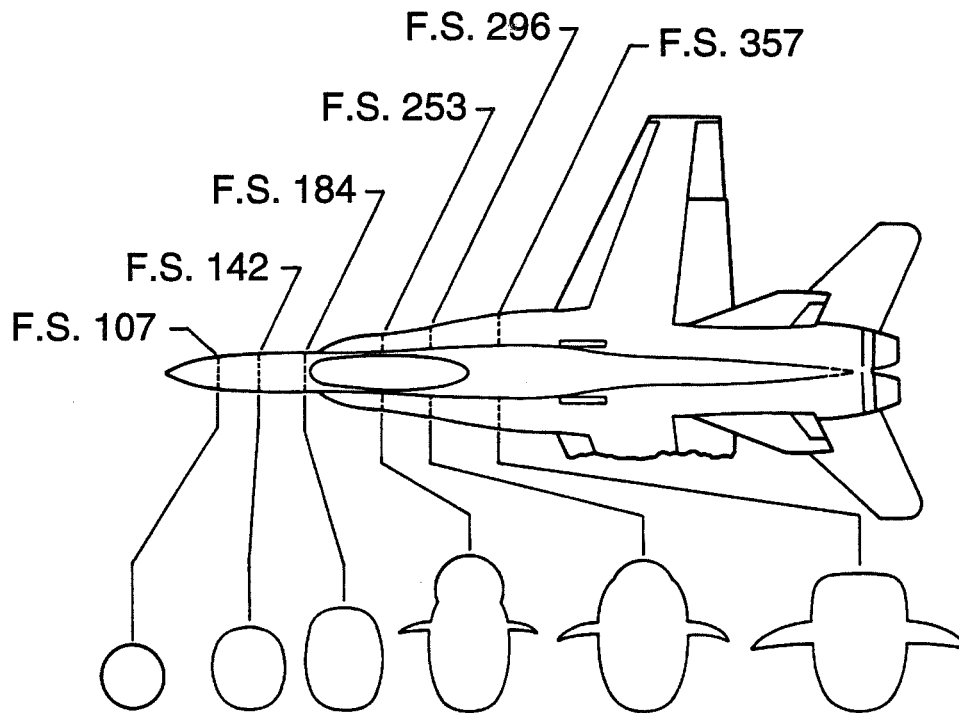
- Tested pressure instrumented 6% forebody and LEX on afterbody with constant cross section
- Only pressure data recorded
- Conditions:
 - $0.1 < M_\infty < 0.3$
 - $1 < p_t < 10$ atms
 - $0.48 \text{ million} < R_c < 6.9 \text{ million}$
 - $-10^\circ < \alpha < 50^\circ$
- Tested 5 different gritting patterns



1994 Experiment in the Langley Low-Turbulence Pressure Tunnel (LTPT)

The same Langley pressure-instrumented forebody was also outfitted with a constant cross section afterbody attachment, called a shroud. The constant cross section shroud afterbody begins where the leading edge flaps would intersect the fuselage. The length of the forebody/shroud configuration is 37.52 inches. While this forebody/shroud configuration was originally used for CFD code validation, see reference 12, it has also proved to be a useful tool for forebody studies. All values of Reynolds numbers, R_c , are calculated using the full configuration mean aerodynamic chord length. As will be discussed, gritting patterns designed for high- α flows were also tested. LTPT, which is a pressure tunnel capable of operating at $M_\infty = 0.2$ up to 10 atmospheres of pressure, is ideal to explore Reynolds number variations. The tunnel is 3 feet wide and 7.5 feet high, which makes it ideal for a slender body test such as this.

FOREBODY AND LEX SURFACE STATIC PRESSURE MEASUREMENT STATIONS

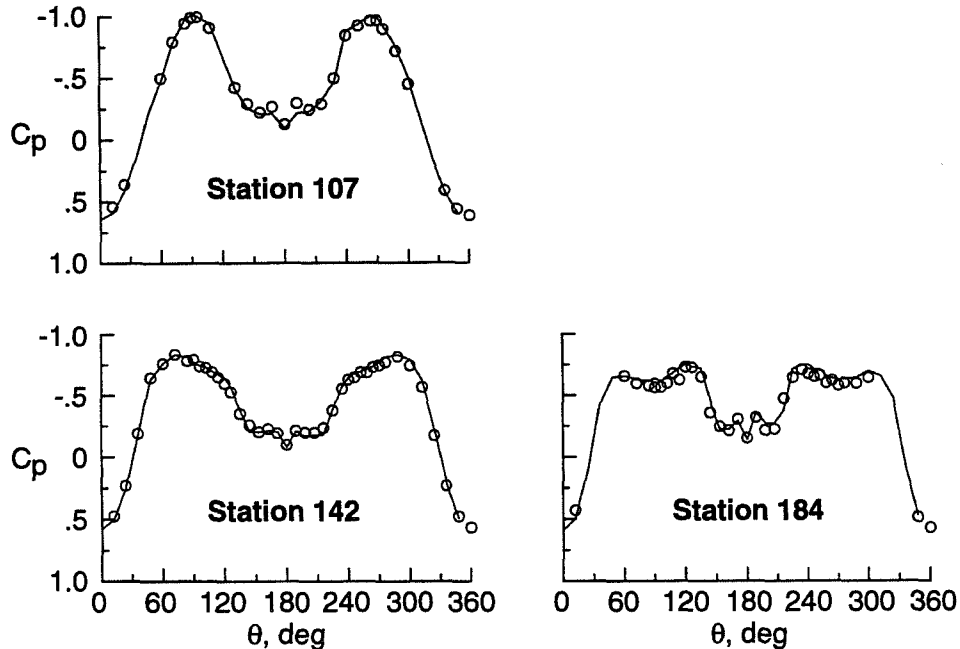


Forebody and LEX surface static pressure measurement stations

The location of the pressure rows on the forebody and the LEX are shown here for the entire configuration and are, of course, the same for the forebody/shroud configuration.

VALIDATION OF FOREBODY / SHROUD MODEL

Test	α , deg	β , deg	M_∞	Re_C , millions
— LTPT	40.0	0.0	0.30	1.41
○ 7 x 10	40.3	0.0	0.30	1.36

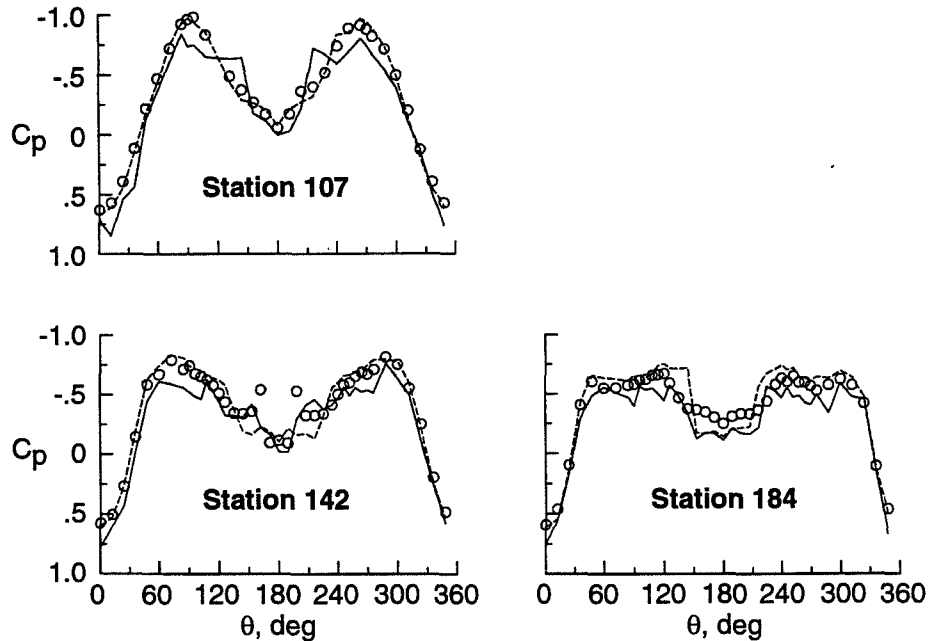


Validation of the forebody pressures from the forebody/shroud model

The pressures from forebody Stations 107, 142, and 184 of the forebody/shroud model are compared to the forebody pressures from the complete configuration tested in the Langley 7- by 10-Foot HST. The plots show pressure coefficient as a function of azimuthal location, θ , around the forebody. Values of θ equal to 0° and 360° are on the windward plane of symmetry while 180° represents the leeward plane. Values of θ increase in a clockwise direction as viewed from the pilot's perspective. The forebody pressures are not influenced by the presence or absence of the wing and empennage of the full configuration, as evidenced by the good agreement in the figure. (While not shown here, the LEX pressures are different between the forebody/shroud model and the complete configuration.) The large minimum pressure peaks at Fuselage Station 107 result from the attached flow accelerating about the body maximum breadth at 90° and 270° . The attached flow maximum velocities occur at Fuselage Station 142 at approximately 72° and 288° . At Fuselage Station 142, the distribution in the region between 144° and 216° , while relatively flat in these comparisons, will be the area that will be most sensitive to Reynolds number.

REYNOLDS NUMBER EFFECTS IN LTPT

Test	α , deg	β , deg	M_∞	Re_C , millions
— LTPT	40.0	0.0	0.10	0.48
- - - LTPT	40.0	0.0	0.20	0.96
○ LTPT	40.0	0.0	0.20	6.76

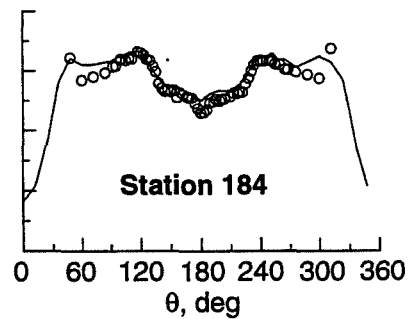
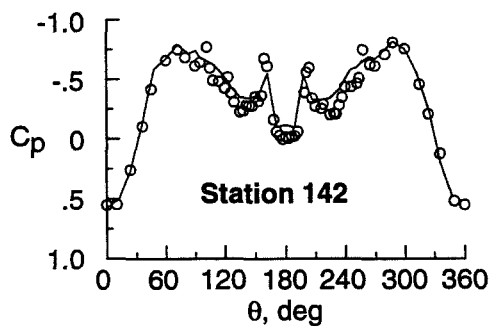
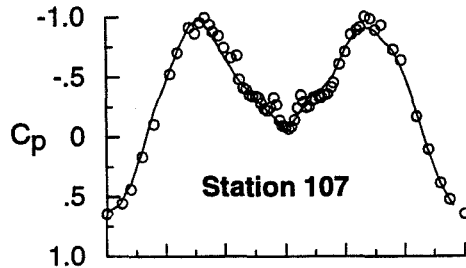


Reynolds number effects in LTPT

This figure summarizes three data points taken over a wide range of Reynolds number. As discussed by Polhamus in reference 8, Mach number effects on the forebody are insignificant as long as the cross-flow component of M_∞ is less than 0.15. For $\alpha = 40^\circ$, consequently, any differences between data for $M_\infty = 0.1$ and for $M_\infty = 0.2$ would only be the result of Reynolds number differences. However, the values of pressure coefficient for the lowest Reynolds number data are subject to the largest error bars. Assuming a nominal accuracy of the electronically scanned pressure transducer of 0.2 percent of full scale, the respective uncertainty in C_p for the different test points comes out to be ± 0.2 for the 0.48 million data, ± 0.05 for the 0.96 million data, and ± 0.007 for the 6.76 million data. This difference in error bars helps to explain why the lowest Reynolds number data appear rough compared to the other data. Turning our attention to the Station 142 distribution, it is seen that at the low Reynolds numbers, there are vortex footprints at azimuthal locations of 153° and 216° . These footprints go away for intermediate values of Reynolds number, such as for the 0.96 million example and as seen in the previous figure for the comparison with the 7- by 10-Foot HST data. At much higher values of Reynolds number, these footprints come back, as seen for 6.76 million. Unfortunately, much of wind tunnel testing at high- α falls in the intermediate Reynolds number range where the vortex footprints do not resemble the high Reynolds number limits. While the lower Reynolds number data do show the vortex footprints, please note that other significant differences in the pressure distributions are quite obvious at all three fuselage stations.

CORRELATION OF LTPT DATA WITH FLIGHT

Test	α , deg	β , deg	M_∞	Re_C , millions
— LTPT	40.0	0.0	0.20	6.76
o Flight	39.7	-0.3	0.25	9.57



Correlations of the LTPT high Reynolds number data with flight

Since the pressures over the forebody/shroud model represent the forebody pressures of the entire configuration, it is now possible to determine if the high Reynolds number data out of the LTPT entry match the flight data from the HARV. The values of R_c are of the same magnitude, with a value of 6.76 million for the LTPT test and a value of 9.57 million for the flight data. The agreement is reasonable, in general, and good in the vortex footprint region at Station 142 for $144^\circ < \theta < 216^\circ$. As will be described in more detail by Fisher and Lanser, see reference 13, some of the spikes in the flight data are due to external protuberances on HARV.

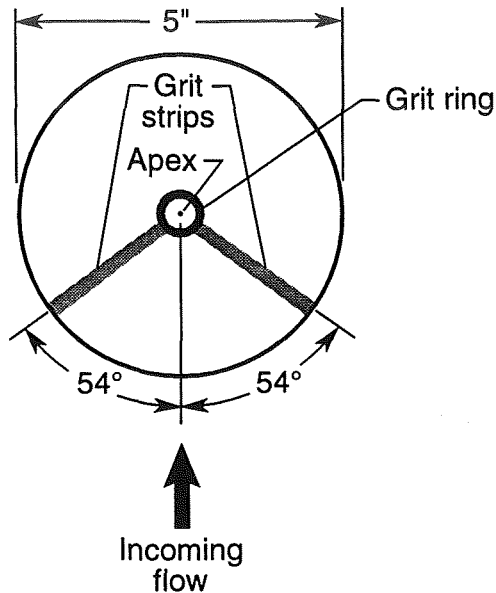
IMPROVED CORRELATIONS WITH GRITTING

- Approach
- 7- by 10-Foot High Speed Tunnel entry
- LTPT entry

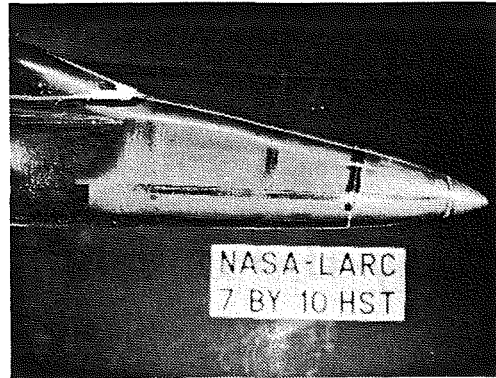
Improved correlations with gritting

Although correlations of high Reynolds number data from LTPT with flight data are good, low speed data are often limited to significantly lower Reynolds numbers. Therefore, test techniques to simulate the high Reynolds number flow, such as high- α gritting, are important to develop. While gritting for low- α has been successfully employed for many years, see reference 14, no similar systematic approach has been documented in the literature for high- α gritting. For the high- α application, the grit must be able to trigger boundary layer transition at model attitudes where the streamlines are predominantly in the cross-flow direction, and not in the longitudinal direction. Background information will be presented on gritting strategy and data from two Langley experiments will be given.

SCHEMATIC OF GRITTING APPROACH



(a) For generic ogive / cylinder model



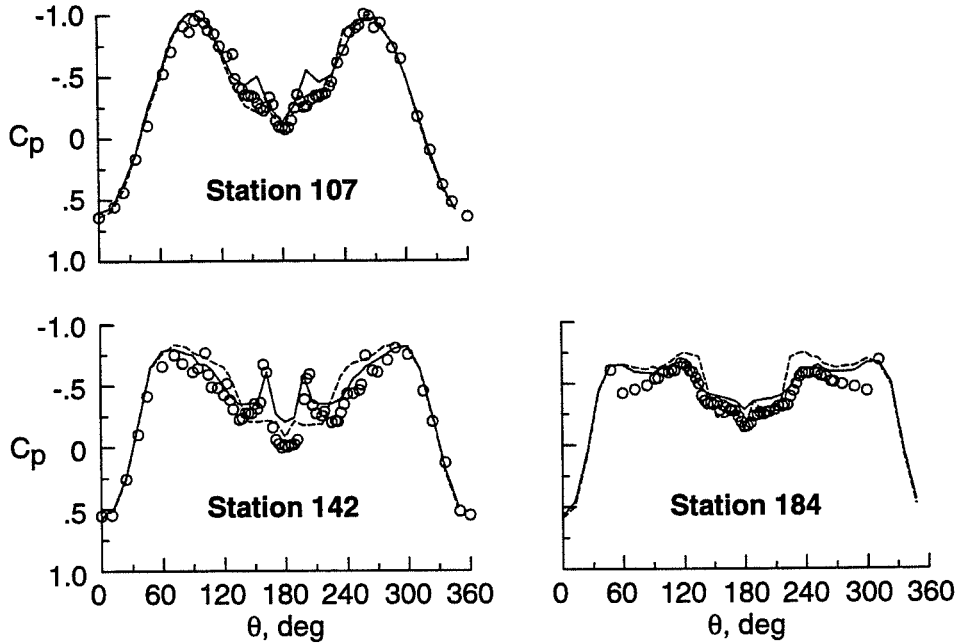
(b) For 6% F-18 model

Schematic of gritting approach

The most successful approach found during the Langley development of high- α gritting is the twin strip pattern. The idea is to place strips of grit longitudinally along the body so that the flow, when traversing the body in the cross-flow direction will pass over the grit and transition not only before separating but also before reaching its maximum attached flow velocity, see reference 15. For a generic ogive/cylinder, an azimuthal angle that works well is about 54° . For the F-18 configuration, azimuthal angles on the order of 54° or 72° seem to work well. An example of a twin strip pattern on the 6% F-18 forebody is also shown. While the traditional grit ring is ineffective at high- α , it is retained to trip the flow at lower values of α as seen both in the schematic and in the photograph of the F-18 forebody.

CORRELATION OF LTPT GRITTING DATA WITH FLIGHT

Test	Grit	α , deg	β , deg	M_∞	Re_c , millions
— LTPT	Twin, #180	40.0	0.0	0.30	1.41
--- LTPT	No grit	40.0	0.0	0.30	1.41
o Flight	No grit	39.7	-0.3	0.25	9.57

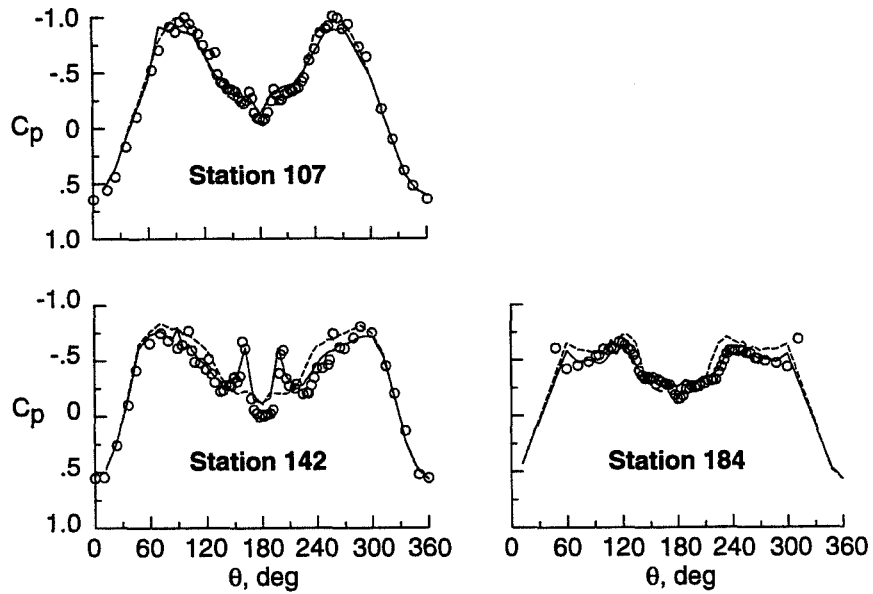


Correlation of the LTPT gritting data with flight data

The worth of the gritting pattern is whether it improves the correlation with high Reynolds number, flight data. This figure compares LTPT data for 1 atmosphere and $M_\infty = 0.3$ for both gritted and ungritted cases compared to flight. With the exception of overpredicting vortex strength at Station 107 (the suction peaks at azimuthal locations of 156° and 204°), the gritting greatly improved correlations at Station 142 in terms of matching vortex suction peaks as well as more closely matching pressure gradients on the leeward side of the maximum attached flow suction peaks. Agreement is also enhanced at Station 184. The grit size used was #180.

CORRELATION OF 7-by 10-FOOT HST GRITTING DATA WITH FLIGHT

Test	Grit	α , deg	β , deg	M_∞	Re_C , millions
— 7 x 10	Twin, #180	39.4	0.1	0.30	1.39
--- 7 x 10	Nose ring only	40.3	0.0	0.30	1.36
o Flight	No grit	39.7	-0.3	0.25	9.57

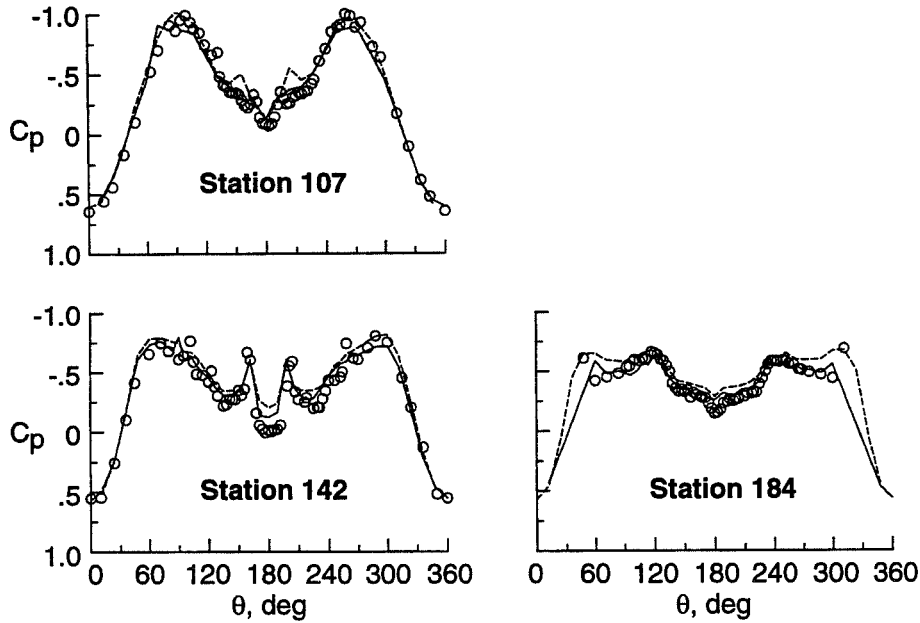


Correlation of the 7- by 10-Foot HST gritting data with flight data

This agreement between the gritted data and flight is also good. This application of grit did not produce excessive vortex footprints at Station 107, but again matched well at Stations 142 and 184.

REPEATABILITY OF GRIT APPLICATIONS

Test	Grit	α , deg	β , deg	M_∞	Re_C , millions
— 7 x 10	Twin, #180	39.4	0.1	0.30	1.39
--- LTPT	Twin, #180	40.0	0.0	0.30	1.41
o Flight	No grit	39.7	-0.3	0.25	9.57

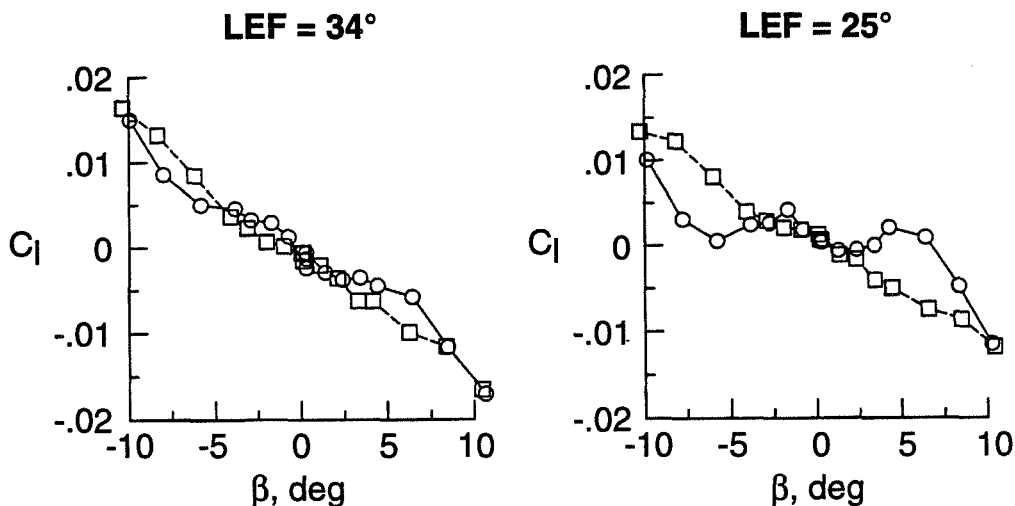


Assessing repeatability of grit applications

This figure compares the application of #180 grit in both the 7- by 10-Foot HST and the LTPT entry and correlates these data to flight. The agreement between these independent applications of grit is generally good. The areas of difference between the gritting occur for Station 107 near the leeward side and involves apparently too large a vortex footprint for the LTPT gritting pattern. There are some differences in magnitude of the gritted pressure distributions on the leeward side at Station 142. The large differences in the gritted patterns at Station 184 between 0° and 60° and 300° and 360° are due to linear extrapolation between data points. For the 7- by 10-Foot data, there are no points between 12° and 60° or between 300° and 348° . An additional entry of the forebody/shroud model in the 7- by 10-Foot HST during 1990 showed nearly identical results for gritting as well.

IMPACT OF FOREBODY GRITTING ON LATERAL CHARACTERISTICS

Test	Grit	α , deg	M_∞	Re_C , millions
—○ 7 x 10	Nose ring only	37.3	0.303	1.35
---□ 7 x 10	Twin, #180	37.4	0.303	1.39



Gritting effects on lateral aerodynamic coefficients

Not only do the pressures change with the addition of the forebody gritting, but the lateral characteristics can be affected as well. Shown in the above figure are plots of rolling moment, C_l , as a function of β for the 7- by 10-Foot HST 6% high speed model entry. While the impact of gritting is small for the present flight leading-edge flap (LEF) deflection angle of 34°, the impact of gritting is significant for the 25° LEF deflection used by the prototype. It is also interesting to note that the presence of gritting does not appear to influence the values of C_l for $|\beta| < 3^\circ$. Although not shown, the effects of gritting on yawing moment are small. While applying gritting enhanced static stability, other factors, such as the presence of a flight test nose boom, may have been responsible for the unpredicted departures, see reference 11.

SUMMARY OF CORRELATION IMPROVEMENT WITH GRITTING

- Reynolds number effects for smooth-sided forebodies are significant and can impact lateral characteristics
- Simulation of higher Reynolds number flows can greatly enhance ground test to flight correlations
- Test to test comparisons of high- α gritting applications have been good

Summary of correlation improvement with gritting

While high- α gritting patterns do not necessarily give perfect agreement over the entire forebody, they have the potential to greatly improve wind tunnel to flight correlations. This is crucial for vehicles with smooth-sided forebodies, where Reynolds number effects can significantly change the pressure distributions over the forebody and can impact lateral characteristics. As demonstrated by comparing two independent gritting applications on the same forebody but in two different tunnels, grit applications have acceptable repeatability. Just how grit is applied is important and excessive gritting, as discussed in reference 15, can lead to excessive normal loading and premature boundary-layer separation.

HATP EXPERIMENTAL AERODYNAMICS WORKING GROUP

- Identify key HATP data to be archived and key tunnel / flight correlations to be made
- Coordinate remainder of testing and analysis
- Determine if original wind tunnel / flight discrepancies can be addressed

HATP Experimental Aerodynamics Working Group

The charter of this working group, which functions under the direction of the HATP Steering Committee, is to identify important HATP data and to encourage that the data are archived and appropriately made available for key correlations. It has also coordinated current testing and analyses of the configuration aerodynamics data. The last charter of resolving the original wind tunnel to flight discrepancies is also being addressed. While resolving this issue is important, the first priority of the Working Group is to make sure that the community fully understands the more recent HATP data and the correlations between model-to-model, tunnel-to-tunnel, and tunnel-to-flight data that are now possible using models that reflect the current flight vehicle.

WORKING GROUP ACCOMPLISHMENTS AND STATUS

- Have identified significant HATP data bases and established points of contact
- Developing, in concert with the Steering Committee, a procedure for appropriate access to the data
- Will present a much more complete set of correlations between ground test and flight at the High-Alpha Conference in 1996

Working Group Accomplishments and Status

One of the first tasks of the Working Group members was to summarize the significant HATP-related experiments that have occurred. Within this summary, descriptive information is included with regard to test objectives, configurations tested, and points of contact. The Working Group has also served to increase communication between the Centers and has helped to coordinate the remainder of the testing and analyses. An important issue is the need of industry for ready access to the data. This question has been discussed and the current status is that a request for data will be filtered through the respective Center's Steering Committee member for approval of the data release. Of course, providing a summary of final correlations between tunnel-to-flight, tunnel-to-tunnel, and model-to-model is a main objective for the High- α Conference in 1996.

CLOSE-OUT TESTING PLANNED AT LANGLEY

- Objectives
 - Assess ground test to flight differences with and without gritting
 - Assess tunnel-to-tunnel differences
 - Assess model-to-model differences
- 30- by 60-Foot Tunnel of 16% low speed model
 - Pressures on forebody, LEX, and over wing
 - Leading edge flap deflections and gritting patterns
- 14- by 22-Foot Subsonic Tunnel test of both 16% low speed and 6% high speed models
 - Pressures on forebody and LEX for 6% model
 - Pressures on forebody, LEX and over wing for 16% model
 - Leading edge flap deflections and gritting patterns

Close-out testing planned at Langley

Two test entries are currently planned for later this year. The first entry involves testing the low speed 16% model in the Langley 30- by 60-Foot Tunnel. The key objective for this test is to measure pressures and determine lateral/directional characteristics at low values of dynamic pressure. High- α gritting studies will also be performed. A second entry at Langley will occur in the 14- by 22-Foot Subsonic Tunnel. This entry will also test the same low speed 16% model with and without grit to evaluate tunnel-to-tunnel differences. Also during the 14- by 22-Foot entry, the 6% NAVAIR/McDonnell Douglas high speed model will be tested with and without grit to evaluate model-to-model differences in the same facility.

SUMMARY - WORKING GROUP

- Monitoring final experimental activities of HATP configuration aero work
- Working Group is open to feedback from the user community

Summary–Working Group

The HATP Experimental Aerodynamics Working Group is monitoring the final experimental activities concerning configuration aerodynamics. If the user community has any feedback concerning the experimental program or about correlations, please contact any member of the Working Group. Member names and telephone numbers are listed below.

Robert M. Hall, NASA-Langley, 804-864-2883, Chairman
Daniel W. Banks, NASA-Langley, 804-864-5067
David F. Fisher, NASA-Dryden, 805-258-3705
Farhad Ghaffari, NASA-Langley, 804-864-2856
Daniel G. Murri, NASA-Langley, 804-864-1160
James C. Ross, NASA-Ames, 415-604-6722

References

1. Chambers, J. R.: High-Angle-of-Attack Aerodynamics: Lessons Learned. AIAA Paper No. 86-1774-CP, June 1986.
2. Lamont, P. J.: The Complex Asymmetric Flow Over a 3.5D Ogive Nose and Cylindrical Afterbody at High Angles of Attack. AIAA Paper No. 82-0053, January 1982.
3. Lamont, P. J.: Pressures Around an Inclined Ogive Cylinder with Laminar, Transitional, or Turbulent Separation. AIAA Journal, Vol. 20, No. 11, November 1982, pp. 1492-1499.
4. Lamont, P. J.: The Effect of Reynolds Number on Normal and Side Forces on Ogive-Cylinders at High Incidence. AIAA Paper No. 85-1799, August 1985.
5. Hall, R. M.: Influence of Reynolds Number on Forebody Side Forces for 3.5-Diameter Tangent-Ogive Bodies. AIAA Paper No. 87-2274, August 1987.
6. Hunt, B. L.: Asymmetric Vortex Forces and Wakes on Slender Bodies. AIAA Paper No. 82-1336, August 1982.
7. Champigny, P.: Reynolds Number Effect on the Aerodynamic Characteristics of an Ogive-Cylinder at High Angles of Attack. AIAA Paper No. 84-2176, August 1984.
8. Polhamus, E. C.: A Review of Some Reynolds Number Effects Related to Bodies at High Angles of Attack. NASA CR-3809, August 1984.
9. Ericsson, L. E.; and Reding, J. P.: Asymmetric Flow Separation and Vortex Shedding on Bodies of Revolution. In Hensch, M. J. (Ed.), Progress in Astronautics and Aeronautics, Tactical Missile Aerodynamics: General Topics, Vol. 141, New York, AIAA, 1992.
10. Keener, E. R.: Flow-Separation Patterns on Symmetric Forebodies. NASA TM 86016, January 1986.
11. Banks, D. W., Hall, R. M., Erickson, G. E., and Fischer, D. F., Forebody Flow Field Effects on the High Angle-of-Attack Lateral-Directional Aerodynamics of the F/A-18. AIAA Paper No. 94-0170, January, 1994.
12. Luckring, J. M.; Ghaffari, F.; and Bates, B. L.: Status of Navier-Stokes Computations about the F/A-18 with Structured Grids. Paper presented at the NASA High-Angle-of-Attack Technology Conference, Hampton Virginia, October 30 to November 1, 1990.

13. Fisher, David F.; and Lanser, Wendy R.: Flight and Full-Scale Wind Tunnel Comparison of F/A-18 Pressure Distributions at High Angles of Attack. Fourth NASA High Alpha Conference, Dryden Flight Research Center, July 12-14, 1994.

14. Braslow, A. L.; and Knox, E. C.: Simplified Method for Determination of Critical Height of Distributed Roughness Particles for Boundary Layer Transition at Mach Numbers from 0 to 5. NACA TN 4363, 1958.

15. Hall, R. M.; and Banks, D. W.: Progress in Developing Gritting Techniques for High Angle of Attack Flows. AIAA Paper 94-0169, January 1994.

20 pg

1995107817
324023

N95-14231

16080
P-20

Flight and Full-Scale Wind-Tunnel Comparison
of Pressure Distributions from an F-18
Aircraft at High Angles of Attack

David F. Fisher
NASA Dryden Flight Research Center
Edwards, California

Wendy R. Lanser
NASA Ames Research Center
Moffett Field, California

Fourth NASA High Alpha Conference
NASA Dryden Flight Research Center
Edwards, California
July 12-14, 1994

Abstract

Pressure distributions were obtained at nearly identical fuselage stations and wing chord butt lines in flight on the F-18 HARV at NASA Dryden Flight Research Center and in the NASA Ames Research Center's 80- by 120-ft wind tunnel on a full-scale F/A-18 aircraft. The static pressures were measured at the identical five stations on the forebody, three stations on the left and right leading-edge extensions, and three spanwise stations on the wing. Comparisons of the flight and wind-tunnel pressure distributions were made at $\alpha = 30^\circ$, 45° , and $60^\circ/59^\circ$. In general, very good agreement was found. Minor differences were noted at the forebody at $\alpha = 45^\circ$ and 60° in the magnitude of the vortex footprints and a Mach-number effect was noted at the leading-edge extension at $\alpha = 30^\circ$. The inboard leading-edge flap data from the wind tunnel at $\alpha = 59^\circ$ showed a suction peak that did not appear in the flight data. This was the result of a vortex from the corner of the leading-edge flap whose path was altered by the lack of an engine simulation in the wind tunnel.

Flight and Full-Scale Wind-Tunnel Comparison of Pressure Distributions from an F/A-18 Aircraft at High Angles of Attack

David F. Fisher

NASA Dryden Flight Research Center
Edwards, California

and

Wendy R. Lanser

NASA Ames Research Center
Moffett Field, California

RESEARCH REPORT



94-277

Introduction

The High Alpha Technology Program (ref. 1), initiated in 1986, encompasses many research efforts within NASA combining wind-tunnel testing, analytical predictions, piloted simulation, and full-scale flight research. In the program objectives (listed in the figure), full-scale flight validation was essential in developing high-angle-of-attack (high- α) technology. The flight portion of the program at NASA Dryden Flight Research Center focused on the F-18 High Alpha Research Vehicle (HARV), a highly instrumented preproduction F/A-18 aircraft. For the first objective, a new technology that was developed to improve agility at high- α and expand the usable high- α envelope has been thrust vectoring (ref. 2), which is currently being tested on the F-18 HARV. Actuated forebody strakes, ref. 3, soon be tested in flight, may enhance the controllability and maneuverability of the HARV even more. Other similar concepts such as forebody slot blowing have only been tested in the wind tunnel (ref. 4).

The second objective was to "provide flight-validated prediction/analysis methodology including experimental and computational methods that accurately simulate high-angle-of-attack aerodynamics, flight dynamics, and flying qualities" (ref. 1). Definitive surface and off-surface flow visualization (ref. 5) and pressure distribution results from flight (ref. 6) have been used to validate the three-dimensional Navier-Stokes computational fluid dynamics (CFD) solutions obtained for the F/A-18 at high- α for both the steady (ref. 7) and unsteady cases (ref. 8). New techniques in grid generation and flow modeling were developed to simulate the flight results of the highly vortical and separated flows.

Extensive ground testing of 0.06- and 0.16-scale models has been performed at high- α and compared to full-scale flight results (ref. 9). One result of this testing of subscale models is a new method of applying boundary-layer transition strips to the model forebodies to simulate flight results at high- α (refs. 10 and 11). Full-scale tests of an F/A-18 aircraft in the NASA Ames Research Center's 80- by 120-ft wind tunnel have focused on tail buffet, forebody controls, and surface pressures (refs. 4, 12, and 13). This paper compares the pressure distributions obtained on the forebody, leading-edge extensions (LEXs), and wings of a full-scale F/A-18 in the wind tunnel with corresponding pressure distributions obtained on the F-18 HARV in 1-g flight. Unlike the subscale model testing, the F/A-18 was tested at slightly higher Reynolds numbers than are generated in flight, though at a slightly lower Mach number. One would expect that these wind-tunnel results would show the best comparison with flight results, especially for those effects for which Reynolds numbers are important.



HAPT Objectives

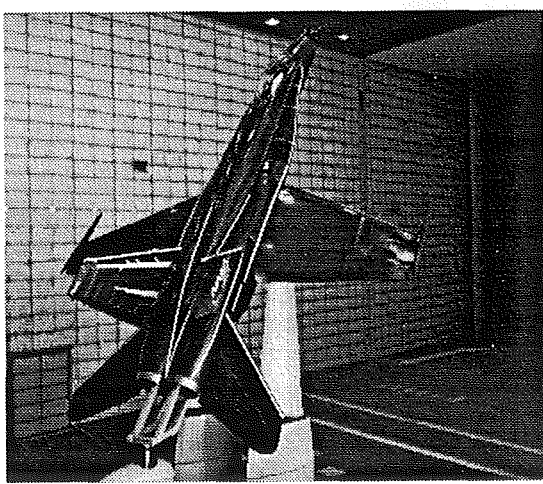
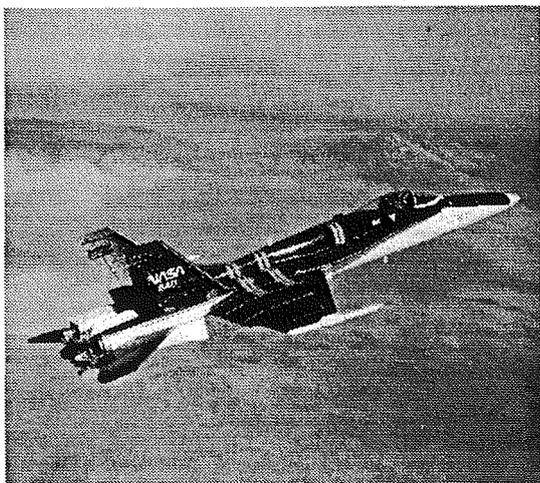
- Enable expanded high-alpha maneuverability and flight envelopes
- Provide flight-validated high alpha prediction/analysis methods for superior design methods

Ref. AGARD CP-465, paper #3
Gilbert, Nguyen, Gera

Test Conditions

Extensive pressure distributions were obtained on the F-18 HARV in flight and on a full-scale F/A-18 in the NASA Ames 80- x 120-ft wind tunnel. Data were obtained over a wide range of angles of attack and sideslip, both in flight and in the wind tunnel. However, only data at $\alpha = 30^\circ$, 45° , and 60° from flight and $\alpha = 30^\circ$, 45° , and 59° from the wind tunnel are presented. The data from the F-18 HARV were obtained in flight at stabilized 1-*g* conditions between 20,000- and 30,000-ft altitude with the engines set at military power. The Mach numbers (*M*) in flight ranged from 0.23 to 0.27, while the Reynolds numbers based on wing mean aerodynamic chord ranged from 8.9 to 10 million. Data from the atmospheric wind tunnel were obtained with the full-scale F/A-18 at $M = 0.15$ and a Reynolds number of 12 million. The F/A-18 aircraft was mounted on a three-strut configuration shown in the figure with a production radome, both engines removed, and inlets and exhaust exits open.

Test Conditions



F-18 HARV in flight

F/A-18 in 18- x 120-ft wind tunnel

RESEARCH REPORT 94-279

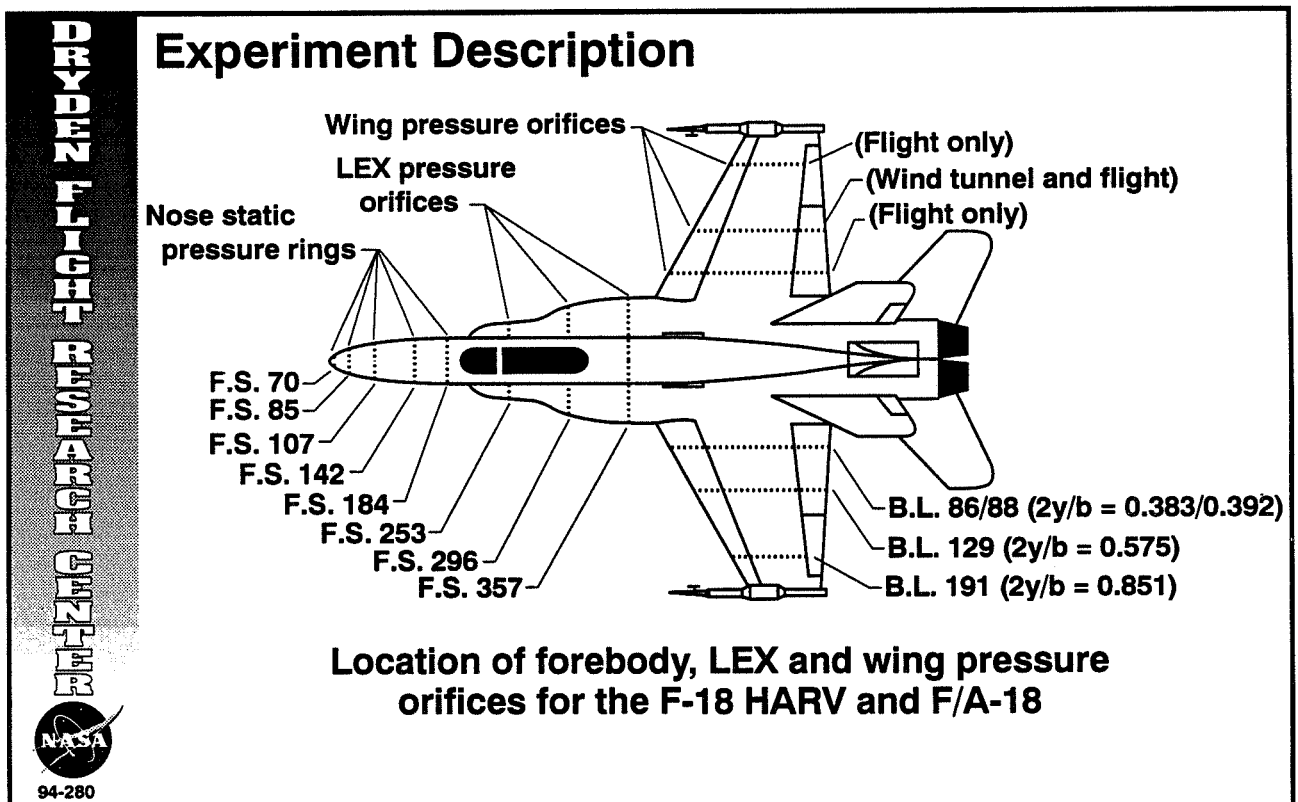


94-279

Experiment Description

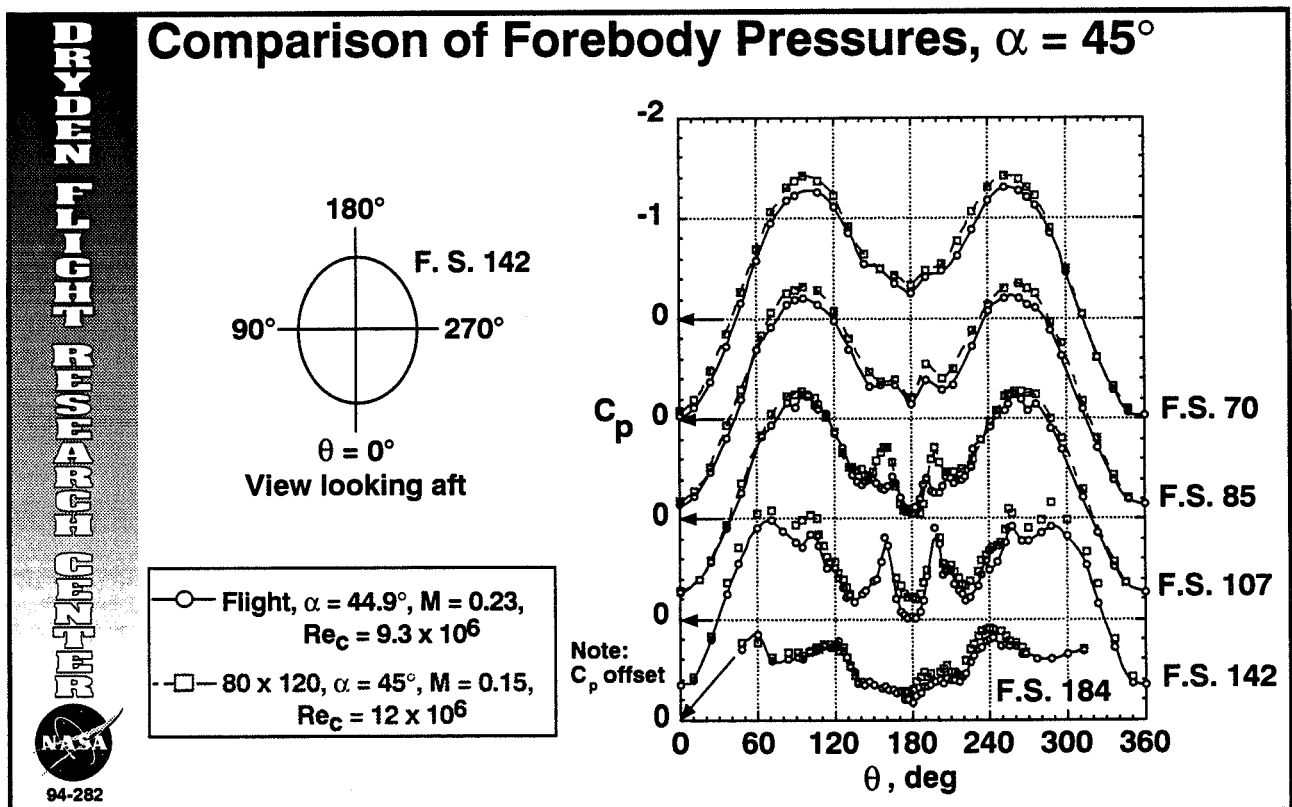
As shown in the figure, pressure distributions were obtained from five circumferential rows of flush orifices on the forebody and three rows of flush orifices on each LEX at identical stations both in flight and in the wind tunnel. Pressure distributions were also obtained on the upper and lower surface of the wings and at three span stations on the left and right wing in flight. In the wind tunnel, pressure distributions were obtained at nearly identical span stations on the left wing and at the midspan location only on the right wing. Flush orifices were installed on the left wing for the wind-tunnel-tested F/A-18 and on the leading-edge flaps of the flight-tested F-18 HARV. On the main wing box and trailing-edge flaps of the F-18 HARV, orifices were drilled in externally installed strip-of-tubing. At W.S. 129 on the left wing of the wind-tunnel experiment, strip-of-tubing was used for data comparison.

Data from the wind tunnel have been corrected for blockage effects using the techniques described in reference 14. The correction for blockage varied with angle of attack. For example, a measured pressure coefficient of -1.0 at $\alpha = 30^\circ$ had a correction of 0.058; at $\alpha = 45^\circ$, a correction of 0.069; and at $\alpha = 59^\circ$, a correction of 0.078.



Forebody, $\alpha = 45^\circ$

At 45° angle of attack the suction peaks at $\theta \approx 100^\circ$ and 260° at F.S. 70 and the following stations are more negative for both the flight and wind-tunnel data as compared with the results at $\alpha = 30^\circ$. At F.S. 70 and F.S. 85 the data from the wind tunnel show slightly more negative pressure coefficients than those from flight. At F.S. 107 the suction peaks resulting from the forebody vortex pair from the wind tunnel are significantly more negative than those from flight, while the rest of the pressure distribution shows good agreement. The wind-tunnel data at F.S. 142 and F.S. 184 show generally good agreement with the flight data. A slight asymmetry is noted at F.S. 184 for both wind-tunnel and flight data.

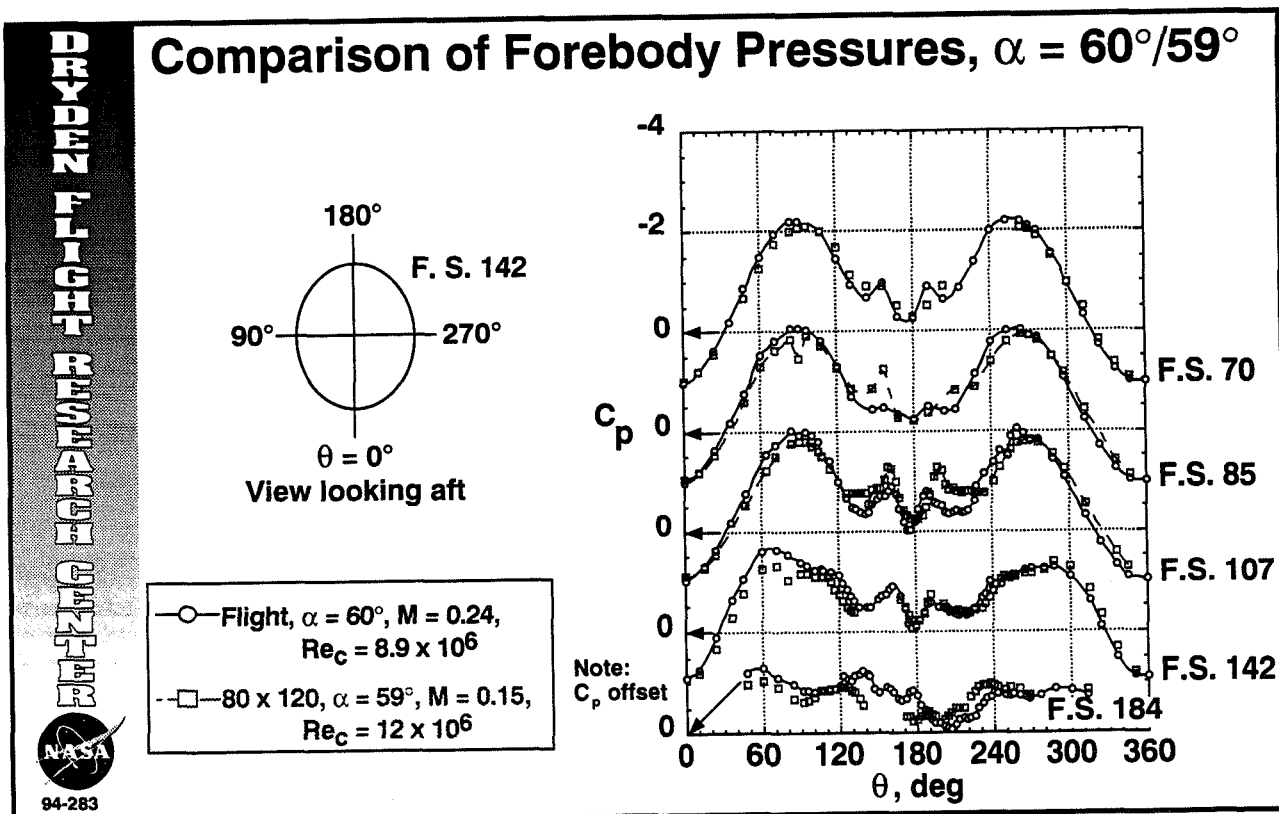


94-282

NASA

Forebody, $\alpha = 60^\circ/59^\circ$

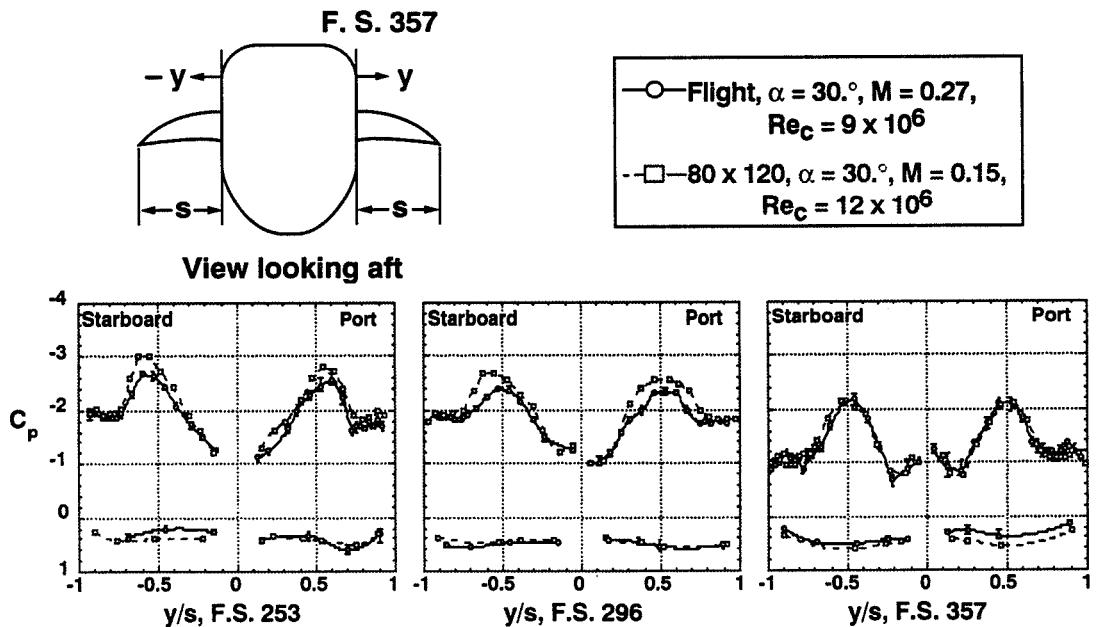
In the figure above, data from the wind tunnel at $\alpha = 59^\circ$ are compared with flight data at $\alpha = 60^\circ$. The angle-of-attack limit in the wind tunnel was 59° . Both the flight and wind-tunnel data show asymmetries in the pressure distributions. This could be the result of slight differences in the surface finish or contour of the forebody between the F-18 HARV and F/A-18 and the presence of a laminar separation bubble (ref. 5) and the difference in the boundary-layer transition location. In reference 15 it was shown that symmetric longitudinal transition strips can reduce forebody asymmetries. The effect of small changes in radome contour was also described in reference 15.



Leading-Edge Extensions, $\alpha = 30^\circ$

The figure shows comparisons of the static pressures from identical stations on the LEXs of the F-18 HARV (in flight) and the F/A-18 (in the 80- by 120-ft wind tunnel). These pressure distributions represent only the pressures on the LEXs and not on the fuselage. At this angle of attack the LEX vortex breakdown occurs at approximately F.S. 340 (ref. 16), i.e., between the second and third orifice stations. The static pressures measured below and behind vortex core breakdown tend to be very unsteady. The data from flight are shown with error bars that represent the minimum and maximum values of the 10 samples used to compute the mean. (See the following two figures to see the error bars more clearly.) These pressure fluctuation values are biased in that the transducers were not flush on the surface but sensed the pressures through 0.062-in. diameter tubing that was 1.5 ft long at F.S. 253 and 3.0 ft long at F.S. 357. At this angle of attack the pressure variations from minimum to maximum are relatively small, generally within the size of the symbol. The large suction peaks shown in pressure distributions result from the strong primary vortex shed by the sharp edge of each LEX (ref. 5). The highest suction pressures are at the forward stations and are reduced behind the vortex core breakdown position. At F.S. 253 and 296 the suction peaks in the pressure distributions from the wind tunnel are higher than those from flight. This difference results from the lower Mach number in the wind tunnel, 0.15, as compared with flight, 0.27. This effect of Mach number was shown previously in reference 6 at this angle of attack.

Comparison of Leading Edge Extension Pressures, $\alpha = 30^\circ$

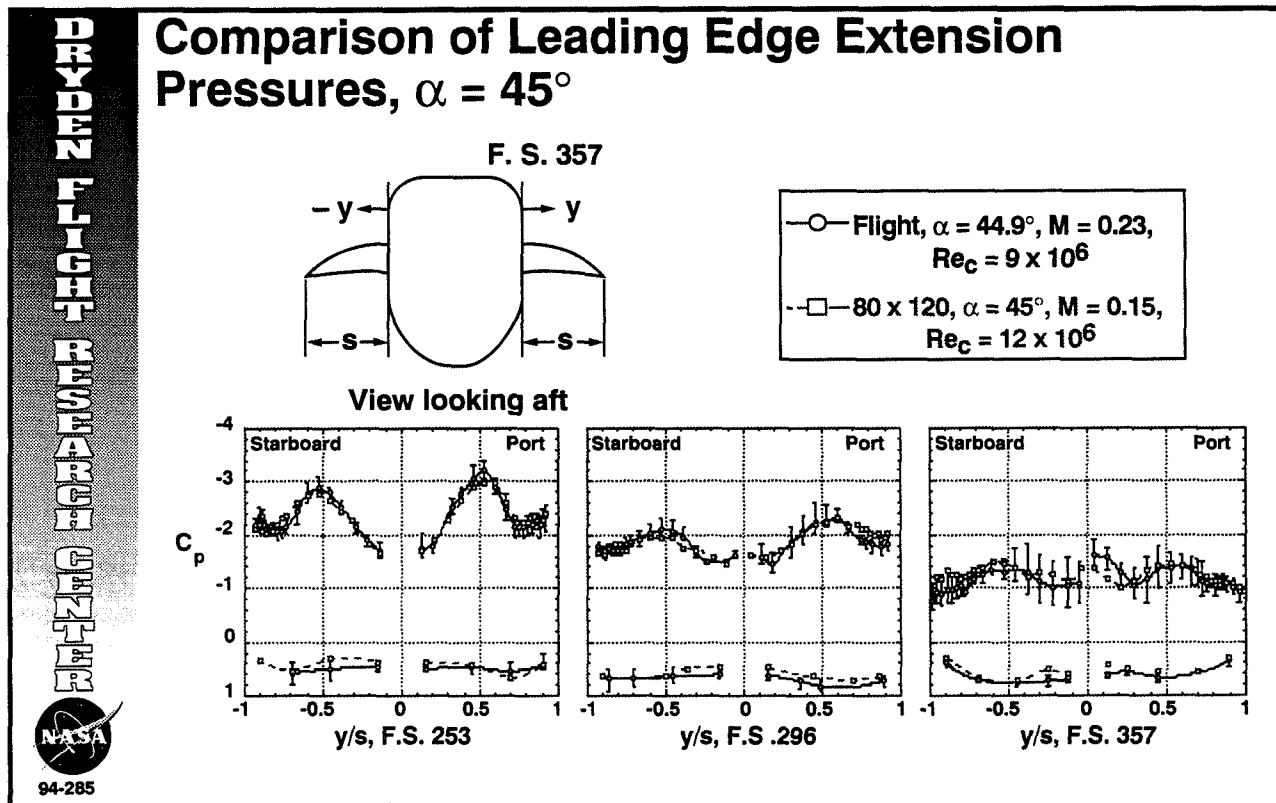


ADVANCED TECHNOLOGY RESEARCH CENTER
 WRIGHT-PATTERSON AIR FORCE BASE
 DAYTON, OHIO 45433-3941



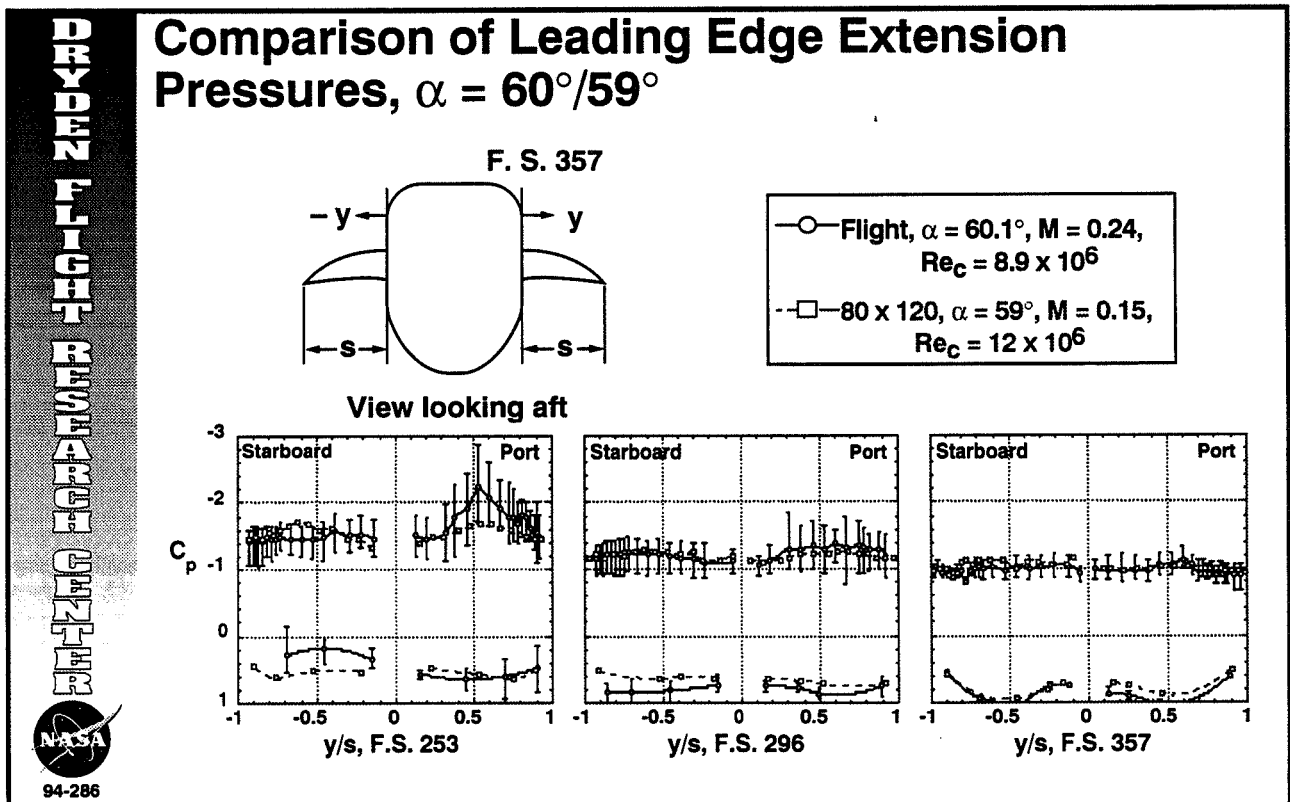
Leading-Edge Extensions, $\alpha = 45^\circ$

LEX pressure distributions at an angle of attack of 45° are shown above. At this angle of attack, LEX vortex core breakdown occurs slightly forward of the first orifice station at F.S. 253. Note the reduction and flattening of the suction peaks from the forward orifice station to the aft orifice stations. Also note the large increase in the pressure fluctuations as noted by the length of the error bars for the flight data at this angle of attack as compared with $\alpha = 30^\circ$. At this angle of attack, the wind tunnel data show good agreement with the flight data, even showing similar asymmetries. The effect of Mach number present at $\alpha = 30$ is not noted here.



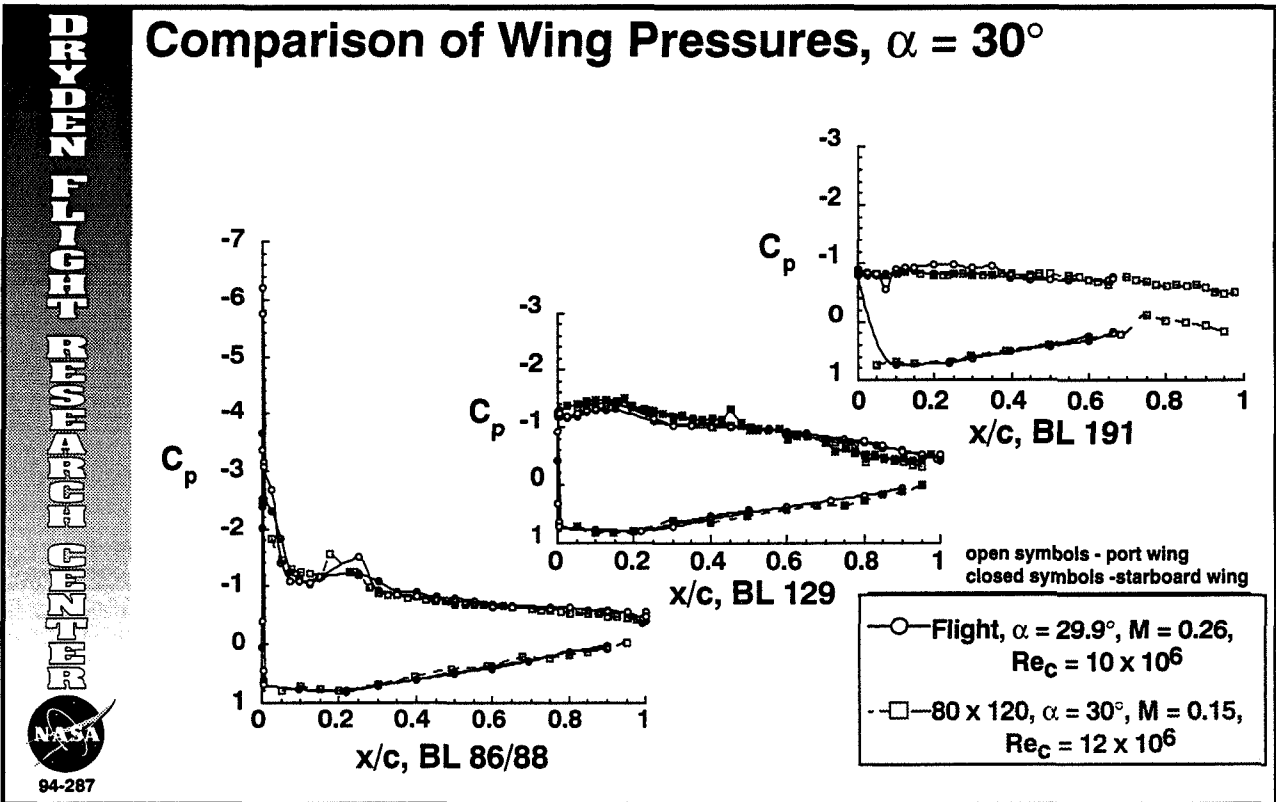
Leading-Edge Extensions, $\alpha = 60^\circ/59^\circ$

The comparison of the LEX pressure distributions at $\alpha = 60^\circ$ from flight and $\alpha = 59^\circ$ from the wind tunnel is shown above. At this angle of attack the LEX vortex cores are completely broken down at the LEX apex and the pressure distributions are generally flat. The pressure fluctuations in the flight data are greatest at the forward station. The wind-tunnel data generally fall well within the band of pressure fluctuations. Some asymmetry is noted, especially at the forward station for the flight data.



Wing, $\alpha = 30^\circ$

Chordwise pressure distributions at $\alpha = 30^\circ$ obtained from the F-18 HARV in flight and F/A-18 in the wind tunnel are shown above. At this angle of attack and higher the 20-percent chord leading-edge flaps are deflected down 33° while the trailing-edge flaps are undeflected. The trailing-edge flaps and ailerons begin at 68-percent chord. Pressure distributions from both the left and right wing are shown for the HARV at all three span stations, but not on the ailerons at BL 191. Pressure distributions were obtained at all three span stations on the left wing and only at the midspan station on the right. In general the data showed very good agreement. Suction peaks at the leading edge were noted at the inboard station, indicating that the leading-edge flow is still attached. At the outboard station the flat pressure distribution and trailing-edge pressure deficit indicate extensive separated flow. This is in agreement with in-flight flow visualization at $\alpha \approx 30^\circ$, in which tufts showed attached chordwise flow near the inboard station on the leading-edge flap and reversed flow was shown near the outboard station. The tufts also showed significant spanwise flow near the two inboard stations over the main wing and reversed flow near the outboard station. Similar flow visualization results were observed in the wind-tunnel experiment using flow cones and tufts.

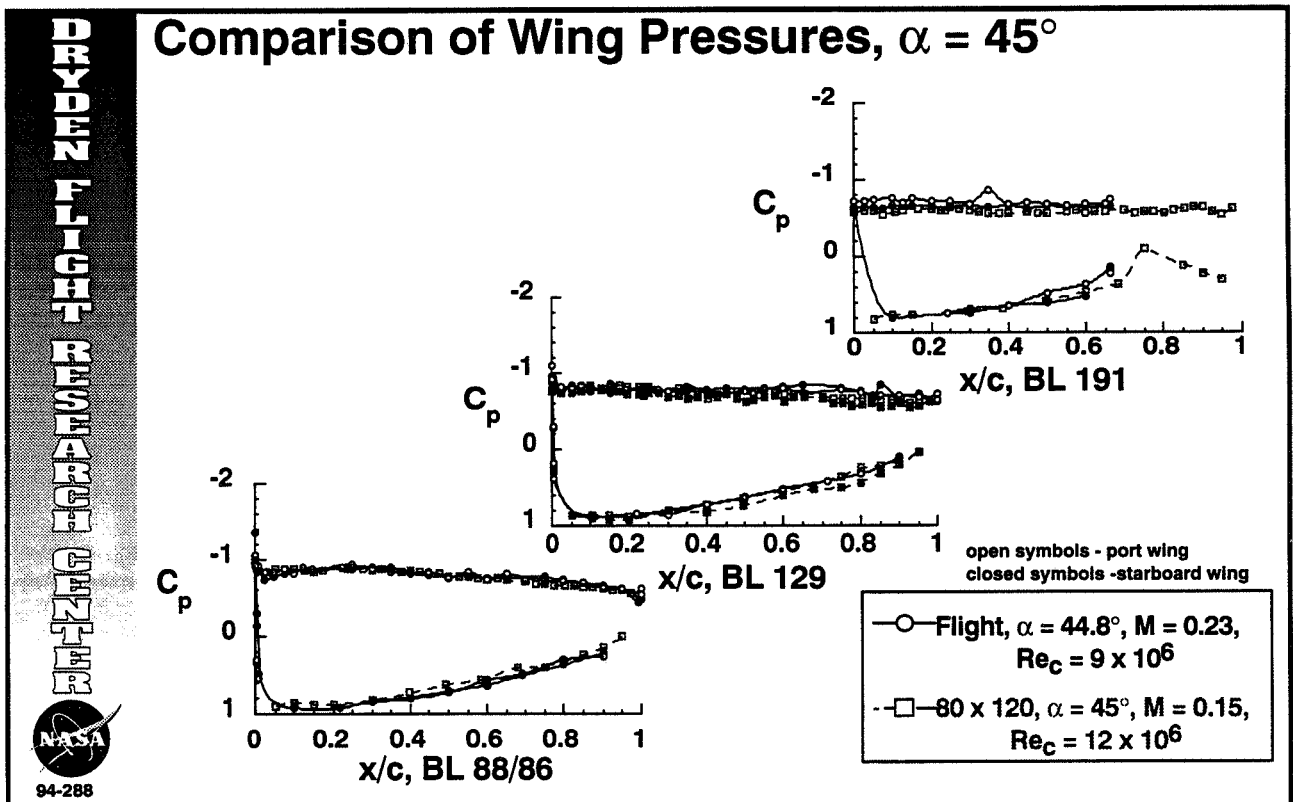


WIND TUNNEL TESTS FOR THE F-18 HARV



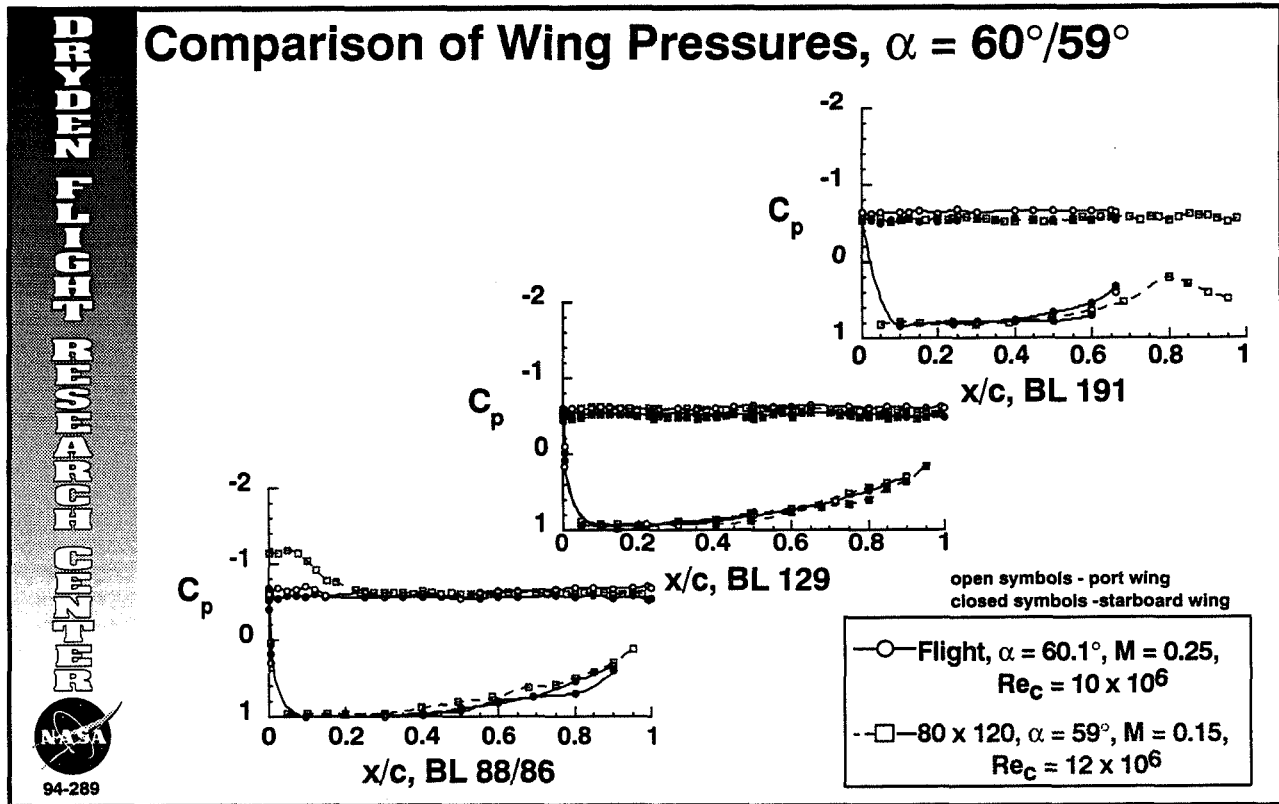
Wing, $\alpha = 45^\circ$

At $\alpha = 45^\circ$ the pressure distributions from both flight and wind tunnel show very good agreement. The flat pressure distributions and trailing-edge deficits indicate extensively separated flow over the entire wing. A comparison of the externally mounted pressure orifices on the starboard wing with the flush orifices on the port wing of the F/A-18 was made. The root-mean-square of the difference between the flush-measured pressure coefficients and the externally measured coefficients was approximately 0.1, with the externally measured pressure coefficients tending to be slightly more negative than those for the flush orifices. This is in good agreement with reference 17 for a similar installation at Mach numbers of 0.5, 0.9, and 0.97.



Wing, $\alpha = 60^\circ/59^\circ$

Wing pressure distributions shown in the figure were obtained in flight at $\alpha = 60^\circ$ and in the wind tunnel at $\alpha = 59^\circ$. The flight and wind-tunnel results show very good agreement at the two outboard stations with very flat pressure distributions and an average pressure coefficient of ≈ -0.6 . At BL 88, the wind-tunnel data show a suction peak on the leading-edge flap that the flight data do not show. The wind-tunnel data were obtained without engines allowing airflow through the inlets and through the exhaust while the flight data were obtained with the engines at military power setting. To further examine the effects of no engines, these conditions were simulated in the NASA Dryden water tunnel. For the wind-tunnel simulation with flow through inlets and open exhaust, a vortex emanating from the inboard corner of the leading-edge flap traveled spanwise across the orifice station. In the flight simulation, with the mass flow of the engines simulated, the leading-edge flap vortex was much more chordwise and farther from the flap surface.



Summary

Pressure distributions obtained from the forebody, leading-edge extensions (LEXs) and wings obtained in flight from the F-18 HARV at NASA Dryden Flight Research Center were correlated with similar pressure distributions obtained on an F/A-18 in the NASA Ames Research Center's 80- x 120-ft wind tunnel. Pressure distributions were obtained at five circumferential rings on the forebodies and spanwise rows at three fuselage stations on both the LEXs. Pressure distributions were also obtained at three span stations on both wings in flight while pressure distributions were obtained at the nearly identical station on the left wing but only the midspan station on the right wing. The following results were observed.

At $\alpha = 30^\circ$ the pressure distributions obtained on the forebody and wings in the wind tunnel were in excellent agreement with those obtained in flight. The pressure distributions obtained on the LEX, however, were not in agreement because of an effect of Mach number.

At $\alpha = 45^\circ$ the forebody pressure distributions from the wind tunnel had larger suction peaks than those from flight. The pressure distributions for the LEX from both wind tunnel and flight were in good agreement with the flight data indicating unsteady pressures at the aft station. Data from the wing were in very good agreement and indicated extensive separated flow by the flat pressure distributions and pressure deficit at the trailing edge.

At $\alpha = 60^\circ$ the asymmetries were noted in the pressure distributions from both the wind tunnel and flight. On the LEX large pressure fluctuations were observed in the flight data, and the wind-tunnel data generally fell within those bounds. The pressure distributions from the wings were flat and extensively separated except for the leading-edge flap at the inboard station for the wind tunnel. It is postulated that because of the difference in inlet flow between wind tunnel and flight, a vortex from the corner of the leading-edge flap sweeps over this location causing a suction peak in the wind-tunnel case.



Summary

- At $\alpha = 30^\circ$, forebody and wing pressure distributions in excellent agreement; effect of Mach number present at LEX
- At $\alpha = 45^\circ$, suction peaks in the forebody pressure distribution were larger than in flight; LEX and wing pressure distributions in good agreement; extensive separated flow on wings
- At $\alpha = 60^\circ/59^\circ$, forebody asymmetries were noted for both flight and wind-tunnel pressure distributions; unsteady pressures noted in flight; lack of simulated engine flow affected flow over inboard leading edge flap in wind tunnel

References

1. Gilbert, William P., Luat T. Nguyen, and Joseph Gera, "Control Research in the NASA High-Alpha Technology Program," in *Aerodynamics of Combat Aircraft Controls and of Ground Effects*, AGARD CP-465, paper #3, 1990.
2. Regenie, Victoria, Donald Gatlin, Robert Kempel, and Neil Matheny, *The F-18 High Alpha Research Vehicle: A High-Angle-of-Attack Testbed Aircraft*, NASA TM-104253, Sept. 1992 (also published as AIAA 92-4121).
3. Murri, Daniel G., Gautam H. Shah, Daniel J. DiCarlo, and Todd W. Trilling, "Actuated Forebody Strake Controls for the F-18 High Alpha Research Vehicle," AIAA 93-3675, Aug. 1993.
4. Lanser, Wendy R. and Daniel G. Murri, "Wind Tunnel Measurements on a Full-Scale F/A-18 with Forebody Slot Blowing or Forebody Strakes," AIAA 93-1018, Feb. 1993.
5. Fisher, David F., John H. Del Frate, and David M. Richwine, *In-Flight Flow Visualization Characteristics of the NASA F-18 High Alpha Research Vehicle at High Angles of Attack*, NASA TM-4193, May 1990.
6. Fisher, David F., Daniel W. Banks, and David M. Richwine, *F-18 High Alpha Research Vehicle Surface Pressures: Initial In-Flight Results and Correlation With Flow Visualization and Wind-Tunnel Data*, NASA TM-101724, Aug. 1990. (Also available as AIAA 90-3018.)
7. Ghaffari, Farhad, James M. Luckring, James L. Thomas, Brent L. Bates, and Robert T. Biedron, "Multiblock Navier-Stokes Solutions About the F/A-18 Wing-LEX-Fuselage Configuration," *J. Aircraft*, vol. 30, no. 3, May-June 1993, pp. 293-303.
8. Rizk, Yehia M. and Ken Gee, "Unsteady Simulation of Viscous Flowfield Around F-18 Aircraft at Large Incidence," *J. Aircraft*, vol. 29, no. 6, Nov.-Dec. 1992, pp. 986-992.
9. Erickson, G. E., R. M. Hall, D. W. Banks, J. H. Del Frate, J. A. Schreiner, R. J. Hanley, and C. M. Pulley, "Experimental Investigation of the F/A-18 Vortex Flows at Subsonic Through Transonic Speeds, Invited Paper," AIAA 89-2222, July-Aug. 1989.
10. Hall, R. M. and D. W. Banks, "Progress in Developing Gritting Techniques for High Angle of Attack Flows," AIAA 94-0169, Jan. 1994.
11. Banks, Daniel W., Robert M. Hall, Gary E. Erickson, and David F. Fisher, "Forebody Flow Field Effects on the High Angle-of-Attack Lateral-Directional Aerodynamics of the F/A-18," AIAA-94-0170, Jan. 1994.
12. James, K. D. and L. A. Meyn, "Dependence of Integrated Vertical-Tail Buffet Loads for F/A-18 on Sensor Density," SAE 941140, Apr. 1994.
13. Meyn, Larry A., Wendy R. Lanser, and Kevin D. James, "Full-Scale High Angle-of-Attack Tests of an F/A-18," AIAA 92-2676, June 1992.
14. Rae, William H., Jr., and Alan Pope, *Low-Speed Wind Tunnel Testing*, Second Edition, John Wiley & Sons, New York, 1984.
15. Fisher, David F. and Brent R. Cobleigh, *Controlling Forebody Asymmetries in Flight—Experience With Boundary Layer Transition Strips*, NASA TM- 4595, July 1994. (Also available as AIAA 94-1826.)
16. Del Frate, John H. and Fanny A. Zuniga, "In-Flight Flow Field Analysis on the NASA F-18 High Alpha Research Vehicle With Comparisons to Ground Facility Data," AIAA 90-0231, Jan. 1990.

17. Montoya, Lawrence C. and David P. Lux, *Comparisons of Wing Pressure Distribution from Flight Tests of Flush and External Orifices for Mach Numbers from 0.50 to 0.97*, NASA TM X-56032, Apr. 1975.

PAPER NOT AVAILABLE FOR PREPRINT

Correlation of F/A-18 Tail Buffet Results, Larry Meyn, NASA Ames Research Center, Moffett Field, CA and Kevin D. James, Sterling Federal Systems, Inc., Moffett Field, CA, and Robert Geenan, PRC Inc., Edwards, CA

**NUMERICAL SIMULATION OF THE FLOW
ABOUT AN
F-18 AIRCRAFT IN THE HIGH-ALPHA REGIME**

**Scott M. Murman
MCAT Institute, Moffett Field, CA**

**Yehia M. Rizk
NASA Ames Research Center, Moffett Field, CA**

**Presented at
NASA 4th High Alpha Conference
July 12-14, 1994
Dryden Flight Research Facility**

3409

1995107818
324024

53-uc
16081
p. 33

N95-14232

The current research is aimed at developing and extending numerical methods to accurately predict the high Reynolds number flow about the NASA F-18 HARV at large angles of attack. The resulting codes are validated by comparison of the numerical results with in-flight aerodynamic measurements and flow visualization obtained on the HARV. Further, computations have been used to provide an analysis and numerical optimization of a pneumatic slot blowing concept, and a mechanical strake concept, for use as potential forebody flow control devices in improving high-alpha maneuverability (cf. Gee, et al. These proceedings).

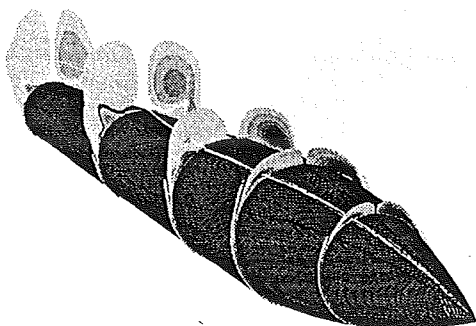
MOTIVATION

- * PROVIDE FLIGHT-VALIDATED NUMERICAL METHODS FOR COMPUTING THE FLOW ABOUT AIRCRAFT OPERATING IN THE HIGH-ALPHA REGIME**

- * USE THESE METHODS TO PROVIDE AN ANALYSIS AND OPTIMIZATION OF NEW CONTROL CONCEPTS FOR HIGH-ALPHA MANEUVERABILITY**

Computation of the flow about the F-18 HARV at high alpha provides a challenge for numerical methods because of the complex physics involved and the complex geometry of a full-aircraft configuration. Since the computations are carried out to match actual flight operating conditions, the Navier-Stokes equations must be solved. Further, the flow about the majority of the aircraft is turbulent, and the computations must include suitable turbulence models. These models must be applied in a rational manner to account for the massive 3-D separation that occurs at large incidence. The complex aircraft geometry is modeled using structured, overlapped grids in what is termed a Chimera approach. This method allows grids to be generated about the separate components of the aircraft and then combined, greatly simplifying the grid generation procedure. This approach also allows the use of different numerical schemes in different regions of the aircraft, depending upon the physics encountered.

CHALLENGES TO HIGH-ALPHA CFD

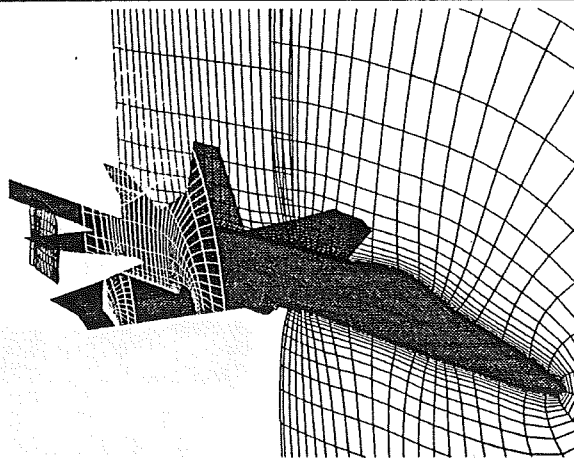


COMPLEX PHYSICS

+

COMPLEX GEOMETRY

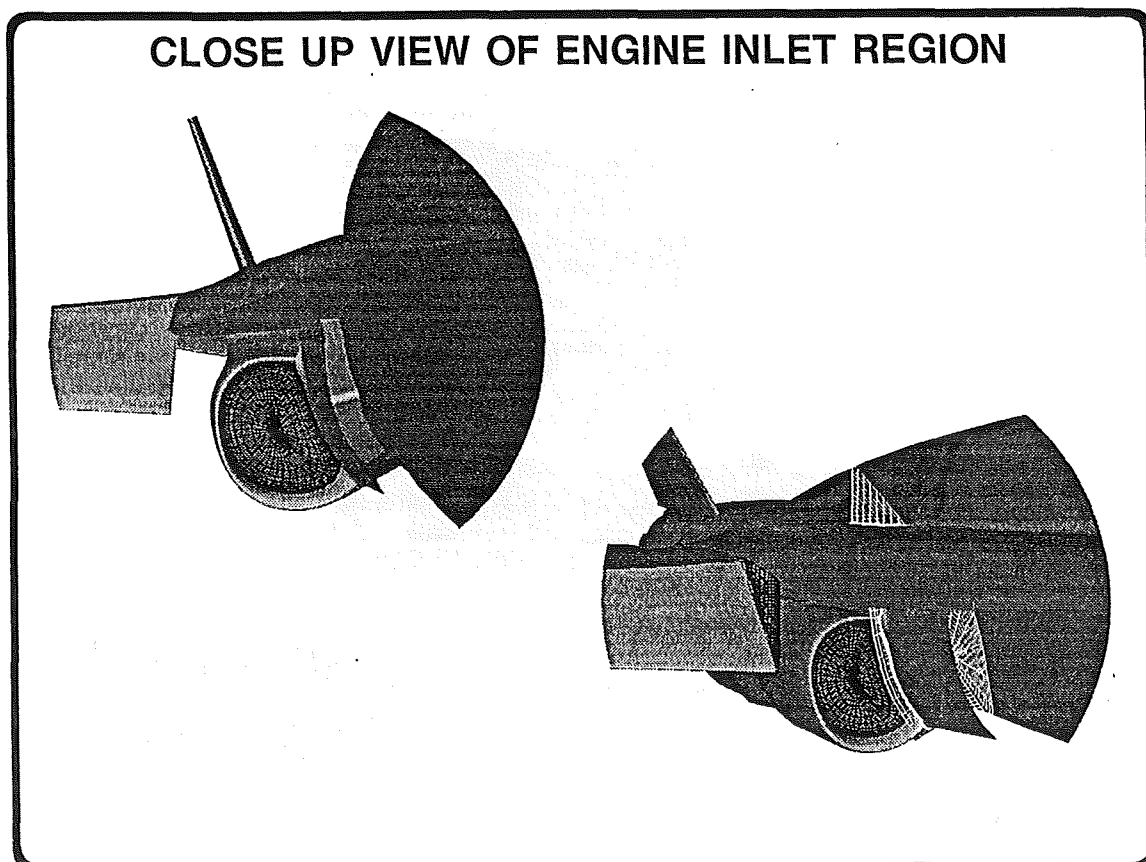
The computational model of the F-18 HARV is a continuing evolution of previous models. The current model has a finer grid spacing in the fuselage and LEX regions, and resolves the engine inlet region in greater detail. The figure shows the separate grids about the major components of the aircraft and how they overlap in the Chimera approach. The model contains 1.7 million grid points in 14 separate zones (15 zones for the $\alpha = 45^\circ$ computations). It models all of the major components of the HARV, including the LEX, wing and leading-edge flap, and the horizontal and vertical tails. The wing-leading-edge flap and horizontal stabilizer are both scheduled with angle of attack in the computations.



CURRENT F-18 COMPUTATIONAL MODEL

- * 1.7 MILLION GRID POINTS FOR A SYMMETRIC COMPUTATION
- * 14 STRUCTURED ZONES (13 NAVIER-STOKES)
- * MODELS LEX, EMPENNAGE, DEFLECTED FLAP, AND INLET REGION
- * MATCHES IN-FLIGHT ENGINE MASS FLOW RATES

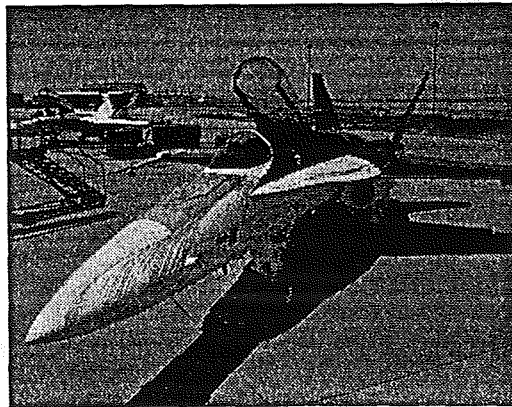
This figure shows a close-up view of the engine inlet region of the HARV computational geometry. The major details of the region are modeled, including the boundary layer diverter and vent, and the engine cowling and diffuser. At the engine compressor face, a nozzle is added which forces the flow to choke at the throat of the nozzle. In this manner, different engine inlet mass flow rates can be simulated by opening or constricting the throat of this nozzle. The current computations are carried out at the maximum engine power setting in all cases (≈ 60 lbm/sec per engine).



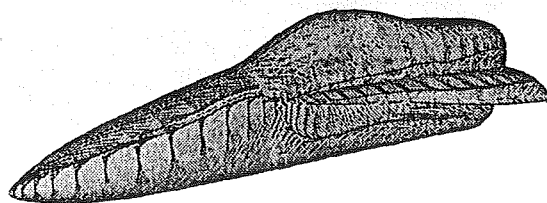
This view graph compares the computed and flight-test oil-flow patterns on the F-18 forebody and LEX at $\alpha = 30^\circ$. The computations were carried out using the full-aircraft configuration. The HARV oil-flow pattern shows the lines of primary and secondary crossflow separation on the fuselage forebody. A primary crossflow separation occurs at the leading edge of the LEX, and the oil flow photo shows lines of secondary and tertiary separation on the upper surface of the LEX. The current computation shows an improvement in the resolution of the forebody secondary separation in comparison to that of a previous solution. The current computation also resolves the details of the secondary and tertiary separation patterns on the leeward side of the LEX. In addition, details of an additional primary and secondary crossflow separation pattern located on the side of the fuselage under the LEX can be seen in the present solution.

FUSELAGE SURFACE FLOW VISUALIZATION

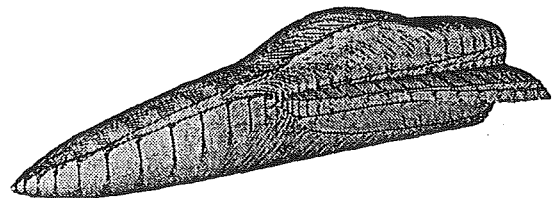
($\alpha = 30.3^\circ$, $M_{inf} = 0.243$, $Re_c = 10.9 \times 10^6$)



FLIGHT-TEST OIL FLOW



PREVIOUS COMPUTATION

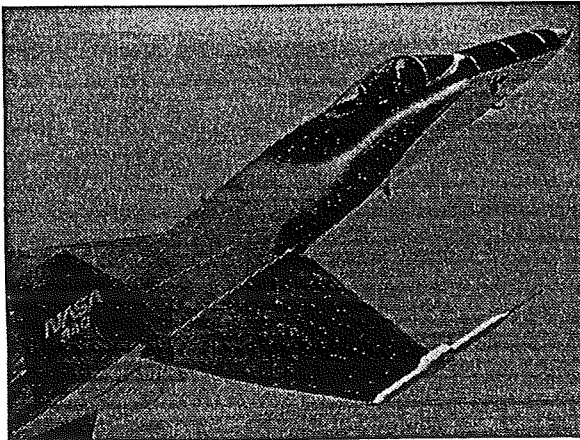


CURRENT COMPUTATION

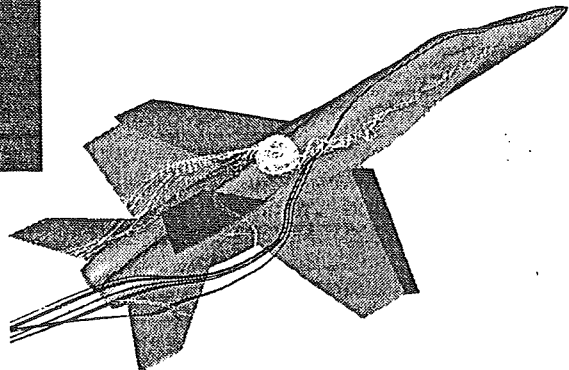
Particle trajectories (instantaneous streaklines) released from the tip of the forebody and the apex of the LEX in the present $\alpha = 30^\circ$ computation show the path of the forebody and LEX vortices. The flight-test smoke flow visualization is shown for comparison. The slow expansion of the vortex core upstream of breakdown, and the loss of core structure starting in the vicinity of the LEX-wing junction can be seen. The computed vortex breakdown occurs slightly further downstream than is observed in flight.

LEX VORTEX PARTICLE TRAJECTORY

($\alpha = 30.3^\circ$, $M_{inf} = 0.243$, $Re_c = 10.9 \times 10^6$)

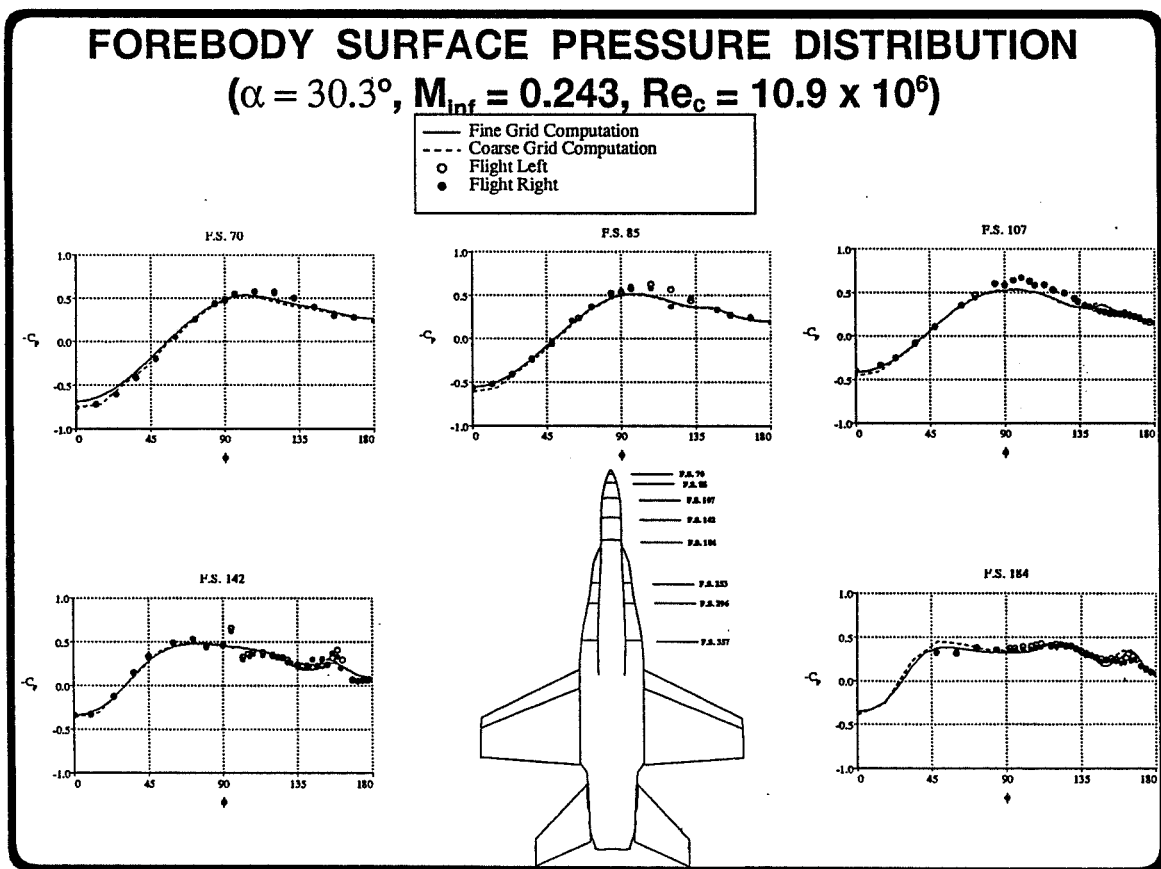


FLIGHT-TEST VISUALIZATION

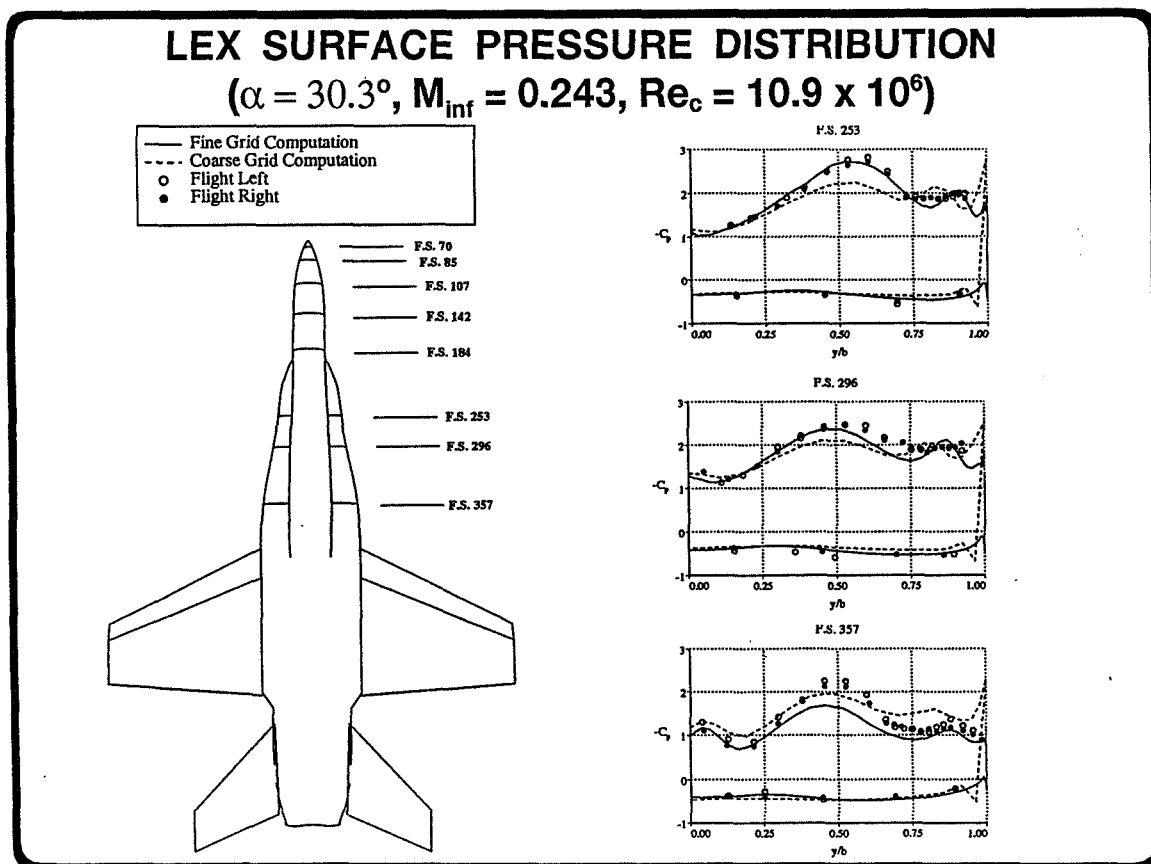


CURRENT FINE-GRID COMPUTATION

Here, the computed surface pressure distribution on the fuselage forebody at axial stations corresponding to the F-18 HARV pressure port locations are shown. The present computed results and previous results obtained on a coarser computational grid are compared to the flight-test data. Both computations show a good agreement with the flight data at all stations on the forebody, including the region of the primary forebody vortices which are seen at F.S. 142 and F.S. 184 near $\phi = 160^\circ$. The discrepancy at $\phi = 90^\circ$ and F.S. 142 is caused by an antenna fairing on the aircraft which is not modeled in the computation.

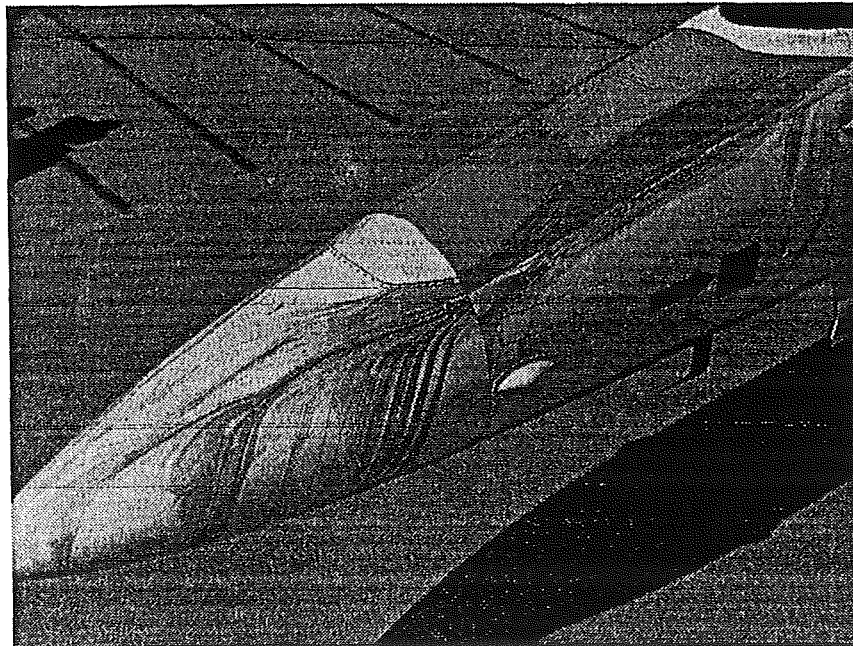


The current computational results show a markedly improved comparison with the flight measurements in the region of the LEX vortex. At F.S. 253 and F.S. 296, upstream of the LEX vortex breakdown position, the present computational suction peaks are in good agreement with the flight measurements. In contrast, the coarser-grid results do not adequately resolve the primary vortex suction peak. At $\alpha = 30^\circ$, vortex breakdown occurs on the aircraft at a fuselage station of F.S. ≈ 335 . This results in the change in the shape of the pressure distribution between that measured at F.S. 296 and that measured at F.S. 357 in the flight data. The present computations indicate that vortex breakdown occurs at F.S. ≈ 375 , aft of that observed in the flight testing. Thus, the comparison between computation and flight at F.S. 357 are not in as good agreement. Note that the coarser-grid solutions indicate vortex breakdown occurs at F.S. ≈ 435 , even farther aft of the actual breakdown position, and the vortex suction peak for the coarser-grid computation remains high between F.S. 296 and F.S. 357.

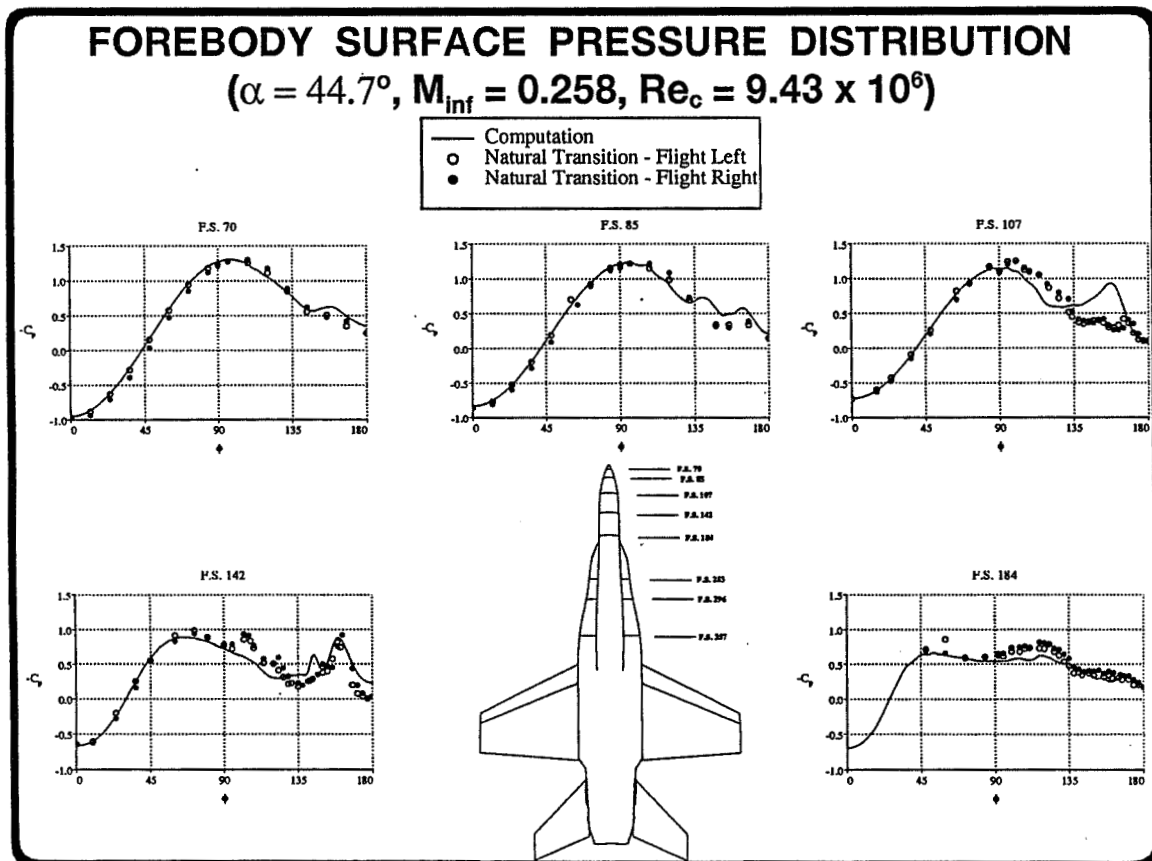


The current computational model has also been used to compute the flow about the F-18 HARV at 45° angle of attack. At $\alpha = 45^\circ$, the HARV forebody flow was found to contain relatively large regions of laminar and transitional flow, extending approximately 4 ft. aft from the tip of the nose (cf. Fisher et al. "In-Flight Flow Visualization Characteristics of the NASA F-18 High Alpha Research Vehicle at High Angles of Attack," NASA TM 4193). In order to promote transition and thus contract this region, the HARV was also flown with transition strips applied along the forebody. The flowfield at this higher angle of attack has been computed as fully turbulent, and the accuracy of this approximation is evaluated by comparison with flight-test data having both natural transition, and forced transition using the fuselage strips.

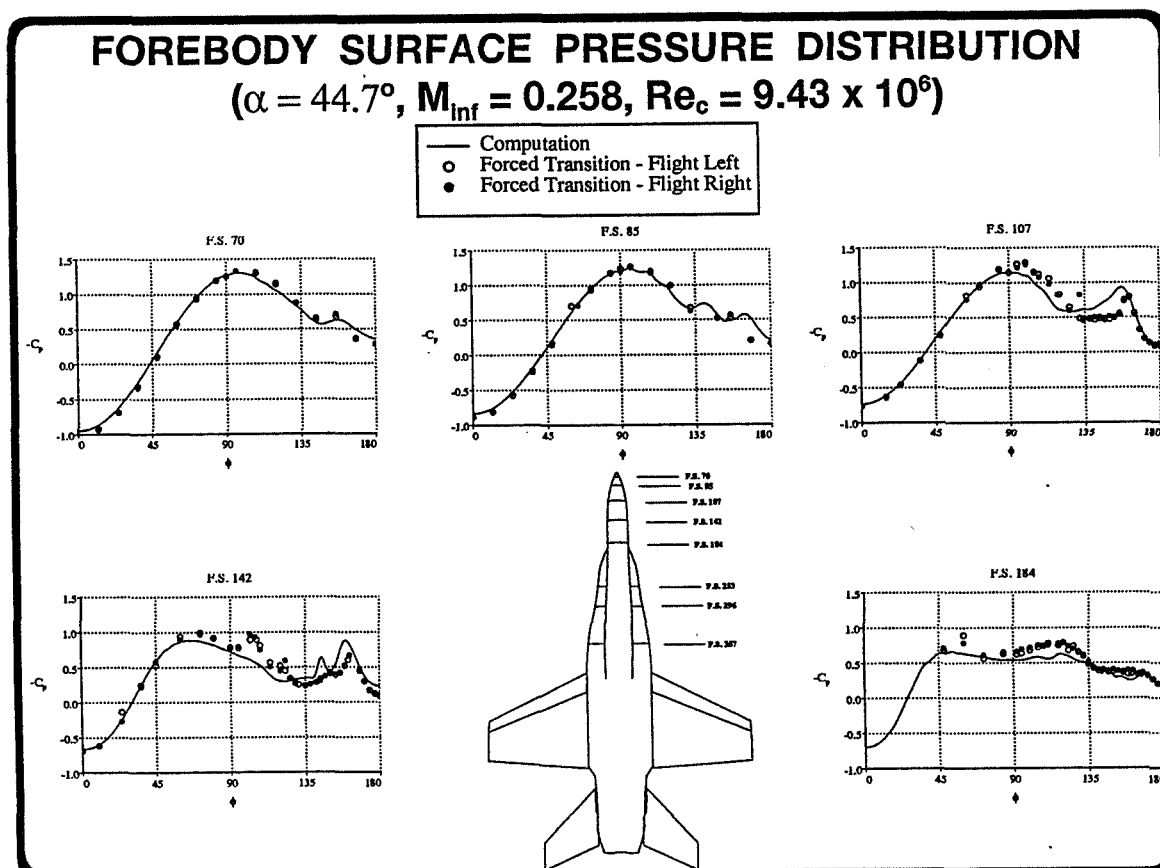
FLIGHT-TEST SURFACE FLOW VISUALIZATION $\alpha = 47^\circ$



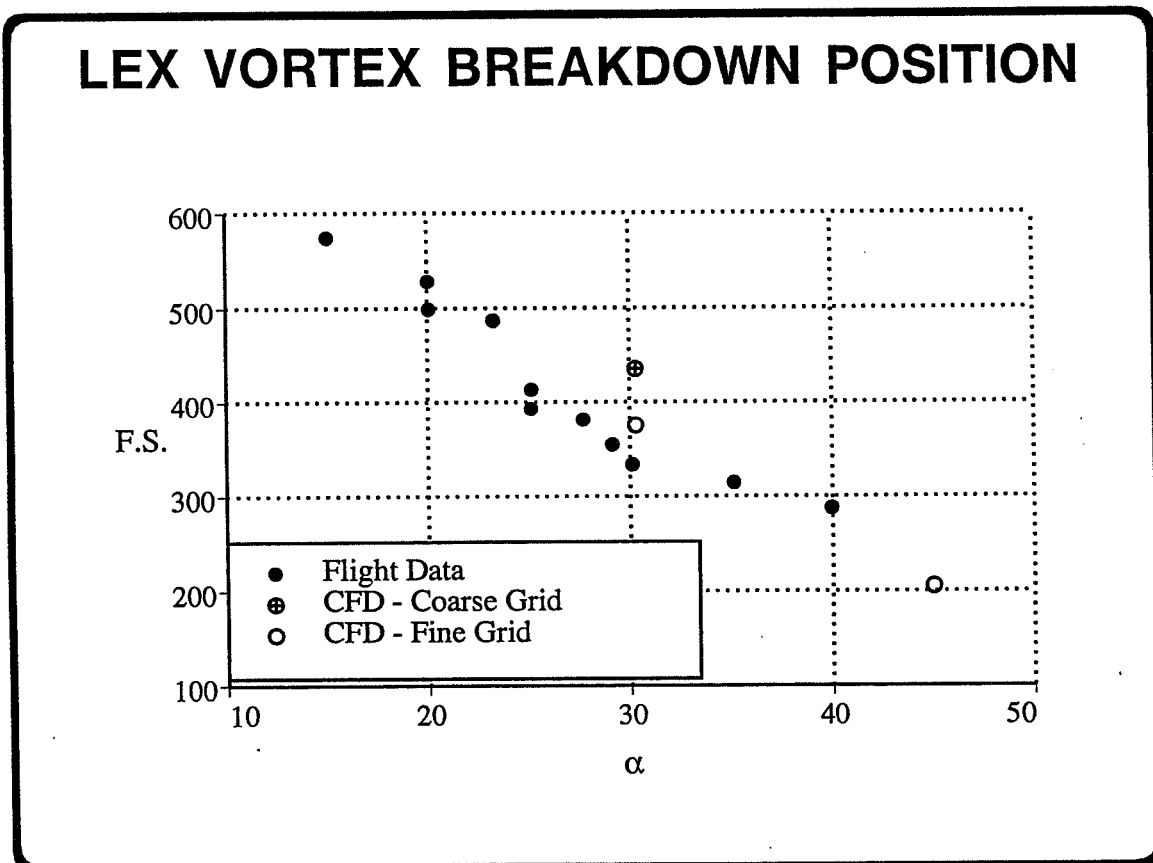
The computed surface pressure distributions on the fuselage forebody at $\alpha = 45^\circ$ are compared to the flight data obtained allowing natural transition on the forebody. The computed results show a good agreement with the flight data at all stations on the windward side of the body where the boundary layer remains attached. On the leeward side of the body ($\phi = 135^\circ - 190^\circ$), the agreement is not as good at the first three axial locations. A strong primary vortex suction peak is seen in the computations, but does not appear in the flight-test data until F.S. 142. This discrepancy is likely due to the assumption of fully turbulent flow which is made in the computations.



Here, the computed surface pressure distributions at $\alpha = 45^\circ$ are compared to the flight-test data that was obtained with the transition strips in place. The comparison of the computed results with the flight data is improved, especially at F.S. 107, where the flight data with forced transition shows a primary vortex suction peak has formed. At the stations further downstream of the nose the flow is more nearly fully turbulent, and the accuracy of the fully turbulent computations improves. Again, an antenna fairing is present near $\phi = 90^\circ$ at F.S. 142 on the aircraft.

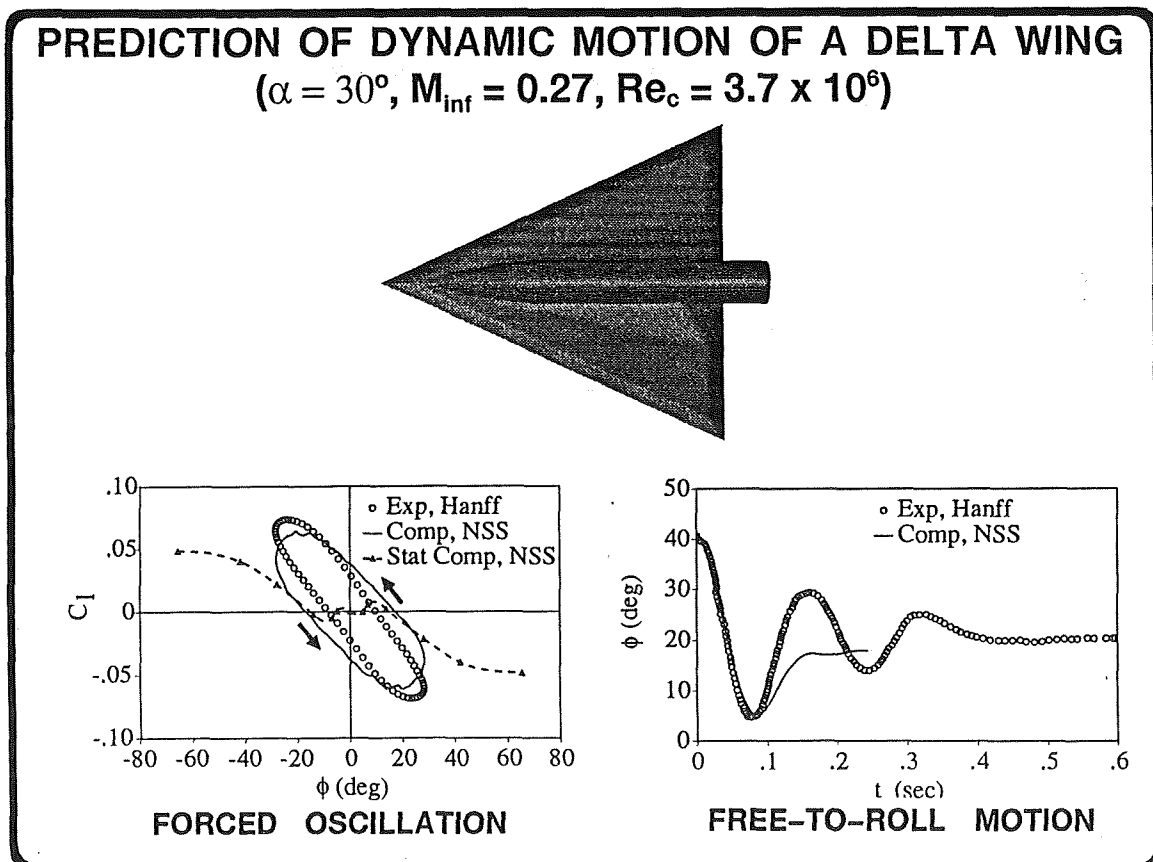


The computed LEX vortex breakdown position is compared to the measured vortex breakdown in the flight tests. The current computational model shows an improvement in the predicted breakdown position. At $\alpha = 45^\circ$, the LEX vortex breaks down very near the apex of the LEX.



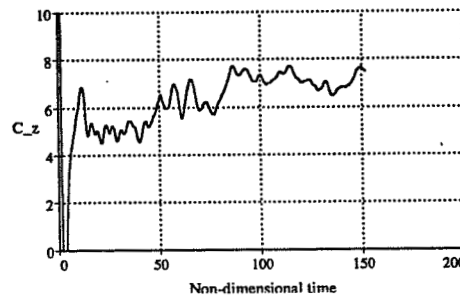
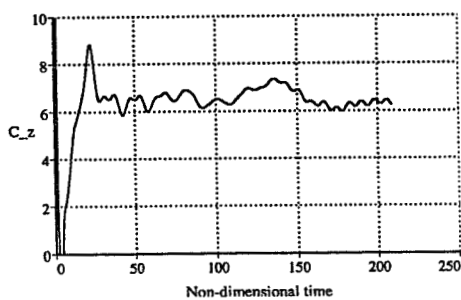
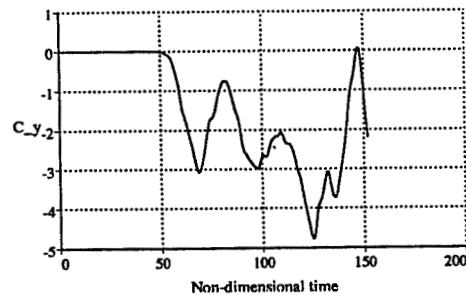
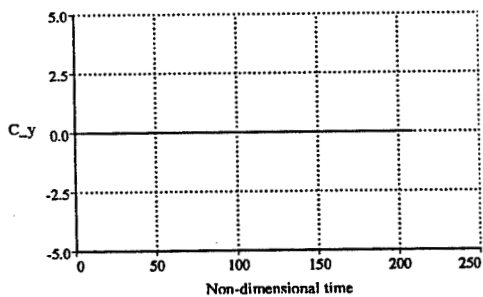
At sufficiently high angles of attack, vortex asymmetries can form over the F-18 and induce dynamic motions such as wing rock. Recently, numerical methods similar to those used in the F-18 computations have been used to investigate aerodynamic-induced roll motions. This view graph presents an overview of the research done by Chaderjian and Schiff for a 65° sweep delta wing¹. The results of two dynamic computations are presented, one a large-amplitude, high-rate forced-roll motion, and the second a damped free-to-roll motion. The free-to-roll motion is computed by coupling the Navier-Stokes equations with the flight dynamic equation of roll motion. In the forced-roll case, the computed and experimental dynamic rolling-moment coefficients (C_l) are in good agreement with each other. The area enclosed by a dynamic C_l curve indicates the amount of work done by the fluid on the wing. The computation shows a larger enclosed area than the experiment, indicating that the computation is more highly damped. The effect of increased damping can be seen in the free-to-roll case as the computed time-history of rolling angle agrees well with the experimental data in the first half-cycle, then decays more rapidly. The computed and experimental frequencies are in good agreement.

¹ Chaderjian, N.M. and Schiff, L.B., "Navier-Stokes Prediction of Large-Amplitude Forced and Free-to-Roll Delta-Wing Oscillations," AIAA Paper 94-1884, June, 1994.



Prior to computing the full-aircraft configuration at higher angles of attack ($\alpha = 60^\circ$ and 70°), computations were carried out for the simpler geometry of an ogive-cylinder. The results of these computations show that at $\alpha = 60^\circ$ the ogive-cylinder develops a numerically-induced lateral force. This lateral force does not appear in the similar $\alpha = 40^\circ$ computation. It is important to understand the cause of this behavior before undertaking a more complex full-aircraft computation at $\alpha = 60^\circ$. Research is currently investigating the source of this numerical asymmetry and means of its alleviation.

OGIVE-CYLINDER COMPUTED FORCE HISTORIES



The computational results for the flow about the F-18 HARV at $\alpha = 30^\circ$ show both a good qualitative and quantitative agreement with the flight-test data. The current computational model was able to resolve the details of the forebody and LEX surface flow pattern, better predict the suction peak due to the primary LEX vortex, and improve the predicted position of vortex breakdown. The computations carried out at $\alpha = 45^\circ$ conditions show a good agreement with the flight-data, although the correlation is not as favorable as at $\alpha = 30^\circ$. This is primarily due to the assumption of a fully turbulent flowfield in the computations, while the actual flow contains significant laminar and transitional regions. Finally, similar numerical methods have been used to compute the flow about a delta wing in roll motions.

SUMMARY

- * **COMPUTATIONS AT $\alpha = 30^\circ$ SHOW IMPROVED CORRELATION WITH FLIGHT-TEST DATA**
 - * **DETAILS OF THE FOREBODY AND LEX SURFACE FLOW PATTERN**
 - * **PREDICTION OF THE LEX PRESSURE DISTRIBUTION**
 - * **PREDICTION OF THE LEX VORTEX BREAKDOWN POSITION**
- * **COMPUTATIONS AT $\alpha = 45^\circ$ SHOW A GOOD AGREEMENT WITH THE FLIGHT-TEST PRESSURE DATA, THOUGH NOT AS FAVORABLE AS THE COMPARISON AT 30°**
- * **SIMILAR NUMERICAL METHODS HAVE BEEN SUCCESSFULLY APPLIED TO THE PREDICTION OF DYNAMIC ROLL MOTIONS AT HIGH-ALPHA FLIGHT CONDITIONS**

The areas that are currently being investigated are the development of a transition model suitable for use in high-alpha flows about slender bodies, and the cause of the numerical asymmetry that develops in computations about ogive-cylinder configurations at $\alpha = 60^\circ$. When these issues are resolved, it is intended that the flowfield about the full F-18 aircraft will be re-computed at $\alpha = 45^\circ$ and a computation will be undertaken at $\alpha = 60^\circ$.

FUTURE RESEARCH

- * DEVELOP A TRANSITION MODEL FOR HIGH-ALPHA FLOWFIELDS AND APPLY IT TO THE F-18 HARV FUSELAGE FOREBODY**
- * RESOLVE THE SOURCE AND INFLUENCE OF THE NUMERICALLY INDUCED ASYMMETRIC FLOW DEVELOPED ABOUT OGIVE-CYLINDER CONFIGURATIONS AT $\alpha = 60^\circ$**
- * COMPUTE THE FLOW ABOUT THE F-18 HARV AT 45° AND 60° ANGLE OF ATTACK**

The current research is aimed at developing and extending numerical methods to accurately predict the high Reynolds number flow about the NASA F-18 HARV at large angles of attack. The resulting codes are validated by comparison of the numerical results with in-flight aerodynamic measurements and flow visualization obtained on the HARV. Further, computations have been used to provide an analysis and numerical optimization of a pneumatic slot blowing concept, and a mechanical strake concept, for use as potential forebody flow control devices in improving high-alpha maneuverability (cf. Gee, et al. These proceedings).

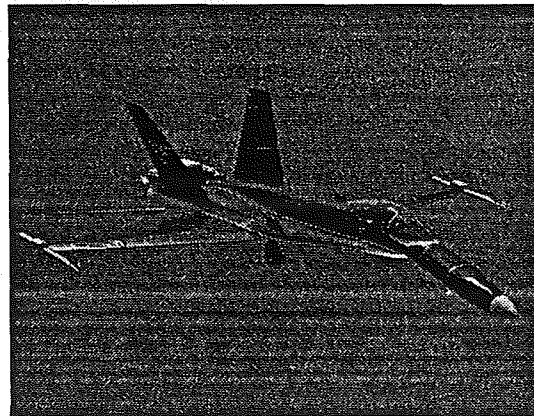
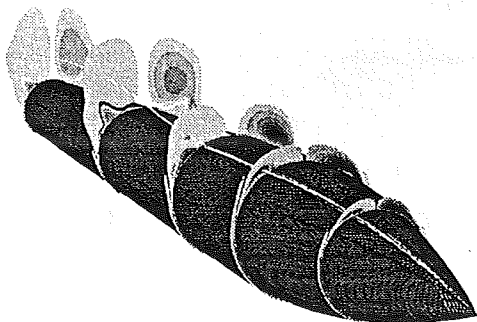
MOTIVATION

- * PROVIDE FLIGHT-VALIDATED NUMERICAL METHODS FOR COMPUTING THE FLOW ABOUT AIRCRAFT OPERATING IN THE HIGH-APLHA REGIME**

- * USE THESE METHODS TO PROVIDE AN ANALYSIS AND OPTIMIZATION OF NEW CONTROL CONCEPTS FOR HIGH-ALPHA MANEUVERABILITY**

Computation of the flow about the F-18 HARV at high alpha provides a challenge for numerical methods because of the complex physics involved and the complex geometry of a full-aircraft configuration. Since the computations are carried out to match actual flight operating conditions, the Navier-Stokes equations must be solved. Further, the flow about the majority of the aircraft is turbulent, and the computations must include suitable turbulence models. These models must be applied in a rational manner to account for the massive 3-D separation that occurs at large incidence. The complex aircraft geometry is modeled using structured, overlapped grids in what is termed a Chimera approach. This method allows grids to be generated about the separate components of the aircraft and then combined, greatly simplifying the grid generation procedure. This approach also allows the use of different numerical schemes in different regions of the aircraft, depending upon the physics encountered.

CHALLENGES TO HIGH-ALPHA CFD

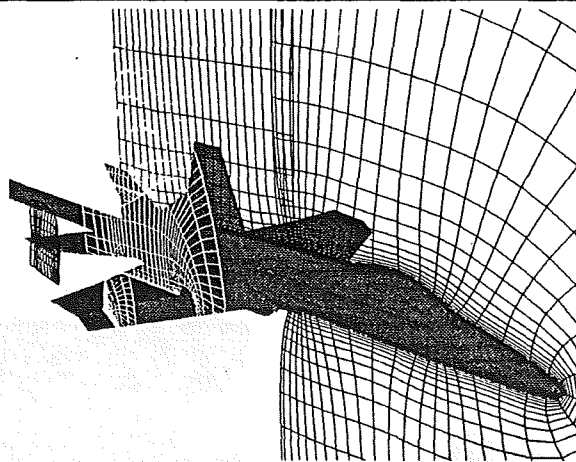


COMPLEX PHYSICS

+

COMPLEX GEOMETRY

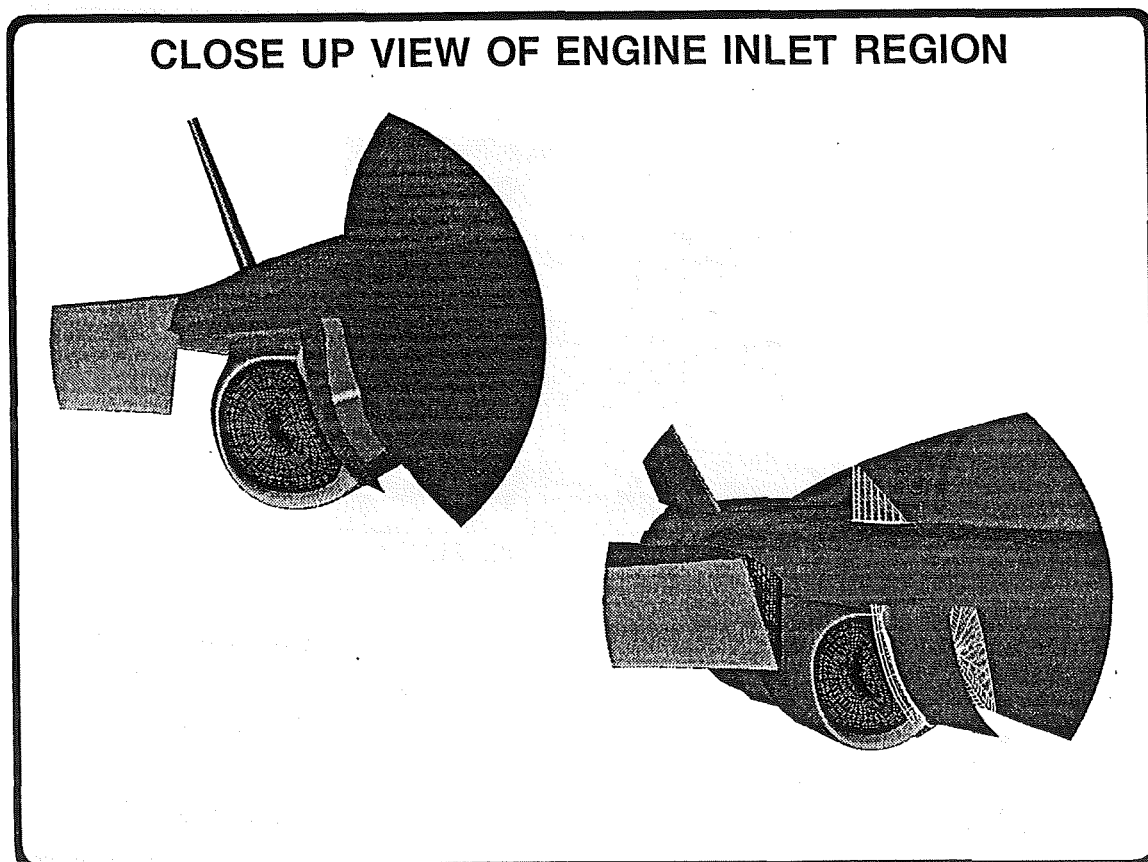
The computational model of the F-18 HARV is a continuing evolution of previous models. The current model has a finer grid spacing in the fuselage and LEX regions, and resolves the engine inlet region in greater detail. The figure shows the separate grids about the major components of the aircraft and how they overlap in the Chimera approach. The model contains 1.7 million grid points in 14 separate zones (15 zones for the $\alpha = 45^\circ$ computations). It models all of the major components of the HARV, including the LEX, wing and leading-edge flap, and the horizontal and vertical tails. The wing-leading-edge flap and horizontal stabilizer are both scheduled with angle of attack in the computations.



CURRENT F-18 COMPUTATIONAL MODEL

- * 1.7 MILLION GRID POINTS FOR A SYMMETRIC COMPUTATION
- * 14 STRUCTURED ZONES (13 NAVIER-STOKES)
- * MODELS LEX, EMPENNAGE, DEFLECTED FLAP, AND INLET REGION
- * MATCHES IN-FLIGHT ENGINE MASS FLOW RATES

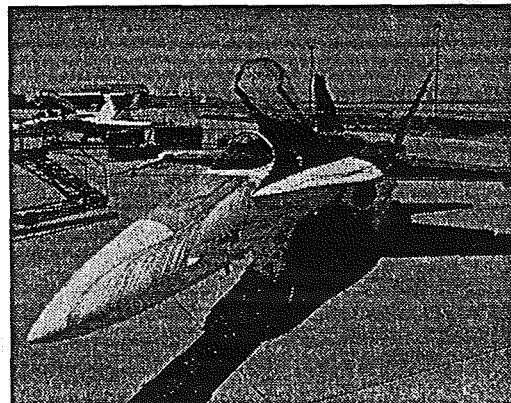
This figure shows a close-up view of the engine inlet region of the HARV computational geometry. The major details of the region are modeled, including the boundary layer diverter and vent, and the engine cowling and diffuser. At the engine compressor face, a nozzle is added which forces the flow to choke at the throat of the nozzle. In this manner, different engine inlet mass flow rates can be simulated by opening or constricting the throat of this nozzle. The current computations are carried out at the maximum engine power setting in all cases (≈ 60 lbm/sec per engine).



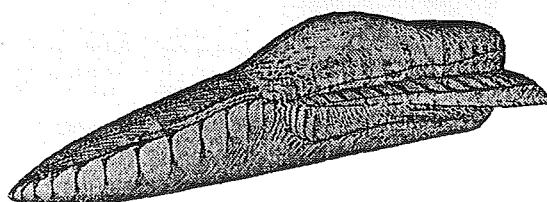
This view graph compares the computed and flight-test oil-flow patterns on the F-18 forebody and LEX at $\alpha = 30^\circ$. The computations were carried out using the full-aircraft configuration. The HARV oil-flow pattern shows the lines of primary and secondary crossflow separation on the fuselage forebody. A primary crossflow separation occurs at the leading edge of the LEX, and the oil flow photo shows lines of secondary and tertiary separation on the upper surface of the LEX. The current computation shows an improvement in the resolution of the forebody secondary separation in comparison to that of a previous solution. The current computation also resolves the details of the secondary and tertiary separation patterns on the leeward side of the LEX. In addition, details of an additional primary and secondary crossflow separation pattern located on the side of the fuselage under the LEX can be seen in the present solution.

FUSELAGE SURFACE FLOW VISUALIZATION

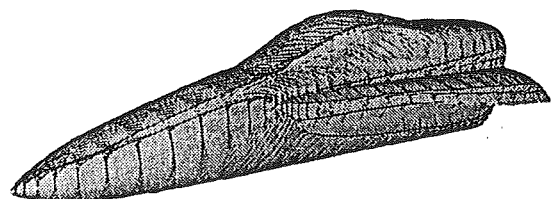
($\alpha = 30.3^\circ$, $M_{inf} = 0.243$, $Re_c = 10.9 \times 10^6$)



FLIGHT-TEST OIL FLOW



PREVIOUS COMPUTATION

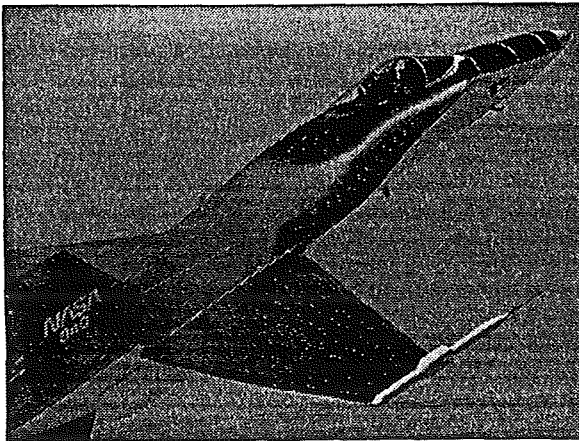


CURRENT COMPUTATION

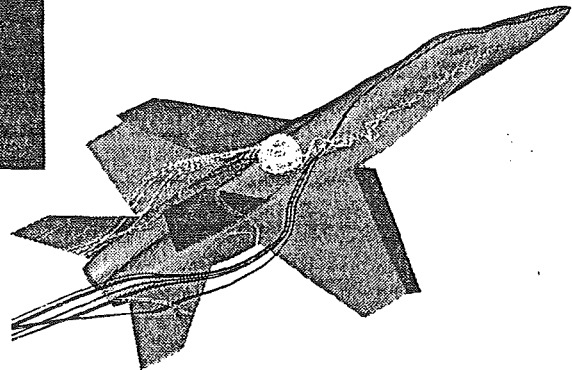
Particle trajectories (instantaneous streaklines) released from the tip of the forebody and the apex of the LEX in the present $\alpha = 30^\circ$ computation show the path of the forebody and LEX vortices. The flight-test smoke flow visualization is shown for comparison. The slow expansion of the vortex core upstream of breakdown, and the loss of core structure starting in the vicinity of the LEX-wing junction can be seen. The computed vortex breakdown occurs slightly further downstream than is observed in flight.

LEX VORTEX PARTICLE TRAJECTORY

($\alpha = 30.3^\circ$, $M_{inf} = 0.243$, $Re_c = 10.9 \times 10^6$)

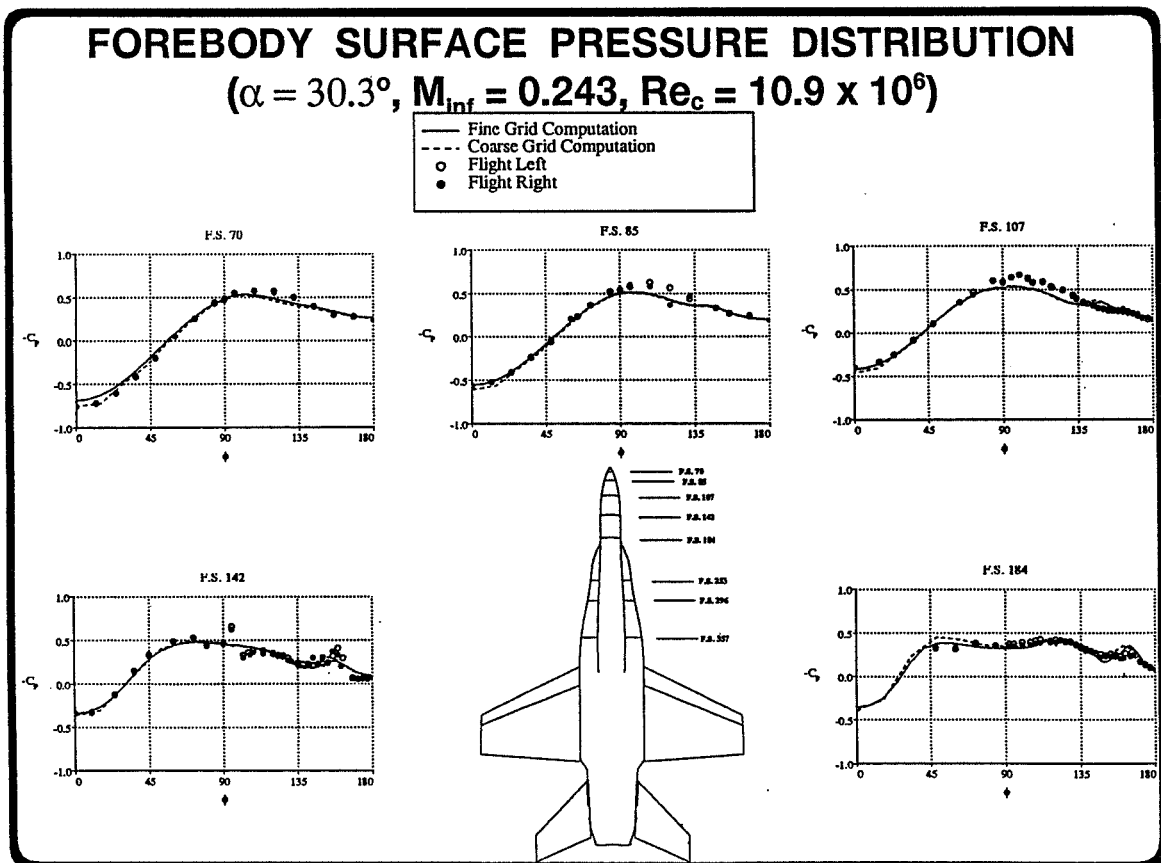


FLIGHT-TEST VISUALIZATION

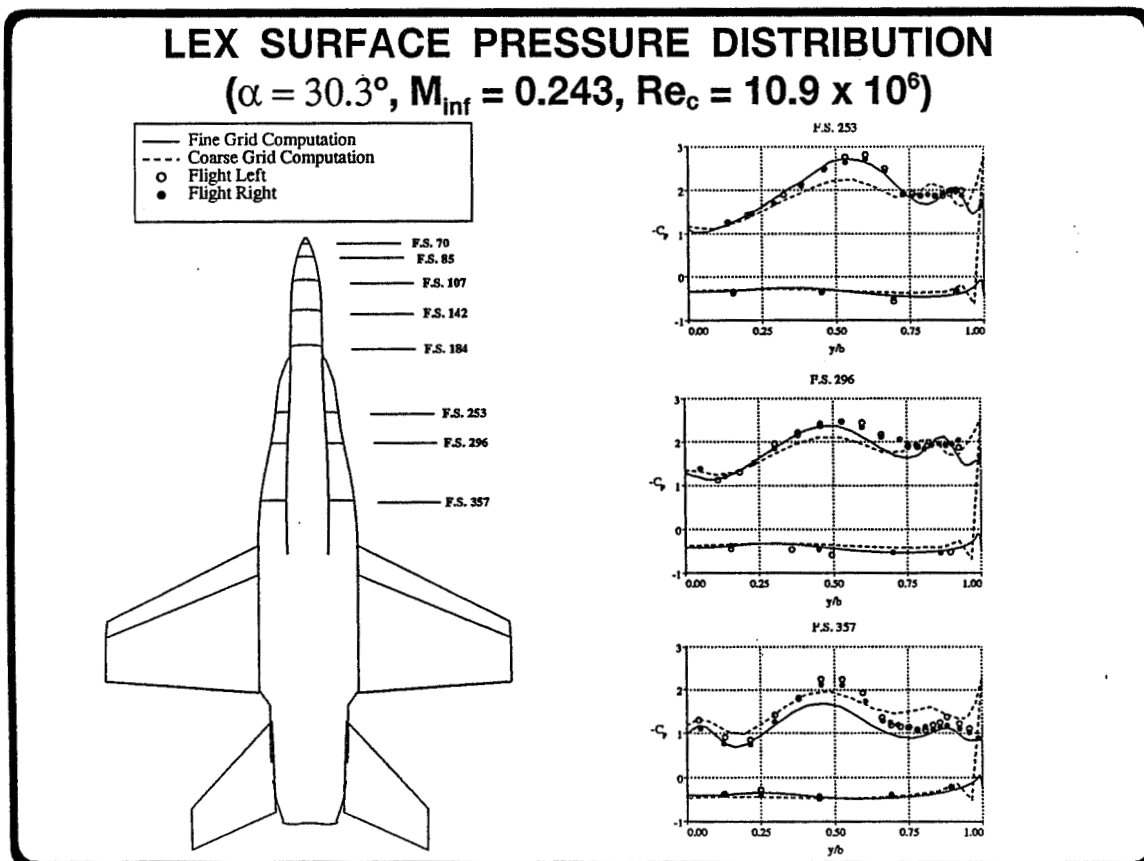


CURRENT FINE-GRID COMPUTATION

Here, the computed surface pressure distribution on the fuselage forebody at axial stations corresponding to the F-18 HARV pressure port locations are shown. The present computed results and previous results obtained on a coarser computational grid are compared to the flight-test data. Both computations show a good agreement with the flight data at all stations on the forebody, including the region of the primary forebody vortices which are seen at F.S. 142 and F.S. 184 near $\phi = 160^\circ$. The discrepancy at $\phi = 90^\circ$ and F.S. 142 is caused by an antenna fairing on the aircraft which is not modeled in the computation.

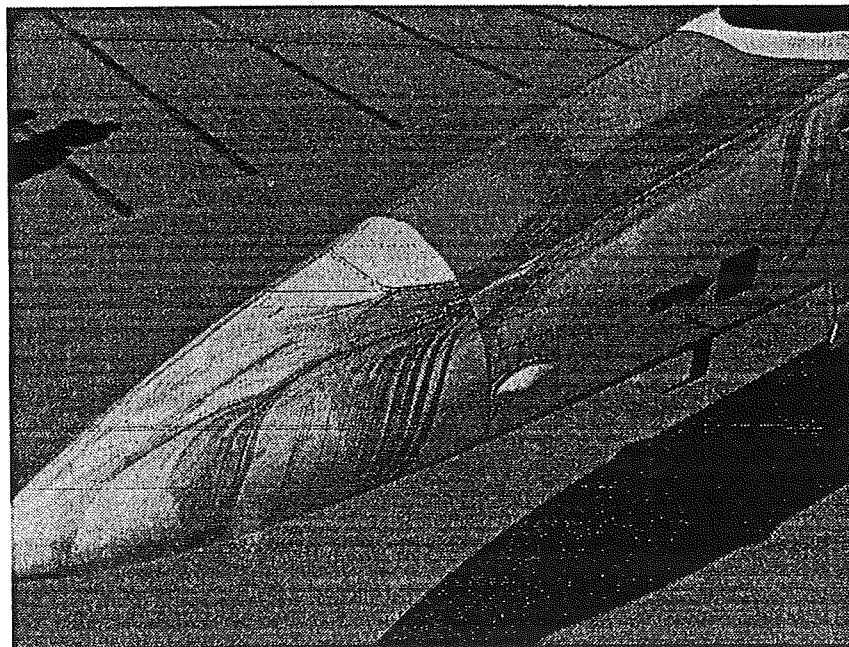


The current computational results show a markedly improved comparison with the flight measurements in the region of the LEX vortex. At F.S. 253 and F.S. 296, upstream of the LEX vortex breakdown position, the present computational suction peaks are in good agreement with the flight measurements. In contrast, the coarser-grid results do not adequately resolve the primary vortex suction peak. At $\alpha = 30^\circ$, vortex breakdown occurs on the aircraft at a fuselage station of F.S. ≈ 335 . This results in the change in the shape of the pressure distribution between that measured at F.S. 296 and that measured at F.S. 357 in the flight data. The present computations indicate that vortex breakdown occurs at F.S. ≈ 375 , aft of that observed in the flight testing. Thus, the comparison between computation and flight at F.S. 357 are not in as good agreement. Note that the coarser-grid solutions indicate vortex breakdown occurs at F.S. ≈ 435 , even farther aft of the actual breakdown position, and the vortex suction peak for the coarser-grid computation remains high between F.S. 296 and F.S. 357.

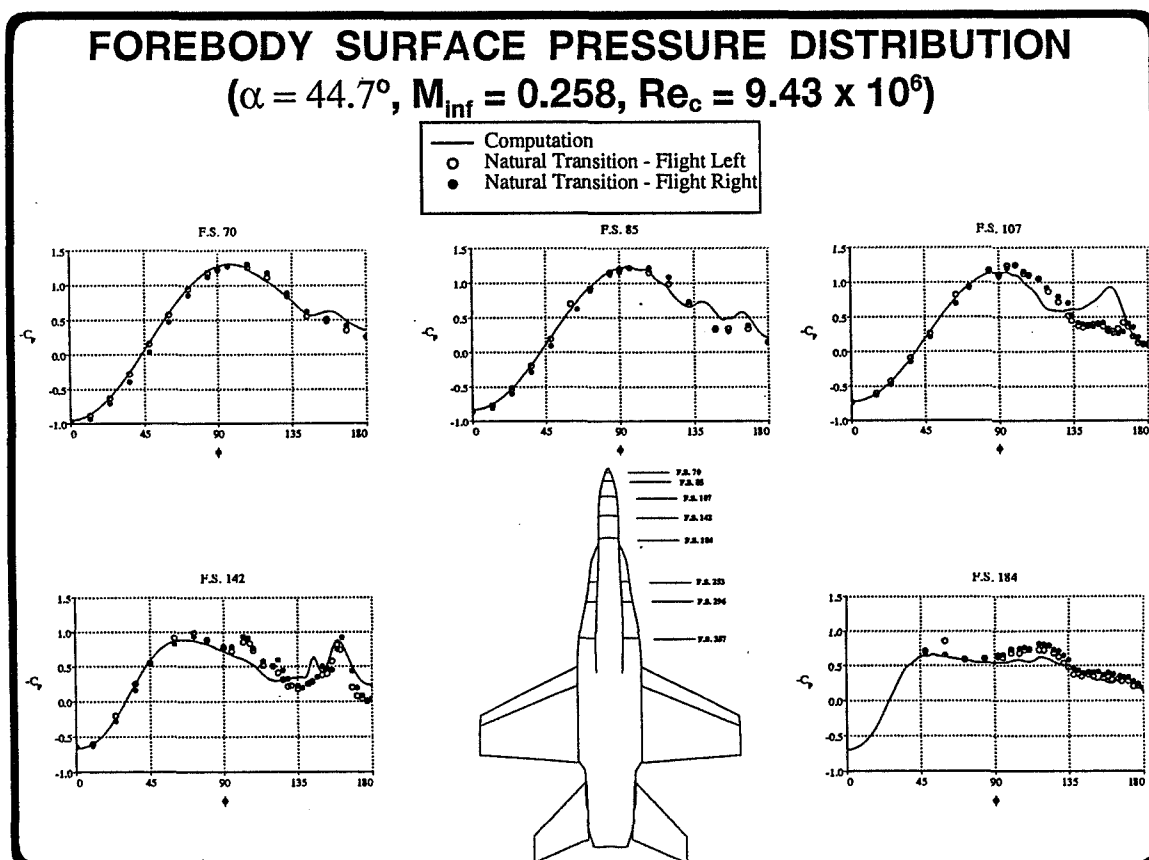


The current computational model has also been used to compute the flow about the F-18 HARV at 45° angle of attack. At $\alpha = 45^\circ$, the HARV forebody flow was found to contain relatively large regions of laminar and transitional flow, extending approximately 4 ft. aft from the tip of the nose (cf. Fisher et al. "In-Flight Flow Visualization Characteristics of the NASA F-18 High Alpha Research Vehicle at High Angles of Attack," NASA TM 4193). In order to promote transition and thus contract this region, the HARV was also flown with transition strips applied along the forebody. The flowfield at this higher angle of attack has been computed as fully turbulent, and the accuracy of this approximation is evaluated by comparison with flight-test data having both natural transition, and forced transition using the fuselage strips.

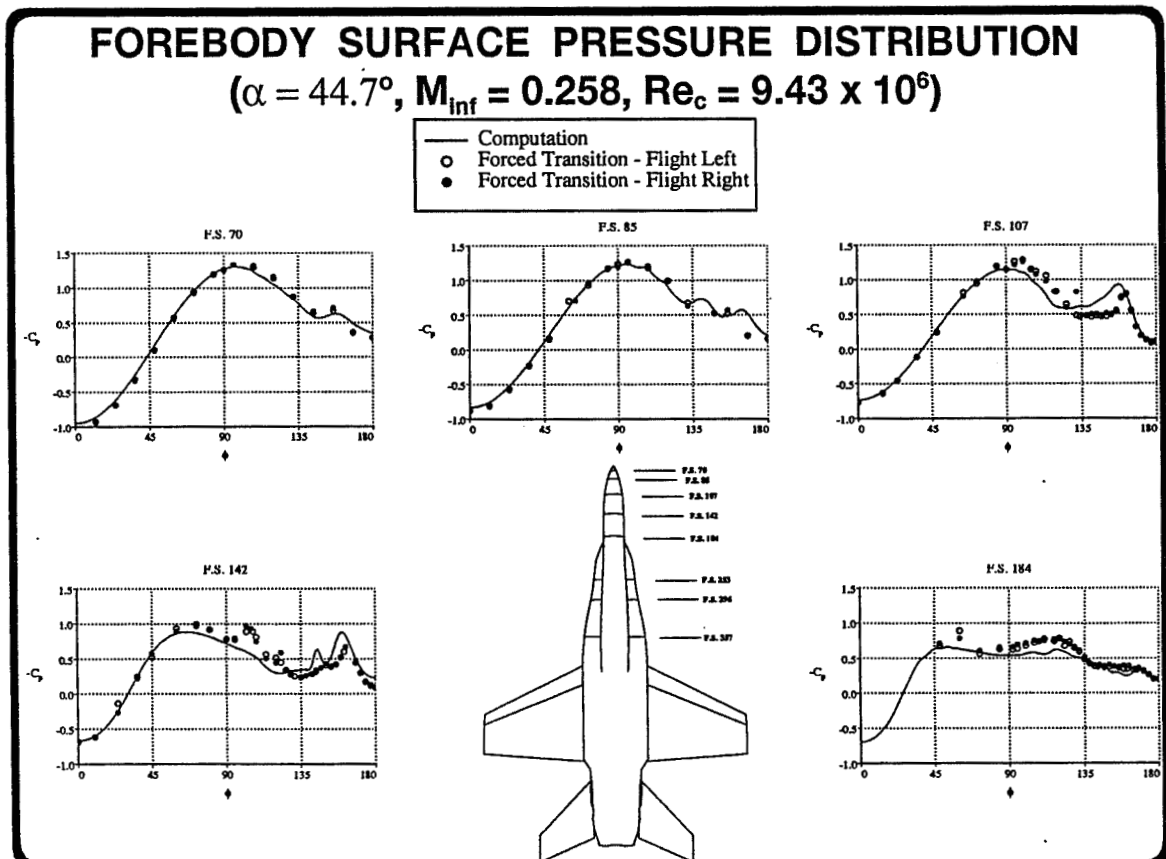
FLIGHT-TEST SURFACE FLOW VISUALIZATION $\alpha = 47^\circ$



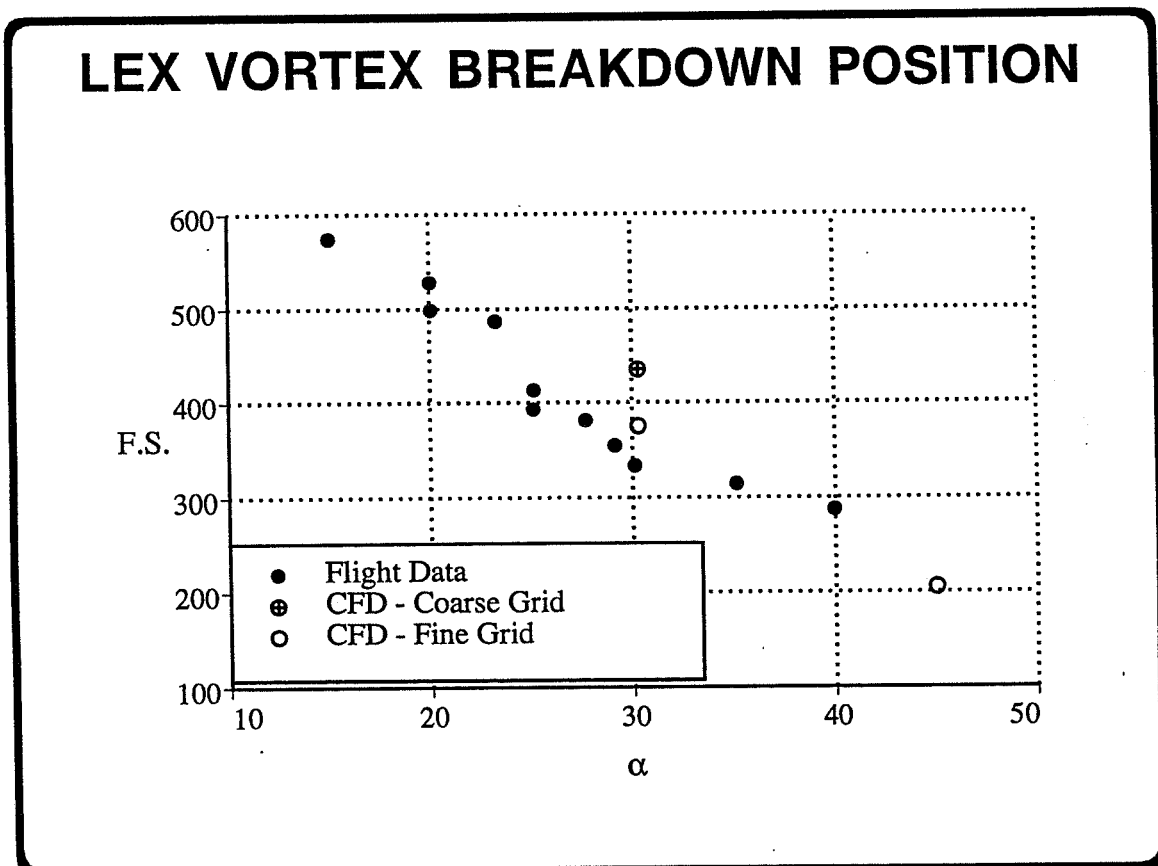
The computed surface pressure distributions on the fuselage forebody at $\alpha = 45^\circ$ are compared to the flight data obtained allowing natural transition on the forebody. The computed results show a good agreement with the flight data at all stations on the windward side of the body where the boundary layer remains attached. On the leeward side of the body ($\phi = 135^\circ - 190^\circ$), the agreement is not as good at the first three axial locations. A strong primary vortex suction peak is seen in the computations, but does not appear in the flight-test data until F.S. 142. This discrepancy is likely due to the assumption of fully turbulent flow which is made in the computations.



Here, the computed surface pressure distributions at $\alpha = 45^\circ$ are compared to the flight-test data that was obtained with the transition strips in place. The comparison of the computed results with the flight data is improved, especially at F.S. 107, where the flight data with forced transition shows a primary vortex suction peak has formed. At the stations further downstream of the nose the flow is more nearly fully turbulent, and the accuracy of the fully turbulent computations improves. Again, an antenna fairing is present near $\phi = 90^\circ$ at F.S. 142 on the aircraft.



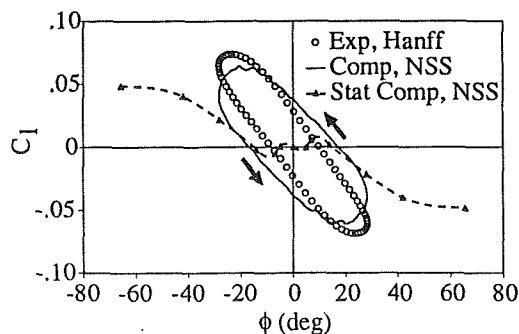
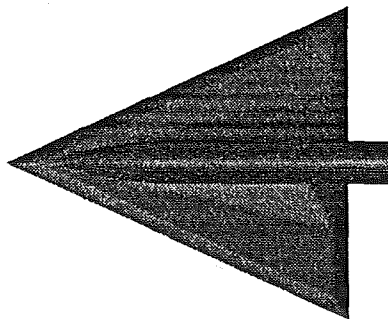
The computed LEX vortex breakdown position is compared to the measured vortex breakdown in the flight tests. The current computational model shows an improvement in the predicted breakdown position. At $\alpha = 45^\circ$, the LEX vortex breaks down very near the apex of the LEX.



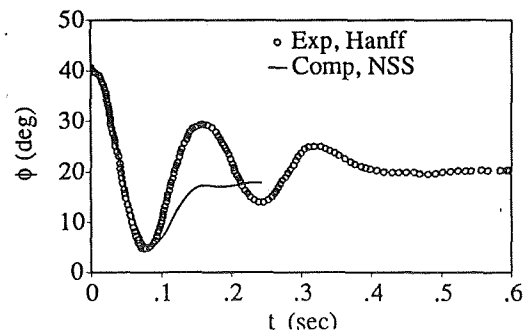
At sufficiently high angles of attack, vortex asymmetries can form over the F-18 and induce dynamic motions such as wing rock. Recently, numerical methods similar to those used in the F-18 computations have been used to investigate aerodynamic-induced roll motions. This view graph presents an overview of the research done by Chaderjian and Schiff for a 65° sweep delta wing¹. The results of two dynamic computations are presented, one a large-amplitude, high-rate forced-roll motion, and the second a damped free-to-roll motion. The free-to-roll motion is computed by coupling the Navier-Stokes equations with the flight dynamic equation of roll motion. In the forced-roll case, the computed and experimental dynamic rolling-moment coefficients (C_l) are in good agreement with each other. The area enclosed by a dynamic C_l curve indicates the amount of work done by the fluid on the wing. The computation shows a larger enclosed area than the experiment, indicating that the computation is more highly damped. The effect of increased damping can be seen in the free-to-roll case as the computed time-history of rolling angle agrees well with the experimental data in the first half-cycle, then decays more rapidly. The computed and experimental frequencies are in good agreement.

¹ Chaderjian, N.M. and Schiff, L.B., "Navier-Stokes Prediction of Large-Amplitude Forced and Free-to-Roll Delta-Wing Oscillations," AIAA Paper 94-1884, June, 1994.

PREDICTION OF DYNAMIC MOTION OF A DELTA WING
 $(\alpha = 30^\circ, M_{inf} = 0.27, Re_c = 3.7 \times 10^6)$



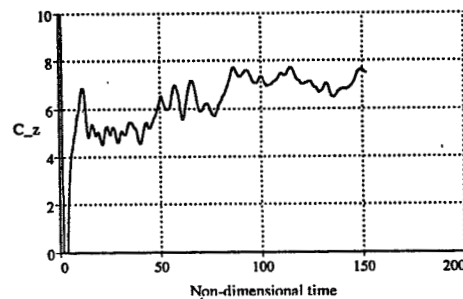
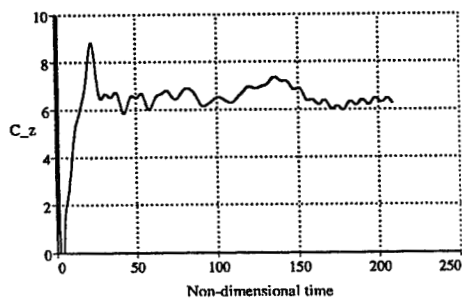
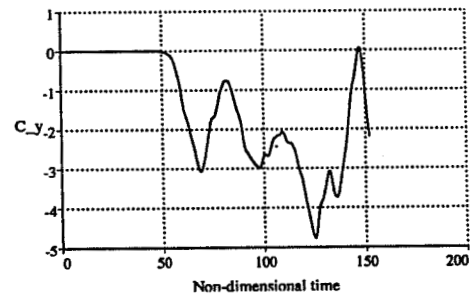
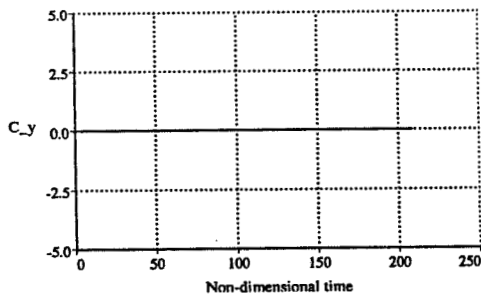
FORCED OSCILLATION



FREE-TO-ROLL MOTION

Prior to computing the full-aircraft configuration at higher angles of attack ($\alpha = 60^\circ$ and 70°), computations were carried out for the simpler geometry of an ogive-cylinder. The results of these computations show that at $\alpha = 60^\circ$ the ogive-cylinder develops a numerically-induced lateral force. This lateral force does not appear in the similar $\alpha = 40^\circ$ computation. It is important to understand the cause of this behavior before undertaking a more complex full-aircraft computation at $\alpha = 60^\circ$. Research is currently investigating the source of this numerical asymmetry and means of its alleviation.

OGIVE-CYLINDER COMPUTED FORCE HISTORIES



The computational results for the flow about the F-18 HARV at $\alpha = 30^\circ$ show both a good qualitative and quantitative agreement with the flight-test data. The current computational model was able to resolve the details of the forebody and LEX surface flow pattern, better predict the suction peak due to the primary LEX vortex, and improve the predicted position of vortex breakdown. The computations carried out at $\alpha = 45^\circ$ conditions show a good agreement with the flight-data, although the correlation is not as favorable as at $\alpha = 30^\circ$. This is primarily due to the assumption of a fully turbulent flowfield in the computations, while the actual flow contains significant laminar and transitional regions. Finally, similar numerical methods have been used to compute the flow about a delta wing in roll motions.

SUMMARY

- * **COMPUTATIONS AT $\alpha = 30^\circ$ SHOW IMPROVED CORRELATION WITH FLIGHT-TEST DATA**
 - * **DETAILS OF THE FOREBODY AND LEX SURFACE FLOW PATTERN**
 - * **PREDICTION OF THE LEX PRESSURE DISTRIBUTION**
 - * **PREDICTION OF THE LEX VORTEX BREAKDOWN POSITION**
- * **COMPUTATIONS AT $\alpha = 45^\circ$ SHOW A GOOD AGREEMENT WITH THE FLIGHT-TEST PRESSURE DATA, THOUGH NOT AS FAVORABLE AS THE COMPARISON AT 30°**
- * **SIMILAR NUMERICAL METHODS HAVE BEEN SUCCESSFULLY APPLIED TO THE PREDICTION OF DYNAMIC ROLL MOTIONS AT HIGH-ALPHA FLIGHT CONDITIONS**

The areas that are currently being investigated are the development of a transition model suitable for use in high-alpha flows about slender bodies, and the cause of the numerical asymmetry that develops in computations about ogive-cylinder configurations at $\alpha = 60^\circ$. When these issues are resolved, it is intended that the flowfield about the full F-18 aircraft will be re-computed at $\alpha = 45^\circ$ and a computation will be undertaken at $\alpha = 60^\circ$.

FUTURE RESEARCH

- * **DEVELOP A TRANSITION MODEL FOR HIGH-ALPHA FLOWFIELDS AND APPLY IT TO THE F-18 HARV FUSELAGE FOREBODY**
- * **RESOLVE THE SOURCE AND INFLUENCE OF THE NUMERICALLY INDUCED ASYMMETRIC FLOW DEVELOPED ABOUT OGIVE-CYLINDER CONFIGURATIONS AT $\alpha = 60^\circ$**
- * **COMPUTE THE FLOW ABOUT THE F-18 HARV AT 45° AND 60° ANGLE OF ATTACK**

18 p3

1995101819

324025

N95-14233

**Hybrid Structured/Unstructured Grid Computations for the
F/A - 18 at High Angle of Attack**

54-02
16082
p-17

***Hybrid Structured/Unstructured
Grid Computations for the F/A-18
at High Angle of Attack***

***Robert T. Biedron and David L. Whitaker*
Analytical Services and Materials, Inc.
Hampton, Virginia***

**** Currently with Cray Research, Inc., Eagan, Minnesota***

Background

At high angles of attack, vortical flows play a crucial role in the maintenance of lift for fighter aircraft. However, under certain conditions, the vortical flow can have an adverse effect on the aircraft. On the F/A-18 the LEX vortex can impinge on the tail; at high angles of attack the unsteady flow from vortex bursting can cause structural fatigue on the vertical tails.

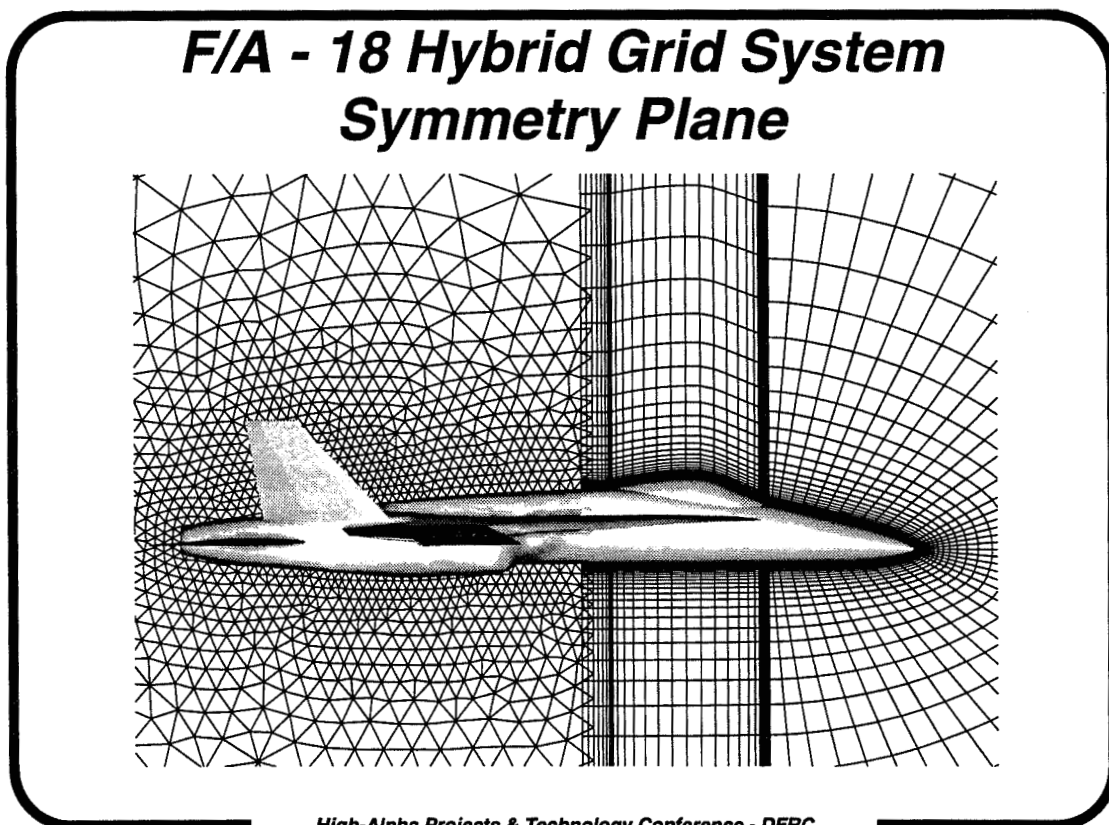
At high angles of attack, the flow field can be quite complex, and a computational analysis challenging. A full configuration analysis with viscous structured grids can be computationally expensive and the task of generating the requisite grids can be quite difficult. To mitigate these difficulties and provide a medium-fidelity analysis tool, a hybrid structured/unstructured approach was adopted for this work. In this analysis, the formation and roll-up of the LEX vortex is computed with a structured Navier-Stokes solver, and the resulting vortex propagated downstream with an unstructured Euler solver.

Background

- ***Motivation: Analysis of vortex-tail interaction***
 - ***At high alpha, LEX vortex impinges on tail, causing structural fatigue***
 - ***Full configuration analysis with viscous structured grid computationally expensive; grid generation difficult***
- ***Adopt a hybrid structured/unstructured approach***
 - ***Model formation and roll-up of vortex with structured NS solution on forebody/LEX***
 - ***Propagate vortex to tail with unstructured Euler solution over remainder of aircraft***

F/A - 18 Hybrid Grid System, Symmetry Plane

The figure shows the symmetry-plane grids of the structured/unstructured hybrid-grid system. The structured zone consists of four blocks, with patched-grid interfaces between blocks (block faces lie on a common surface, but points do not match). The unstructured zone consists of tetrahedra. There is a small amount of overlap between the structured and the unstructured zones, with the overlap occurring near FS 345.



Methodology

Two flow solvers were used in this analysis: CFL3D for the structured, viscous zone and UNS3D for the unstructured Euler zone. Both codes are upwind, finite-volume schemes. CFL3D is cell-center based whereas UNS3D is node based.

Communication between the structured and unstructured zones is obtained via a common overlap region, near station 345 (aft of the canopy). A modified “chimera” scheme is used to transfer data between the zones: volume-weighted interpolation is used to transfer data from the unstructured zone to the structured zone, while tri-linear interpolation is used to transfer data from the structured zone to the unstructured zone.

Methodology

- **Flow solvers**
 - **CFL3D for structured viscous zone**
 - **Upwind, finite-volume; cell-center based**
 - **UNS3D for unstructured Euler zone**
 - **Upwind, finite-volume; node based**
- **Communication between zones via common overlap region, near FS 345 (aft of canopy)**
 - **Volume-weighted interpolation from unstructured zone to structured zone**
 - **Tri-linear interpolation from structured zone to unstructured zone**

Solutions

Solutions have been obtained for three angles of attack: 19, 26 and 30 degrees. Data from the HARV are available at these angles-of-attack for comparison with the computed solutions. The solutions are obtained with local time stepping, that is they are not time accurate. The solutions are obtained as follows. A fixed number of iterations are run in the viscous zone, after which data is transferred to the unstructured zone. A fixed number of iterations is then performed in the unstructured zone, followed by data transfer to the structured zone. This process completes one global iteration. For the results presented here, 10 iterations were used in each zone. Solutions require on the order of 100 global iterations, translating into approximately 10 hours on a Cray YMP.

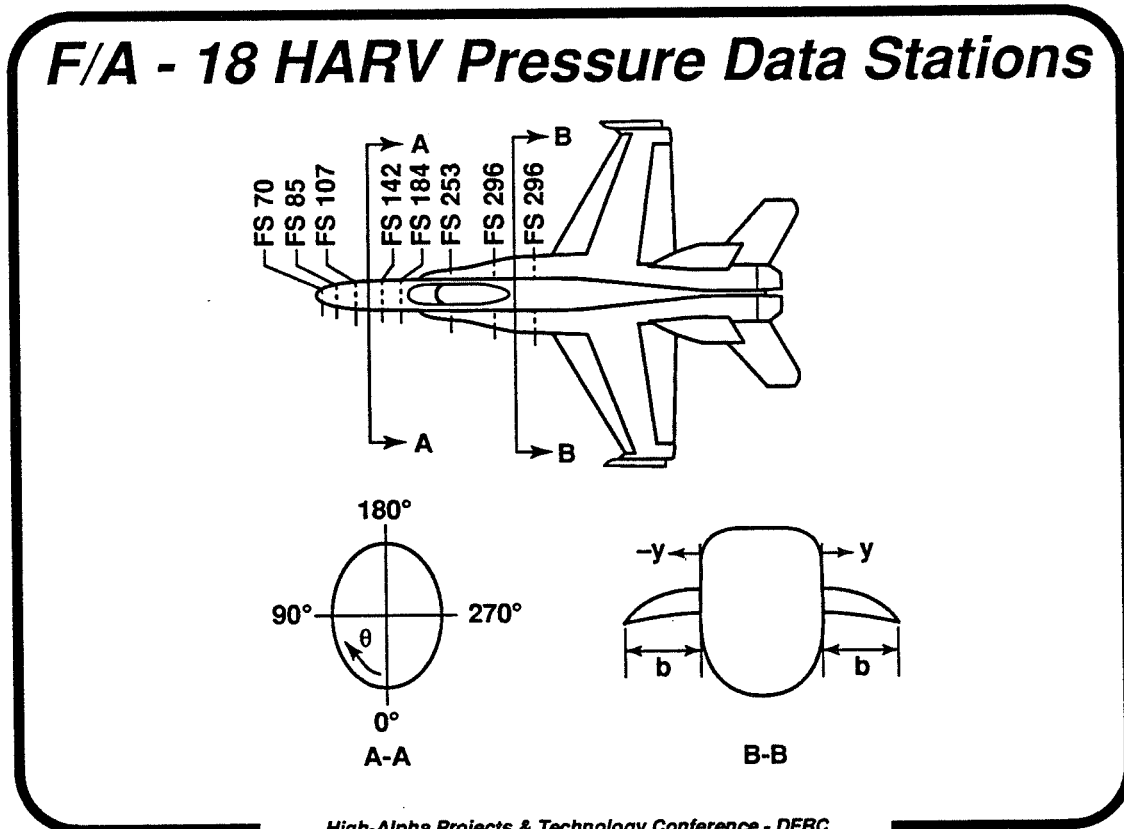
The structured forebody grid system consisted of 4 blocks, with a total of approximately 250,000 cells. The unstructured zone over the aft end of the aircraft consisted of approximately 90,000 nodes forming approximately 495,000 tetrahedra. In the structured zone, the number of unknowns to be solved for is proportional to the number of cells is, whereas in the unstructured zone, the number of unknowns is proportional to the number of nodes

Solutions

- **Solutions obtained for $\alpha = 19^\circ$, $\alpha = 26^\circ$, and $\alpha = 30^\circ$ with local time stepping**
 - **Fixed number of iterations in each zone (~10) comprises 1 global iteration**
 - **Solutions require ~100 global iterations**
 - **Total solution time ~10 hours on Cray YMP**
- **Composite grid statistics**
 - **Forebody (structured) grid comprised of 4 blocks with a total of 250,000 cells**
 - **Aft (unstructured) grid comprised of a single block with 90,000 nodes (495,000 tetrahedra)**

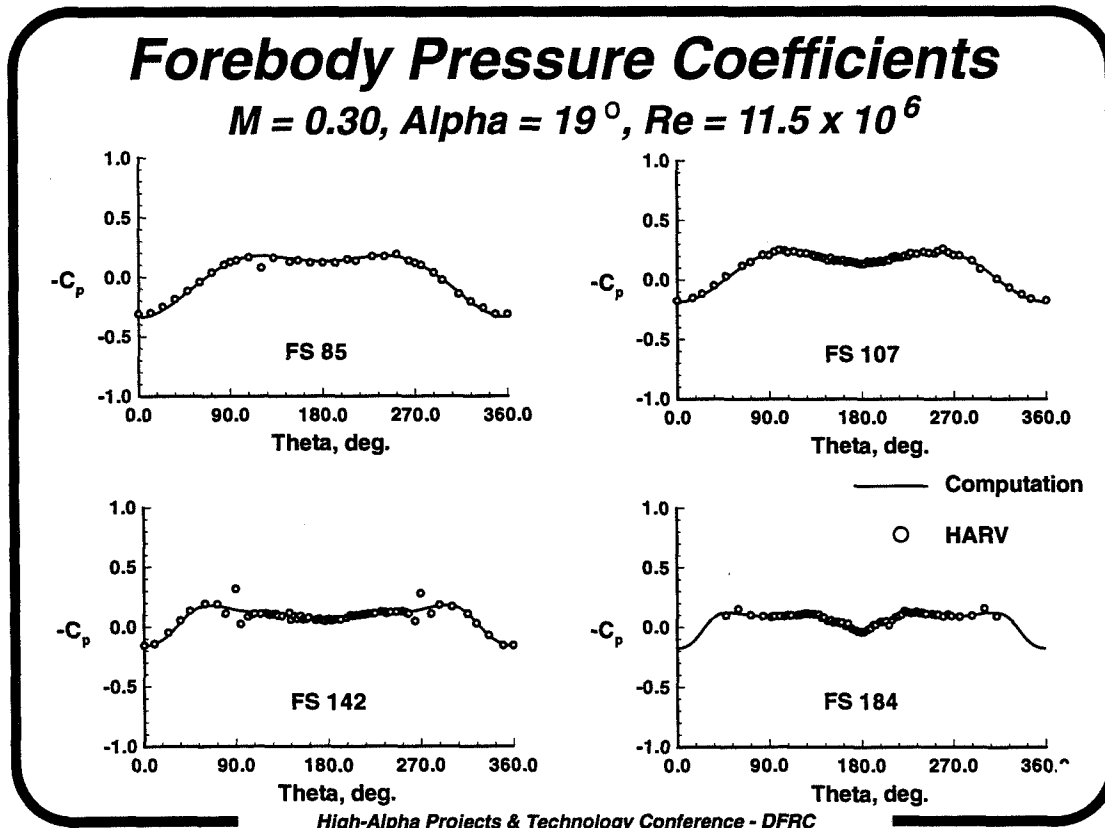
F/A - 18 HARV Pressure Data Stations

The figure shows a layout of the locations at which pressure data were taken during HARV flight tests. Computed pressures will be shown at the same stations. The figure also illustrates the format in which the data is presented. On the forebody, pressures are given versus theta, the angle measured from bottom dead center. On the LEX, data are given versus the dimensionless LEX span. The cross section identifier "BB" happens to be positioned at the approximate location of the zonal interface between the structured and the unstructured computational zones.



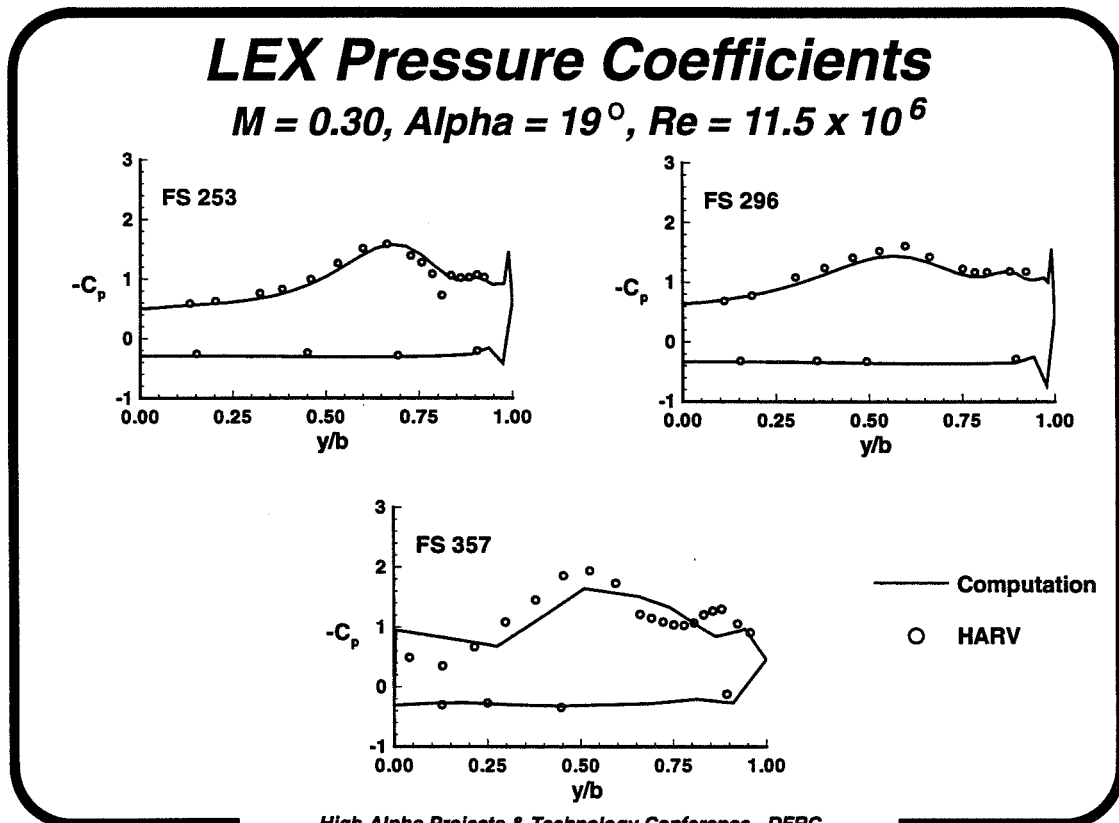
Forebody Pressure Coefficients, Alpha = 19°

The figure shows the computed pressure coefficients on the forebody surface for an angle of attack of 19°. The agreement between the computation and the flight data is generally good. It should be noted that at FS 142, near $\theta = 90^\circ$ and $\theta = 270^\circ$, the HARV pressure distribution exhibits a local suction peak not captured in the computed results. This is because a pair of antenna fairings, present on the HARV, are not modeled in the computational geometry.



LEX Pressure Coefficients, Alpha = 19°

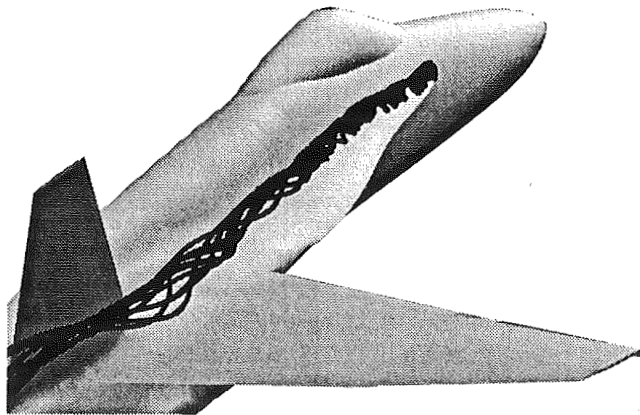
The figure shows the computed pressure coefficients on the LEX surface for an angle of attack of 19°. The agreement between the computation and the flight data is generally quite good. Stations FS 253 and FS 296 lie inside the structured computational zone, while station FS 357 lies inside the unstructured computational zone. The coarser spanwise spacing in the unstructured zone is apparent, although the primary features - the footprint of the primary LEX vortex near $y/b = 0.5$ and the footprint of the secondary vortex near $y/b = 0.9$ - are predicted reasonably well.



LEX Vortex, Alpha = 19°

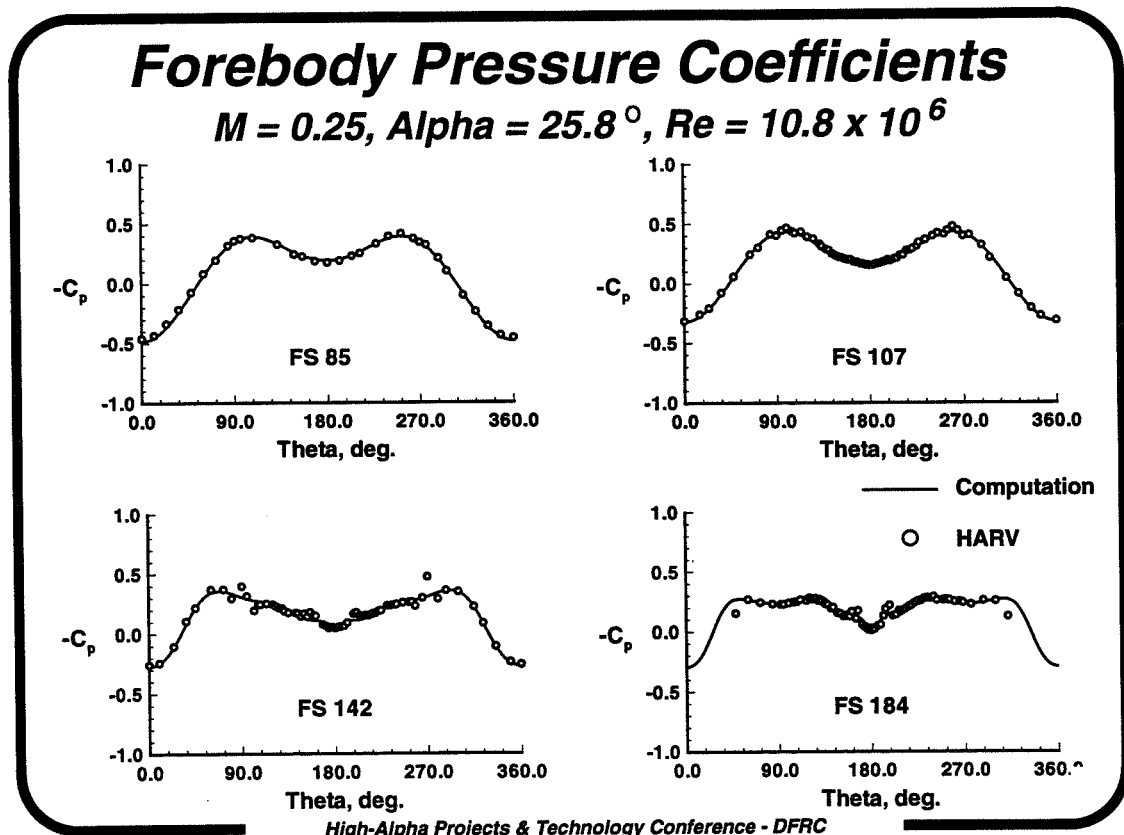
The figure shows the computed streamline traces following the LEX vortex core for an angle of attack of 19°. The particles were released near the apex of the LEX. The computed vortex shows no sign of bursting at this angle of attack. In contrast, data from the HARV indicates that the vortex bursts at a streamwise position corresponding to the intersection of the leading edge of the vertical tail and the fuselage.

LEX Vortex - Alpha = 19°



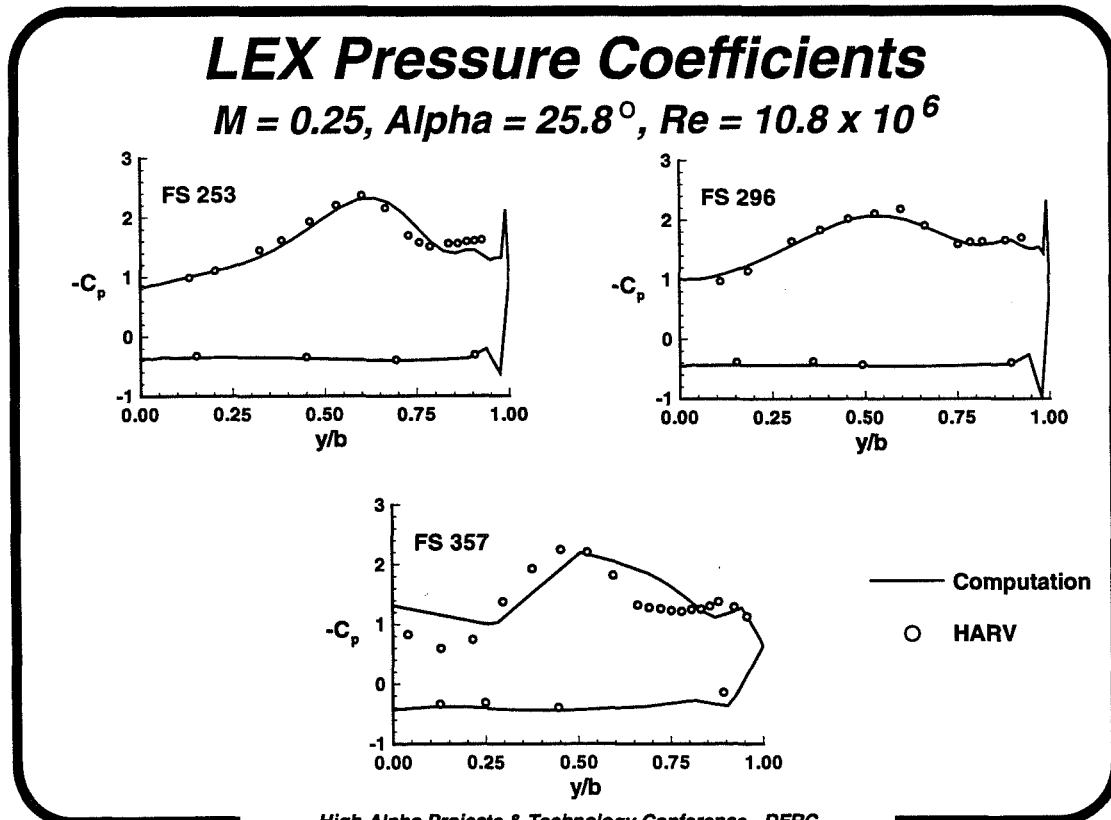
Forebody Pressure Coefficients, Alpha = 25.8°

The figure shows the computed pressure coefficients on the forebody surface for an angle of attack of 25.8°. The agreement between the computation and the flight data is again generally good.



LEX Pressure Coefficients, Alpha = 25.8 °

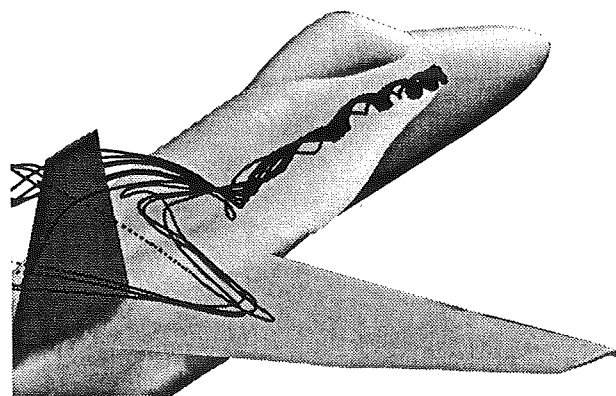
The figure shows the computed pressure coefficients on the LEX surface for an angle of attack of 25.8°. The agreement between the computation and the flight data is quite good. Compared to 19°, the LEX vortex is stronger at all three stations, as indicated by increased suction on the upper surface of the LEX.



LEX Vortex, Alpha = 26 °

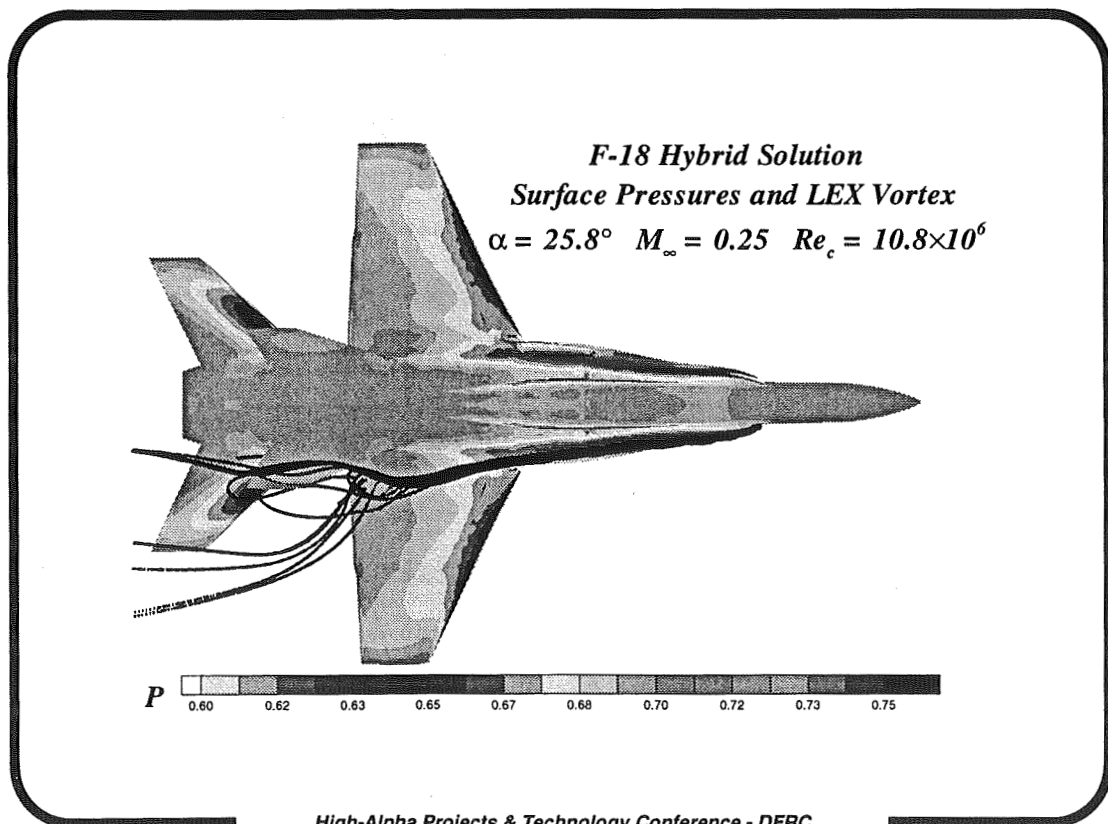
The figure shows the computed streamline traces following the LEX vortex core for an angle of attack of 25.8°. The particles were released near the apex of the LEX. For this angle of attack, the computed vortex exhibits a sudden expansion of the core, indicative of burst. In addition, the axial velocity in the vortex core becomes negative at a point slightly downstream of the region in which the core begins to expand. If the burst point is defined as the location at which the axial velocity in the core first becomes negative, then the computed results predict bursting at FS 535, or $X/L = 0.7$, where L is the length of the aircraft. The burst position observed in flight is given in published reports (AIAA-90-0231) as approximately $X/L = 0.52$.

LEX Vortex - Alpha = 26 °



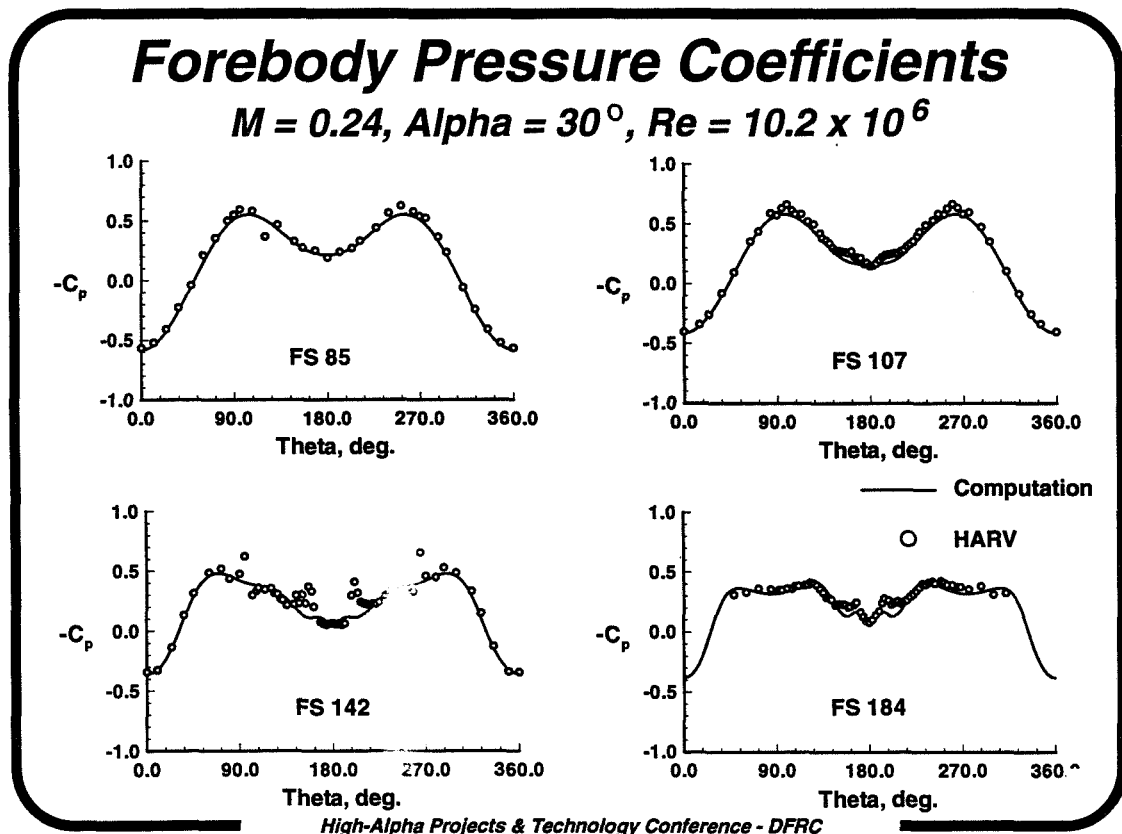
LEX Vortex and Surface-Pressure Contours, Alpha = 26 °

The figure shows the both the computed streamline traces following the LEX vortex core and surface pressure contours for an angle of attack of 25.8°. The computed results, obtained for conditions of zero yaw, were reflected about the vertical plane of symmetry to produce the view shown here. The vortex trace was omitted from the reflected half in order to better show the pressure contours on the LEX.



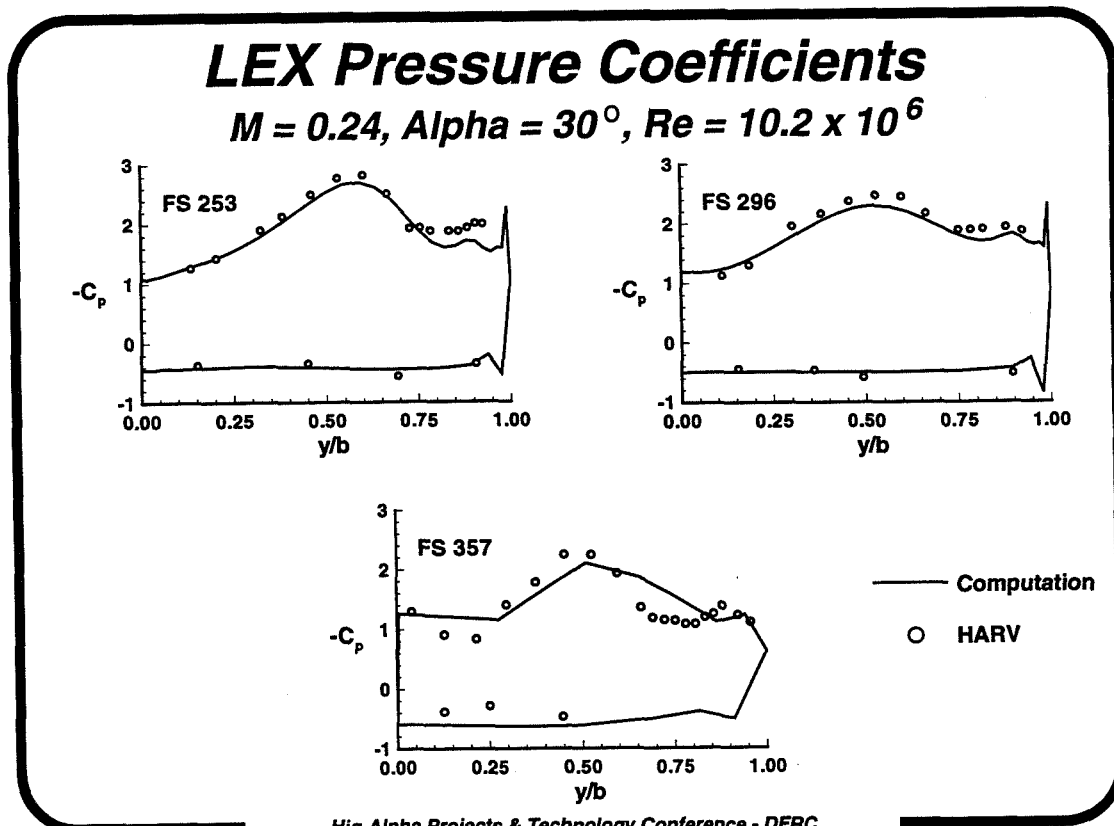
Forebody Pressure Coefficients, Alpha = 30°

The figure shows the computed pressure coefficients on the forebody surface for an angle of attack of 30°. The agreement between the computation and the flight data is generally good, although the footprint of the forebody vortex - seen as the local suction peak on either side of $\theta = 180^\circ$ - is underpredicted. The footprint is not observed in the computational results until FS 142, whereas in the HARV data the footprint is evident as far forward as FS 107. This is likely due to insufficient circumferential resolution near the top of the forebody.



LEX Pressure Coefficients, Alpha = 30°

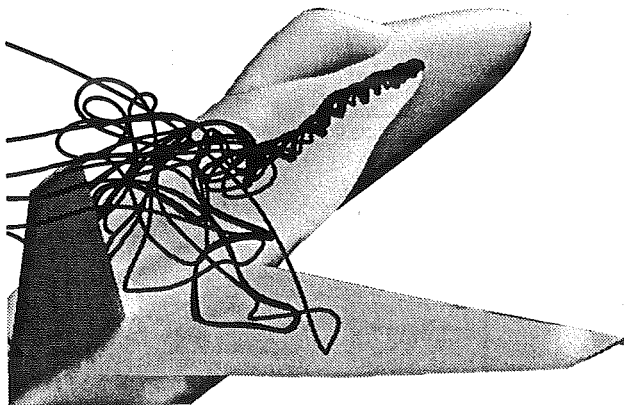
The figure shows the computed pressure coefficients on the LEX surface for an angle of attack of 30°. The peak suction pressure has increased at both FS 253 and FS 296, compared to the corresponding suction pressures at an angle of attack of 26°. However, the suction level at FS 357 remains essentially unchanged from the alpha = 26° case, and is observed in the flight data as well. Interestingly, although the flight-test burst point given in AIAA-90-0231 for alpha = 30° is X/L = 0.42, corresponding to FS 333, no loss of suction pressure is observed at FS 357. The computed vortex burst point, as defined as the point where the core axial velocity first becomes negative, is X/L = 0.68 (FS 502).



LEX Vortex, Alpha = 30 °

The figure shows the computed streamline traces following the LEX vortex core for an angle of attack of 30°. As at alpha = 26°, the computed vortex exhibits the characteristics of a burst vortex, with a burst point at X/L = 0.68.

LEX Vortex - Alpha = 30 °



SUMMARY

A methodology for coupling a structured, Navier-Stokes code to an unstructured Euler code has been developed and applied to the F/A - 18 at high angle of attack. The hybrid code has been used to compute flows at 19, 26 and 30 degrees angle of attack. The computed pressure distributions show generally good agreement with the HARV flight test data, particularly on the LEX surface. No vortex burst was predicted at 19 degrees. The predicted burst points for the two higher angles of attack were in qualitative agreement with flight-test observations, with the burst points located downstream of those observed in flight. A grid refinement study is necessary to assess the effect grid density has on the computed burst locations.

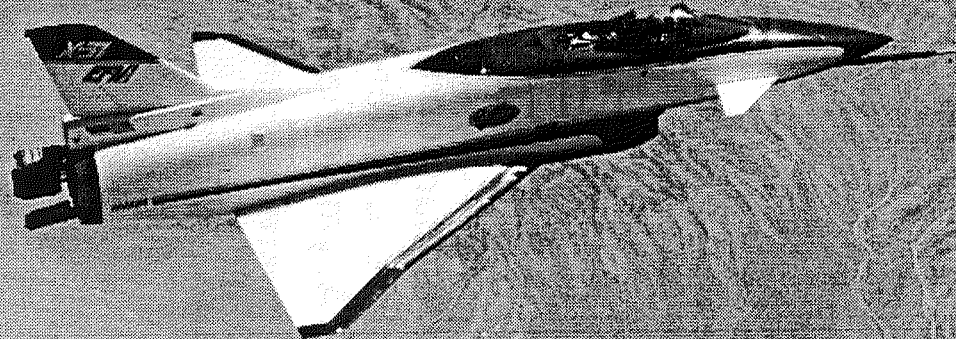
Summary

- ***Developed methodology for coupling structured, Navier-Stokes code to unstructured Euler code***
- ***Hybrid code used to compute flows at $\alpha = 19^\circ$, $\alpha = 26^\circ$, and $\alpha = 30^\circ$***
- ***Computed LEX pressures in good agreement with HARV flight data***
- ***Burst predicted at $\alpha = 26^\circ$ and $\alpha = 30^\circ$, but not at $\alpha = 19^\circ$; bursting, when predicted, occurs downstream of the location observed in flight***
- ***Grid refinement necessary to assess the effect on burst location***

Comparison of X-31 Flight, Wind-Tunnel, and Water-Tunnel Yawing Moment Asymmetries at High Angles of Attack

Brent R. Cobleigh
PRC Inc.
Edwards, California

Mark A. Croom
NASA Langley Research Center
B. F. Tamrat
Rockwell NAA



Fourth NASA High Alpha Conference
Edwards, California
July 12-14, 1994



94-152

22908

1995107820
324027

N95-14234

16083
p. 21

Program and Vehicle Description

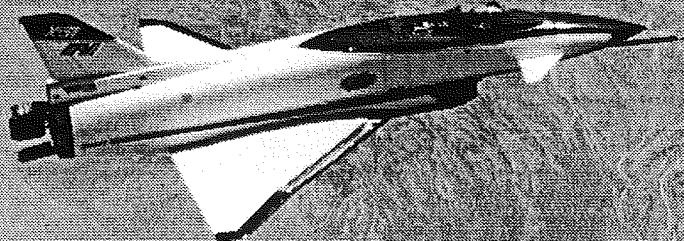
The X-31 aircraft are being used in the enhanced fighter maneuverability (EFM) research program, which is jointly funded by the (U.S.) Advanced Research Projects Agency (ARPA) and Germany's Federal Ministry of Defense (FMOD). The flight test portion of the program, which involves two aircraft, is being conducted by an International Test Organization (ITO) comprising the National Aeronautics and Space Administration (NASA), the U.S. Navy, the U.S. Air Force, Rockwell International, and Deutsche Aerospace (DASA). The goals of the flight program are to demonstrate EFM technologies, investigate close-in-combat exchange ratios, develop design requirements, build a database for application to future fighter aircraft, and develop and validate low-cost prototype concepts.

For longitudinal control the X-31 uses canards, symmetrical movement of the trailing-edge flaps, and pitch deflection of the thrust vectoring system. The trim, inertial coupling, and engine gyroscopic coupling compensation tasks are performed primarily by the trailing-edge flaps. For lateral-directional control the aircraft uses differential deflection of the trailing-edge flaps for roll coordination and a conventional rudder combined with the thrust vectoring system to provide yaw control. The rudder is only effective up to about 40° angle of attack (α), after which the thrust vectoring becomes the primary yaw control effector. Both the leading-edge flaps and the inlet lip are scheduled with the angle of attack to provide best performance.

Comparison of X-31 Flight, Wind-Tunnel, and Water-Tunnel Yawing Moment Asymmetries at High Angles of Attack

Brent R. Cobleigh
PRC Inc.
Edwards, California

Mark A. Croom
NASA Langley Research Center
B. F. Tamrat
Rockwell NAA



Fourth NASA High Alpha Conference
Edwards, California
July 12-14, 1994



Nomenclature

AB	afterburner	S1	20-in. long by .60-in. wide strake
C_d	drag force coefficient	S2	47-in. long by .60-in. wide strake
C_n	yawing moment coefficient	V	velocity
C_y	side force coefficient	α	angle of attack, deg
d	body diameter	β	sideslip angle, deg
EFM	enhanced fighter maneuverability	μ	dynamic viscosity
FB	forebody	ρ	density
g	aircraft normal load factor		
KCAS	knots calibrated airspeed		
l	body length		
L	characteristic length		
M	Mach number		
NB	noseboom		
q_{bar}	dynamic pressure, lb/ft ²		
Re	Reynolds number, $\rho LV/\mu$		

Subscripts

d	based on noseboom diameter of 3.5 in.
D	based on forebody base diameter of 3.2 ft
max	maximum
0	at zero sideslip angle

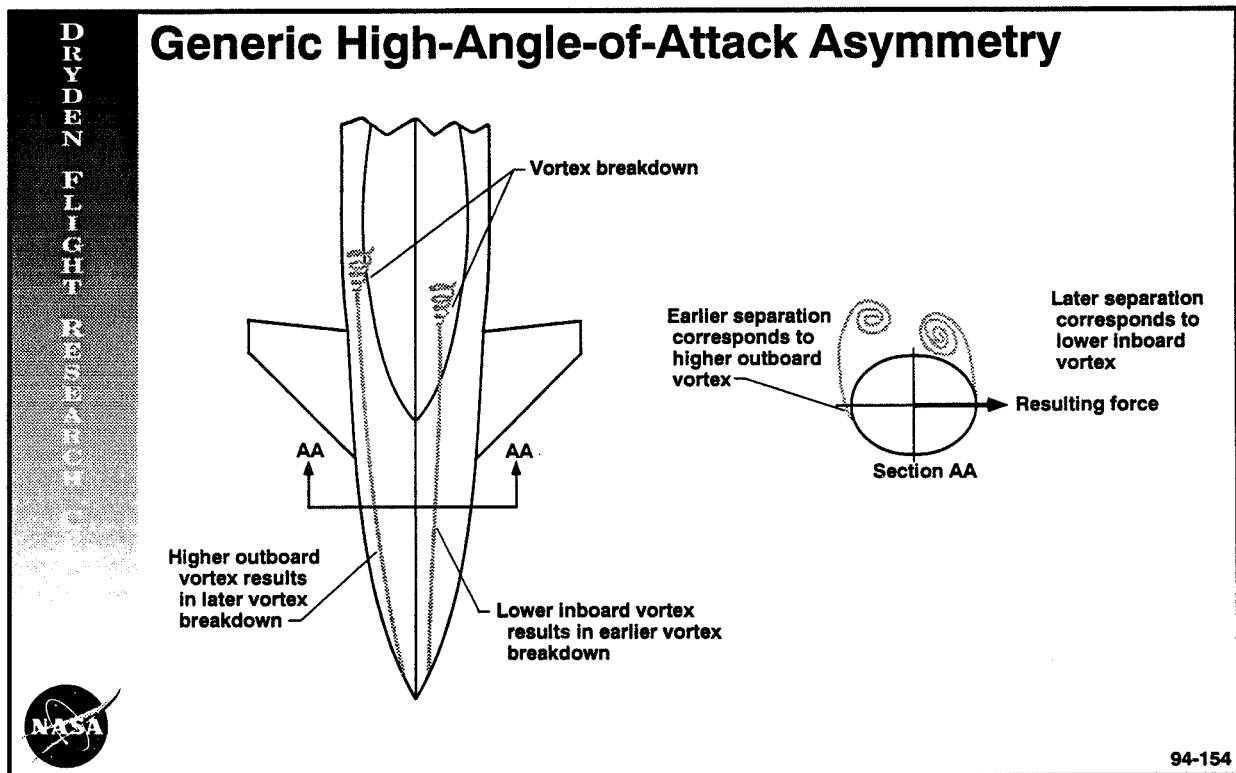
Outline

- Background
- Flight history
- Analysis method
- Results
 - Flight test
 - Comparison with wind tunnel
 - Comparison with water tunnel
- Conclusions
- Current status



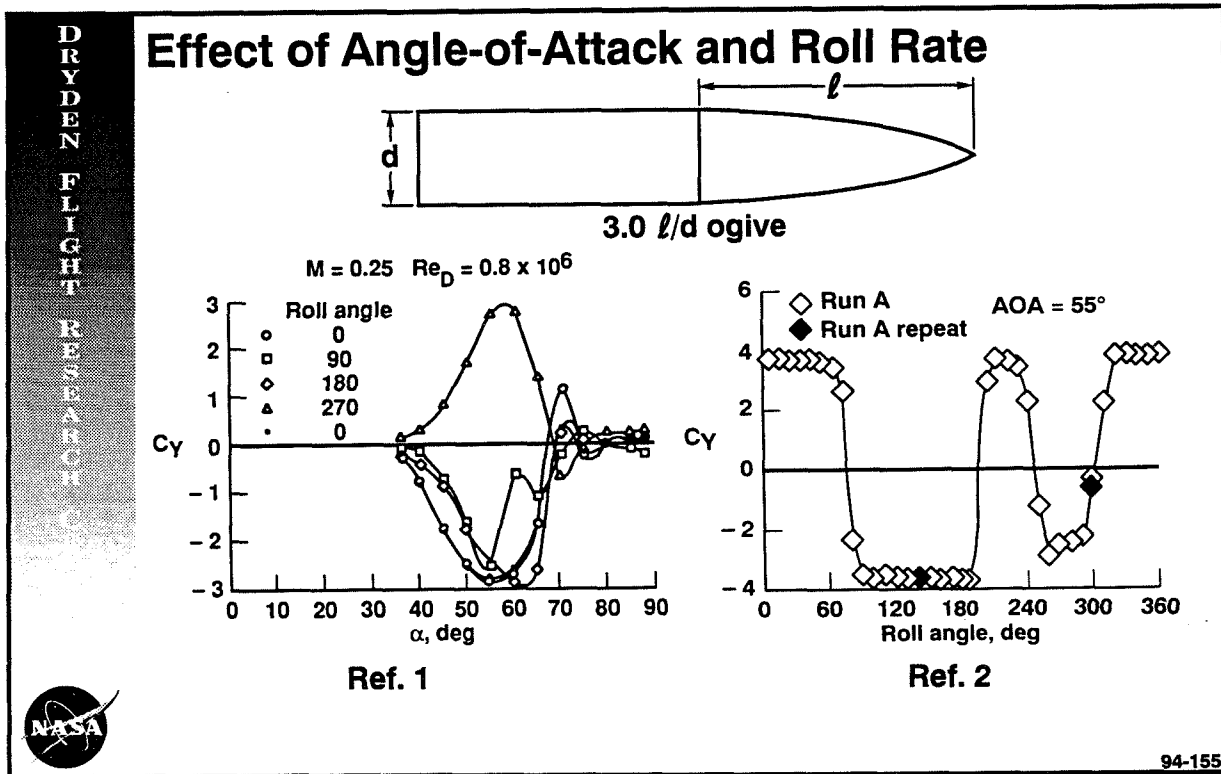
Generic High-Angle-of-Attack Asymmetry

The long slender forebody shapes of modern fighter aircraft make them susceptible to the body side-force phenomena. This side force is the result of surface pressure imbalances around the forebody of the aircraft caused by an asymmetric forebody boundary layer and vortex system at high angles of attack. In this scenario, the boundary layer on each side of the forebody separates at different locations as shown in the figure. At separation, corresponding vortex sheets are generated that roll up into an asymmetrically positioned vortex pair. The forces on the forebody are generated primarily by the boundary layer and to a lesser extent by the vortices, depending on their proximity to the forebody surface. The figure shows a typical asymmetrical arrangement where the lower, more inboard vortex corresponds to a boundary layer that separated later and, the higher, more outboard vortex corresponds to the boundary layer that separated earlier. The suction generated by the more persistent boundary layer and the closer vortex combine to create a net force in their direction. Since the center of gravity of the aircraft is well aft of the forebody, a sizable yawing moment asymmetry develops.



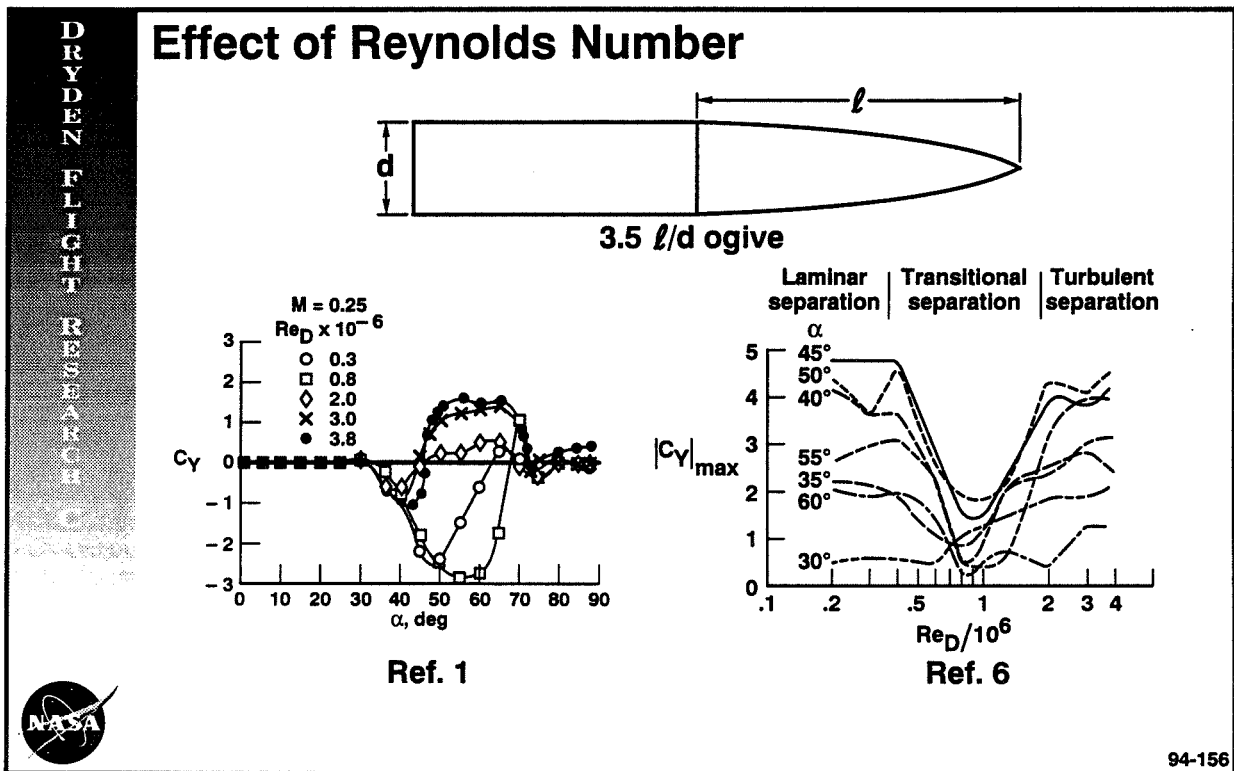
Effect of Angle of Attack and Roll Angle

An illustration of the asymmetry problem was shown by measuring the side force on an axisymmetric body at different roll angles at a given angle of attack. Because the model is axisymmetric, no lateral-directional forces or moments would be expected. The left plot (ref. 1), however, shows that a large asymmetry develops on a 3.0 l/d fineness ratio ogive model starting at approximately $\alpha = 35^\circ$, that continues up past $\alpha = 70^\circ$. In addition the sign of the asymmetry switches for a roll angle of 270° . Further tests by other researchers confirmed that the magnitude of the largest asymmetry does not change smoothly with changing roll angle (right plot, ref. 2). Instead, as the ogive cylinder is rolled through 360° , four changes in the sign of the asymmetry occur. Thus, at high angles of attack, the vortex cores can have bi-stable states, neither of which is symmetric. Other tests have shown that rotation of the nosetip alone produces the same result, suggesting that micro-asymmetries near the model tip are significant in the asymmetry formation. 1,3,4,5



Effect of Reynolds Number

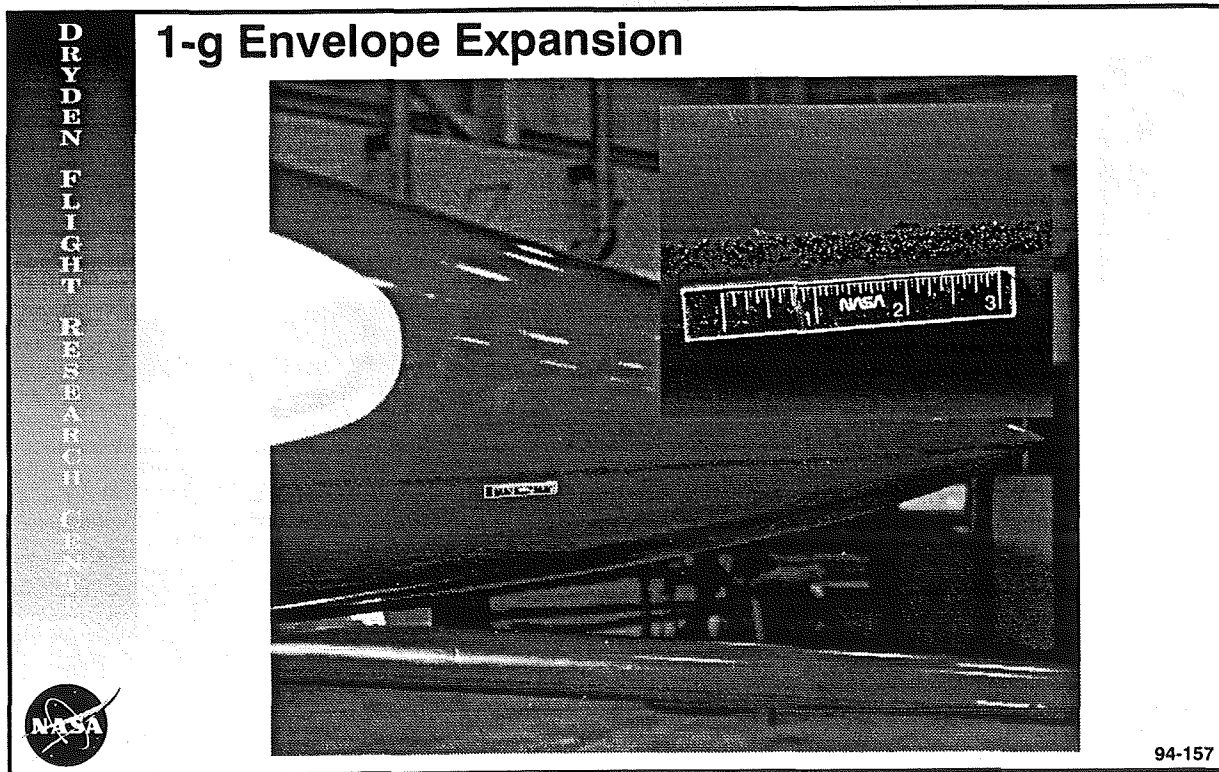
Reynolds number has also been shown to affect the asymmetry characteristic of slender bodies. The left plot (ref. 1) shows that large changes in the magnitude and sign of the asymmetry can be affected by Reynolds number; however, the angle-of-attack range over which the aircraft is susceptible to asymmetries remains unchanged. The nature of the boundary-layer separation on the forebody—whether it be laminar, transitional, or fully turbulent—is dependent on the Reynolds number. Above $\alpha = 30^\circ$, the maximum side force on a $3.5 l/d$ ogive is significantly larger for laminar and turbulent separation conditions than it is with transitional flow (right plot, ref. 6). This Reynolds number effect is important when comparing flight derived asymmetry information with either wind-tunnel or water-tunnel data.



1-g Envelope Expansion

During the 1-g, high- α envelope expansion of the X-31, both test aircraft exhibited significant, but different, yawing moment asymmetries at 0° sideslip above $\alpha = 40^\circ$. Among the resulting aircraft responses were slow rollovers and "lurches" (small, sharp heading changes). Although pilot compensation was attainable, up to 50 percent of roll stick deflection was required to counter the asymmetry. As a result the full-stick velocity vector roll rate of each aircraft was found to be faster in the direction of the asymmetry at a given angle of attack. To coordinate maneuvering with the yawing moment asymmetries, the control system had to increase the amount of control deflection required. In many cases this increase resulted in a position saturation of one of the trailing-edge flaps or thrust vector paddles.

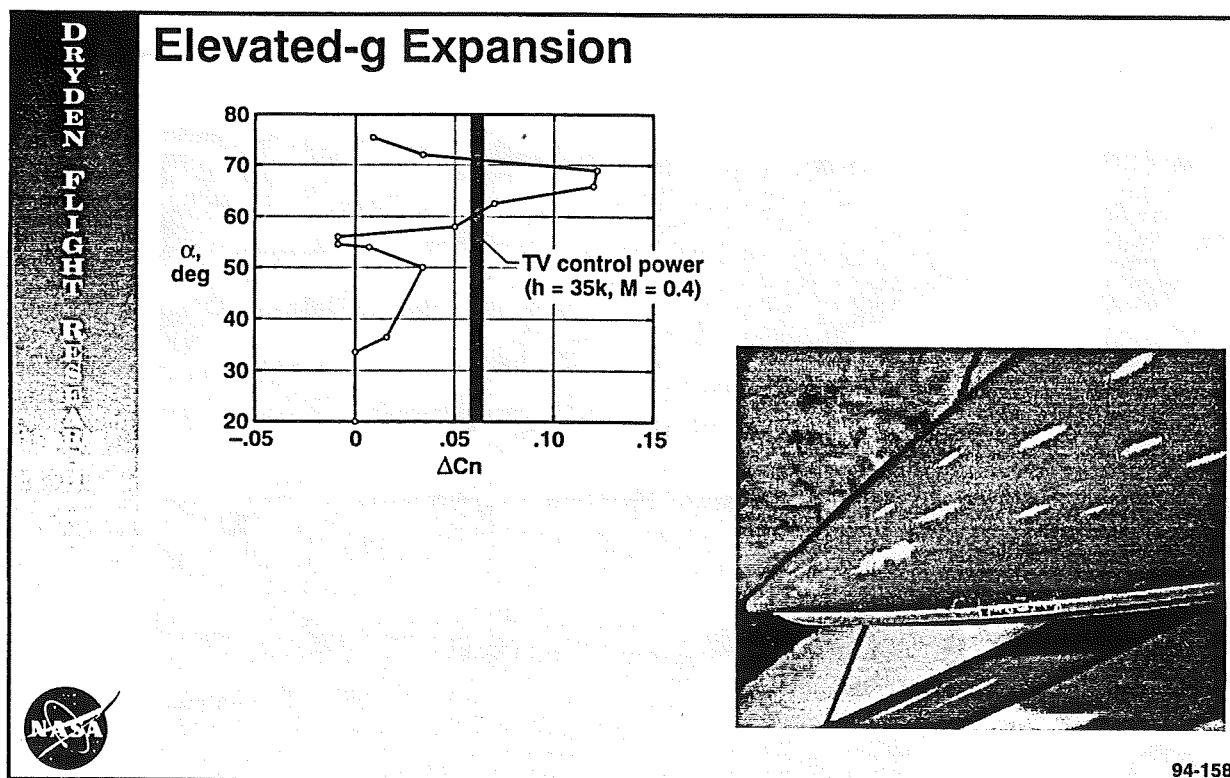
To reduce the asymmetry, transition grit strips were applied along the forebody to force boundary-layer transition at the same location on both sides of the forebody. This method had shown some promise in reducing high- α yawing asymmetries during earlier tests on the F-18 High Alpha Research Vehicle (HARV).⁷ Transition strips were also installed along the noseboom in the hope that a turbulent separation from the cylindrical cross-section would result in a reduced wake impinging on the forebody. These configuration changes improved the pilot-reported handling qualities somewhat; however, the asymmetries were not eliminated. The transition devices allowed the flight testing to complete the 1-g maneuvering envelope expansion of the X-31 successfully out to $\alpha = 70^\circ$.



Elevated-g Expansion

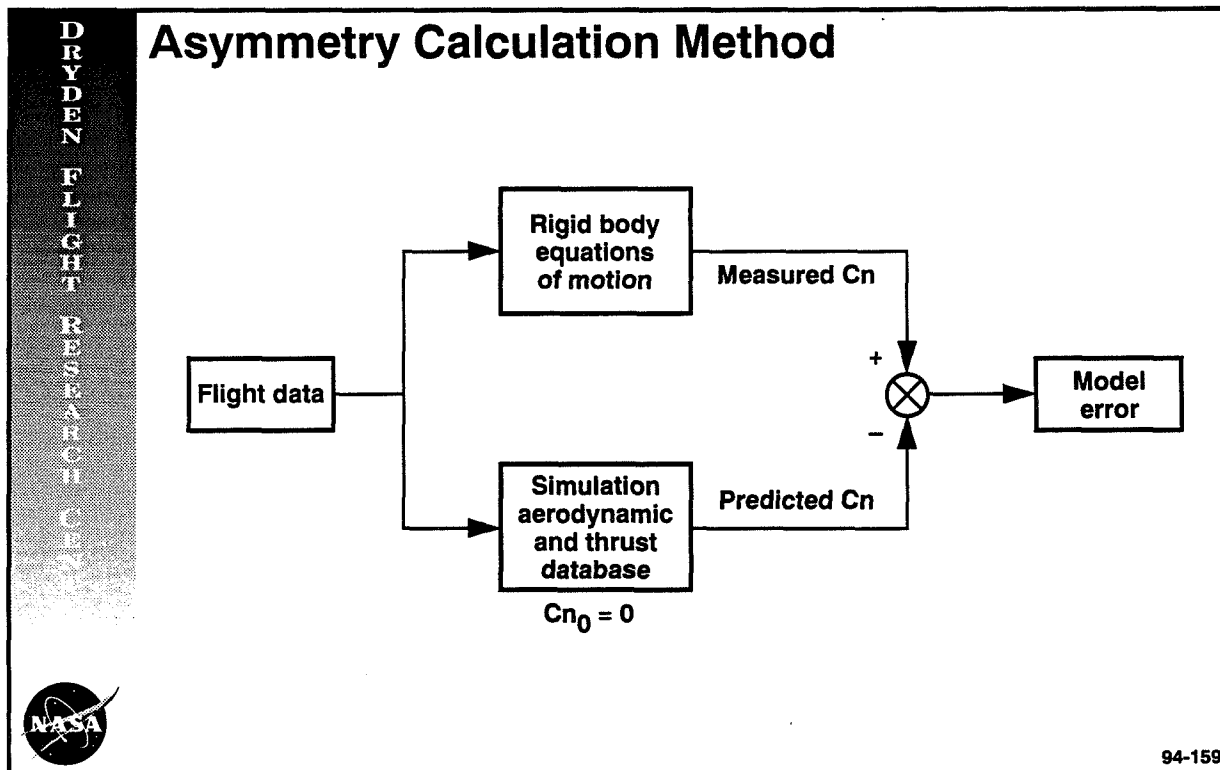
Shortly into the high- α , elevated-g phase of the envelope expansion, a departure from controlled flight occurred on ship 2 as the pilot was performing a 2-g split-S maneuver to $\alpha = 60^\circ$. Data analysis showed that a large yawing moment, in excess of the available control power, had triggered the departure (left figure). Again the forebody vortex system was suspected to be the moment generator. An effort was begun to design and test forebody strakes with the intent of improving the forebody vortex symmetry by eliminating the large-amplitude flow asymmetries that caused the departure. Towards this goal a wind-tunnel test was conducted in the NASA Langley Research Center's 30-FT by 60-FT Tunnel to define the strake design and document the impact of the strake on the static aerodynamics.

The tests showed that strakes positioned longitudinally along the waterline of the forebody from the nosetip reduced the model yawing moment asymmetry. The effectiveness of the strakes at reducing the asymmetry was not a function of the strake width, although the length of the strakes affected the amount of undesirable nose-up pitching moment. Based on the wind-tunnel results, two different length strake sets were evaluated in flight. A 20-in. and a 46-in. long strake design were manufactured and then were flight tested in separate tests. Both strakes were 0.60-in. wide. The radius of the X-31 radome tip was rounded to a 1.2-in. diameter simultaneously with the strake installation.



Asymmetry Calculation Method

To better understand and quantify the high-angle-of-attack yawing moment asymmetry characteristic of the X-31 aircraft, a method was developed to calculate time histories of the asymmetric forces and moments on the aircraft from flight data.⁸ The figure shows a block diagram of the method. The flight-measured yawing moment was computed by substituting the flight-measured variables into the rigid body equation of motion. The flight-measured yawing moment was then subtracted from that predicted from the simulation aerodynamic and thrust databases to calculate the missing, unmodeled components. By restricting data analysis to symmetrical maneuvers in which sideslip, roll rate, and yaw rate were small, the cause of the missing aerodynamic yawing moment was narrowed to three main sources: (1) errors in the thrust vectoring model, (2) errors in the control effectiveness model, and (3) aerodynamic asymmetries. Because the control effectiveness database was verified and updated with parameter identification results and the thrust model errors were not expected to be a strong function of angle of attack, any changes in the missing components with increases in angle of attack were attributed to aerodynamic asymmetries. An analysis of multiple decelerations, pullups, and split-S maneuvers with the same aircraft configuration resulted in a "fingerprint" of the asymmetry characteristic for a given configuration at a given flight condition.



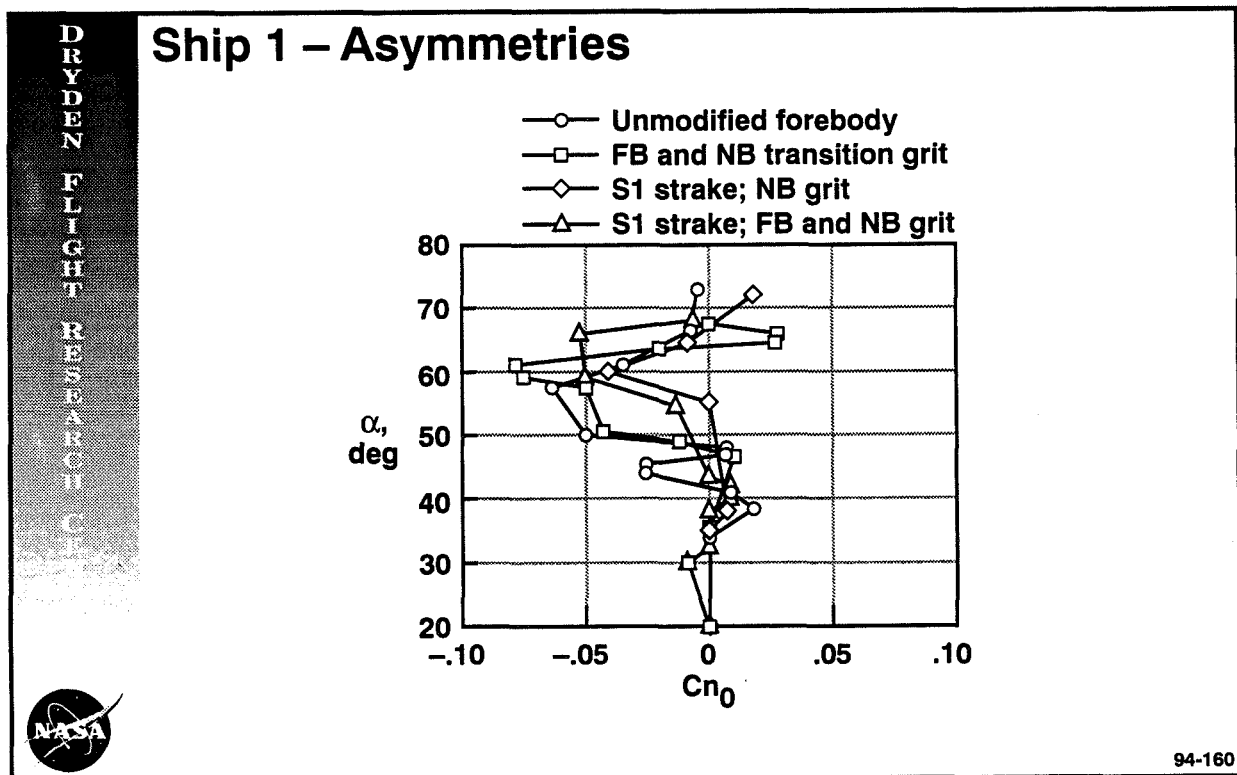
Ship 1 Asymmetries

The figure shows yawing moment asymmetry for ship 1 during slow (essentially 1-g) decelerations to high- α conditions for several of the flight configurations. The largest asymmetry started to build up beginning at $\alpha = 48^\circ$ to a peak of $C_{n0} = -0.063$ at approximately $\alpha = 57^\circ$. The asymmetry diminished significantly in magnitude by $\alpha = 66^\circ$.

In response to these asymmetries a transition grit strip was installed on both sides of the forebody and along the sides of the noseboom. Unfortunately, the data as plotted in the figure indicate that the asymmetry problem was magnified. Although the largest asymmetry began to build at the same angle of attack (48°), the peak asymmetry increased to $C_{n0} = -0.078$. The addition of the transition strips increased the angle at which the largest asymmetry occurred from 58° to 61° .

The replacement of the forebody transition strip with the S1 strake, along with the blunting of the nosetip, effectively delayed the initiation of the yawing moment asymmetry up to an angle of attack of 55° . A peak asymmetry of $C_{n0} = -0.040$ occurred at $\alpha = 60^\circ$, after which the asymmetry diminished. As with the unmodified forebody, the aircraft became nearly symmetric by $\alpha = 65^\circ$.

The addition of a boundary-layer transition strip along the forebody aft of the strake resulted in an increase in the asymmetry level. A sharp change in the asymmetry occurred near $\alpha = 55^\circ$. An asymmetry level of $C_{n0} \approx -0.050$ remained over a range of $\alpha = 59^\circ$ to 66° . Thus, the addition of the forebody transition strip increased the yawing moment asymmetry and caused it to remain at its largest level for a broader angle-of-attack range.

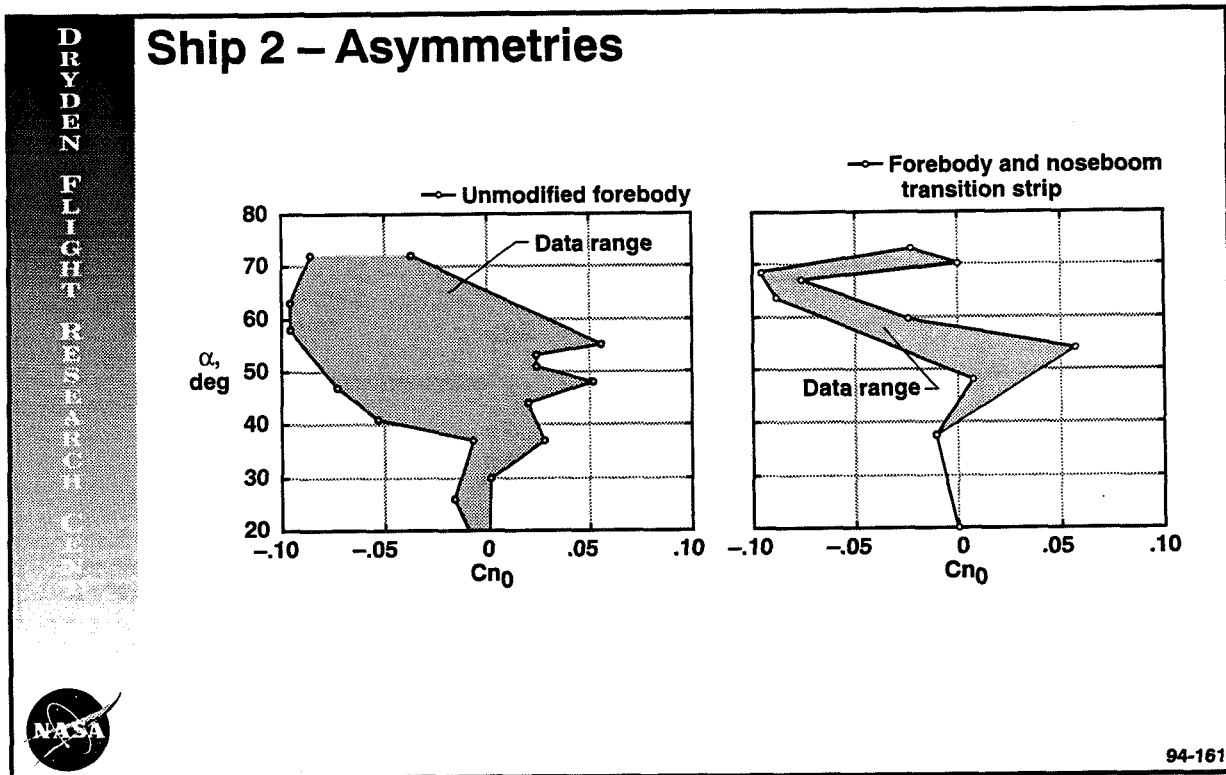


Ship 2 Asymmetries

The yawing moment asymmetry characteristic of ship 2 was significantly more troublesome than that of ship 1. As a result, greater effort was made to reduce the asymmetry on ship 2 through configuration changes. In addition to the configurations changes flown with ship 1, an extended length strake, S2, was also tested.

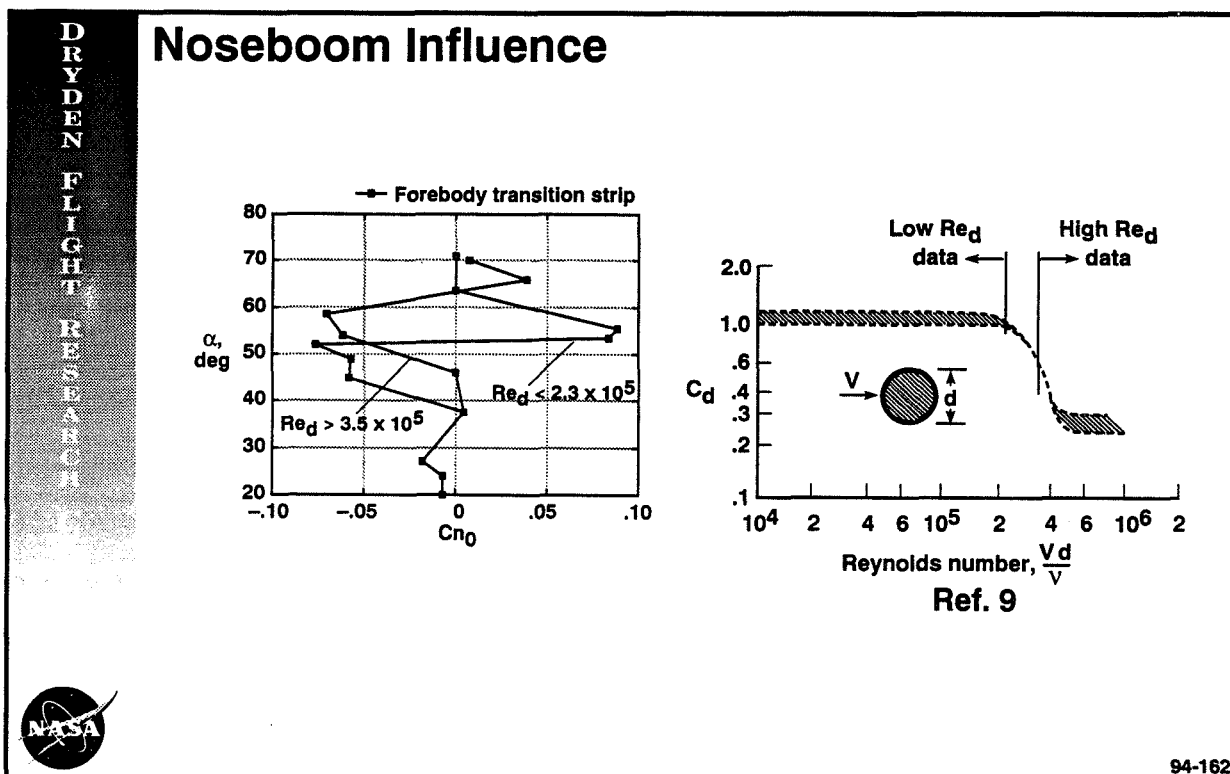
The asymmetry plot for the unmodified forebody during 1-g maneuvers did not show easily distinguishable trends in the asymmetry with angle of attack. Each maneuver appeared to have a random asymmetry pattern. Plots of the asymmetry range as a function of angle of attack (left figure) show that the maximum yawing moment asymmetry appears to be bounded at $|C_{n0}| < 0.10$.

The addition of forebody and noseboom transition strips resulted in a more regular asymmetry characteristic than that for the unmodified forebody during 1-g decelerations; however, some scatter still existed about the average asymmetry. The figure plots the range of the scatter for this configuration. The asymmetry initially goes to the right to a peak of up to $C_{n0} = 0.050$ at an angle of attack between 48° and 54° . As the angle increased, the asymmetry switched to the left, eventually reaching its maximum asymmetry near $\alpha = 67^\circ$. The switching of the asymmetry from the right to left resulted in a change in the yawing moment of about $\Delta C_{n0} \approx 0.10$.



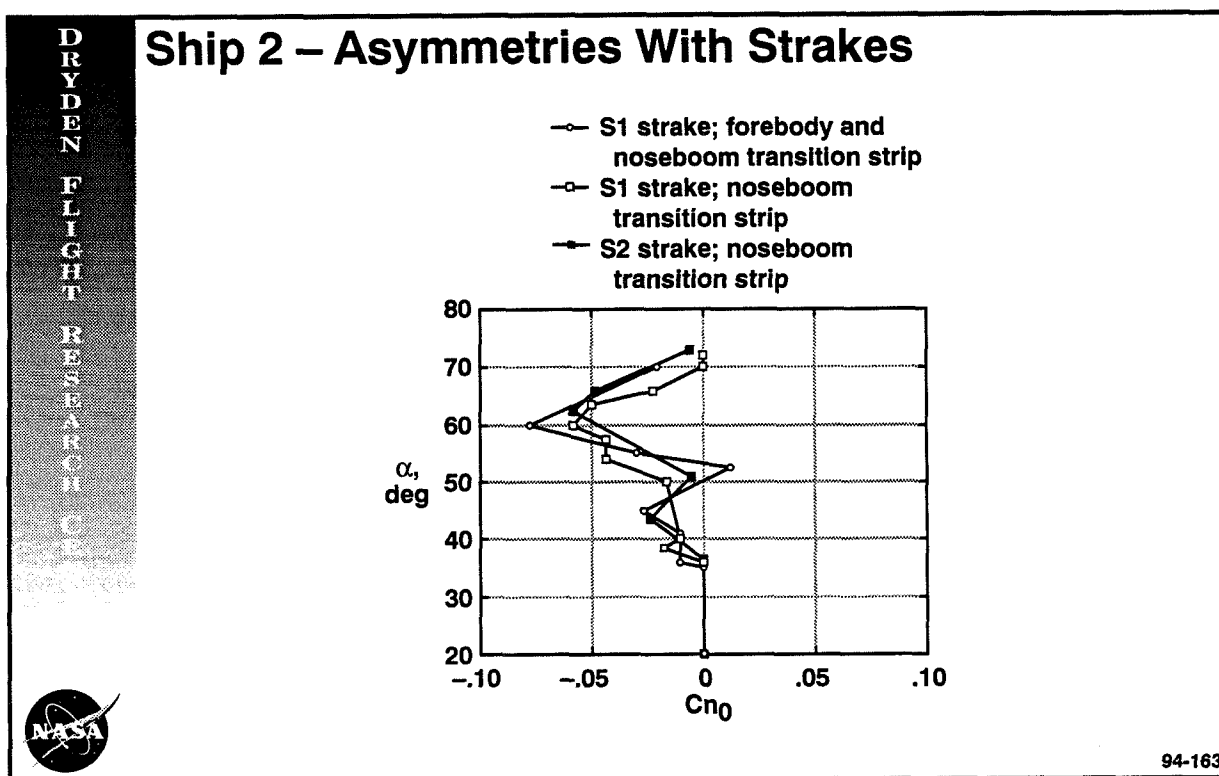
Noseboom Influence

The initial purpose of the noseboom transition strip was to ensure that the boundary layer on the flight test noseboom was turbulent before separation. It is well known that a turbulent boundary layer on a circular cylinder stays attached longer, thereby reducing the wake and resulting drag (right figure). Without the transition strip the separation state was subject to the local Reynolds number and noseboom roughness. The left figure shows that two different asymmetry characteristics developed on ship 2 when the noseboom transition strip was removed. Calculating the approximate Reynolds number based on noseboom diameter for each of the maneuvers showed that the two asymmetry characteristics occurred over different Reynolds-number ranges. Plotting both Reynolds-number ranges on a chart of the boundary-layer separation state of a circular cylinder as a function of Reynolds number (right figure) shows that a difference in the boundary-layer state at separation could have existed between the two sets of data. The lower Reynolds-number data, which would result in a large separation wake, had a sharp change in the asymmetry above $\alpha = 50^\circ$ that built up to a large right asymmetry. On the other hand, the higher Reynolds-number flow, which would produce a smaller separation wake, had a milder buildup in asymmetry. The higher Reynolds-number data more closely matched the data with the noseboom transition strips installed, suggesting that the strip was successful in eliminating a laminar separation, as it was originally intended to do.



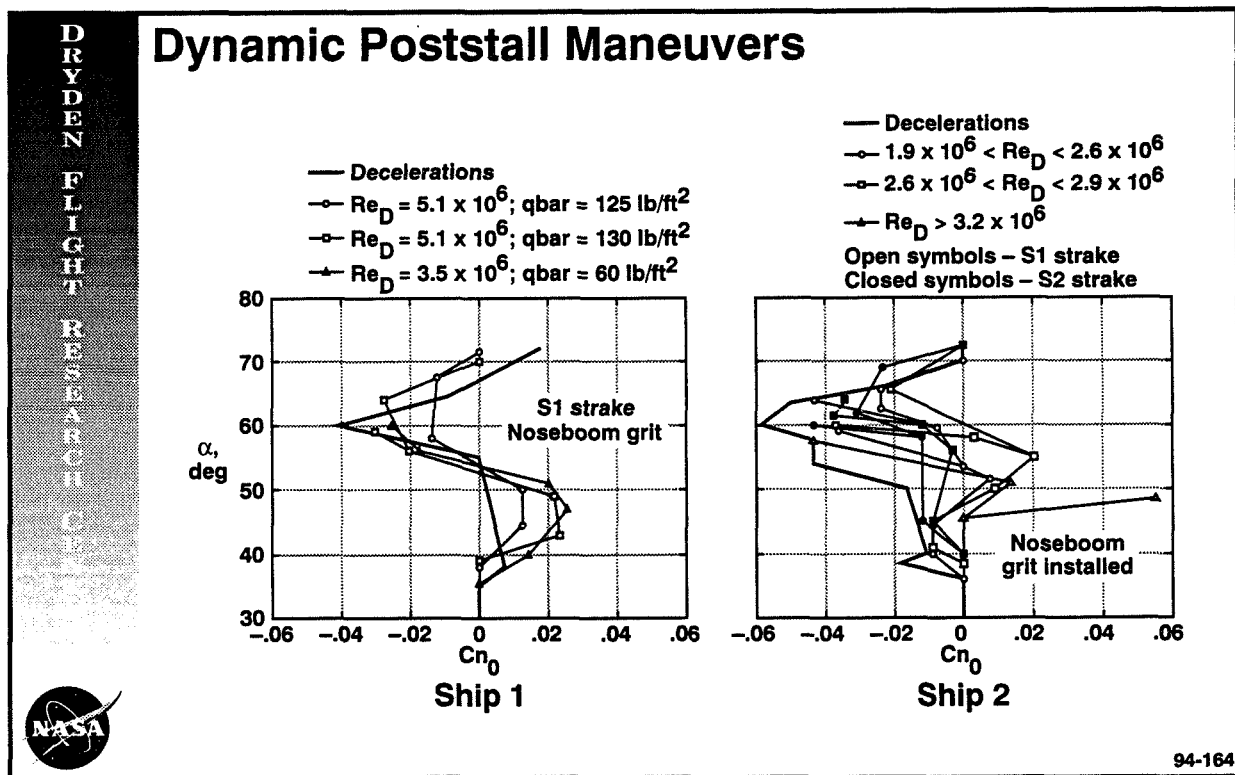
Ship 2 Asymmetries With Strakes

The first real improvement in the yawing moment asymmetries on ship 2 was found with the addition of forebody strakes and the blunting of the nosetip. The figure shows data from the S1 and S2 strake flight tests. The S1 strake, 1.0-in. diameter blunt nosetip, and noseboom transition strip combination resulted in a comparably slow buildup of asymmetry starting at approximately $\alpha = 50^\circ$. The asymmetry reached a peak value of $C_{n0} = -0.059$ at $\alpha = 60^\circ$. As with most other configurations the asymmetry diminished to near zero by $\alpha = 70^\circ$. The addition of a transition strip aft of the S1 strake increased the maximum asymmetry from $C_{n0} = -0.059$ to -0.078 . This increase was similar to that seen on ship 1. Because the 20-in. long S1 strake reduced the maximum yawing moment asymmetry level, a longer 46-in. strake, S2, was installed and flight tested with the blunt nosetip. Unfortunately, little change in the 1-g deceleration asymmetries resulted. The longer strake did shift the asymmetry to a higher angle of attack by approximately 2° .



Dynamic Poststall Maneuvers

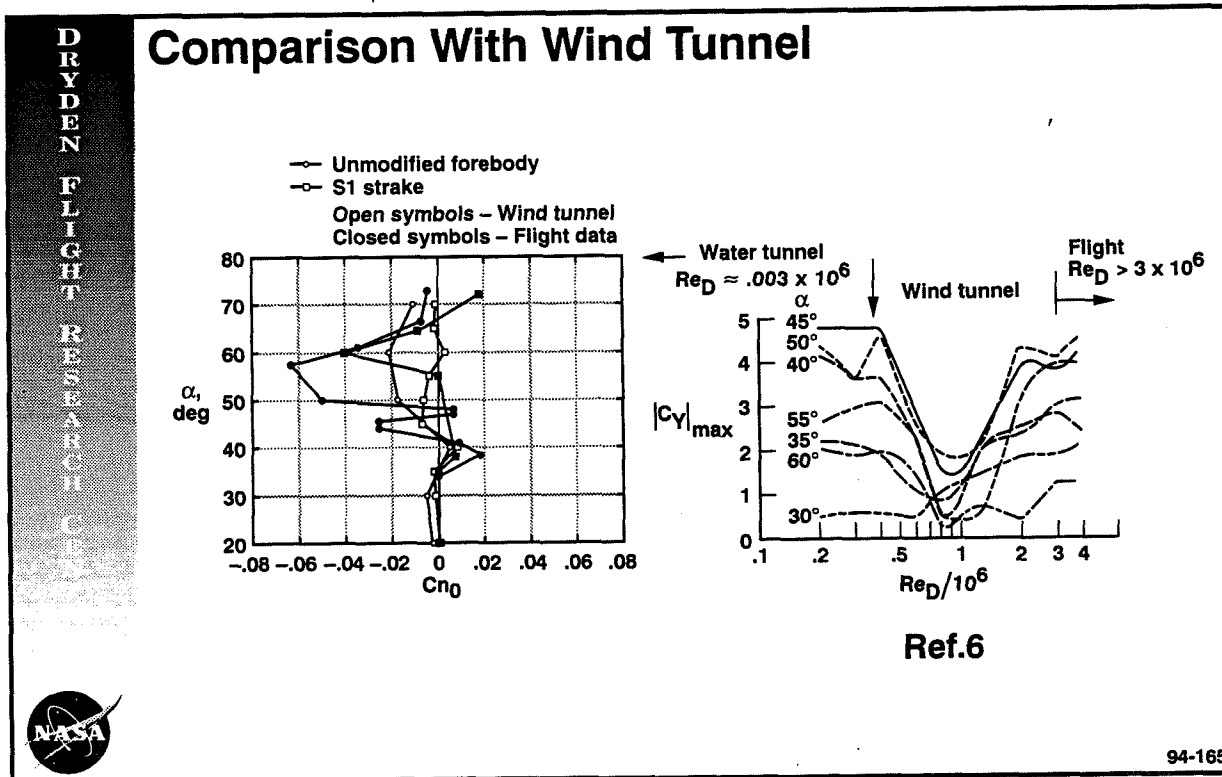
The figures present the asymmetries calculated during rapid pullups to high angle of attack for the S1 strake, blunted nose, and noseboom transition strip configuration. The data obtained from the steady-state decelerations are plotted along with the dynamic data for comparison. In general the asymmetry level during the dynamic maneuvers was less than or equal to the value seen in the 1-g maneuvers at the maximum asymmetry angle of attack (near 60°). This reduction in asymmetry level during the dynamic portion of the maneuver, however, was not entirely useful. As the aircraft reached its target angle of attack and the load factor decayed to unity, the asymmetry often built up to the steady-state value. Thus, the maximum asymmetry defined by the 1-g decelerations provided the worst-case levels for which the flight control system had to account. Although the dynamic maneuvers reduced the maximum asymmetry near $\alpha = 60^\circ$, an increase in the asymmetry was seen at lower angles of attack near $\alpha = 45^\circ$ to 50° . In addition the maximum asymmetry measured when capturing $\alpha = 50^\circ$ on ship 2 increased with increasing aircraft velocity. Although the addition of the S2 strake did not appear to reduce the maximum asymmetry at $\alpha = 60^\circ$, the tendency of the asymmetry to go right at $\alpha = 50^\circ$ during dynamic maneuvers appeared to be significantly reduced.



Comparison With Wind Tunnel

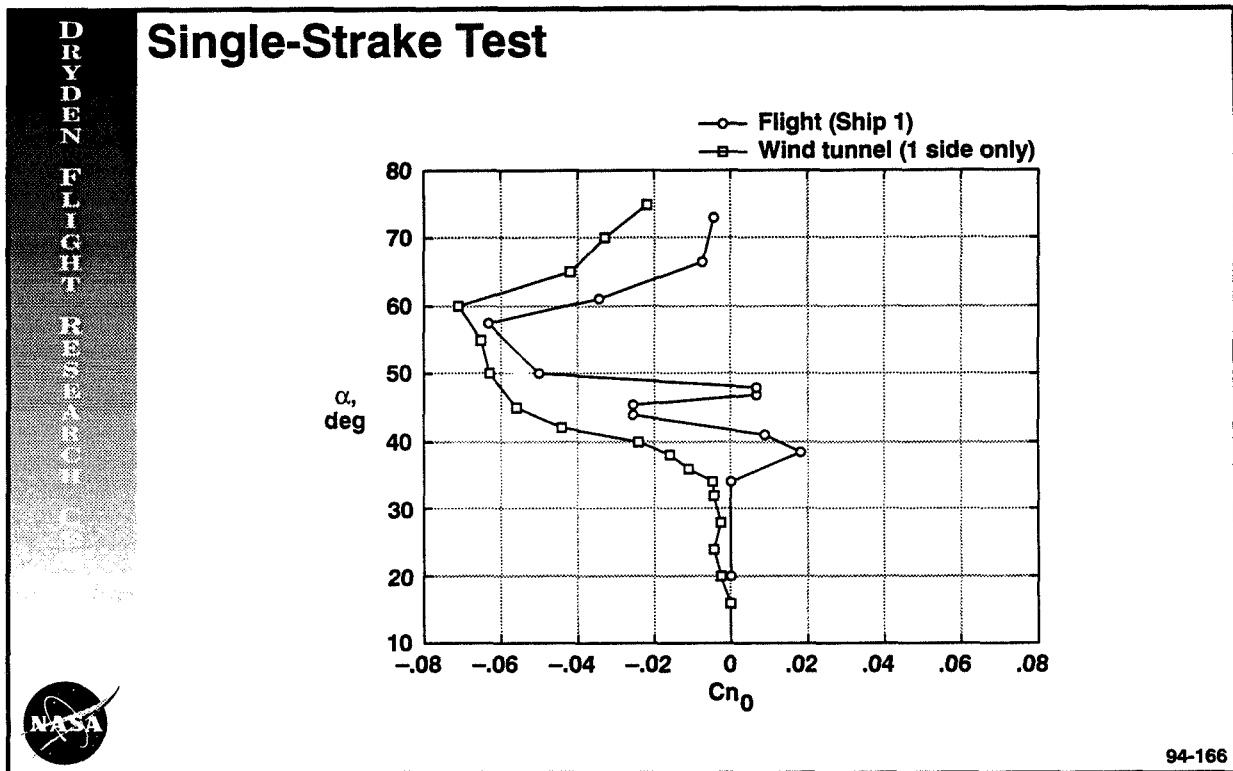
Although some yawing moment asymmetry was predicted in the wind tunnel at the high- α condition, the magnitude was significantly less than that seen in flight (left figure). One possible explanation has to do with Reynolds number. A plot of the asymmetry as a function of Reynolds number for an ogive (right figure) shows a significant decrease in the asymmetry at Reynolds numbers causing mixed boundary layer states on the forebody. The boundary layers that are dominated by laminar or turbulent flow result in similar, large-amplitude asymmetries. If this phenomenon holds true for realistic forebodies in flight, then the Reynolds number of this test could have fallen within this reduced asymmetry region. Both the water-tunnel and the flight test Reynolds numbers appear to be well clear of this Reynolds-number range.

The wind tunnel did show that the strake pair reduced the yawing moment asymmetry, which was why the strakes were installed on the flight vehicles. In addition the tunnel test was used to predict the changes to the basic aircraft static aerodynamics caused by the strakes. This was important because several of the candidate strake designs caused undesirable changes to $C_{n\beta}$ and/or unacceptable nose-up increments to the static pitching moment, C_m . Once the field of candidate strakes was reduced to one, the impact of the strake on the overall flying qualities under realistic dynamic conditions was using the NASA Langley drop model technique.¹⁰ Utilizing these scale-model test methods resulted in rapid acceptance of the final strake design taken to flight.



Single-Strake Test

To see what level of asymmetry could be generated on the forebody in the wind tunnel, a test was run with a strake only on one side of the forebody. A comparison of the asymmetry measured with the one-sided strake to the asymmetry measured in flight with no strake shows a reasonably good comparison, both of magnitude and of α range. The yawing moment asymmetry magnitude was slightly larger with the one-sided strake than the flight data. Thus, using a small strake to force asymmetric boundary-layer separation resulted in data that more closely matched that measured in flight. This method may have the promise of simulating a higher Reynolds-number condition to get better estimates of the asymmetries. These estimates could then be used to define control power requirements and aid in control law design.

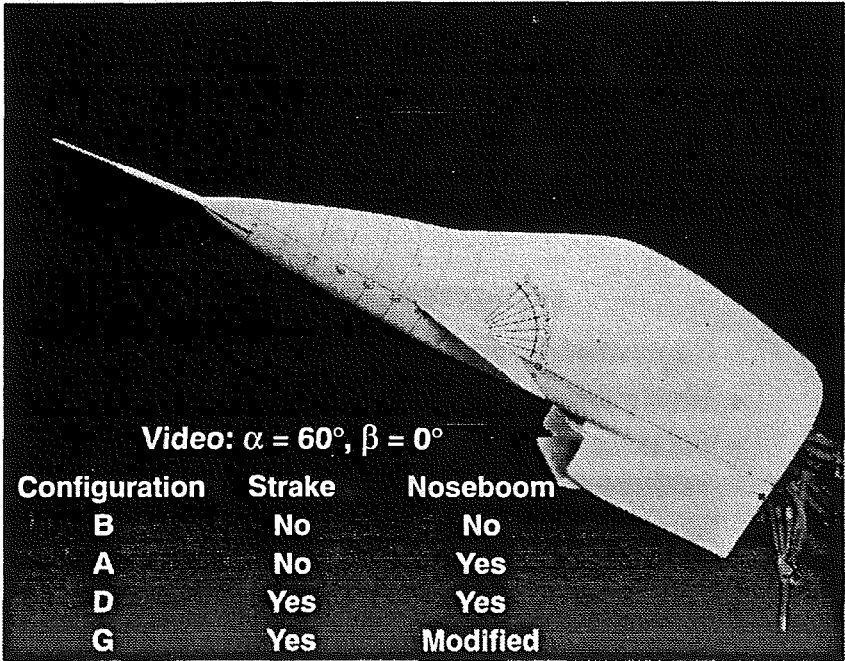


Water-Tunnel Results

Shortly before the first flight with the new forebody strakes, a water-tunnel test of a 4.4-percent scale forebody-only model of the X-31 was conducted at the NASA Dryden Flow Visualization Facility.¹¹ The study primarily focused on determining the relative effects of the different configurations on the stability and symmetry of the high-angle-of-attack forebody vortex flowfield. Although no force balance data were obtained, extensive flow visualization was conducted. Tests were conducted with varying strake and noseboom configurations. Notes, photographs, and video data were taken at each of the angle of attack conditions.

DRYDEN FLIGHT RESEARCH CENTER

Water Tunnel Results



Video: $\alpha = 60^\circ$, $\beta = 0^\circ$

Configuration	Strake	Noseboom
B	No	No
A	No	Yes
D	Yes	Yes
G	Yes	Modified



94-167

Comparison With Water Tunnel

Although no quantitative data were taken, the water-tunnel flow visualization results compared reasonably well with the flight data. Asymmetries in the boundary layer separation and vortex cores were seen between $\alpha = 50^\circ$ and 65° , as was the case with the flight results. The largest deviation between the left and right vortex and boundary-layer positions was seen at $\alpha = 60^\circ$, which is the angle of the greatest asymmetry magnitude in flight. The installation of the strakes on the model did not eliminate the asymmetry, as was the case with the flight results.

Tests without the noseboom installed were also completed to see what effect that might have. Surprisingly, no asymmetries were found at any angle of attack, regardless of the strake configuration. The unsteady wake of the noseboom appeared to be the catalyst that triggered the asymmetries to form. This oscillating wake initiated around $\alpha = 50^\circ$. An alternative L-shaped noseboom—whose wake did not intersect the forward portion of the forebody—did not produce asymmetries in the vortex cores. A nosetip boom (similar to the X-29 noseboom) failed to improve the forebody vortex system asymmetry.

Comparison With Water Tunnel

(+) agrees (–) disagrees

- + Asymmetry range $\alpha = 50^\circ$ to 65°
- + Maximum asymmetry at $\alpha = 60^\circ$
- + Strakes do not eliminate asymmetry (unsteadiness reduced somewhat)
- Strakes delay asymmetry to higher angle-of-attack (flight – yes, water tunnel – no)

-
-
- Flight test noseboom is primary cause of unsteady flow that caused vortex asymmetry
 - Asymmetry eliminated with noseboom redesign or removal





Conclusions

Flight test

- **Combination of S1 forebody strakes and blunt-nose tip**
 - Increased the angle-of-attack at which the asymmetry initiated by 7° to 12°
 - Reduced the maximum asymmetry
 - Made the asymmetry repeatable
- **Forebody boundary layer transition strips**
 - Increased the level of the yawing moment asymmetry
 - Widened the angle-of-attack range over which the asymmetries acted
 - Reduced the random asymmetry behavior of the unmodified forebody on Ship 2
- **Noseboom boundary-layer transition strips**
 - Ensured that a turbulent separation existed on the noseboom, thereby minimizing the noseboom wake
 - The S2 strakes reduced the additional asymmetry present during dynamic maneuvers (Ship 2)

94-169



Conclusions

Wind tunnel

- **Showed that strakes reduced the asymmetry**
- **Predicted asymmetry angle-of-attack range, but did not predict yawing moment asymmetry magnitude**
- **Separating boundary layer on one side resulted in asymmetry magnitudes near flight**

Water tunnel

- **Qualitatively predicted the asymmetry angle-of-attack range and the angle of maximum asymmetry**
- **Showed noseboom position is a catalyst for asymmetric condition**
- **Alternate or removal of noseboom eliminates asymmetry**

94-170

Current Flight Status

The combination of the forebody strakes, rounded nosetip, noseboom grit, increased thrust vector vane travel (from 26° to 35°), and minor control law changes has allowed the elevated-*g* envelope expansion out to about 5.5-*g* entry conditions to be completed on ship 1. An 8-in. strake extension combined with a further blunting of the X-31 nosetip have allowed the same envelope to be completed on ship 2 as well. Although some asymmetry still exists, enough control power is available to coordinate maneuvering. Once maximum afterburner is set, the X-31 has been cleared for all stick inputs at all angles of attack—essentially carefree handling. The pilots have reported good handling qualities throughout the high- α envelope. Typical high- α combat maneuvering results in sideslip values less than 3°.

Current Flight Status

- Strake, rounded nosetip, noseboom grit, and increased thrust vector vane travel allowed Ship 1 to complete envelope expansion
- After increasing strake length by 8 in. and increasing nose radius, Ship 2 completed envelope expansion
- Current envelope
 - $\alpha < 30^\circ$, 6-g maximum
 - $\alpha > 30^\circ$, 265 KCAS (M = 0.7, 30k)
 - Maximum afterburner above $\alpha = 30^\circ$
 - No limitation on pilot input ("carefree handling")
 - p-stab > 40 deg/sec, $\beta < 3^\circ$
- No restrictions on tactical utility



References

1. Keener, Earl P., Gary T. Chapman, Lee Cohen, and Jamshid Taleghani, *Side Forces on a Tangent Ogive Forebody with a Fineness Ratio of 3.5 at High Angles of Attack and Mach Numbers from .1 to .7*, NASA TM X-3437, 1977.
2. Lamont, P. J., "Pressure Measurements on an Ogive-Cylinder at High Angles of Attack With Laminar, Transitional, or Turbulent Separation," AIAA-80-1556, Jan. 1980.
3. Moskovitz, C., R. Hall, and F. DeJarnette, "Experimental Investigation of a New Device to Control the Asymmetric Flowfield on Forebodies at Large Angles of Attack," AIAA-90-0069, 28th Aerospace Sciences Meeting, Reno, NV, Jan. 8-11, 1990.
4. Chapman G. T., Keener E. R., Malcolm G. N., "Asymmetric Aerodynamic Forces on Aircraft Forebodies at High Angle of Attack—Some Design Guides," AGARD CP-199, Nov. 1975.
5. Kruse, Robert L., Earl R. Keener, Gary T. Chapman, and Gary Claser, *Investigation of the Asymmetric Aerodynamic Characteristics of Cylindrical Bodies of Revolution With Variations in Nose Geometry and Rotational Orientation at Angles of Attack to 58° and Mach Numbers to 2*, NASA TM-78533, 1979.
6. Lamont, P. J., "The Complex Asymmetric Flow Over a 3.5D Ogive Nose and Cylindrical Afterbody at High Angles of Attack," AIAA-82-0053, 20th Aerospace Sciences Meeting, Orlando, FL, Jan. 11-14, 1982.
7. Fisher, David F. and Brent R. Cobleigh, "Controlling Forebody Asymmetries In-Flight-Experience with Boundary Layer Transition Strips," AIAA-94-1826, Applied Aerodynamics Conference, June 20, 1994.
8. Cobleigh, Brent R., "High-Angle-of-Attack Yawing Moment Asymmetry of the X-31 Aircraft from Flight Test," AIAA-94-1803, Applied Aerodynamics Conference, June 20, 1994.
9. Shevell, Richard S., *Fundamentals of Flight*, Prentice-Hall Inc., Englewood Cliffs, NJ, 1983.
10. Croom, Mark A., David J. Fratello, Raymond D. Whipple, Matthew J. O'Rourke, and Todd W. Trilling, "Dynamic Model Testing of the X-31 Configuration for High Angle of Attack Flight Dynamics Research," AIAA-93-3674, Flight Mechanics Conference, Monterey, CA, Aug. 9-11, 1993.
11. Cobleigh, Brent R., *Water-Tunnel Flow Visualization Study of a 4.4-Percent Scale X-31 Forebody*, NASA TM-104276, 1994.

324028

1995107821

N95-14235

Parameter Identification for X-31A at High Angles of Attack

10001

The U.S./German experimental aircraft X-31A was designed and constructed to demonstrate enhanced fighter maneuverability. Post-stall maneuvering is enabled by applying new technologies such as high angle of attack aerodynamics and flight control system integrated thrust vectoring. p-12

Two demonstrator aircraft have been built by the main contractors Rockwell International and Deutsche Aerospace (formerly MBB). Flight testing started in October 1990 and before the end of 1992 both aircraft had accomplished a significant number of flights covering the entire AoA regime from about -5 to 70 deg.

Throughout the envelope expansion, DLR Institute of Flight Mechanics conducted parameter identification (PID) to determine the aerodynamic parameters of the aircraft from flight test data and to compare the results to the predictions from the aerodynamic dataset (ADS).

The application of system identification to high AoA / post-stall flight data raises some major problems, which are discussed in this paper. Results from both longitudinal and lateral-directional motion will be presented.

Deutsche Forschungsanstalt für Luft- und Raumfahrt e.V.

Parameter Identification for X-31A at High Angles of Attack

S. Weiss, D.Rohlf, E. Plaetschke
DLR Institute of Flight Mechanics



Overview

The presentation will start with a description of the problems arising when applying parameter identification to high AoA flight test data. Possible approaches for solving or circumventing the different problems are discussed.

The problems are further illustrated with examples from longitudinal and lateral-directional motion identification. The different identification approaches are discussed and selected results are presented.

At the end, an outlook for the upcoming identification activities will be given.

Deutsche Forschungsanstalt für Luft- und Raumfahrt e.V.

Overview

- **Problems of Identification at High Angles of Attack**
- **Lateral-Directional Motion**
 - **Instability and Process Noise**
 - **Insufficient Aircraft Excitation for PID**
 - **Aero-Update based on PID Results**
- **Longitudinal Motion**
 - **Thrust and Weight**
 - **Correlations**
 - **Influence of Aft Strakes**
- **Outlook**



Problems of Identification at High Angles of Attack

The identification of aerodynamic parameters from high AoA / post-stall data is made more difficult due to the following facts:

The basic (uncontrolled) aircraft is unstable. This instability leads to divergence of the system solutions which are derived by integration of the state equations. This problem can be circumvented by application of (1) estimation methods that stabilize the solutions (e.g. output error method with artificial stabilization, filter error method, and Extended Kalman Filter method) or (2) estimation algorithms which avoid integration of the state equations (regression method or frequency domain methods).

The aircraft states and controls are highly correlated. This leads to high correlations in the corresponding stability and control derivatives, such that not all derivatives can be estimated independently. Therefore, only a reduced model is identifiable, i.e. some derivatives are fixed on their predictions and/or two correlated derivatives are combined in one common parameter. The correlation problem would be overcome by single effector excitation.

The aircraft motion is disturbed by process noise induced e.g. by forebody vortices. Filter error method, Extended Kalman Filter and regression account for process noise and are therefore suitable for parameter estimation at high angles of attack.

The aircraft motion is often not sufficiently excited for PID because the (excellent) flight control system suppresses all undesired motion, e.g. sideslip is kept close to zero.

Thrust, weight and CG location are not known with sufficient accuracy.

Deutsche Forschungsanstalt für Luft- und Raumfahrt e.V.

Problems of Identification at High Angles-of-Attack

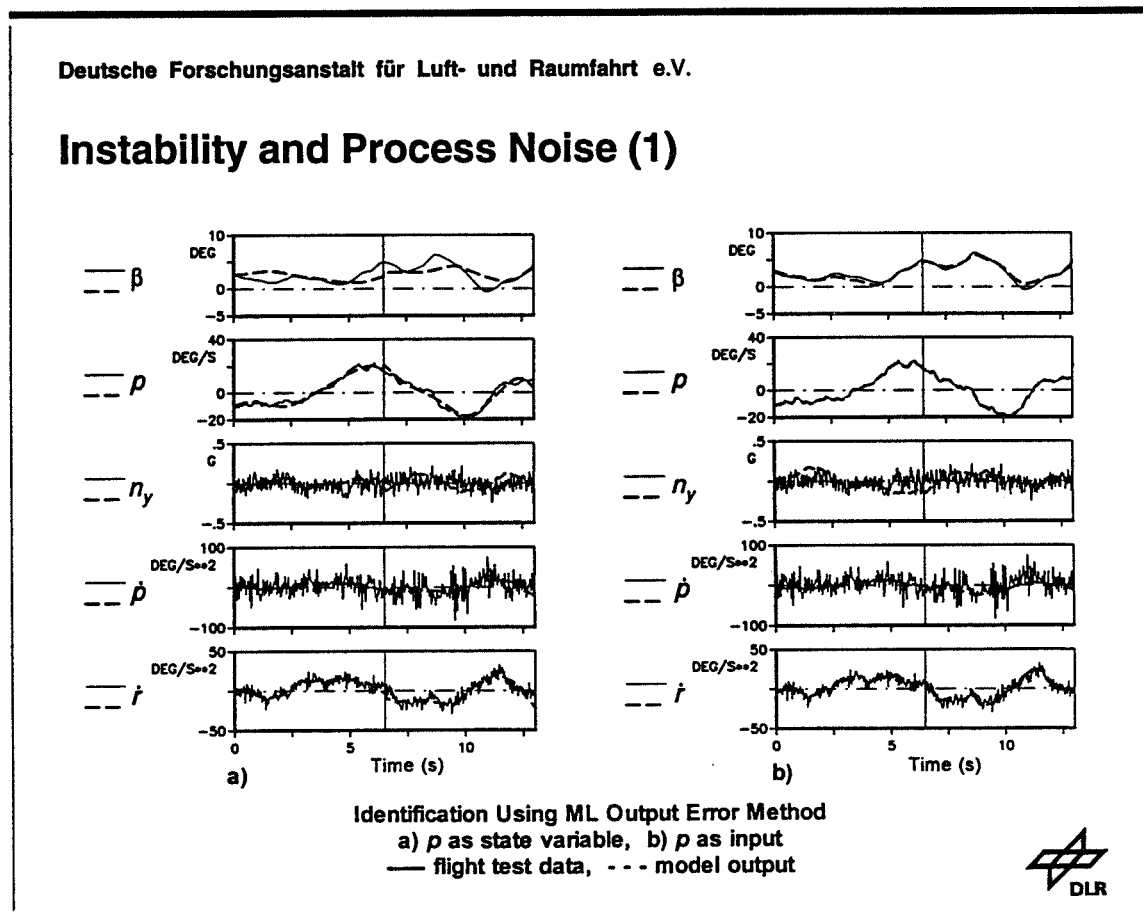
- Instability of the Basic Aircraft
- Correlation of Aircraft States and Controls
- Process Noise
- Insufficient Aircraft Excitation for PID
- Thrust, Weight, CG Location not Known Exactly



Instability and Process Noise

The figures show a bank-to-bank maneuver at 54 deg AoA. Parameter estimation was first carried out by using the ML output error method with artificial stabilization (left). As the stabilization affects the parameter estimates, it was reduced step by step to zero. This, however, led again to stability problems such that only part of the complete bank-to-bank maneuver could be evaluated and the shorter maneuver had to be split into two time segments, each requiring estimation of initial values of the state variables.

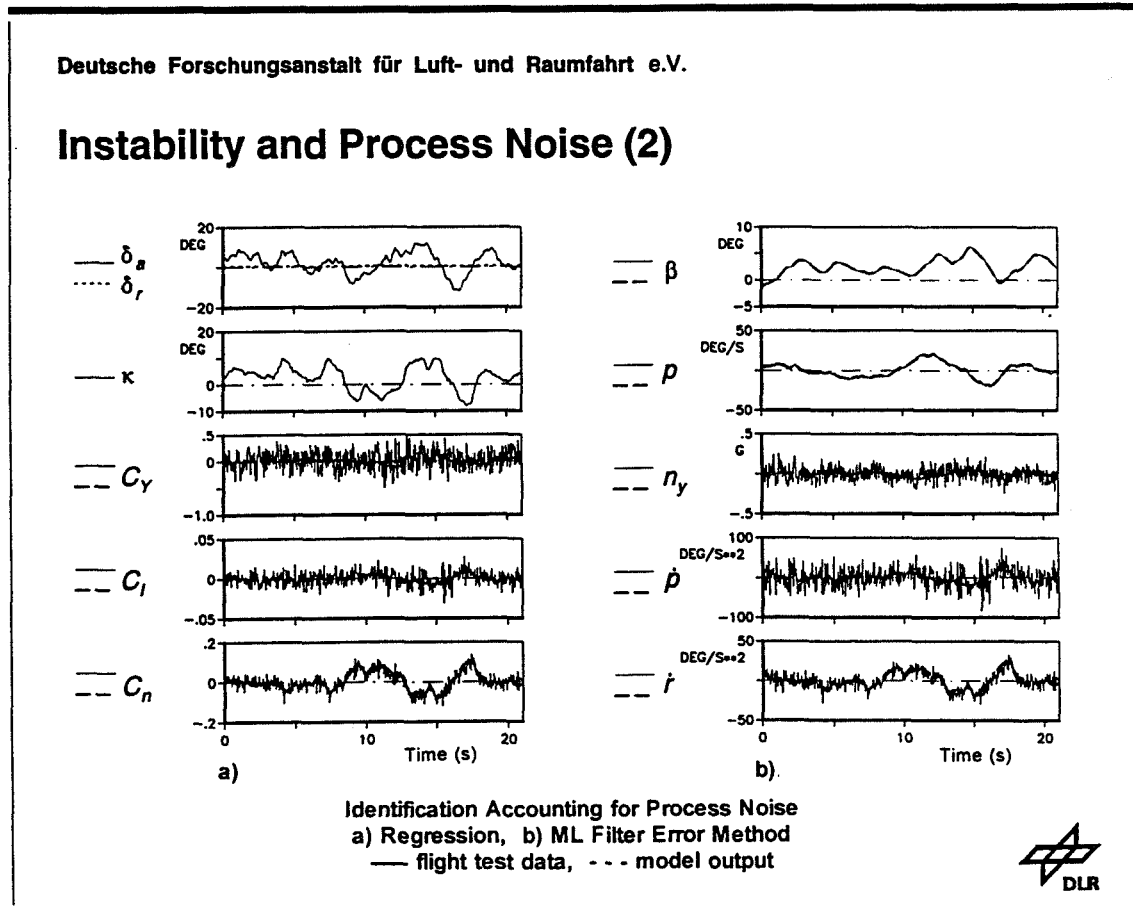
It can be seen that particularly the roll rate p is corrupted by process noise which cannot be modeled by the output error method. The roll rate has considerable influence on the sideslip angle β . (The ADS predictions indicate that the sideforce due to roll rate is important and must not be neglected as is usually done for conventional aircraft.) Consequently, also the sideslip angle β cannot be modeled correctly. To make this evident, the roll rate p was treated in a second step as input variable. The right figure shows that thereby a better match between measured and calculated sideslip angle could be achieved. Also the fit in the yaw acceleration has been improved.



These considerations show the necessity for application of estimation methods which account for process noise. As already mentioned, regression and filter error method are suitable. Both methods also overcome the problem related to the system instability. Regression requires the observation variables to be linear in the parameters. This applies to the aerodynamic coefficients C_Y , C_l and C_n . Though they are not directly measured, they can easily be computed from other measurements, essentially from the linear and angular accelerations.

The figures show the complete bank-to-bank maneuver evaluated by regression (left) and ML filter error method (right). The fit between flight test data and model output is perfect for all variables. The match in lateral, roll and yaw accelerations is of the same quality as the match in the corresponding aerodynamic coefficients obtained from regression.

The left figure also shows the correlation between differential trailing edge flap deflection δ_a and horizontal thrust deflection κ . The rudder deflection δ_r is zero, because rudder use is faded out by the flight control laws above 40 deg AoA.



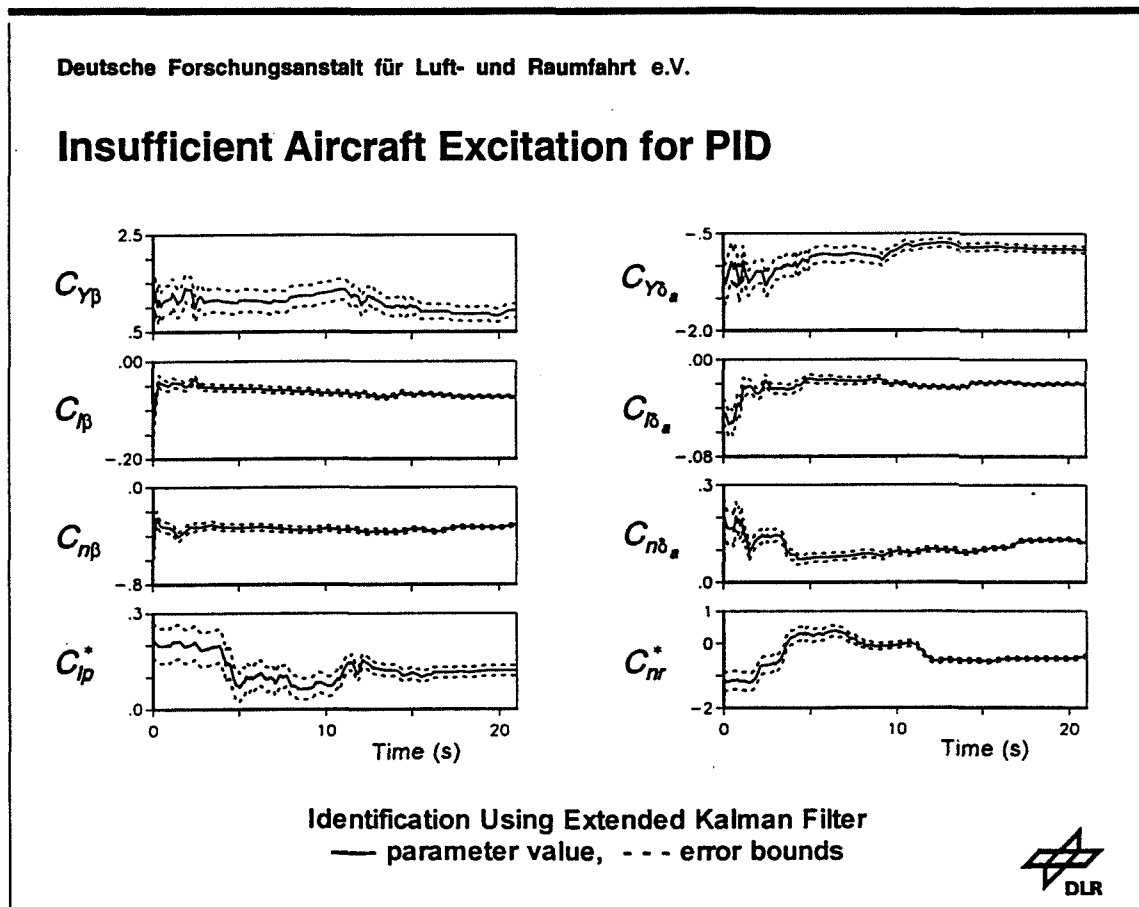
Insufficient Aircraft Excitation for PID

The overall low quality of the estimation results is attributed to the fact that the aircraft motion is insufficiently excited. The flight control system suppresses (as it should) all undesired motion, e.g. sideslip is kept close to zero and consequently the lateral acceleration is hardly excited. Also, the flight control system introduces artificial damping to the unstable aircraft.

That the overall information contents of the flight test data does not allow for the estimation of all aircraft parameters can be seen by the following identification results obtained using an Extended Kalman Filter algorithm (EKF). The EKF treats the aircraft parameters as additional state variables, which are assumed to be constant and are estimated together with the aircraft states.

The figure shows that some of the derivatives, like $C_{l\beta}$ and $C_{l\delta a}$ and the combined yaw damping C_{nr}^* (yawing moment due to roll and yaw rate) converge quickly whereas other parameters, such as the sideforce derivatives $C_{Y\beta}$ and $C_{Y\delta a}$ and the combined roll damping C_{lp}^* , remain with large error bounds.

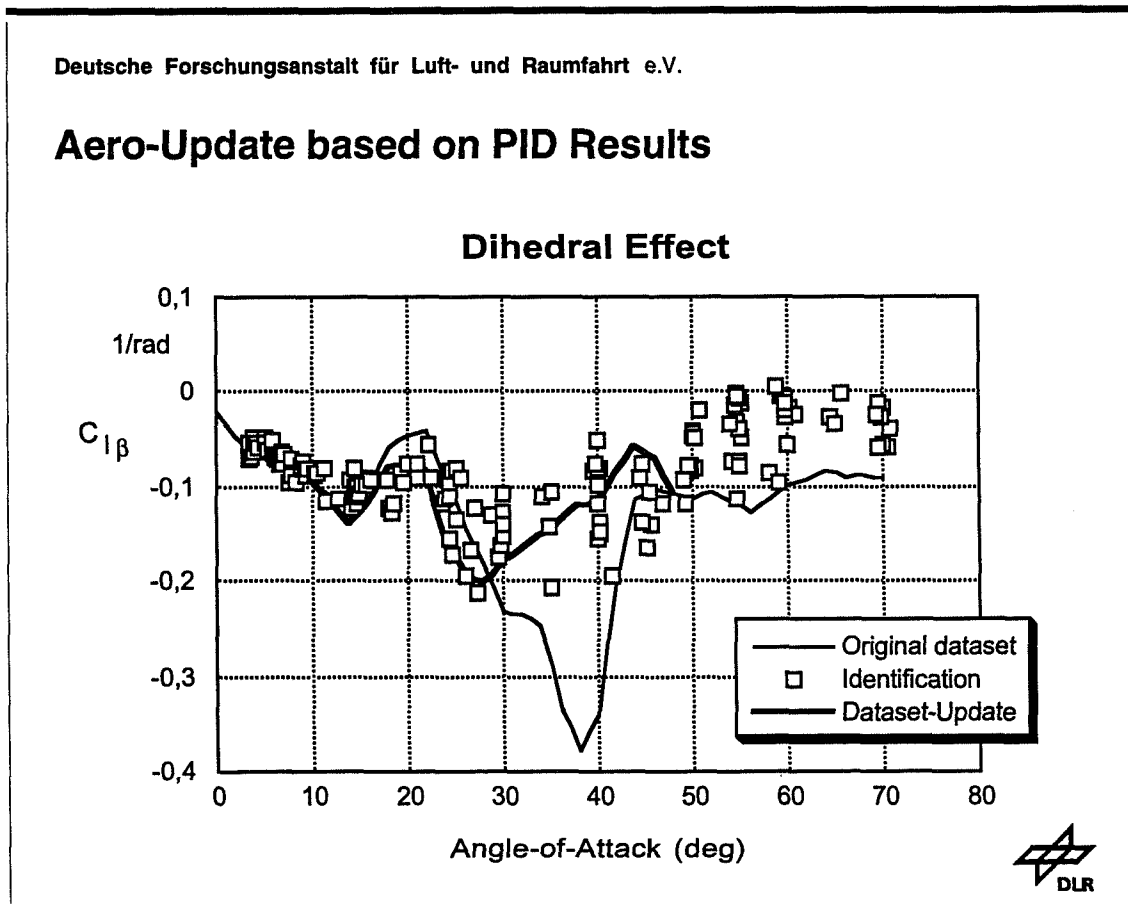
Effective excitation at high AoA is prevented by the X-31A flight control laws and would be achieved only by separate excitation of the different aerodynamic control surfaces and the thrust vectoring system.



Aero-Update based on PID Results

Even though the quality of the parameter identification results suffers from the aforementioned difficulties, some significant deviations from the wind tunnel predictions could be identified. The figure shows the dihedral coefficient as an example. The parameter identification results did not confirm the large negative values predicted by the wind tunnel for angles of attack between 30 and 40 deg.

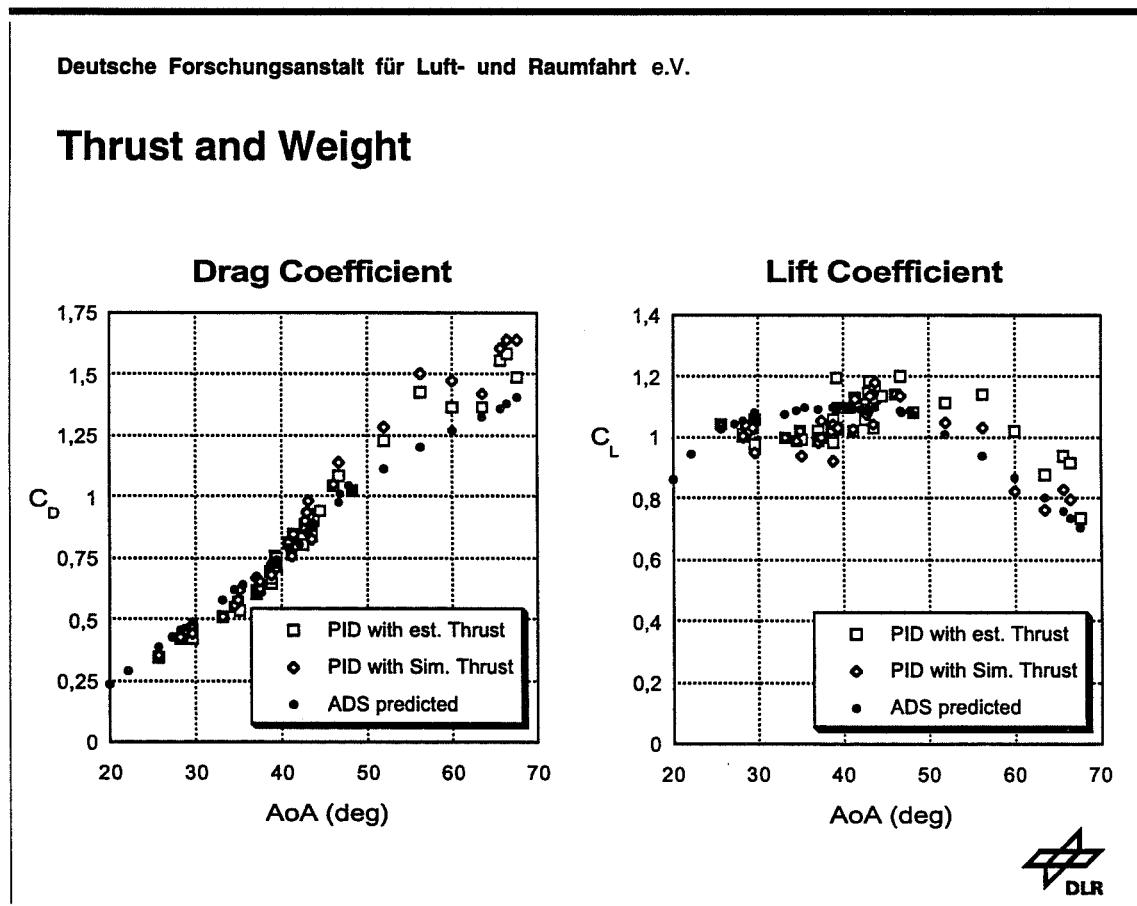
At the beginning of 1992, the aerodynamic database of the X-31 was updated for angles of attack up to 50 deg and the dihedral coefficient was one of the parameters that had to be changed. Identification results obtained for angles of attack above 50 deg indicate that an update of $C_{l\beta}$ in this area would also be appropriate.



Thrust and Weight

Especially for the longitudinal motion, an accurate knowledge of thrust, weight and CG location is crucial to obtain correct identification results. The figures below show the drag and lift coefficients, C_D and C_L , obtained by using (1) the thrust model used in the DASA simulation and (2) the thrust estimator currently implemented in the flight control laws. There are pronounced differences in the results for angles of attack above 45 deg.

Using the simulation thrust yields lift coefficients that are close to the predictions but drag coefficients that are much larger than the ADS values. With the estimated thrust, both lift and drag are somewhat higher than the predictions. This could be explained by the fuel gauge indicating too little fuel weight for high AoA (corresponding to high pitch attitude). The aircraft weight is then underestimated which in turn leads to higher drag and lift coefficients.

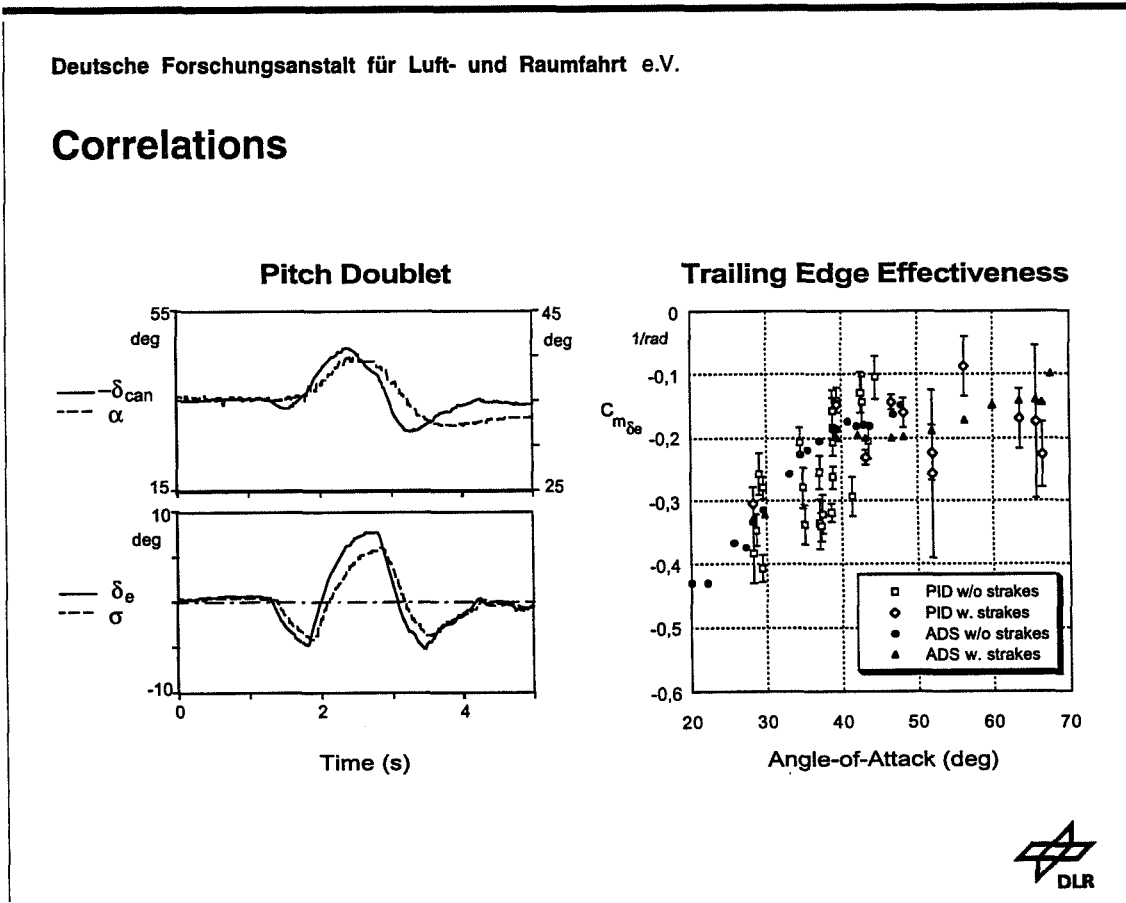


Correlations

As parameter identification is carried out with data from pilot generated maneuvers, control surface deflections and aircraft states are always correlated due to the flight control laws. For the lateral-directional motion, roll stick deflection commands roll around the velocity vector so that roll and yaw rate are correlated as well as aileron and horizontal thrust deflection. Therefore, the derivatives C_{Yr} , C_{lr} and C_{np} were set to zero (resulting in combined derivative estimation) and the TV effectiveness was set to a previously identified value.

In the longitudinal motion, the flight control laws lead to correlations between canard deflection δ_{can} and angle of attack α and between symmetric trailing edge deflection δ_e and vertical thrust deflection σ . This can be seen in the left figure which shows time histories from a pitch doublet at 35 deg AoA. Therefore, canard effectiveness was fixed at its predicted value for parameter identification throughout the entire AoA regime. For the post-stall regime, either trailing edge or thrust vector effectiveness had to be fixed.

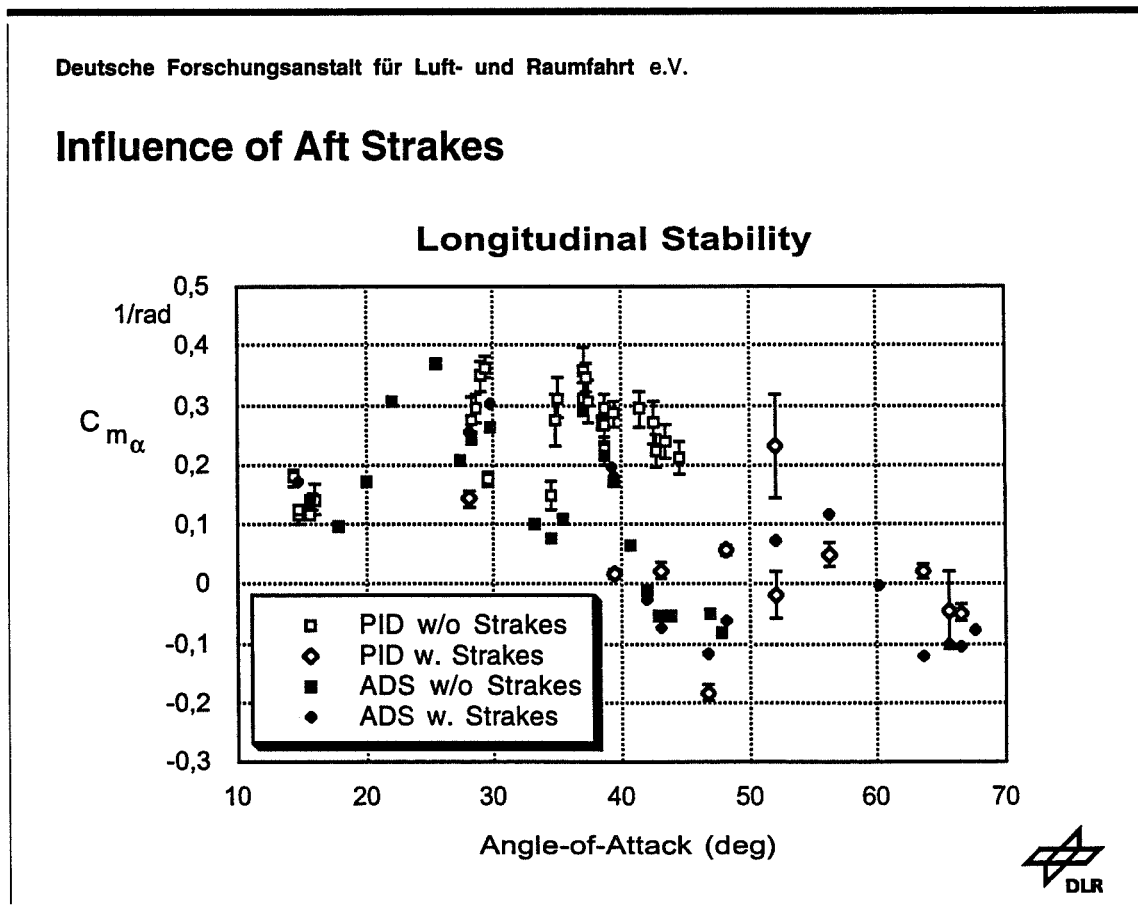
The diagram on the right side shows identification results for the trailing edge flap effectiveness, obtained with thrust vectoring effectiveness as predicted. The uncertainty levels are large, especially for very high angles of attack. No influence of the aft strakes on this parameter could be identified.



Influence of Aft Strakes

During early post-stall envelope expansion, it was discovered that the aircraft had significantly more nose up pitching moment than originally designed. The cause was found in changes made to the aft fuselage during the latter design phase. The problem was solved by installing strakes on the lower aft fuselage below the speedbrakes. The strakes brought the pitching moment sufficiently close to the original value used in the control law design.

The diagram below shows the identified values for the longitudinal stability, again obtained with canard and thrust vectoring effectiveness fixed at their predicted values. The identification results show that the trim changes caused by the aft strakes lead to increased stability as was predicted by the aerodynamic dataset.



Conclusions

X-31A parameter identification was carried out for angles of attack up to 70 deg. Aerodynamic parameters were mainly extracted from pilot generated doublet inputs and bank-to-bank maneuvers. Problems related to system instability and process noise could be overcome by the choice of appropriate estimation algorithms, e.g. regression and filter error method.

High correlations, however, allow only the identification of reduced aerodynamic models. Due to insufficient excitation of the aircraft motion at high AoA, the parameter estimates show large uncertainty levels and scatter.

In spite of the low quality of the estimation results, some deviations from the wind tunnel predictions could be identified in the lateral-directional axis and led to corresponding updates of the aerodynamic dataset.

Deutsche Forschungsanstalt für Luft- und Raumfahrt e.V.

Conclusions

- PID conducted up to 70 deg AoA
- Application of
 - ML Output Error Method
 - ML Filter Error Method
 - Extended Kalman Filter
 - Regression
- Reduced Aerodynamic Models
- PID results led to Update of the ADS



Outlook

Still in 1994, flight tests will be conducted using the flutter test box with a DLR fabricated signal generation card. This will allow single surface excitation of the aerodynamic control surfaces with inputs optimized for parameter identification. However, the thrust vectoring vanes cannot be excited directly by the flutter test box. These maneuvers should yield uncorrelated estimates for the stability and control derivatives up to 45 deg AoA.

Flight test maneuvers aimed at investigating nonlinear and unsteady effects, which were suggested by NASA Langley, have been flown.

Insight gained from both of these sets of parameter identification maneuvers will also aid in further evaluation of the data available so far.

Deutsche Forschungsanstalt für Luft- und Raumfahrt e.V.

Outlook

- **Single Surface Excitation**
 - flight tests with DLR card
- **Modeling of Nonlinear and Unsteady Effects**
 - flight tests (suggested by NASA Langley)
- **Further Evaluation of Current Data**



1995107822

N95-14236

324029

This paper shall discuss the evaluation of the original Dryden X-31 aerodynamic math model, processes involved in the justification and creation of the modified data base and comparison time history results of the model response with flight test.

57-021
16085
p. 23

**Validation of the NASA Dryden X-31
Simulation and Evaluation of Mechanization Techniques**

Edward Dickes

Jacob Kay

John Ralston

Bihle Applied Research, Inc.

**4th NASA High Angle-of-Attack Projects and Technology Conference
Dryden Flight Research Center
July 12-14, 1994**



The aerodynamic capabilities of newer tactical aircraft, such as the X-31, have made modeling of the low-speed end of the envelope increasingly important, particularly at very high angles of attack. The X-31 plans to exploit this region during evaluations of tactical utility of the experimental aircraft with demonstrations of high angle-of-attack, post-stall, 180 degree turns, known as the Herbst maneuver.

On the basis of observations made by Bihrl Applied Research, Inc. it was felt that certain changes to the Dryden X-31 simulation data base and data implementation techniques would improve the modeling of the in-control and departure characteristics of the flight test vehicle.

Program Background

- **Original X-31 Simulation Data Base Did Not Adequately Model the In-control and Departure Characteristics of the Flight Test Vehicle**
 - **The Ability to Confidently Evaluate the High Angle-of-Attack Flight Regime in the Sim Environment was Compromised Because of this Uncertainty**
- **Observed That Proper Implementation of Rotary-Balance Dynamic Data Effects May Improve Modeling**
- **Proposed Simulation Evaluation of Implementation of Static, Forced-Oscillation and Steady Rotational Terms On Model Response**



The present task involved checking the current X-31 data base, state variables and mechanization of the moment components. Particular emphasis was directed toward the lateral and directional properties below Mach=0.8. Data used in the Dryden simulation model were plotted against available wind tunnel data for comparison. The Differences were rationalized to reflect the aircraft configuration changes and updates. Further, the simulation was modified to incorporate known asymmetries and expanded for other functionalities to produce a model that was more representative of the test vehicle. Evaluations were made using the original data base, the revised data base, and with Kalviste's method of incorporating rotary-balance and forced-oscillation data in a six degree-of-freedom aircraft simulation against flight test results. Finally, the revised portions of the simulation data base were translated into a compatible format and delivered to NASA Dryden for use in their simulation model.

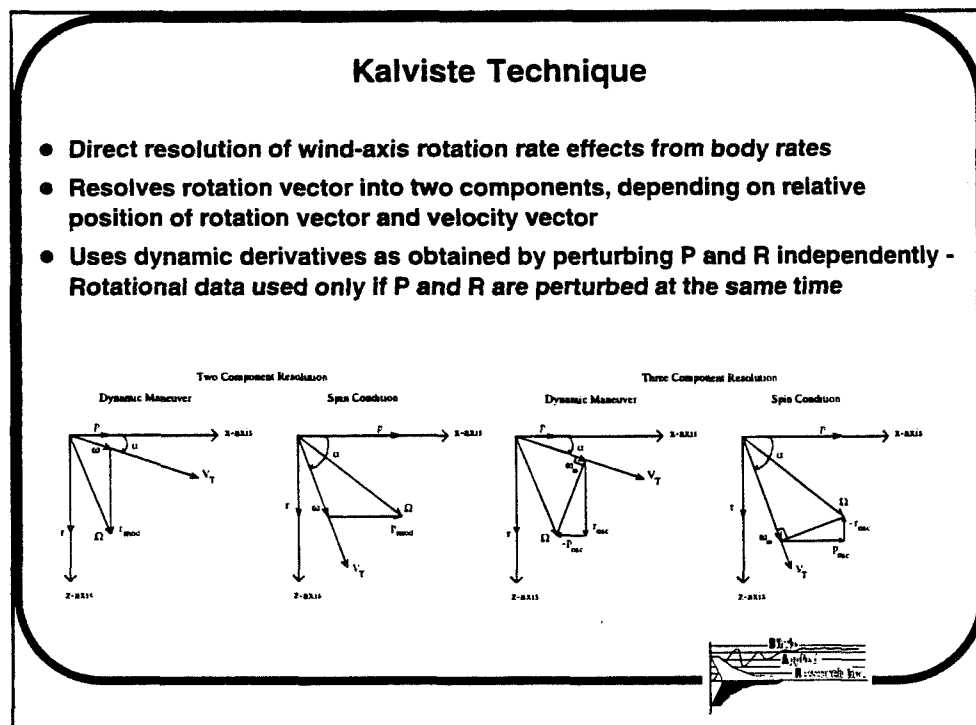
Task Description

- Acquire and Examine Current Data Base, Mechanization of Simulation Model, Flight Test Signals
- Comparison Plot Data Against Available Wind Tunnel Test Data Base, Rationalize Differences, Revisions
- Incorporate Known Asymmetries, Additional Functionalities into Data Base
- Evaluate Original / Revised Data Base, Kalviste Mechanization of Rotational Terms to Flight Test Results
- Re-format Revised Data Base into DRF X-31 Simulation Compatibility
- Document Data Revisions and Simulation Results



The mechanization of rotary-balance data into the simulation has been the subject of much evaluation in the past few years. An early method that was developed to permit the simulation of spins required the filtering of the wind axis roll rate. This method was successfully used on several early spin simulations, but because of the relatively long time constant involved, it had limited (and occasionally adverse) effects on high AOA rolling maneuvers. The most traditional method of implementing rotary data resulted when the filter time constant was reduced to zero, i.e., the rotation vector was resolved directly on to the velocity vector. This methodology is currently in use in a number of simulations, however concerns about the implications of this method raised by Juri Kalviste when an oscillatory residual opposes the total body-axis rate component (see the vector diagrams in the figure) led to the development of a third method of implementation.

A method was devised that distributes the aerodynamic damping effects based on the relationship of the airplane motion to the actual wind tunnel test motions used to derive the various damping terms. By resolving the airplane rotation into a single body-axis component and a wind-axis component, depending on the relationship of the rotation vector and the velocity vector, the residual body-axis term is always a subset of the total body-axis rate.



It has been well documented that forebodies can produce yawing moments in symmetric flight due to asymmetric shedding of the forebody vortices. It has also been demonstrated that the high angle-of-attack aerodynamic characteristics are very configuration dependent and that forebody geometry can have a significant influence on these characteristics.

The X-31 forebody contributes significantly to the propelling yawing moment characteristics of the total airplane at high angles of attack and exhibits static yawing moment offsets. Flight test data also indicates the occurrence of static yawing moments at high angles of attack at zero sideslip. The Dryden X-31 simulation model did not contain the yawing moment asymmetries in the 40 to 80 AOA region that were observed during X-31 wind-tunnel testing and the curve values in the simulation for the basic static directional stability were symmetric.

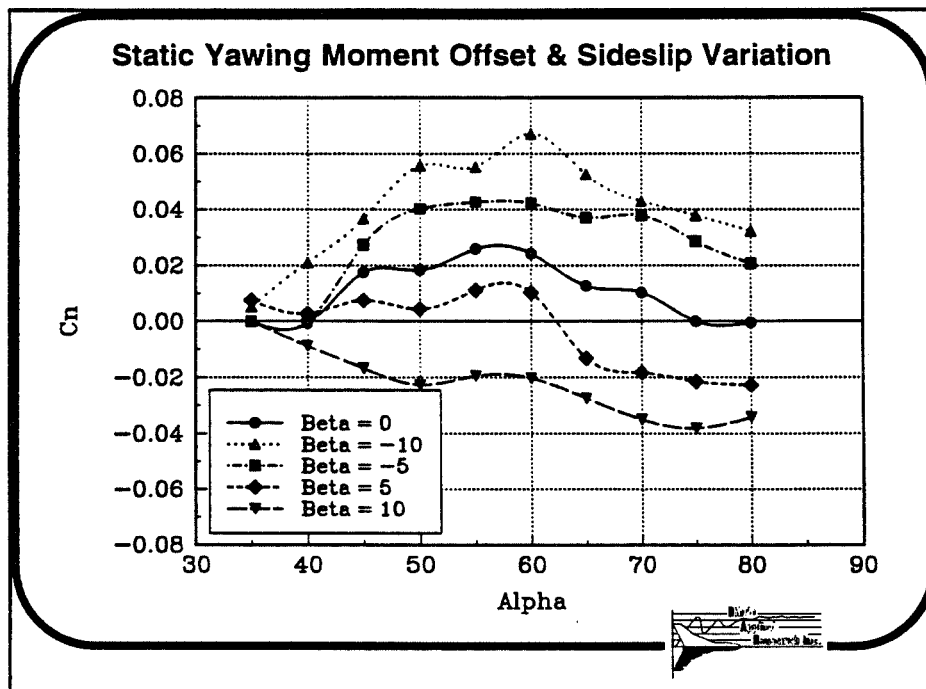
Static data from the NASA Langley 30x60 wind tunnel were obtained to investigate the effect of the yawing moment offset by incorporating the yaw asymmetry at high angles of attack into the simulation model.

Incorporation Of Yaw Asymmetry At High AOA

- **Flight Test Data Indicates Occurance of Static Yawing Moment at High AOA at Zero Sideslip**
 - **Offsets Ignored in Sim Model**
 - **Sideslip Asymmetry Due to Offset Influence Also Needed**
- **Obtained NASA Langley 30x60 Static Data to Investigate Yawing Moment Offset Effect**
 - **Generated Replacement Sim Table for Basic Yawing Moment Incorporating High AOA Offsets on Zero and Non-zero Sideslip**



The static yawing moment versus angle of attack from the wind tunnel tests is presented in this figure. As shown, the zero sideslip offset reaches a maximum value of approximately 0.026 at 55 deg AOA and a non-zero sideslip asymmetry due to the influence of the zero sideslip offset value also occurs for sideslip angles up to 10 deg. A replacement simulation table for the basic yawing moment was generated, incorporating these high angle of attack offsets on zero and non-zero sideslip angles for the tested angle of attack region between 40 and 80 deg. The incorporation of these offsets results in an extended sideslip argument, because of the non-symmetrical nature of the data.



Another concern about the current configuration's rotational yawing moment characteristics was over the presence of the aft fuselage strakes, located along the side of the fuselage, essentially where the unfaired actuators for the thrust paddles were on an earlier tested X-31 configuration. The effect of these aft strakes on the rotational characteristics of the aircraft has never been assessed, but some indication can be gained by examining the actuator effect, found by comparing the earlier (unfaired actuators) configuration with the later (faired actuators) configuration, which indicates a degradation in yaw damping due to the presence of these actuators. Limited free-spin tests also indicated a degradation in the model's characteristics, with the wing rock motions becoming more divergent and the model exhibiting the high-incidence kinematic roll (HIKR) departure more readily.

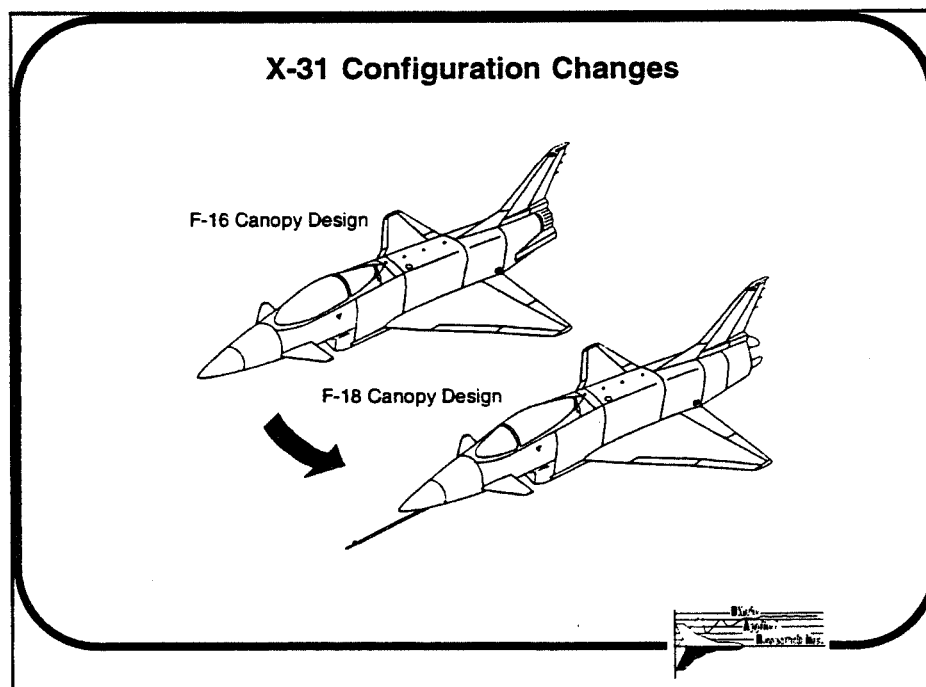
Incorporation Of Aft Strake Rotational Yawing Moment Effect

Aft Strake Considerations

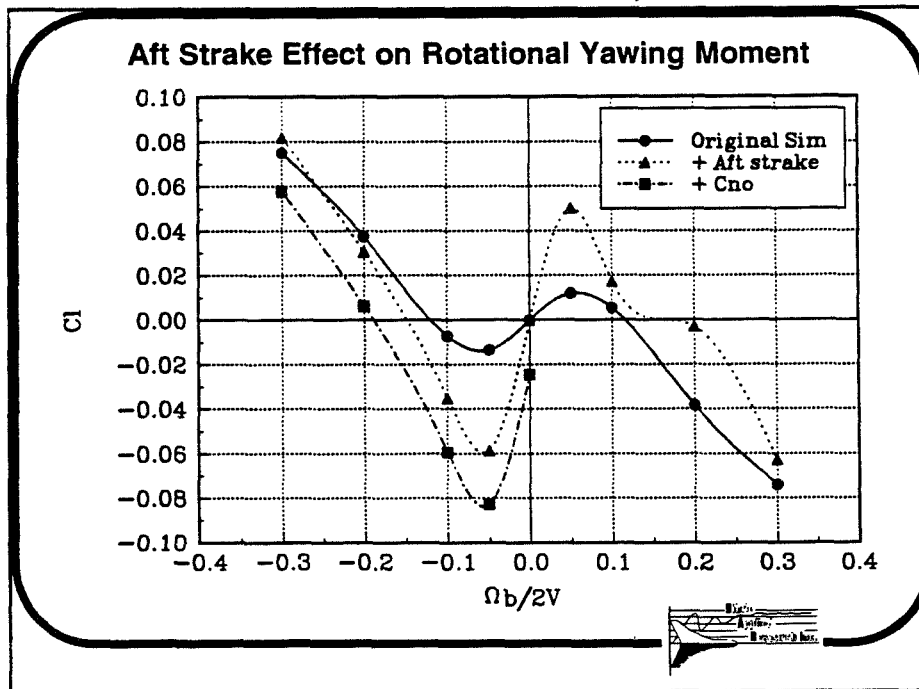
- **Current Configuration Possesses Aft Strakes**
- **Limited Assessment Of High AOA Dynamic Effects**
 - **No Rotary-Balance Tests with Aft Strakes**
 - **Free-spin Testing Indicated Degradation**
- **Comparison to Earlier Configuration Indicates Degradation with Actuator Surfaces Below Vertical Tail**
 - **Past Experience Has Shown Flow Separation Effects Generated Below Vertical Tail Can Induce Adverse Pressure Field When Rotating**
- **Generated 'Quick-Look' Incremental Rotational Yawing Moment Tables for Limited Study of Aft Strake Effect**



A 'quick-look' set of incremental rotational yawing moment tables were generated for a limited study of the aft strake effect in the departure region utilizing the earlier X-31 configuration yaw damping characteristics with the actuator fairings installed. The earlier configuration exhibits propelling yawing moments out to further rotation rates at 50 AOA and is significantly more propelling in yaw about the velocity vector in the 60 degree AOA region. (It should be noted that for this quick-look the rotational data only covered 40 to 80 AOA, and therefore comparisons below 40 AOA in this case are invalid). Past experience with other military configurations has shown that flow separation effects generated below the vertical tail can induce an adverse pressure field on the vertical tail when rotating in this AOA region. This pressure field can result in lower surface pressures on the windward vertical tail surface at low rotation rates, thus producing propelling yawing moments.



Incorporation of the aft strake effect on rotational yawing moment characteristics for the Dryden X-31 simulation model is shown in this figure. LE Flap=40/32, Canard=-40, Sideslip=0 deg, AOA=60 deg. The first two curves represent only the rotational increment for the original model and for the aft strake effect. The last curve represents the addition of the rotational increment to the static offset curve.



The Bihrie Applied Research X-31 simulation contains a built-in validation routine that allows it to be overdriven with flight test data. The advantage of this ability is to duplicate the conditions and pilot inputs of the flight test maneuver exactly, thereby allowing one-to-one comparisons of the resulting time histories in order to determine model fidelity. In addition, it is not necessary to incorporate the aircraft control system for this procedure.

Flight test obtained states and control deflections were used as inputs to drive the closed-loop simulation to compute the data base generated forces and moments. The output values, in the form of moment coefficients, were analyzed by comparison with the flight-test extracted coefficients. In order to isolate the flight-test aerodynamic moment, the contribution due to thrust vectoring had to be removed. Due to time limitations and the complexity of the engine thrust model in the Dryden simulation, the yawing moment generated by thrust vectoring was approximated by an algorithm developed by Bihrie Applied Research. This simplified algorithm was found to be reasonably accurate for small to intermediate vane deflections, and tended to over estimate yaw due to thrust as the vanes approached the limits of their deflection. Regardless, this estimation scheme permitted a rapid assessment of the available flight data for the limited scope of this study. The yawing moment produced by thrust vectoring was then subtracted from the flight-test extracted total moment coefficient to yield the aerodynamic portion of the generated yawing moment which was used to compare with the data base produced results.

Comparison Of Model Response With Flight Test Results

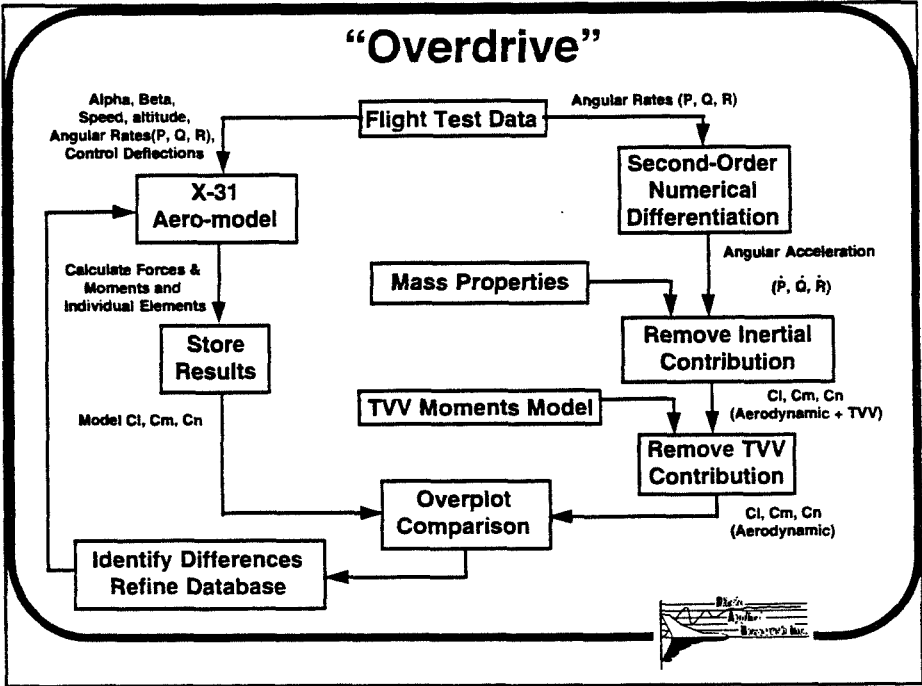
- **Closed Loop Evaluation Using Selected Flight Test Data**
 - **Simulation Driven by Flight Test Rates and State Variables**
 - **Algorithm Developed to Estimate Thrust Effects**
 - **Routine to Plot and Save Aero Coefficients for Comparison to Flight Test Data**

- **Comparison of Flight Test Results and Driven Sim Response**
 - **Ability to Select Specific Components of Total Coefficients**
 - **Assess Contributions of Effects on Resulting Total Moment**



The BAR closed-loop simulation also stores the time history of each element of the aerodynamic forces and moments. Comparison plots of these components before and after modifications to the data base help to assess the contributions of these effects on the total resulting moment, identify poorly modeled effects, and validate changes to the simulation model. In addition, the BAR simulation also provided options to activate/incorporate rotational data, static yawing-moment offsets, strake effects, and the Kalviste technique for mechanization of the rotary-balance and dynamic derivative data. A utility program was used to produce overplots of flight-test results versus simulation response with the various changes to the model data and mechanization.

A flow chart describing the procedure used for the comparison of X-31 flight test results and the simulation model response is shown.



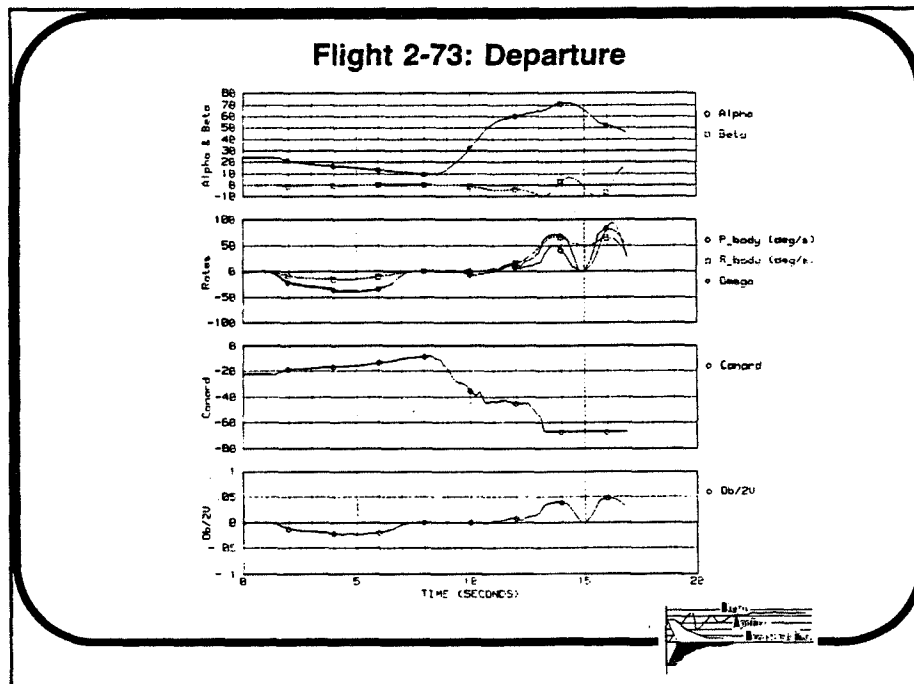
Listed in Table I are the flights investigated in this effort and the corresponding maneuvers performed.

Flights Investigated

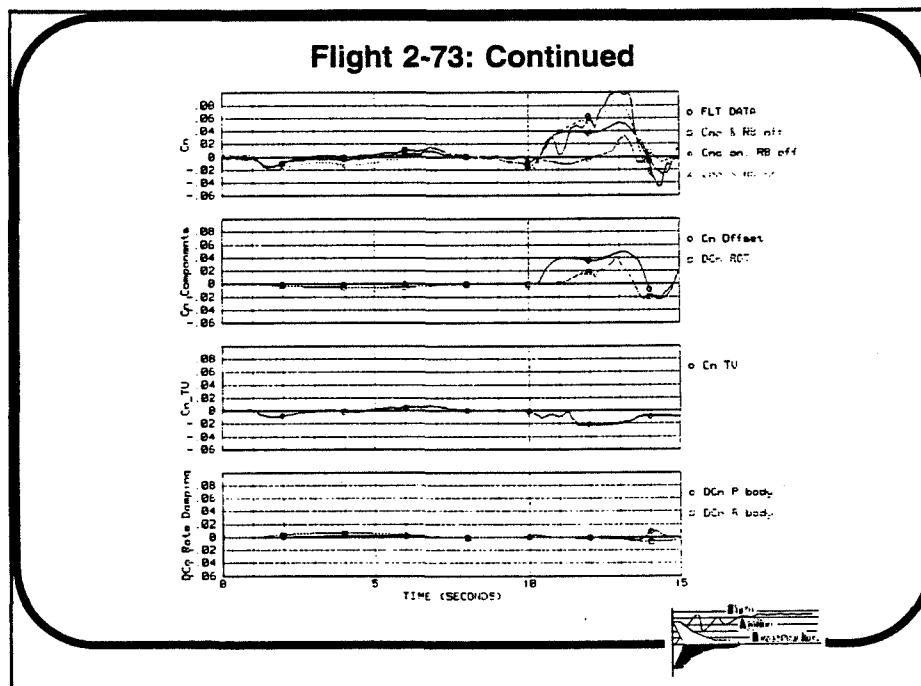
<u>FLIGHT NUMBER</u>	<u>DESCRIPTION</u>
2-73	Departure
2-85	Velocity-vector Roll @ 40 AOA
2-56 (205)	Level Deceleration to 70 AOA
2-56 (360)	360 Left Roll @ 40 AOA
2-56 (361)	360 Right Roll @ 40 AOA
1-116 (.10)	Right Turn + Left Roll + Left Turn @ 10 AOA with Thrust Vectoring
1-116 (.11)	Right Turn + Left Roll + Left Turn @ 10 AOA w/o Thrust Vectoring
1-83 (1083)	Level Deceleration to 50 AOA
1-83 (830)	Full-stick Bank-to-bank @ 50 AOA
1-83 (831)	Full-stick Bank-to-bank @ 55 AOA
1-83 (832)	Full-stick Bank-to-bank @ 60 AOA
1-86	Level Deceleration to 70 AOA, Bank-to-bank



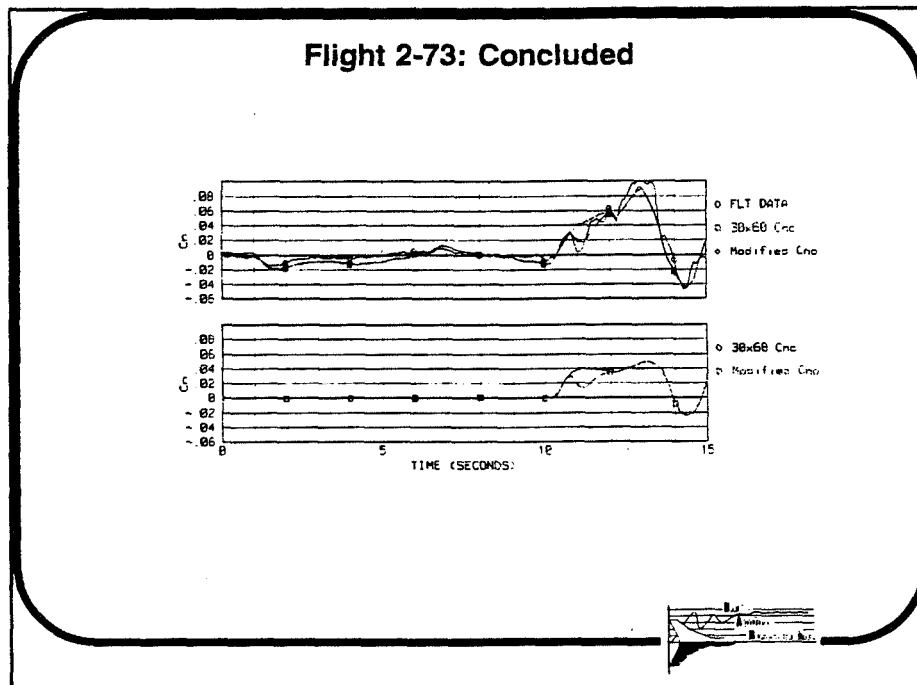
The time history traces for the departure of Flight 2-73 are presented in the accompanying figures. This first figure presents the angle of attack, angle of sideslip, body-axis rates, canard deflection and the non-dimensionalized rotation rate ($\Omega b/2V$) throughout the flight. This flight was flown with Ship 2, Version 1.16 FCS software, with the aft fuselage strakes installed and 'grit strips' on the noseboom and radome. The maneuver was performed at 35,000 ft/0.4 Mach and consisted of a full aft pitch input from inverted flight with maximum afterburner set and the angle of attack limiter set at 60 deg AOA (a split S maneuver). As the aircraft approaches 60 deg AOA, a positive yaw rate and negative sideslip excursion develops. The airplane continues to depart from controlled flight with increasing angle of attack and yaw rate. The angle of attack reached a value of 70 deg, where the aircraft becomes highly damped in yaw again, preventing the aircraft from obtaining further increases in angle of attack, resulting in a fast, flat spin. The pilot initiated recovery with forward stick and with the angle of attack reduction, the yaw rate damped to zero, completing recovery of the aircraft to controlled flight.



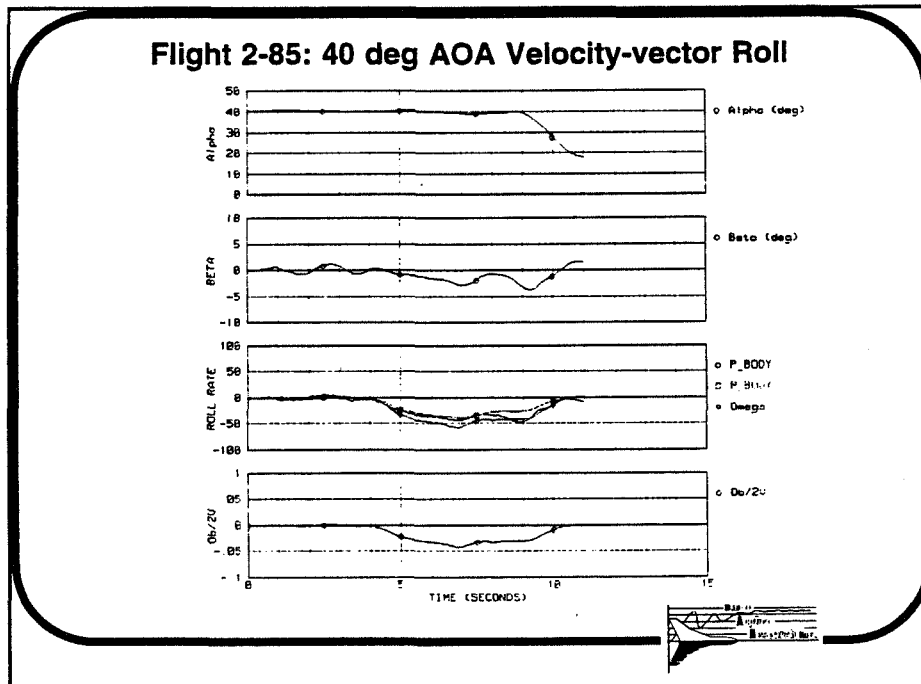
This figure presents the yawing moment propagation for the departure of Flight 2-73, comparing the results of the original simulation model and the modified model response to the flight extracted yawing moment. Also included are the contributions to the total yawing moment of the static offset, rotational effects, thrust vectoring and forced oscillation damping terms (developed when the rotational effects are turned off). The modified model uses Langley 30x60 wind tunnel yawing moment data versus sideslip, including the static offsets, as well as the rotational yawing moment data versus $\Omega b/2V$, updated for the aft strake configuration. As shown in this figure, a result that is close to the airplane response only occurs when including both the offset effects as well as the rotary balance terms with the Kalviste method.



Based on flight extraction performed by Dryden, as well as by BAR, a reduction in the static yawing moment offset value was found to occur near 55 deg AOA. By modifying the offset value to reflect this effect, and maintaining the original sideslip variation, the resulting yawing moment time history exhibits an even closer match to the flight extracted yawing moment.

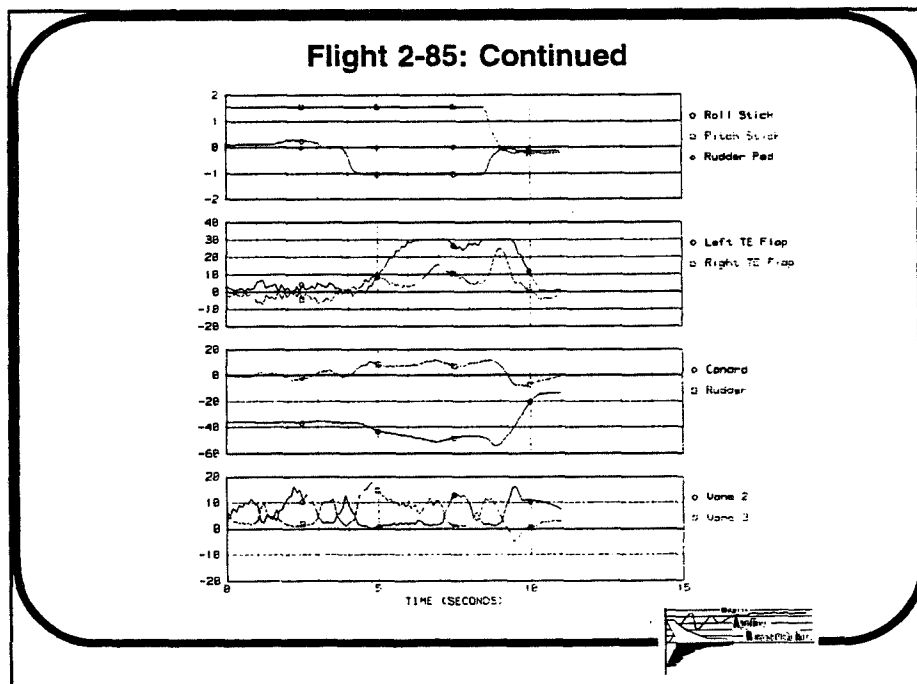


Further evidence of the importance of modeling the rotary terms, particularly in the post-stall region, is shown in the following accompanying figures for Flight 2-85, a 40 deg AOA, 360 deg roll about the velocity vector.

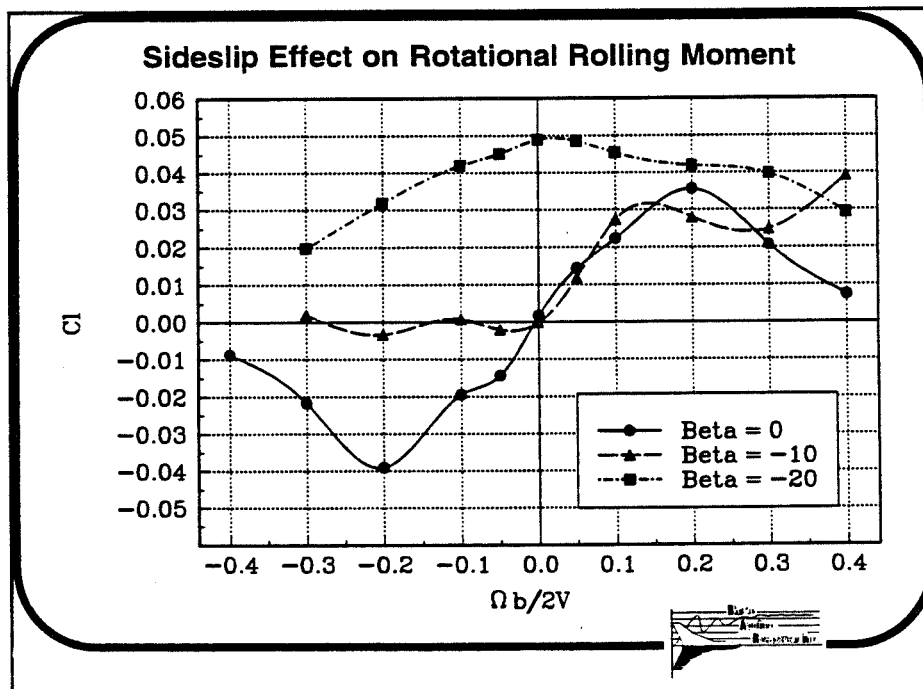


This figure shows the control inputs and deflections of Flt 2-85. It should be noted that the flaperons, following a brief deflection in the direction of the left roll, immediately deflect to near the limit opposing the roll, evidence of a significantly propelling condition at this angle of attack.

When the roll characteristics for this configuration are examined about the velocity vector, this is indeed seen to be the case.

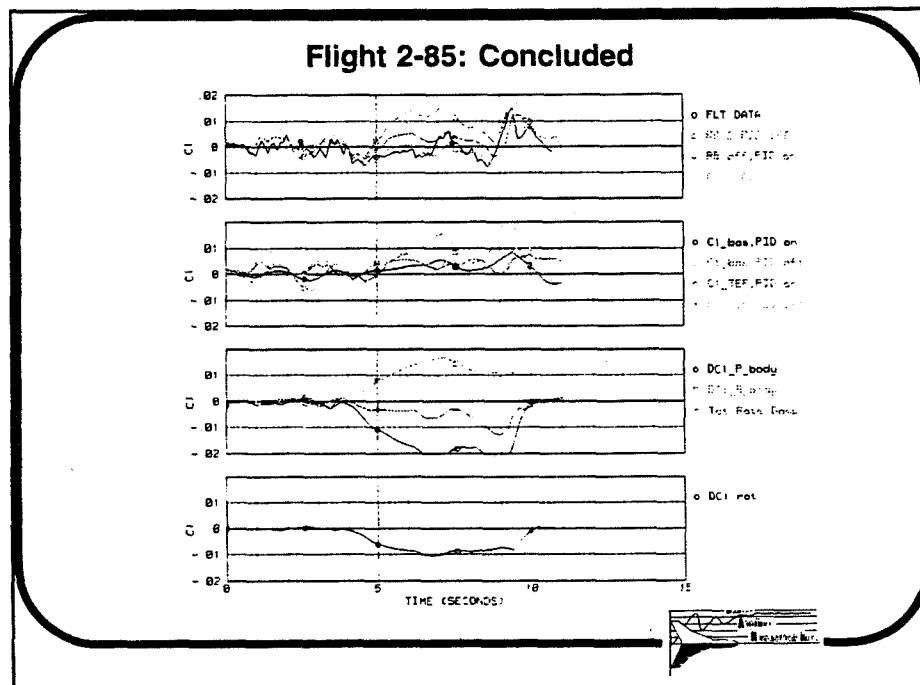


The steady-state rotational aerodynamic characteristics of the X-31 were determined in earlier tests performed by Bihrl Applied Research utilizing the rotary-balance rig located in the NASA Langley 20-Foot Spin Tunnel. In the normal flight regime, the basic airplane is highly damped in roll. However, as the aircraft approaches stall the level of damping is reduced, such that the aircraft becomes highly propelling in roll by 30 deg AOA and remains so through 60 deg AOA. The sideslip effects in this angle-of-attack region are very non-linear and vary significantly with rotation, especially where the aircraft is highly propelling at zero sideslip.

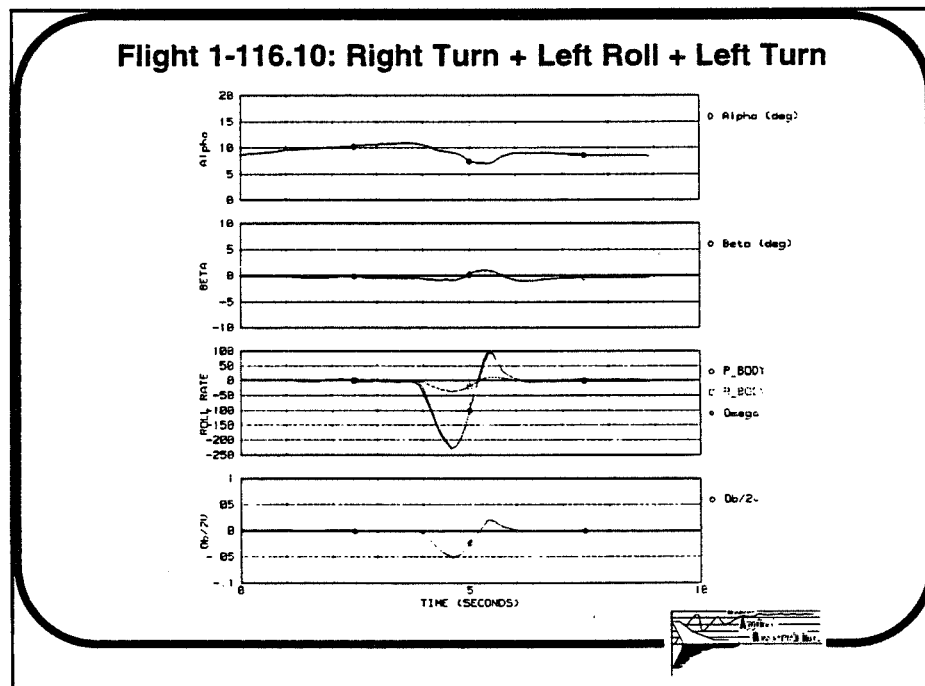


This figure displays the propagation of rolling moment versus time for the flight test data of Flt 2-85 as well as the original simulation, which did not incorporate the rotational data. As shown, the original model exhibited a poor match with flight.

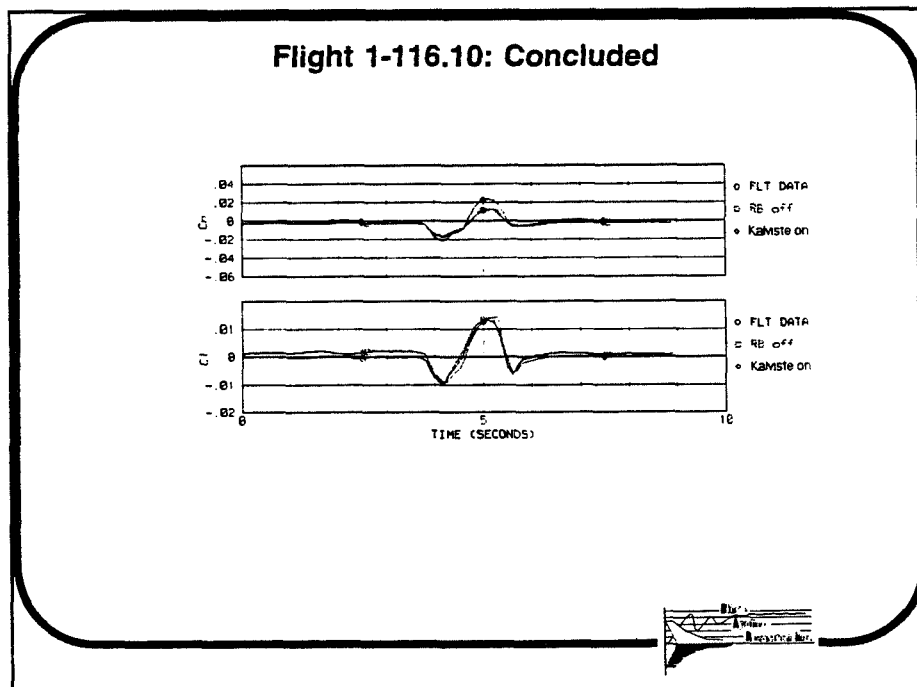
Because the model, as originally mechanized, would roll in the opposite direction when driven with the flight test control inputs, the test center attempted to improve the match by significantly reducing the lateral stability. Even with these changes, the match was less than satisfactory. The total dynamic roll contribution from the combination of the roll and yaw rate damping terms is shown for the coordinated roll using the conventional buildup, and is seen to be significantly less propelling than the rotational damping increment that results if the Kalviste technique is used instead. When this increment is utilized as the dynamic contribution in rolling moment due to the velocity vector roll, as shown in the final rolling moment comparison, a very good match with flight test data is obtained.



Flight 1-116.10, a 10 deg AOA right turn followed by a roll to the left and left turn, was investigated to check the model mechanization technique at low angles of attack. This first figure presents the angle of attack, angle of sideslip, and the rate traces for the maneuver. Because of the low angle of attack and the coordination of the maneuver, the body-axis roll rate is essentially equal to the wind-axis roll rate (ω) throughout the maneuver.



This figure presents a comparison of the total rolling and yawing moment coefficients extracted from Flt 1-116.10 with those obtained for the two cases of using only forced-oscillation data (rotary-balance terms off), and the incorporation of the rotational terms with the Kalviste technique (Kalviste on). Since these curves are identical, the damping contributions from using either the conventional or Kalviste mechanization technique must be the same.



The original NASA Dryden X-31 simulation data base exhibited significant divergence from the behavior of the aircraft seen in flight at many high angle-of-attack conditions. The fidelity of this simulation model has been significantly enhanced by incorporating several revisions to the high angle-of-attack data base and how the dynamic terms are implemented. Comparison of X-31 flight test results to the updated model response, including out-of-control motions, shows greatly improved correlation.

Conclusions

- **Simulation Data Base Needs To Reflect Current Aircraft Configuration Static and Dynamic Characteristics For Proper Modeling**
- **For All High AOA Dynamic Flights Examined to Date, The Inclusion of Rotary Balance Data Using Kalviste Technique Improves Model Fidelity**
 - **Very Pronounced In Post-Stall Rolling Maneuvers as well as Departure**
 - **No Degradation at Low AOA**
- **Configuration Evaluation, Flight Control Development, Training Requirements Dictate Immediate Need For Validated Simulation Technique To Accurately Model High AOA Regime**



References

1. Kalviste, J.: Use Of Rotary Balance And Forced Oscillation Test Data In A Six Degrees Of Freedom Simulation, AIAA Paper 82-1364, August 1982.
2. Dickes, E., Barnhart, B., and Bihrlle, W. Jr.: Analysis Of Static And Rotational Aerodynamics At High Angles Of Attack For The Rockwell X-31A (F-18 Canopy, 1989 Configuration) Including Appendix: Exploratory High Alpha Improvement Study, Bihrlle Applied Research Report 91-7, October 1991.
3. Dickes, E.: Incremental Rotational Aerodynamic Math Model Of The Rockwell/MBB X-31A Configuration For Simulation Of Flight Motions Between 0° And 90° Angle Of Attack, Bihrlle Applied Research Report 89-9, August 1989.
4. Bihrlle, W. Jr., Barnhart, B., and Dickes, E.: Influence Of Forebody Geometry On Aerodynamic Characteristics And A Design Guide For Defining Departure/Spin Resistant Forebody Configurations, Wright Research And Development Center Report WRDC-TR-89-3079, September 1989.
5. Dickes, E.: Analysis Of Static And Rotational Aerodynamics At High Angles Of Attack For The Rockwell X-31A Preliminary Configuration, Bihrlle Applied Research Report 88-1, January 1988.
6. Ralston, J.: Rotary Balance Data And Analysis For The NAVY EA-6B And Proposed ADVCAP EA-6B Airplanes, Bihrlle Applied Research Report 84-7, November 1984.

28pg

1995107823

N95-14237

324030

**FREE-TO-ROLL TESTS OF X-31 AND F-18 SUBSCALE
MODELS WITH CORRELATION TO FLIGHT TEST
RESULTS**

58-02

16086

P-28

David L. Williams II

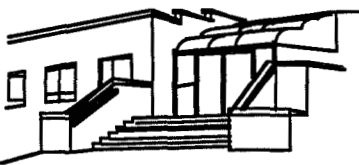
Robert C. Nelson

**Hessert Center for Aerospace Research
University of Notre Dame, Notre Dame, Indiana**

David F. Fisher

NASA-Ames Research Center

Dryden Flight Research Facility, Edwards, California



**The Hessert Center for Aerospace Research
Notre Dame, Indiana**

OUTLINE OF PRESENTATION

This presentation will concentrate on a series of low-speed wind tunnel tests conducted on a 2.5% subscale F-18 model and a 2% subscale X-31 model. The model's control surfaces were unaugmented; and for the most part, were deflected at a constant angle throughout the tests. The tests consisted mostly of free-to-roll experiments conducted with the use of an air-bearing, surface pressure measurements, off-surface flow visualization, and force-balance tests. Where possible the results of the subscale tests have been compared to flight test data, or to other wind tunnel data taken at higher Reynolds numbers.



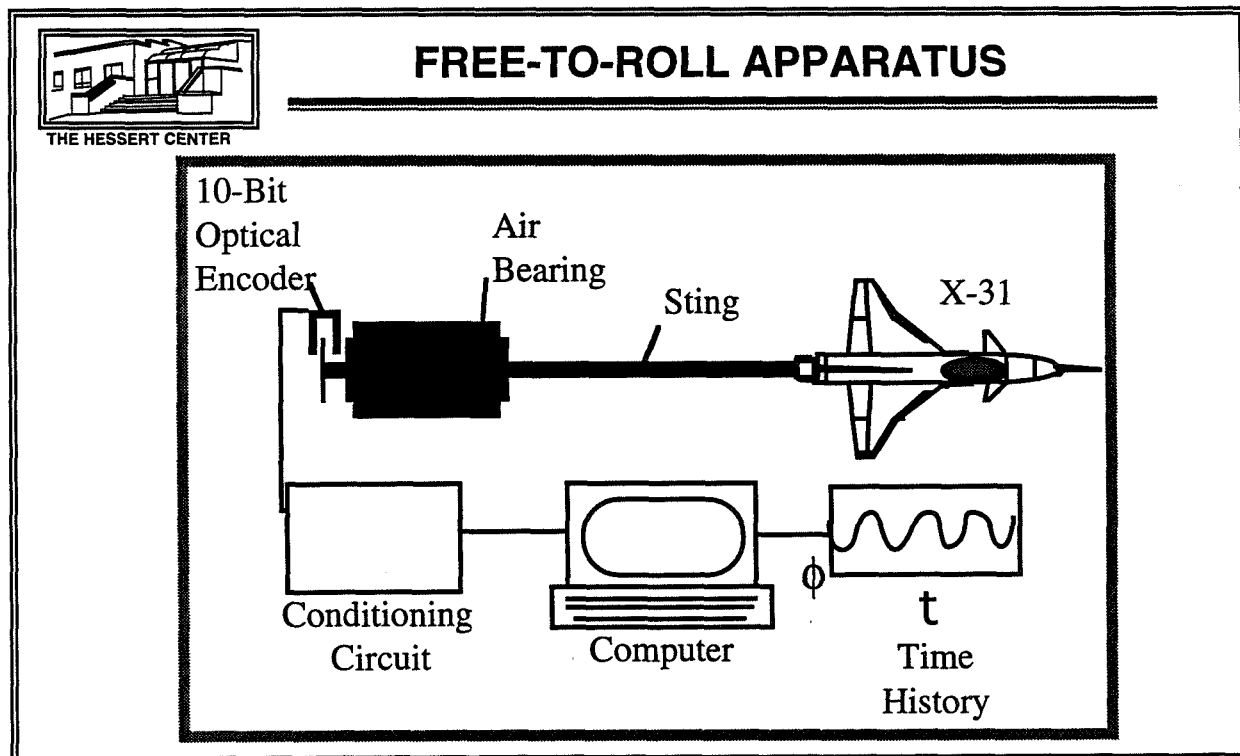
OUTLINE OF PRESENTATION

- **Experimental Procedures and Equipment**
- **F-18 and X-31 Model Configurations**
- **Self-Induced Motion Envelopes of Models Versus Flight Tests or Drop Model Tests**
- **Vortex Behavior During Self-Induced Motions**
- **Reynolds Number Issues for Dynamic Roll Experiments**
- **Concluding Remarks**

FREE-TO-ROLL APPARATUS

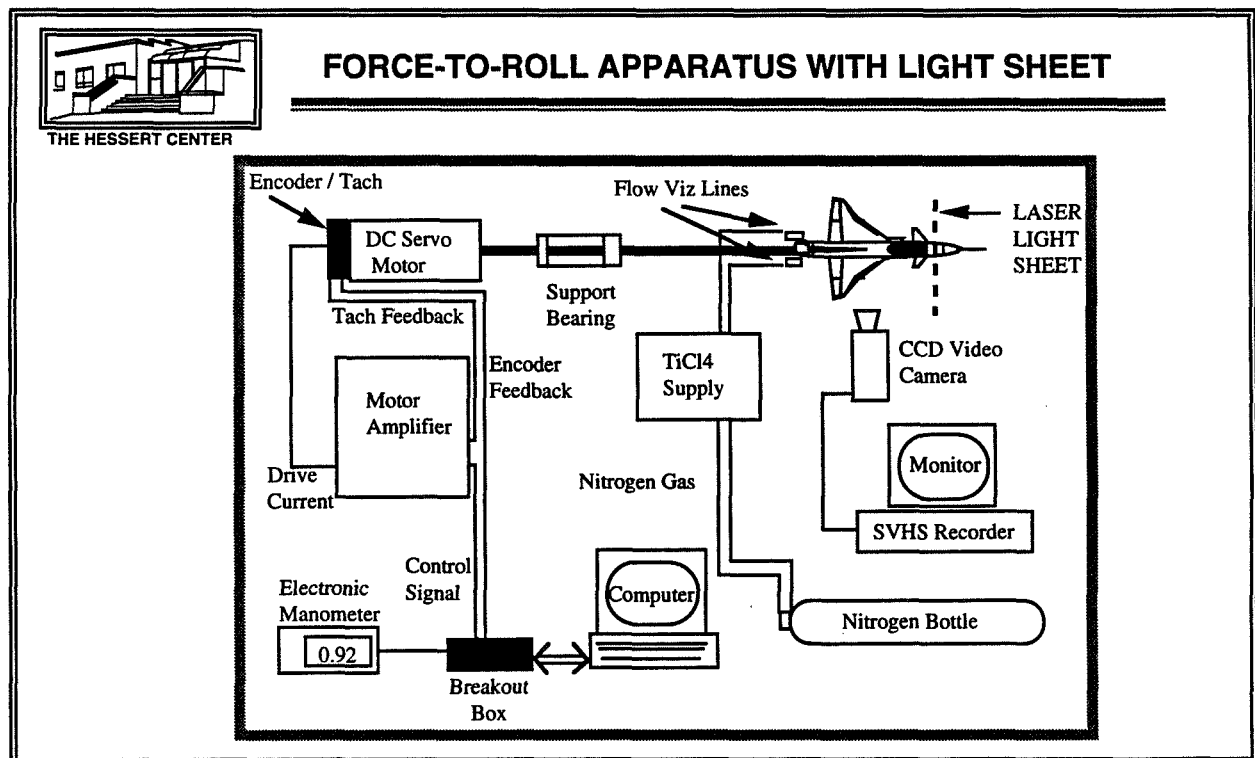
Two unique experimental apparatus have been developed at the University of Notre Dame to study the wing rock characteristics of slender wings and subscale models. The systems consist of a free-to-roll apparatus which is used to measure the rolling histories of a model in the absence of bearing friction, and a controlled motion apparatus for flow visualization and unsteady surface pressure measurements.

A schematic of the free-to-roll apparatus may be seen below. This apparatus was designed to allow for a simulation of the free flight environment for a single-degree-of-freedom. At the heart of the apparatus is the air bearing spindle. The air bearing reduces the bearing friction within the system by an order of magnitude over that achieved with low friction ball bearings. Thus, the free-to-roll system allows the isolation of aerodynamic roll moments acting on the model. Instantaneous roll angle is provided by a 10-bit modular, optical encoder yielding an angular resolution of 0.35° . The use of the modular encoder eliminates any friction in the roll measurement process. The time histories from the encoder are stored and may be used to estimate angular velocity, acceleration, and aerodynamic rolling moments.



FORCE-TO-ROLL APPARATUS WITH LIGHT SHEET

To obtain dynamic flow visualization data on a model undergoing wing rock, a unique motion control / data acquisition system is used. The motion control system is necessary due to smoke injection tubing for flow visualization, and the wire leads from the pressure transducers to the data acquisition computer. The tubes and transducer leads eliminate the free-to-roll nature of the system. A sketch of the system may be seen below. Motion control is accomplished with a DC servo motor connected to a motor amplifier and motion control computer board. Tachometer and encoder signals are used for feedback. The motion controller uses high-speed digital processing and has an accuracy of ± 1 count in 10,000 (0.036°). Digital proportional-integral-derivative (PID) with velocity and acceleration feedforward control is implemented for precision tracking of the time history. All gains are user adjustable so that the system may be fine-tuned for a given model. The servo motor is connected to the model via a sting which rides on conventional ball bearings. Time histories taken with the free-to-roll apparatus were used to provide the input signal to the motion control system to drive the model through the self-induced roll oscillation trajectories. The system accurately reproduces a free-to-roll time history while allowing for an instrumented model to be used.

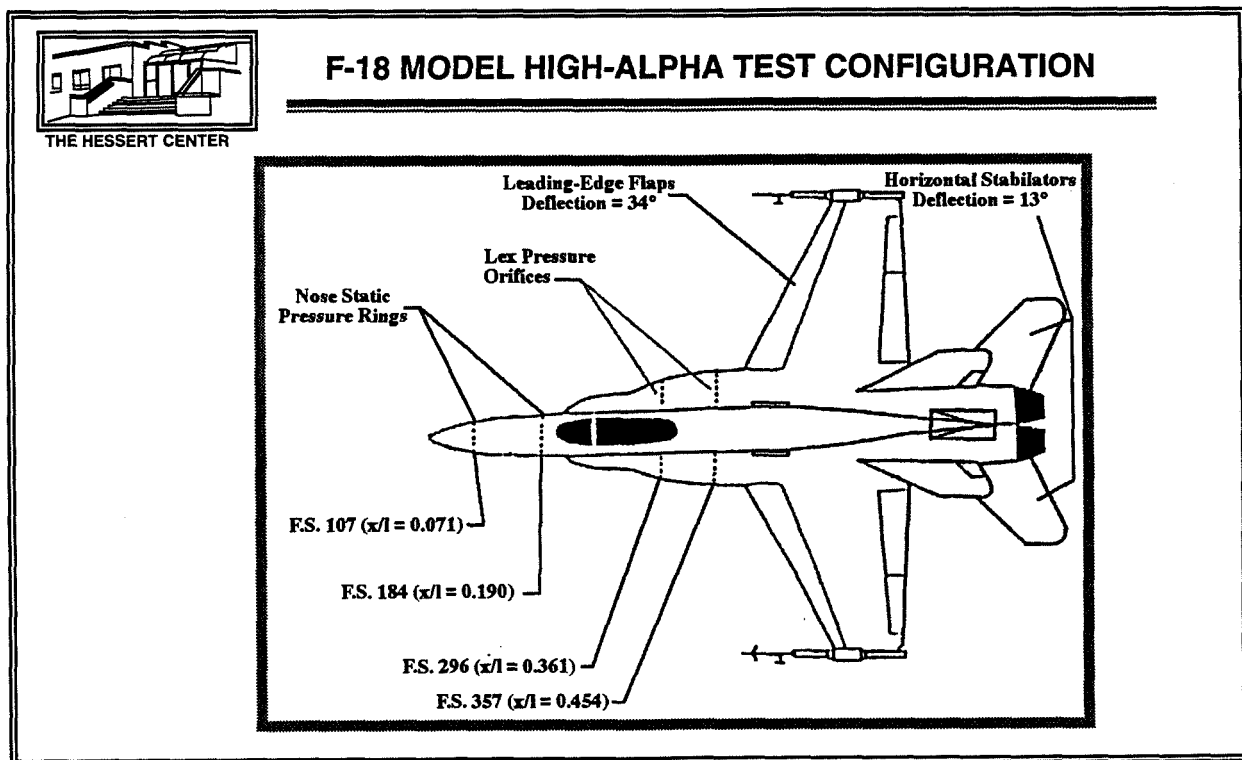


F-18 MODEL HIGH-ALPHA TEST CONFIGURATION

The F-18 model used in these experiments was a 2.5% (1/40th) scale model. Since the model contained stationary flight control surfaces, these were deployed to represent a correct configuration of the HARV vehicle in high-alpha flight conditions. The leading-edge flaps were set to a fixed 34° down since all investigations were at angles-of-attack greater than 20°. In addition, the horizontal stabilators were fixed at a positive 13° rotation which represents a mean deflection over the angle-of-attack range tested. All other control surfaces were set to 0° deflection.

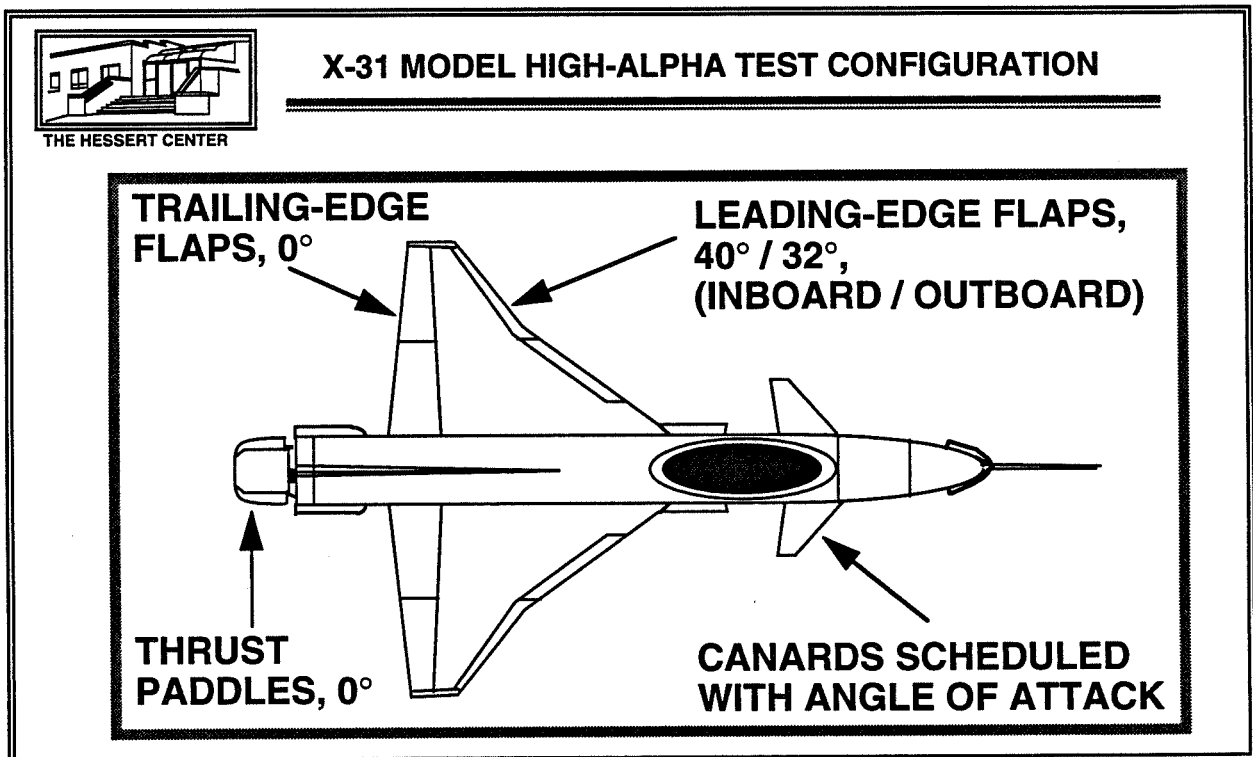
In order to investigate the surface pressures existing on the subscale model during testing, static surface pressure taps were installed at several fuselage stations (F.S.) corresponding to those tested on the HARV vehicle. Due to the small size of the model, the number and spacing of these static pressure taps at each fuselage station was constrained; however, enough were installed to allow comparison of the surface pressures on the 2.5% model to similar measurements completed on the HARV vehicle⁶.

Lastly, to investigate off-surface flow structures, internal flow visualization ports were installed in the forebody and LEX's of the model.



X-31 MODEL HIGH-ALPHA TEST CONFIGURATION

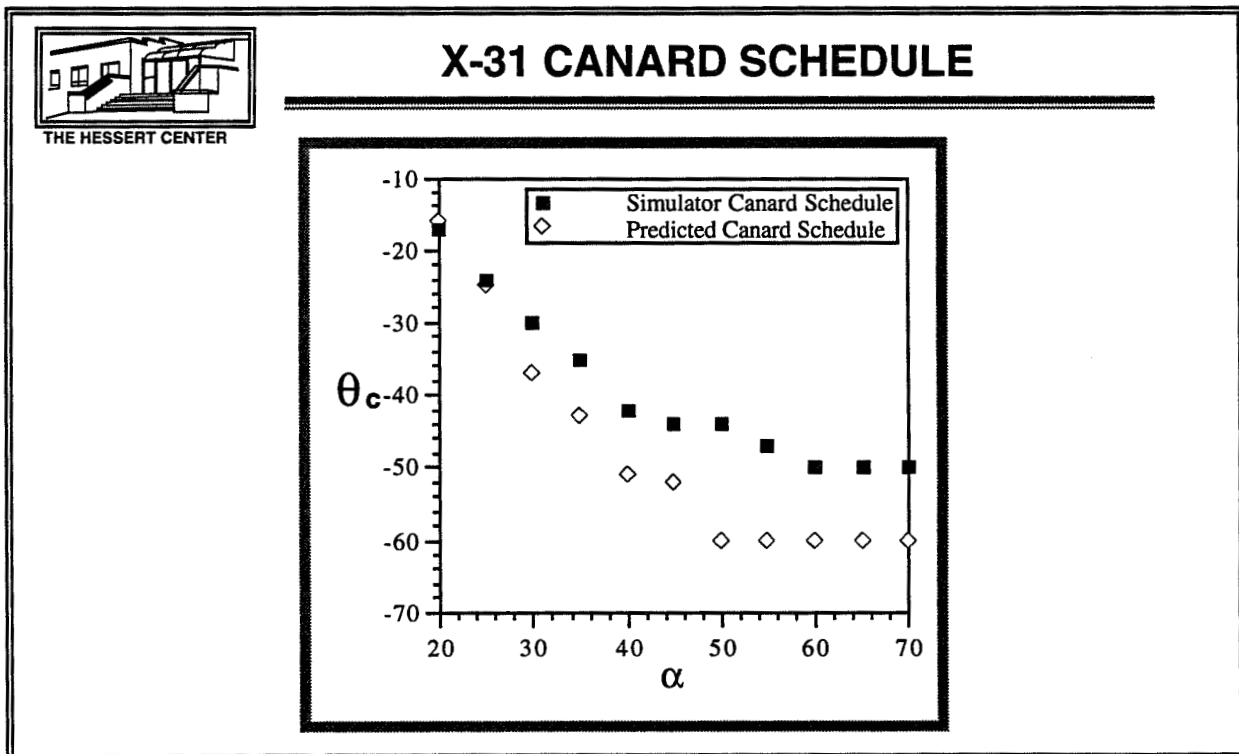
The X-31 model used in the experiments was a 2% scale modified desktop model. It contains both the nose-strakes and empennage strakes found on the X-31 aircraft. The nose strakes installed on the model were 0.394 inches (19.7 inches full-scale). Control surface deflection data for the X-31 during level flight at high angle-of-attack and for an $\alpha = 0^\circ$ to 70° pitch-up maneuver from the X-31 simulator were used to obtain each control surface deflection angle. The leading-edge flap was permanently deflected to $\theta_{LE} = 40^\circ/32^\circ$, (inboard/outboard) flap deflection, since this is the flap schedule for the X-31 aircraft for any $\alpha \geq 27^\circ$. The trailing-edge flap and thrust paddles were set to 0° deflection for all tests. Lastly, the canards on the model were made fully positionable and scheduled with respect to angle of attack as noted above.



X-31 CANARD SCHEDULE

The X-31 canard surfaces were scheduled with respect to angle of attack for each of the tests conducted on the model. Once the model was secured on its sting at a given angle of attack, the canard was fixed at its scheduling value according to the graph below.

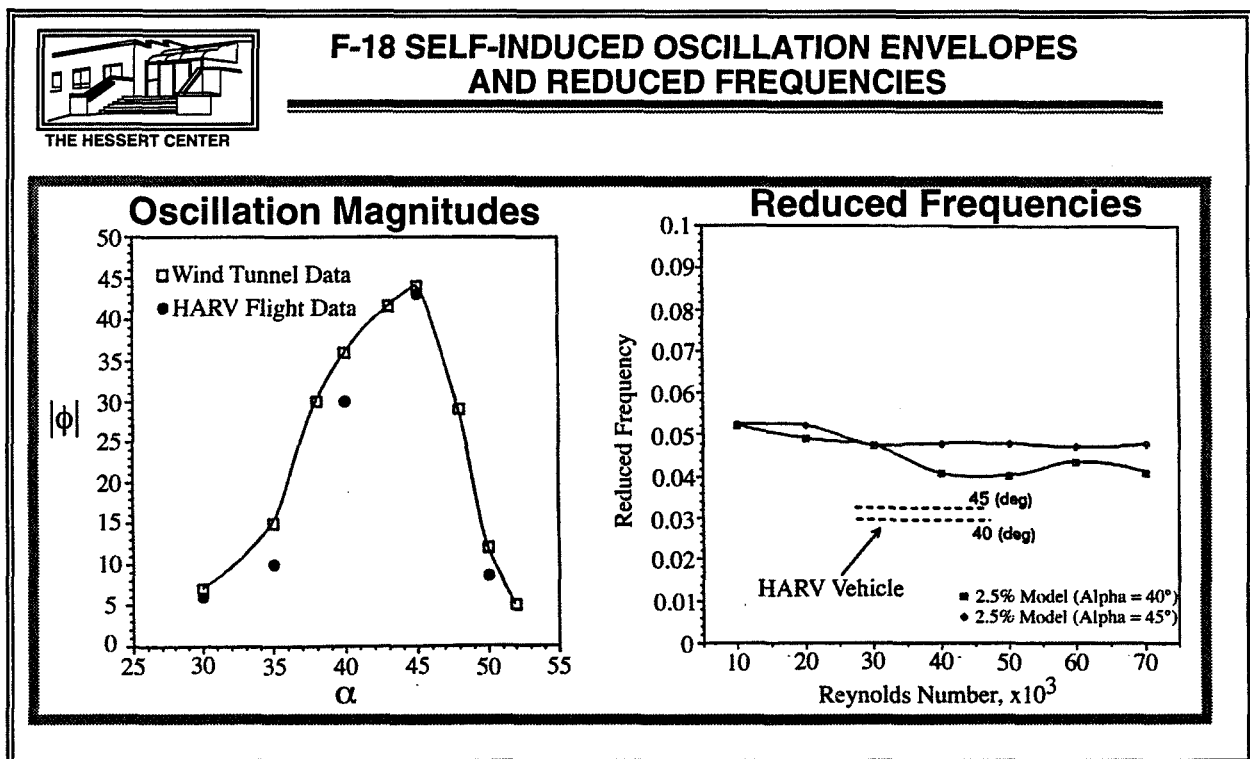
As can be noted, there are two schedules. The first is the canard schedule for an $\alpha = 0^\circ$ to 70° pitch-up maneuver from the X-31 simulator; and, the second is a predicted canard schedule for level flight¹³. For both schedules, a negative value indicates a leading-edge down and trailing-edge up rotation of the canard. Prior to testing it was expected that both schedules would produce similar results in the free-to-roll tests; however, this was not the case. Thus, all tests were repeated for both schedules.



F-18 SELF-INDUCED OSCILLATION ENVELOPES AND REDUCED FREQUENCIES^{11, 12}

The 2.5% F-18 model was tested with the free-to-roll apparatus over $\alpha = 25^\circ$ to 70° with $\beta = 0^\circ$. The model was released from a stationary position of $\phi = 0^\circ$ at each angle of attack and the ensuing model motion recorded.

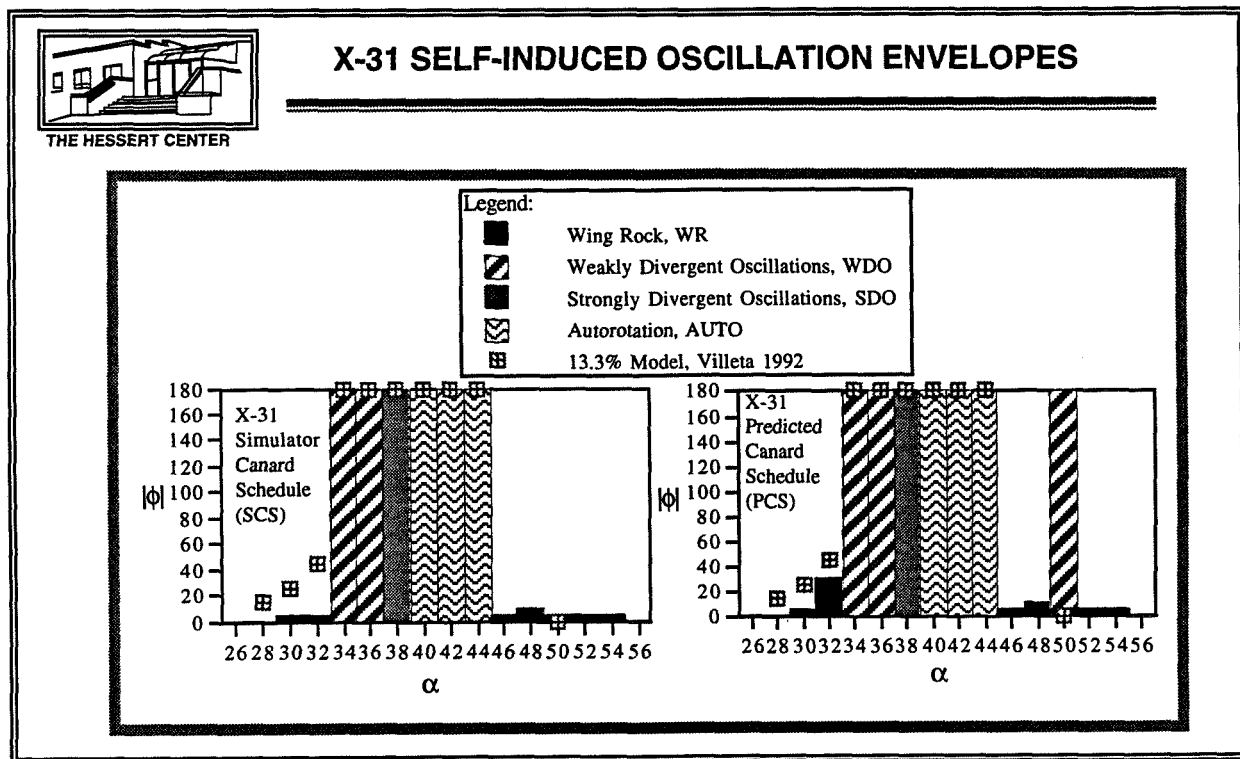
The comparison of wind tunnel and flight test data for the amplitude envelope and reduced frequencies are shown below^{11, 12}. The data shows good agreement in several areas. The first area of agreement is the general trend of the wing rock envelope. Both flight test and wind tunnel data show a rising trend in the wing rock amplitude between $\alpha = 30^\circ$ and 40° . The peak motion occurs at $\alpha = 45^\circ$, after which there is a sharp drop-off in the wing rock motion. Along with the comparable envelope shape, the amplitudes of the data compare reasonably well within the uncertainty of estimating the HARV wing rock amplitudes. This plot helps to identify one area of subscale utility, that being the ability to identify regions in which a particular phenomenon will occur. In this case, it is obvious that there is a range of angle of attack (40° - 47°) where robust wing rock motion occurs. Additionally, it is possible to predict the magnitude of this motion as can be seen from the close correlation in the data. The reduced frequencies of the wing rock motions are also similar; although, the 2.5% model values are slightly higher in value than the HARV vehicle.



X-31 SELF-INDUCED OSCILLATION ENVELOPES

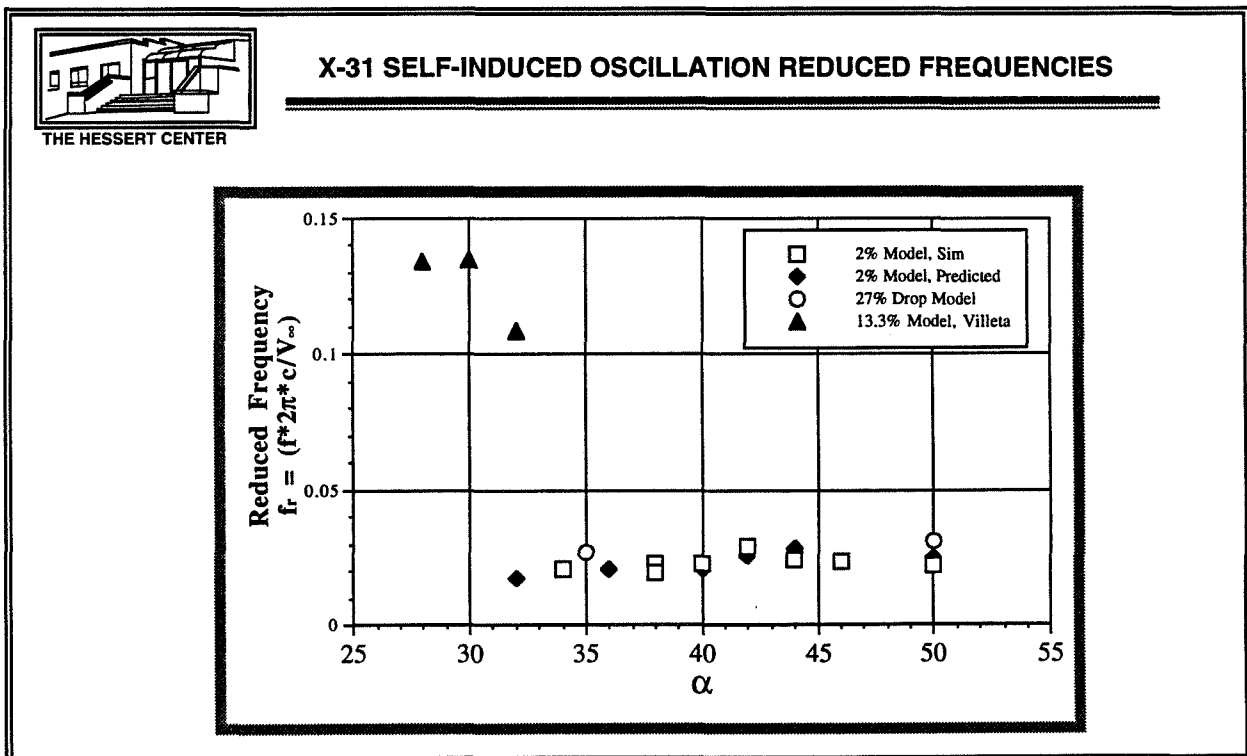
The 2% subscale X-31 model was tested with the free-to-roll apparatus, discussed in the previous section, over $\alpha = 25^\circ$ to 70° with $\beta = 0^\circ$. For each individual case, the model was released from a stationary position of $\phi = 0^\circ$ at each alpha and the resulting model motion recorded. The results of these tests showed several aerodynamic phenomenon occurring with the model. As can be noted from the graphs below, several phenomena occur in the alpha range of 30° to 55° for both canard schedules¹³. In addition, the magnitudes compare favorably to tests conducted by Villeta in 1992 on a 13.3% X-31 model¹⁴. The model did experience wing rock (WR) during the tests; however, most of the envelope was found to be divergent motions. In the divergent portion of the oscillation envelope, $\alpha = 34^\circ - 44^\circ$, three types of divergent motion occur. These are weakly divergent oscillations (WDO), strongly divergent oscillations (SDO), and autorotation (AUTO). In addition, Villeta showed in 1992 that the wing rock and autorotation phenomena experienced by the 27% X-31 drop model were essentially one degree-of-freedom motions¹⁴.

Comparison to the X-31 flight vehicle is not possible due to the highly integrated flight control system on the aircraft. Thus, comparisons are made with X-31 free-flight model tests and other wind tunnel tests.



X-31 SELF-INDUCED OSCILLATION REDUCED FREQUENCIES

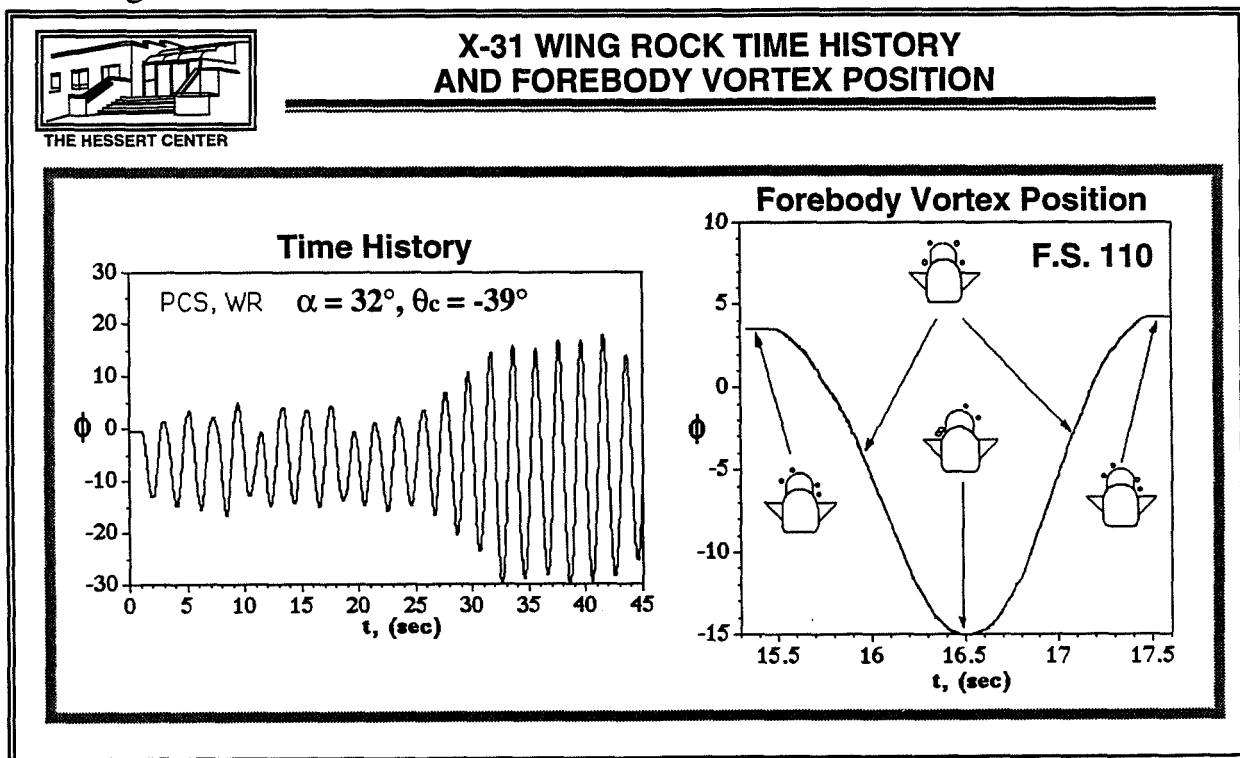
The recorded free-to-roll time histories of the 2% X-31 model also revealed the reduced frequencies of the oscillations motions. These values are shown below with corresponding information from two other X-31 subscale model tests. The values from the 2% X-31 model match well with the 27% X-31 drop model tests conducted at the Plumtree Test Facility of Langley Research Center, reported by Villeta¹⁴. In this case, the 2% X-31 model values are only slightly lower than the 27% X-31 drop model. However, there are some discrepancies between the values when compared with those found by Villeta during low-speed wind-tunnel tests of a 13.3% X-31 model. The values shown for the 13.3% model are the only ones given in Villeta's paper¹⁴. Since the X-31 flight vehicle has such a highly integrated flight control system, it does not experience the oscillations necessary for comparison. Thus, the drop model tests may provide the only source of information near the X-31 aircraft's flight conditions.



X-31 WING ROCK TIME HISTORY AND FOREBODY VORTEX POSITION

As the angle of attack is increased, the first phenomenon encountered is wing rock, WR¹³. This is a self-induced, limit-cycle roll oscillation seen previously on many other aircraft and studied extensively during the past few years with the HARV program. As with other aircraft models, the wing rock encountered on the X-31 is not very smooth during its limit-cycle build-up or its maximum roll angle oscillations, see below. In addition, it should be noted that the values of peak-to-peak wing rock amplitude, $|\phi|$, are different for the two canard schedules. At this angle of attack, the wing rock amplitude values differ by 25°; however, the only difference between the two tests was a 7° difference in canard setting. Thus canard position is a factor in the aircraft's behavior, and this point was found numerous times throughout testing. Another unusual behavior found in X-31 wing rock is observed below. For some cases of wing rock, the model does not oscillate about a $\phi = 0^\circ$ roll angle. As shown below, an offset bias of the wing rock motion is observed in these cases. Both positive and negative offsets were recorded.

The forebody vortices and canard-fuselage junction vortices are shown for a portion of the wing rock cycle. At this stage in the build-up, the vortices pair at the highest roll angles and remain on their respective sides of the canopy. It is possible that interaction between the vortices may provide the instability needed for wing rock.

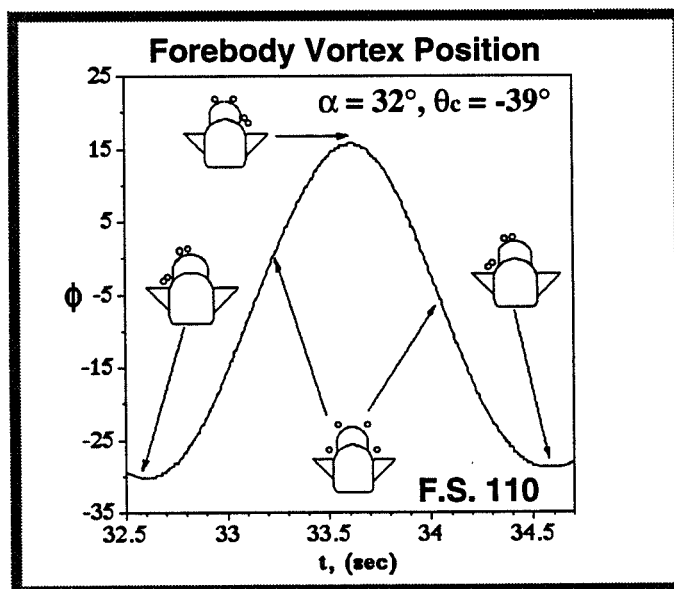


X-31 WING ROCK FOREBODY VORTEX POSITION CONTINUED

The figure below shows the position of the primary forebody vortices and canard-fuselage junction vortices during a large amplitude wing rock episode taken from the previous wing rock time history¹³. The motion of the forebody and canard-fuselage junction vortices is very similar to that seen for the small amplitude wing rock case discussed previously, with one exception. For the large amplitude wing rock case, the opposite side vortices move over the canopy to interact with the other vortex pair. This can be seen in the position of the vortices in this figure versus the position of the vortices shown previously for small amplitude wing rock. This movement of vortices across the top surface of the model is what separates large amplitude wing rock oscillations, $|\phi| > 30^\circ$, and small amplitude wing rock motions, $|\phi| \leq 15^\circ$. Again, the forebody vortices and the canard-fuselage junction vortices interact with each other during the wing rock motion.



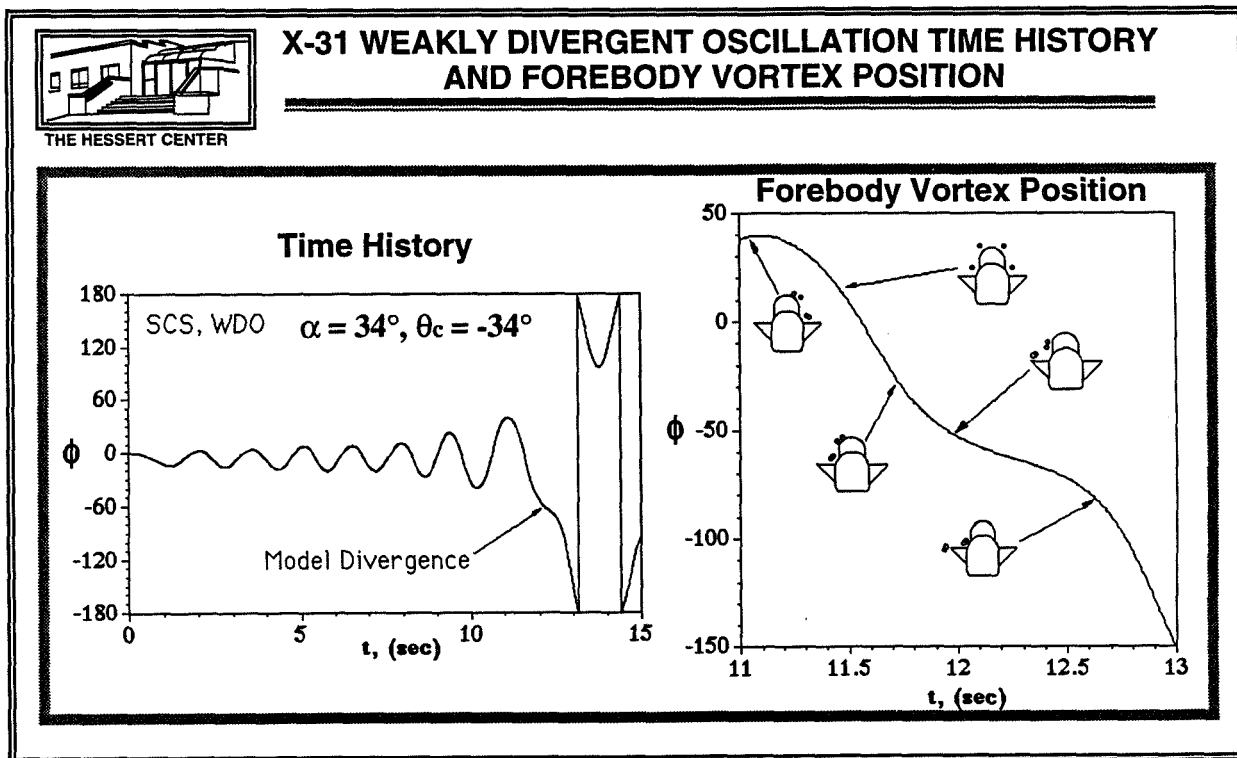
X-31 WING ROCK FOREBODY VORTEX POSITION CONTINUED



X-31 WEAKLY DIVERGENT OSCILLATION TIME HISTORY AND FOREBODY VORTEX POSITION

Between $\alpha = 34^\circ - 36^\circ$, a motion occurs that has been termed a weakly divergent oscillation, WDO¹³. This motion is characterized by a long, slow oscillation build-up period which eventually leads to a roll divergence of the model, see below. In examining the time history, the long gradual build-up can be observed from 0 to approximately 11.5 seconds. Near 11.5 seconds, the model diverges near $\phi = -60^\circ$, and the aircraft continues its rolling motion into an inverted hung stall.

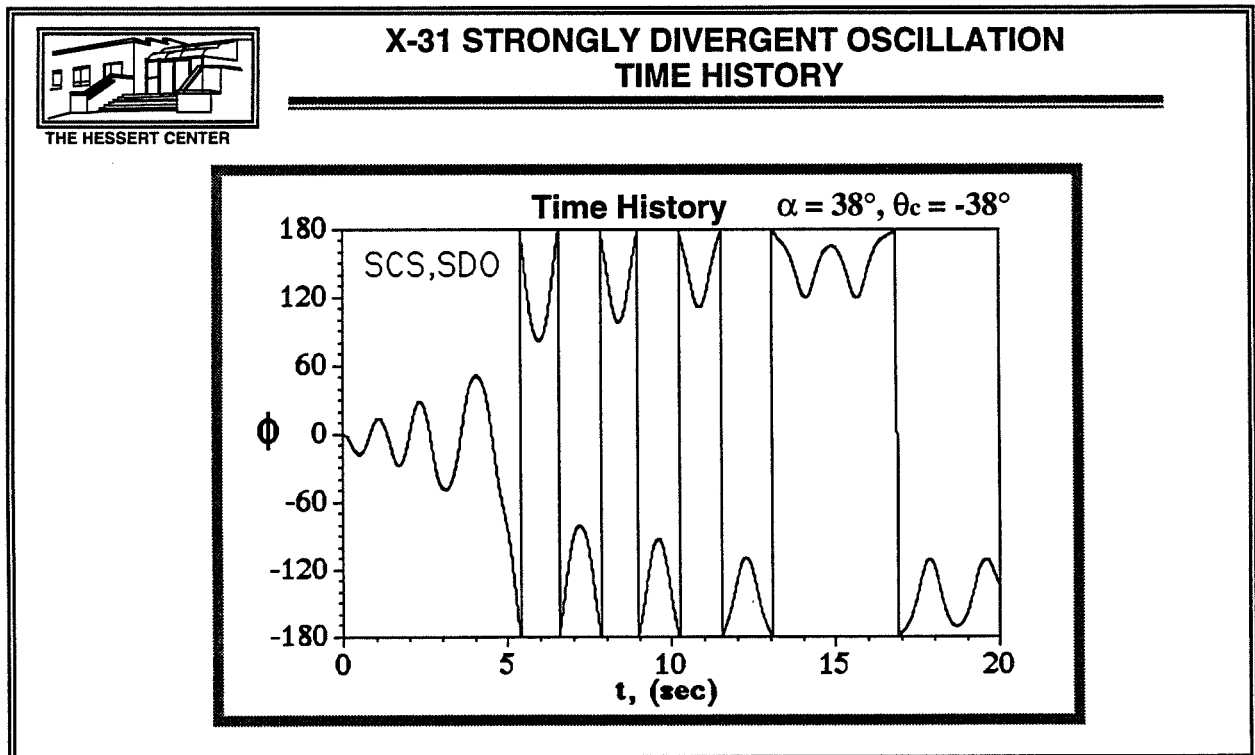
The forebody vortex position graph shows the position of the primary forebody vortices and canard-fuselage junction vortices during a weakly divergent oscillation episode, WDO, from the time history. The vortex motion prior to the divergence is similar to the wing rock discussed previously. Once the model starts to diverge, however, there is a marked difference. The vortex position at ~ 11 seconds is similar to that of large wing rock motions. As the model rolls through its neutral position (0°), ~ 11.4 seconds, the vortices separate and move around the canopy. As the model rolls further, ~ 11.7 seconds, the vortices again pair and move over the top of the canopy. Instead of returning back to its neutral position, however, the model continues to roll and diverge. At ~ 12 seconds, one vortex pair has moved out behind the surface of the canard while the second pair has begun moving down toward the same canard surface. Thus both pair are now acting solely on the same side of the model. As the model rolls further, ~ 12.6 seconds, one pair of vortices has moved behind the tip of the canard surface while the other has moved behind the canard root.



X-31 STRONGLY DIVERGENT OSCILLATION TIME HISTORY

As α continues to increase, a motion termed a strongly divergent oscillation (SDO), occurs near $\alpha = 38^\circ 13'$. As opposed to the weakly divergent oscillation, this motion is characterized by a quick and violent oscillation build-up which rapidly leads to a roll divergence of the aircraft into an inverted hung stall. From the figure below, this quick roll divergence motion can be observed as the model's oscillations quickly build between 0 and 4.5 seconds and diverges afterward into an inverted flight condition. The SDO build-up to divergence occurs in most cases more than twice as fast than similar WDO cases. In addition, this model condition is not merely a low Reynolds number phenomena since the stabilization of the X-31 configuration into an inverted hung stall has been reported from previous high Reynolds number, subscale drop model tests¹⁴.

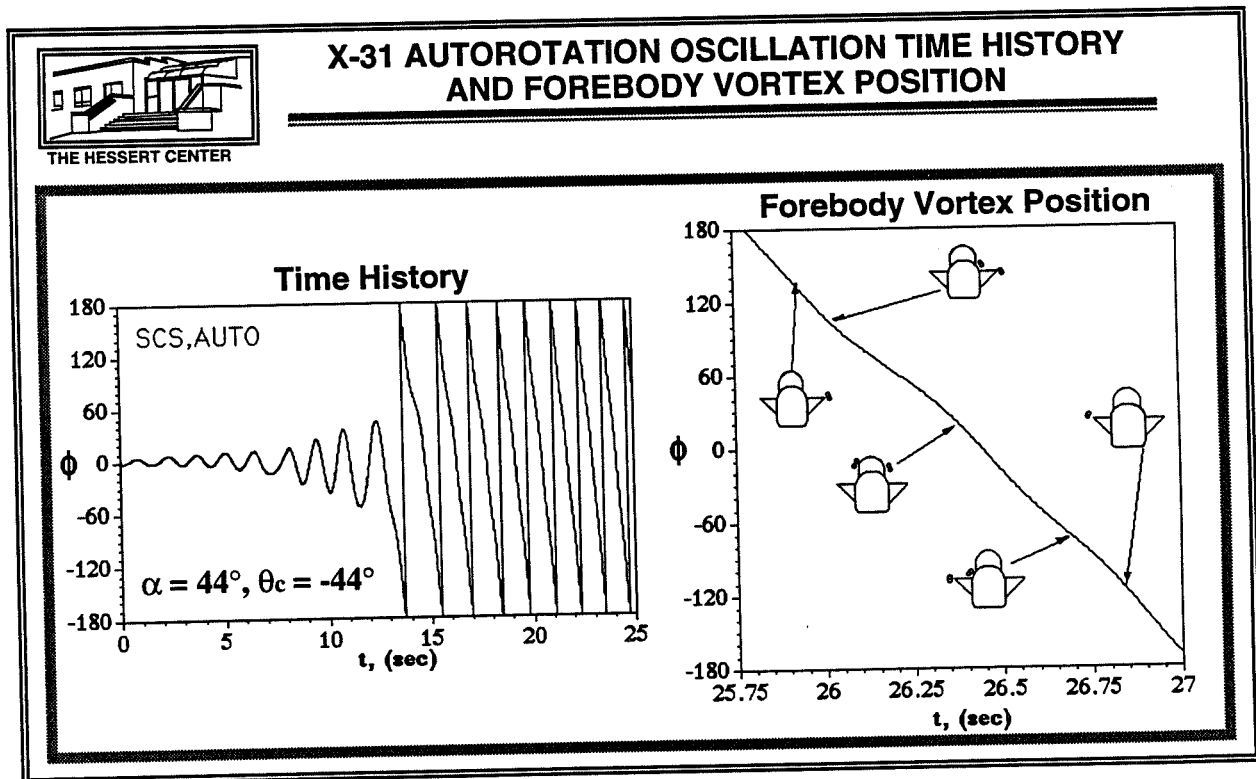
The movement of the forebody vortices and the canard-fuselage junction vortices are similar for both a SDO build-up and a WDO build-up. The only difference seems to be the time needed to build to divergence.



X-31 AUTOROTATION OSCILLATION AND FOREBODY VORTEX POSITION

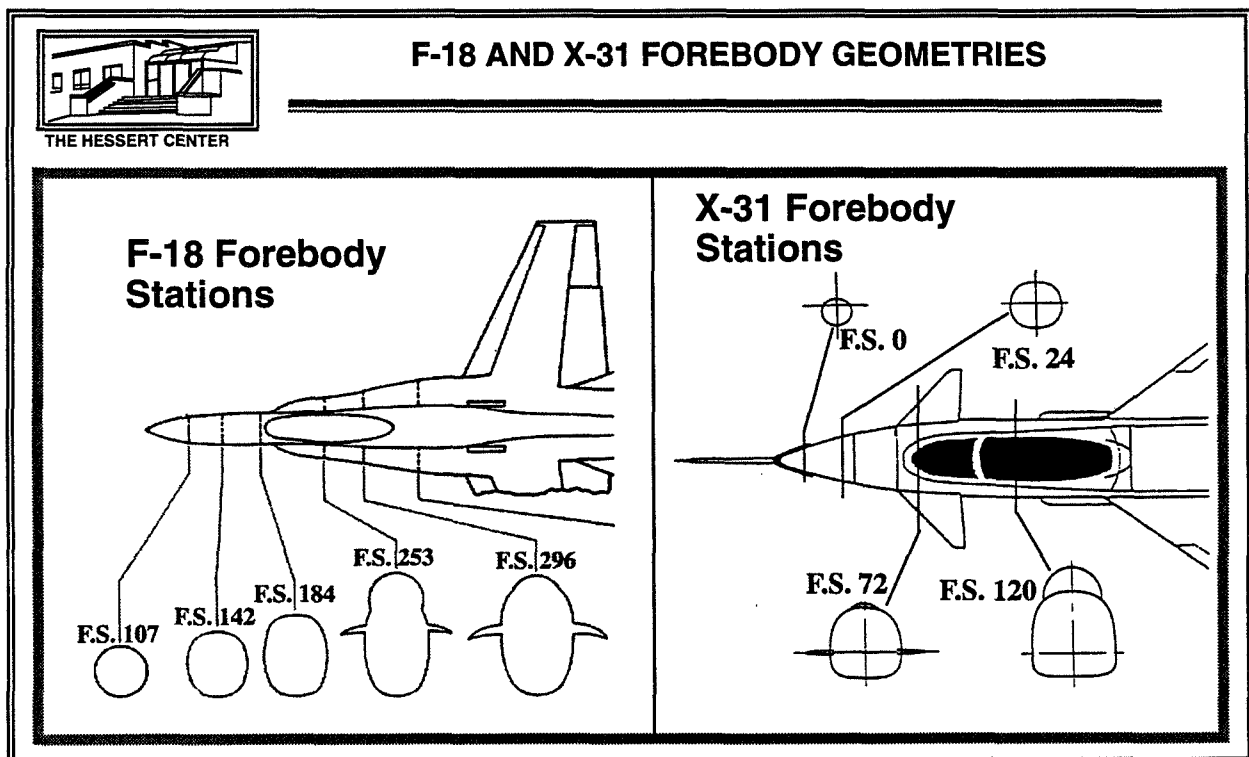
The last type of divergent motion encountered, as alpha continues to increase, is an autorotation divergence motion¹³, also term a High Incidence Kinetic Roll departure or HIKR departure. This motion is found at $\alpha = 40^\circ - 44^\circ$ for both canard schedules. It is characterized by a roll oscillation build-up that diverges into an autorotating motion. Once in the autorotating mode, the vehicle continues to spin, in one roll direction only, while the angular velocity increases to some limiting value, 0.85 Hz for the time history below. This type of behavior has also been reported during the X-31 drop model tests^{1, 14}.

The forebody vortex position graph shows the position of the primary forebody vortices and canard-fuselage junction vortices during the autorotation episode. At this point, the model has already diverged and is continuously rolling in one direction. One difference to be noted is that the vortices move quickly and efficiently across the upper surface of the model during this motion. In addition, they seem to move around the surface of the canards as well.



F-18 AND X-31 FOREBODY GEOMETRIES

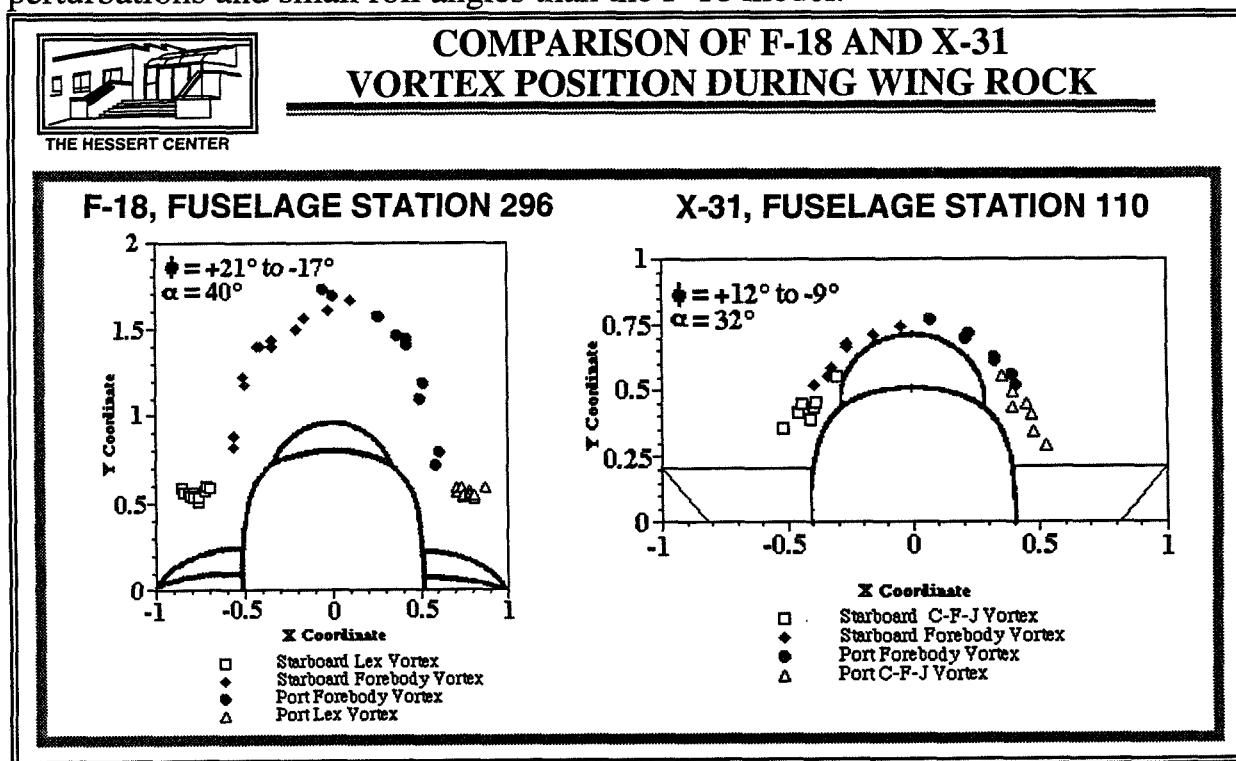
The forebody geometries of the F-18 and X-31 models are different from each other. The l/d ratio of the F-18 forebody is larger than that for the X-31. In addition, the X-31 model has a nose boom which is not present on the F-18. The cross-sections of the forebodies are different also. Both the F-18 and the X-31 start out with circular cross-sections, F.S. 107 (F-18) and F.S. 0 (X-31); however, the forebodies change at the latter fuselage stations. Comparing F.S. 184 of the F-18 and F.S. 24 of the X-31, we can note a difference in shape that will affect vortex strength and stability. Kegelman and Roos showed in 1991 that forebody cross-sections such as F.S. 24 of the X-31 will produce stronger forebody vortices than the cross-section of F.S. 184 of the F-18⁷. In addition, the vortices generated from cross-sections like F.S. 24 will experience greater lateral and normal movement due to flowfield perturbations than vortices generated by cross-sections like F.S. 184. Lastly, the two models have different placements of their canopies. The canopy on the F-18 has a high profile as seen in the cross-section of F.S. 253. The canopy on the X-31 has low profile as seen in the cross-section of F.S. 120. Aerodynamically, these canopies can act as physical barriers to separate the forebody aerodynamics and prevent interaction.



COMPARISON OF F-18 AND X-31 VORTEX POSITION DURING WING ROCK

When the activity of the foreword vortices during wing rock are compared for both the F-18 and X-31 subscale models several differences are observed. The two graphs shown below were picked for their similarity in forebody vortex lateral position (X-coordinate) during wing rock. In addition, the model conditions for each of these graphs has a maximum oscillation peak-to-peak amplitude of approximately 32° . However, there are three important differences between these graphs.

First, the magnitude of the roll angles needed to produce similar lateral movement should be observed. It takes nearly twice the roll angle of the X-31 model to produce the same magnitude of forebody vortex lateral movement on the F-18 model. Thus, forebody vortex movement is more prominent on the X-31 model. Second, the distance between the model surface and the forebody vortices (Y-coordinate) during wing rock are different. Since those of the X-31 model stay very close to the surface, it can be observed that they can have more of an affect on the model's behavior than its counterparts on the F-18 model. Lastly, the LEX vortices of the F-18 model are relatively stable during wing rock when compared to the canard-fuselage junction vortices of the X-31. Thus vortex interactions on the X-31 model are more prevalent and are not confined to a localized area. From this evidence it seems that the X-31 forebody configuration is more susceptible to perturbations and small roll angles than the F-18 model.



COMPARISON OF F-18 AND X-31 VORTEX POSITION DURING PITCH MANEUVERS

Both models were tested using pitch maneuvers to locate any instabilities that might initiate self-induced oscillations. These pitch maneuvers included ramp motions from $\alpha = 10^\circ - 60^\circ$ and sinusoidal pitch motions using various angle-of-attack ranges with varying frequencies of oscillation. Tests were conducted with $\beta = 0^\circ$ and $\phi = 0^\circ$.

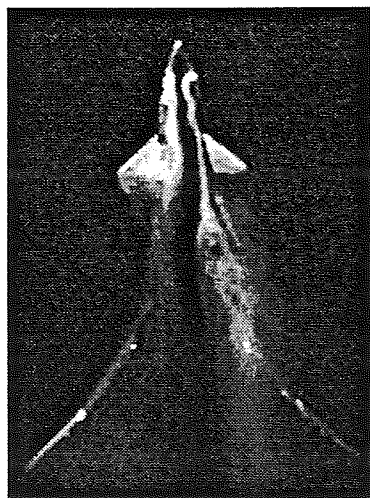
During these tests, the F-18 model showed no unusual activity. Vortex breakdown locations on the forebody vortices, LEX vortices, and wing vortices were found to be symmetric. In addition, no vortex interaction activity was observed. Results of the tests on the X-31 model were not as stable. In fact, the X-31 model showed several instabilities during the same maneuver. Examples of these instabilities are shown below. One of the most easily observable instabilities is the asymmetric forebody vortex position shown on the right. In this case, the starboard side forebody vortex has moved over the canopy to the port side. In addition, both vortices pair together just aft of the port side canard. Another type of instability is shown by the figure on the left. In this figure, asymmetric vortex breakdown has occurred on the forebody vortices. The port side forebody vortex experiences breakdown sooner than the starboard side forebody vortex. Events such as these could provide the initial roll instabilities that lead to self-induced oscillations.



THE HESSERT CENTER

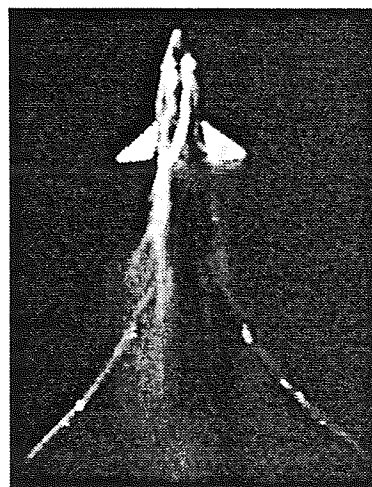
COMPARISON OF F-18 AND X-31 VORTEX POSITION DURING PITCH MANEUVERS

ASYMMETRIC VORTEX BREAKDOWN



X-31 AIRCRAFT
MODEL
PITCHING
FROM
 $\alpha = 10^\circ - 60^\circ$

ASYMMETRIC VORTEX POSITION



COMPARISON OF F-18 AND X-31 VORTEX POSITION DURING PITCH MANEUVERS

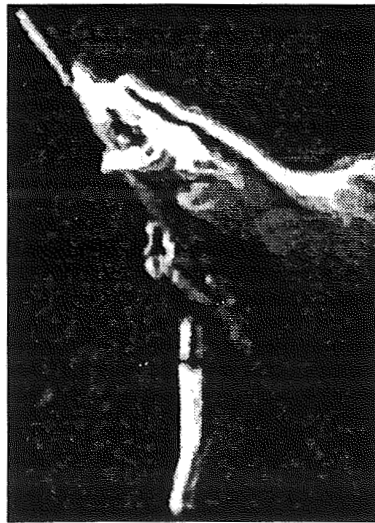
If the asymmetric vortex breakdown experienced by the X-31 model during pitch maneuvers is observed from a slightly different angle, more information about the seriousness of the asymmetry can be obtained. From this view it can be noted that the positions of vortex breakdown are quite different for the two forebody vortices. In addition, it was also found that the starboard side vortex is actually lifting away from the surface of the model; however, the port side vortex is still close to the model surface. Such a forebody vortex configuration will surely induce a lateral instability on the model.

The erratic motion of the forebody vortices seems to be mostly dependent upon the forebody configuration. With a flattened forebody cross-section and a low profile canopy, there are no large physical barriers to oppose the movement of the forebody vortices around the fuselage. In addition, the added complexity of the pressure fields and separated flowfields of the canards seems to affect the stability of the the forebody vortices. These factors seem to provide enough evidence of instabilities to initiate self-induced oscillations on the X-31 model.



COMPARISON OF F-18 AND X-31 VORTEX POSITION DURING PITCH MANEUVERS

ASYMMETRIC VORTEX BREAKDOWN

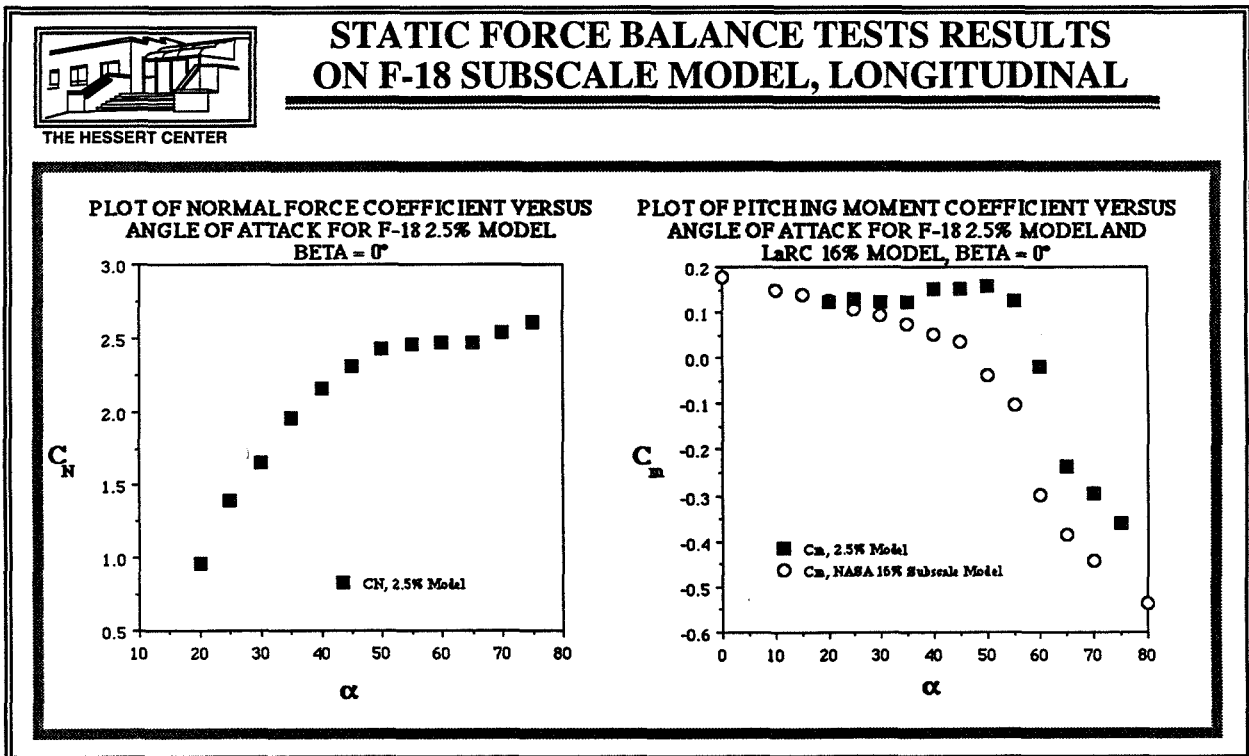


X-31 AIRCRAFT
MODEL
PITCHING
FROM
 $\alpha = 10^\circ - 60^\circ$

STATIC FORCE BALANCE TEST RESULTS ON F-18 SUBSCALE MODEL, LONGITUDINAL

During the pitch testing of the F-18 model, no obvious instabilities were found that could initiate self-induced oscillations. Force balance tests were then conducted to see if the F-18 model was unstable¹⁰.

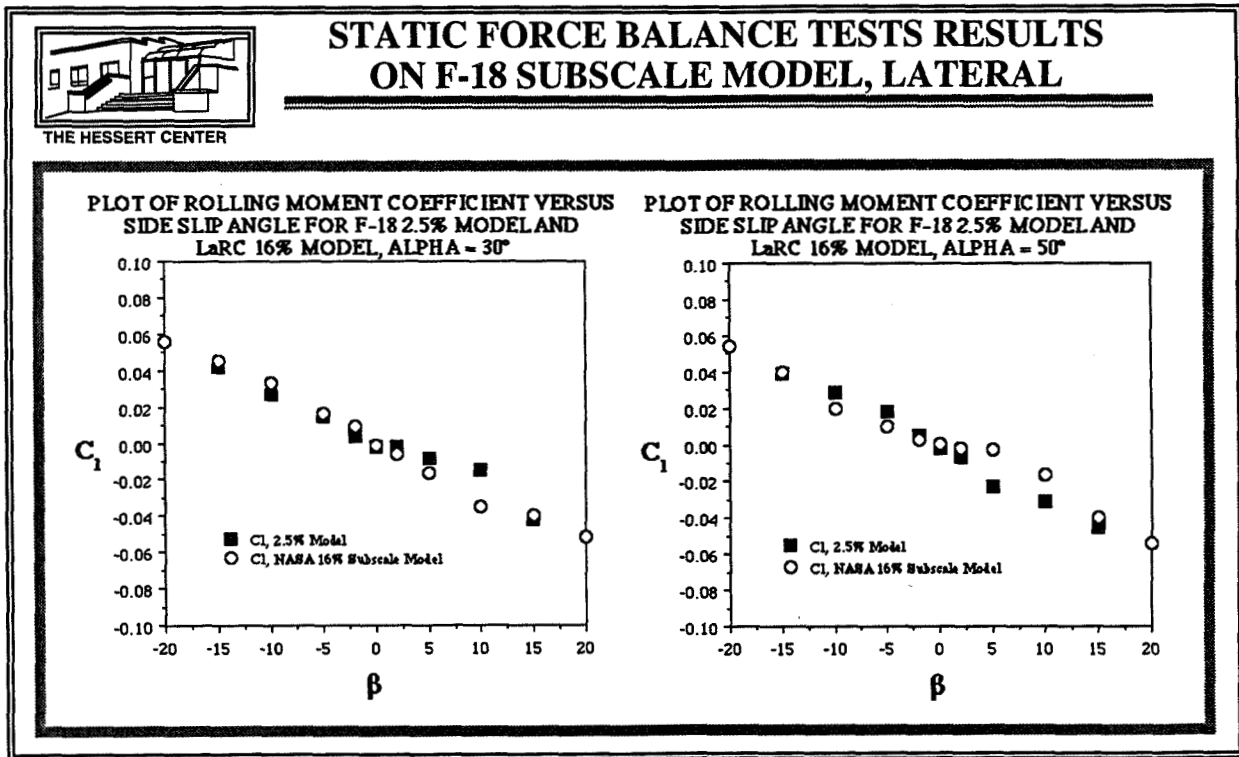
The two longitudinal coefficients, C_N and C_m , are both plotted versus angle of attack. The normal force coefficient, C_N , shows no real surprises. There is a steady increase in the value of the coefficient until $\alpha = 50^\circ$. Then it plateaus between $\alpha = 50^\circ$ and 65° , until the value increases again between $\alpha = 65^\circ$ and 75° . This steady increase in value was expected. The pitching moment coefficient values are compared to 16% subscale F-18 Model tests conducted by NASA⁹. C_m for the 2.5% model was, on average, greater than C_m for the 16% subscale model, reaching its maximum deviation at approximately 50° angle of attack. Thus, in the angle of attack range of 30° to 50° , the aircraft was unstable in pitch. Afterwards, the profile decreases in a similar manner as the full-scale model test, again regaining stability, but at a higher order of magnitude. The reason for this difference in model behavior was found to originate from a difference in surface pressure distribution between the two models.



STATIC FORCE BALANCE TEST RESULTS ON F-18 SUBSCALE MODEL, LATERAL

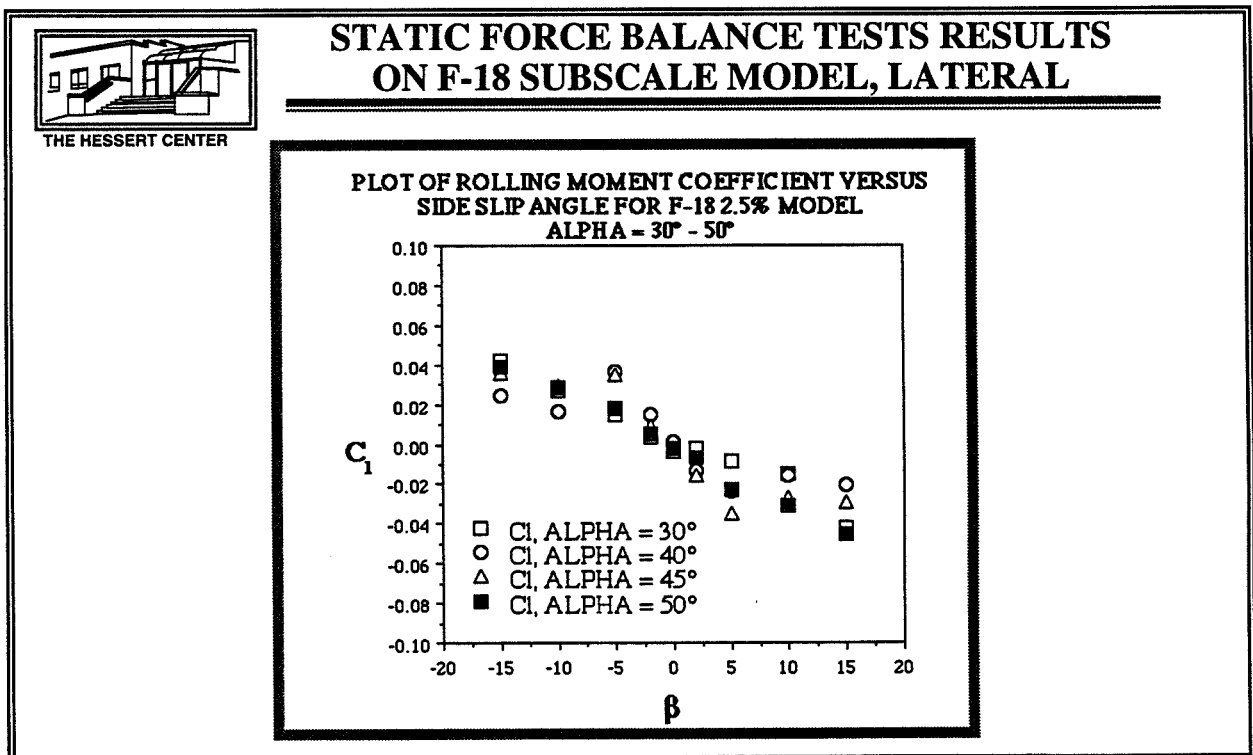
The lateral force and moment coefficients showed very good correlation between the 2.5% F-18 model and the NASA 16% subscale F-18 model⁹. A prime example of this correlation is the rolling moment coefficient, C_l , graphs shown below. For these tests, the values for both the 2.5% and the 16% subscale F-18 models were consistent; and in addition, the slopes of the curves are approximately equal. Thus the rolling moment characteristics of both models are approximately the same as shown by these graphs. In addition, both models showed static stability at these points.

The yawing moment coefficient, C_n , and the side-force coefficient, C_y , were also compared to the results of the 16% subscale F-18 model tests conducted by NASA⁹. In these comparisons, it was also observed that the two models approximated each other very closely in their static lateral behavior¹².



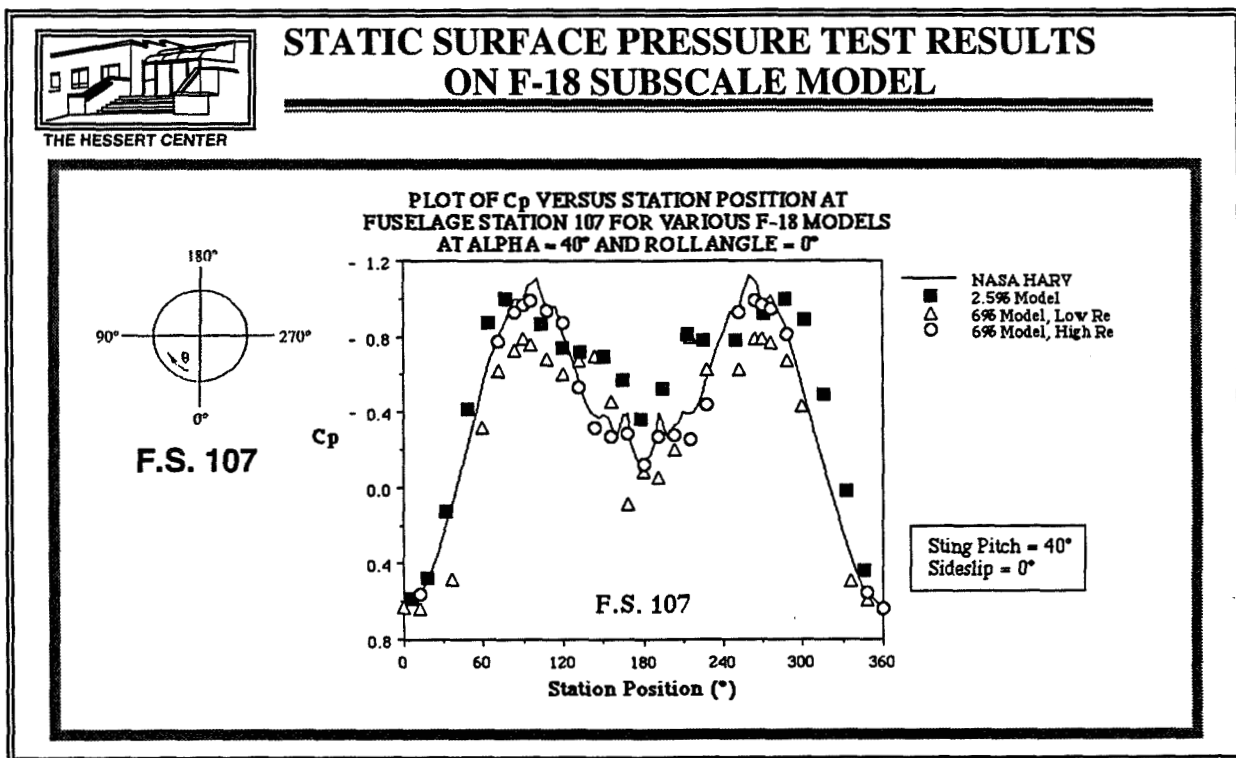
STATIC FORCE BALANCE TEST RESULTS ON F-18 SUBSCALE MODEL, LATERAL

The rolling moment coefficient, C_l , is plotted versus sideslip for various angles of attack, shown below. The four angles of attack chosen were selected from the wing rock boundary shown previously. The roll moment coefficient curves suggest that the model is statically stable (i.e., $C_{l\beta}$ is negative) in roll over the angle of attack range where wing rock occurs. For a model that is constrained to a pure rolling motion, as was the case in the wing rock experiments, an effective sideslip angle is introduced as the model rolls around its longitudinal axis. Thus, the static roll moment characteristics are not the source of the wing rock motion¹⁰. This leads to the conclusion that for the F-18 model the wing rock motion must be due to an instability caused by the rolling motion such as a forebody-LEX vortex interaction during a rolling motion. This is consistent with the ideas suggested by Quast, Nelson, and Fisher in 1991¹¹.



STATIC SURFACE PRESSURE TEST RESULTS ON F-18 SUBSCALE MODEL

Surface pressure measurements conducted on the 2.5% F-18 model¹² were compared to similar information on a 6% F-18 model² and the HARV vehicle⁵. Differences between the HARV and the 2.5% F-18 model pressure coefficient profiles were due mainly to Reynolds number effects. Due to the laminar nature of the 2.5% model tests, the primary separation point on the subscale model occurs earlier than the turbulent primary separation point on the HARV. The first pressure coefficient peak of the HARV is due to the natural acceleration and deceleration of air as it moves around the forebody, whereas the first peak of the model is due to the early primary separation point. Even though two different aerodynamic mechanisms are at work, the profiles compare favorably due to an approximate 30° shift in the pressure coefficient suction peak locations; in addition, both the peaks of the HARV and the 2.5% model are of similar magnitude. Lastly, the leeward pressure recovery region between 150° and 210° compares relatively well, with this region encompassing reattachment points and secondary vortices.



SIMILARITIES AND DIFFERENCES IN F-18 AND X-31 SUBSCALE MODEL BEHAVIOR

Out of all the subscale model tests conducted, several points of comparison and contrast have emerged between the F-18 and X-31 subscale models. First, the self-induced oscillation envelopes for the models occurs at approximately the same angles-of-attack. The motions experienced within the envelope are different for each model, with the X-31 motions being mainly divergent. Second, the reduced frequencies of the models are of the same order of magnitude. In addition, the F-18 model oscillated at a slightly faster rate than the X-31 model. Third, the models showed different levels of aerodynamic stability during the model pitch tests. The F-18 model showed no asymmetric activity during pitching motions; however, the X-31 model showed several different types of asymmetric instabilities during the same type of pitch tests. Lastly, the forebody vortices on each model had different characteristics during the self-induced motions. The forebody vortices of the F-18 model were found to be stable and to interact with the LEX vortices at large roll angles, $\phi \geq \pm 20^\circ$. The forebody vortices of the X-31 model were found to be easily disturbed and easily moved across the canopy to interact with each other at small roll angles, $\phi = \pm 10^\circ$. Thus each model has similar ranges of self-induced behavior; but, the type and cause of these behaviors is different between the two models.



THE HESSERT CENTER

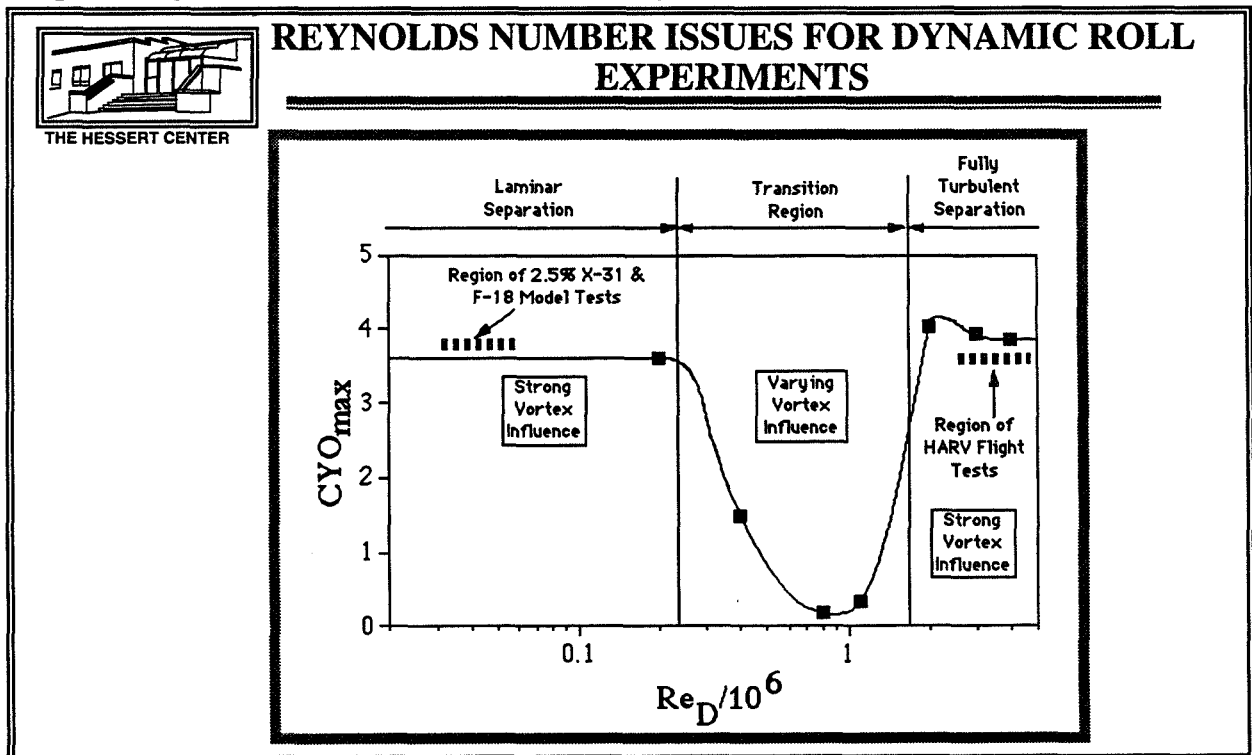
SIMILARITIES AND DIFFERENCES IN F-18 AND X-31 SUBSCALE MODEL BEHAVIOR

Topic	F-18	X-31
Envelope	$\alpha = 30^\circ - 52^\circ$	$\alpha = 30^\circ - 54^\circ$
Reduced Frequency	$f_r = 0.04 - 0.05$	$f_r = 0.02 - 0.03$
Instabilities During Pitch Tests?	NO	YES
Forebody Vortex Motion	Interacts with LEX Vortices at large roll angles.	Easily moves across canopy to interact with each other.

REYNOLDS NUMBER ISSUES FOR DYNAMIC ROLL EXPERIMENTS

In dynamic subscale model testing, a myriad of scaling factors and nondimensional numbers become crucial. During the free-to-roll testing of the F-18 and X-31 subscale aircraft, one factor became increasingly important, Reynolds number. The Reynolds number differences between the HARV vehicle and the 2.5% models were large, two or three orders of magnitude difference. However, this did not keep the subscale tests from replicating the same phenomena found on the flight vehicle.

The reason that subscale tests successfully predicted the flight characteristics is as follows. The roll dynamic characteristic of the two models is driven by the forebody/LEX (F-18) or forebody/canard (X-31) vortex interaction. As shown in the graph below, Reynolds number has an effect on the side-force of a tangent-ogive forebody⁸. As shown, the subcritical and supercritical ranges have very strong and prominent forebody vortex forces and well organized forebody vortices. The transcritical range does not exhibit a well organized vortex flow. Thus, in free-to-roll testing where the model oscillates due to forebody/LEX or forebody/canard vortex interaction, as in the F-18 and X-31 model cases, the transcritical region should be avoided during testing. There will be differences in separation points due to the differences in laminar and turbulent flow around a body; however, the strong and organized forebody vortex flow is maintained. This seems to be the most critical point in replicating the self-induced motions of flight aircraft during subscale model testing.



CONCLUSIONS

Through these subscale tests, several important facts have been reached. First, subscale dynamic testing can be used to predict the roll dynamics of flight vehicles at high angle-of-attack. The agreement of self-induced oscillation envelopes between the subscale wind tunnel tests and flight data is encouraging. Second, from the tests conducted on the subscale models, it appears that the roll dynamic characteristics are governed by forebody/LEX (F-18) or forebody/canard (X-31) vortex interaction. Third, since strong organized vortical flowfields are critical to establish vortex interaction, the transcritical Reynolds number regime should be avoided during model testing. The Reynolds number based on the forebody diameter is of primary importance to create stable, organized vortical forebody flows. Lastly, subscale static aerodynamics agreed favorably with full-scale and other wind tunnel experiments.



THE HESSERT CENTER

CONCLUSIONS

- **Subscale Dynamic Testing can be Used to Predict Roll Dynamics of Flight Vehicles.**
- **Roll Dynamic Characteristics are Governed by Forebody/LEX or Canard Vortex Interactions.**
- **Avoid Transcritical Reynolds Number Regime During Testing. (Based on Forebody Diameter)**
- **Static Aerodynamics Agrees favorably with Full-Scale Wind Tunnel Experiments.**

REFERENCES

- ¹Croom, M.A., et al., "Dynamic Model Testing of the X-31 Configuration for High-Angle-of-Attack Flight Dynamics Research," AIAA 93-3674 CP, August 1993.
- ²Erickson, G.E., et al., "Experimental Investigation of the F/A-18 Vortex Flows at Subsonic Through Transonic Speeds, Invited Paper," AIAA 89-2222, July 1989.
- ³Ericsson, L.E., and Reding, J.P., "Scaling Problems in Dynamic Tests of Aircraft-Like Configurations," AGARD CP-227, Paper 25, February 1977.
- ⁴Fisher, D.F., and Del Frate, J.H., "In-Flight Flow Visualization Characteristics of the NASA F-18 High Alpha Research Vehicle at High Angles of Attack," SAE Technical Paper Series No. 892222, September 1989.
- ⁵Fisher, D.F., Banks, D.W., and Richwine, D.M., "F-18 High Alpha Research Vehicle Surface Pressures: Initial In-Flight Results and Correlation with Flow Visualization and Wind-Tunnel Data," NASA TM-101724, August 1990.
- ⁶Hummel, D., "On the Vortex Formation Over a Slender Wing at Large Angles of Incidence," AGARD CP-247, 1978.
- ⁷Kegelman, J.T., and Roos, F.W., "Influence of Forebody Cross-Section Shape on Vortex Flowfield Structure at High Alpha," AIAA 91-3250, September 1991.
- ⁸Lamont, P.J., "Pressures Around an Inclined Ogive Cylinder with Laminar, Transitional, or Turbulent Separation," *AIAA Journal*, Volume 10, Number 11, Pages 1492 - 1499.
- ⁹Murri, D.G., et al., "Developments of Actuated Forebody Strake Controls for the F-18 High Alpha Research Vehicle," High-Angle-of-Attack Technology Conference, October 1990.
- ¹⁰Nelson, R.C., Arena, A.S., and Williams II, D.L., "The Use of Subscale Models to Predict Self-Induced Oscillations of Flight Vehicles," AIAA 93-0093, January 1993.
- ¹¹Quast, T., Nelson, R.C., and Fisher, D.F., "A Study of High Alpha Dynamics and Flow Visualization for a 2.5% Model of the F-18 HARV Undergoing Wing Rock," AIAA 91-3267, September 1991.
- ¹²Williams II, D.L., Quast, T., and Nelson, R.C., "Comparison of Flight and Sub-scale Model Wing Rock Characteristics of an F-18 Aircraft," Final Report for NASA Grant NCA2-513, April 1993.
- ¹³Williams II, D.L., Nelson, R.C., and Fisher, D.F., "An Investigation of X-31 Roll Characteristics at High Angle-of-Attack Through Subscale Model Testing," AIAA 94-0806, January 1994.
- ¹⁴Villeta, J.R., "Lateral-Directional Static and Dynamic Stability Analysis at High Angles of Attack for the X-31 Configuration," Master's Thesis, George Washington University, August 1992.

26pg

1995/07824
324031

N95-14238

E I D E T I C S

STATIC AND DYNAMIC FORCE/MOMENT
MEASUREMENTS IN THE EIDETICS
WATER TUNNEL

by

59-02
16087
p-24

CARLOS J. SUAREZ AND GERALD N. MALCOLM

SBIR Phase II Contract - Sponsored By NASA Dryden
Technical Monitor - John Del Frate

EIDETICS AIRCRAFT, INC.
3415 LOMITA BLVD.
TORRANCE, CA 90505
(310)-326-8228

Fourth NASA High Alpha Conference/Workshop
Dryden Flight Research Center, Edwards, CA
July 12, 13 and 14, 1994

0-3

4

Water tunnels have been utilized in one form or another to explore fluid mechanics and aerodynamics phenomena since the days of Leonardo da Vinci. Water tunnel testing is attractive because of the relatively low cost and quick turn-around time to perform flow visualization experiments and evaluate the results. The principal limitation of a water tunnel is that the low flow speed, which provides for detailed visualization, also results in very small hydrodynamic (aerodynamic) forces on the model, which, in the past, have proven to be difficult to measure accurately. However, the advent of semi-conductor strain gage technology and devices associated with data acquisition such as low-noise amplifiers, electronic filters, and digital recording have made accurate measurements of very low strain levels feasible.

The principal objective of this research effort was to develop a multi-component strain gage balance to measure forces and moments on models tested in flow visualization water tunnels. A balance was designed that allows measuring normal and side forces, and pitching, yawing and rolling moments (no axial force). The balance mounts internally in the model and is used in a manner typical of wind tunnel balances. The key differences between a water tunnel balance and a wind tunnel balance are the requirement for very high sensitivity since the loads are very low (typical normal force is 0.2 lbs), the need for water proofing the gage elements, and the small size required to fit into typical water tunnel models.

The study was supported by the NASA Dryden Flight Research Center under SBIR Phase II Contract No. NAS2-13571. The technical monitor of the contract was Mr. John Del Frate.

STATIC AND DYNAMIC FORCE/MOMENT MEASUREMENTS
IN THE EIDETICS WATER TUNNEL

by

CARLOS J. SUAREZ AND GERALD N. MALCOLM

SBIR Phase II Contract - Sponsored By NASA Dryden
Technical Monitor - John Del Frate

EIDETICS AIRCRAFT, INC.
3415 LOMITA BLVD.
TORRANCE, CA 90505

Fourth NASA High Alpha Conference/Workshop
Dryden Flight Research Center, Edwards, CA
July 12, 13 and 14, 1994

This paper summarizes results of force/moment (F/M) measurements conducted in a water tunnel with a 5-component internal balance. The importance of having a balance that allows performing static and dynamic experiments in a water tunnel will be reviewed first. The requirements identified during these initial considerations dictate the specific technical objectives of the research program, which will be listed in detail. The most important features of the water tunnel balance will be described and the calibration procedures and results will be briefly discussed.

The following sections contain descriptions of the experimental setup (facility and models) and of the methodologies used in both static and dynamic tests. Of special interest are the results of unique water tunnel dynamic experiments, such as the rotary balance tests. The balance was extensively tested during a wide variety of conditions, and examples of results from selected experiments will be presented to show the performance of the balance. The key findings of this project will be highlighted in the concluding remarks.

OUTLINE

- INTRODUCTION
- TECHNICAL OBJECTIVES
- BALANCE DESCRIPTION AND CALIBRATION
- EXPERIMENTAL SETUP AND METHODOLOGY
- FORCE/MOMENT MEASUREMENT RESULTS
 - STATIC TESTS
 - DYNAMIC TESTS IN PITCH
 - DYNAMIC TESTS IN YAW
 - DYNAMIC TESTS IN ROLL
 - ROTARY BALANCE TESTS
- CONCLUDING REMARKS

The development of a system to measure the small forces and moments generated in a water tunnel would increase the usefulness of this type of research facility significantly. If the water tunnel could determine forces and moments to some level of accuracy simultaneously with the flow visualization, the interpretation of results would be greatly simplified. Also, it would be possible to quantify the changes produced by configuration modifications, conventional and unconventional control techniques, etc. Knowledge of the cause and effect of the complex flows and resulting non-linear aerodynamics at high angles of attack requires the capability to correlate what we see with what we measure in terms of airframe loads.

In addition to static force and moment measurements, the water tunnel force/moment balance may also provide a capability for dynamic experiments. The high flow speed typical of wind tunnel tests requires rapid movement of the model in order to simulate a properly scaled dynamic maneuver and the motions are mechanically difficult to implement. The fast model movement also places demanding requirements on the response of the data acquisition system to acquire data at high sample rates. In contrast, the flow speed of water tunnel tests is typically much lower (2 orders of magnitude or more), and consequently, the model motion required to simulate a dynamic maneuver is also very slow. Thus, the response rates for data acquisition required for force and moment measurements during transient and dynamic situations are less demanding than in a wind tunnel.

INTRODUCTION

IMPORTANCE OF WATER TUNNEL BALANCE

- QUANTITATIVE DATA MAKES WATER TUNNEL TESTING MORE ATTRACTIVE
- FLOW VISUALIZATION AND FORCE MEASUREMENTS CAN BE CONDUCTED SIMULTANEOUSLY
- QUANTITATIVE DYNAMIC TESTS CAN BE PERFORMED, WITH THE ADVANTAGE THAT MODEL MOVEMENT RATES AND DATA ACQUISITION RESPONSE RATES ARE LESS DEMANDING THAN FOR WIND TUNNEL TESTS

The long-term goal of this project was to create and demonstrate a comprehensive test capability in the Eidetics water tunnel for static and dynamic tests including a complete and stand-alone force/moment data acquisition system. To accomplish this, the specific technical objectives were the following:

1. Design and build a 5-component force/moment balance compatible with Eidetics' water tunnel or similar.
2. Design and build a suitable calibration rig and related hardware and software to perform an accurate balance calibration, determining sensitivities and interactions.
3. Increase the test capability of the Eidetics' water tunnel model support system from two axes of motion (pitch and yaw) to three axes (including roll) and modify the model support drive control system to produce high-resolution motions in all three axes to acquire "dynamic" force and moment time-history data. Develop an apparatus for producing a "coning" motion, or a roll motion about the velocity vector with fixed angle of attack and sideslip, commonly performed in wind tunnel tests on a rotary-balance apparatus.
4. Develop the techniques and methodologies for conducting dynamic tests.
5. Perform static and dynamic force and moment measurements on "generic" configurations (delta wing) and on "full" configurations (F/A-18 models) to evaluate the performance of the balance.
6. Compare results to existing wind tunnel data, assessing similarities and/or differences between data.

TECHNICAL OBJECTIVES

- 1) DESIGN AND FABRICATE A FIVE-COMPONENT WATER TUNNEL BALANCE (NO AXIAL FORCE) .
- 2) CALIBRATE THE BALANCE, DETERMINING SENSITIVITIES AND INTERACTIONS
- 3) IMPROVE THE WATER TUNNEL MODEL SUPPORT TO ALLOW FOR PRECISE AND SMOOTH COMPUTERIZED MOTIONS
- 4) DEVELOP THE METHODOLOGY FOR PERFORMING DYNAMIC TESTS IN THE WATER TUNNEL, INCLUDING ROTARY BALANCE TESTS
- 5) CONDUCT STATIC AND DYNAMIC TESTS ON GENERIC CONFIGURATIONS (DELTA WINGS) AND ON FULL CONFIGURATIONS (F/A-18) TO EVALUATE THE PERFORMANCE OF THE BALANCE
- 6) COMPARE THE RESULTS OBTAINED WITH WIND TUNNEL DATA ON SIMILAR CONFIGURATIONS, ASSESSING SIMILARITIES AND/OR DIFFERENCES BETWEEN WATER AND WIND TUNNEL DATA

Basically, the balance is similar to the sting balances used in wind tunnel tests and is located inside the model. It consists of a rolling moment section, two pitching moment sections and two yawing moment sections, all 0.75 inches in diameter. Five components will provide for the simultaneous measurement of pitching, yawing and rolling moments and normal and side forces. The moment of inertia of each section was carefully calculated in order to obtain the required stress levels that produce the desired sensitivity and resolution when the balance is loaded in the plane of interest and maximum stiffness in the other planes.

Semi-conductor strain gages are used to get the desired output, since they have a gage factor (change of resistance with strain) that is 50 to 100 times larger than that of wire or foil strain gages. Each section is composed of four gages, connected using a full Wheatstone bridge, and of some standard resistors added externally. These resistors are used to compensate for differences in the strain gage resistance and to compensate for temperature changes. Temperature compensation for this application is not very critical since the temperature changes during a typical water tunnel test are almost negligible.

The fact that the balance has to operate under water complicates the problem significantly. After the gages, terminals and wires were in place, a thin layer of microcrystalline wax was applied over the gages and terminals. The wax is an excellent water barrier, but since it is quite fragile, is not very good for mechanical protection. In order to protect the strain gages and to seal all of the wire/terminal connections, layers of RTV (silicon rubber) were applied over the wax, covering the entire area where the gages and terminals are located. A rubber sleeve was utilized as a secondary protection.

BALANCE DESCRIPTION

- BALANCE CONSISTS OF SEPARATE COMPONENTS TO ENSURE FLEXIBILITY AND SIMPLICITY
 - 1 ROLLING MOMENT SECTION
 - 2 PITCHING MOMENT SECTIONS
 - 2 YAWING MOMENT SECTIONS
 - DIMENSIONS: 3/4" DIAMETER
 5" LONG

- SEMI-CONDUCTOR STRAIN GAUGES ARE USED TO ENSURE MAXIMUM SENSITIVITY
 - GAUGE FACTOR = 145 (50-100 TIMES LARGER THAN FOIL GAGES)

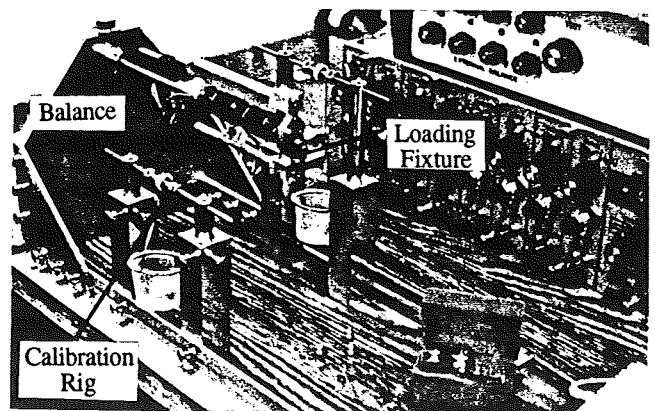
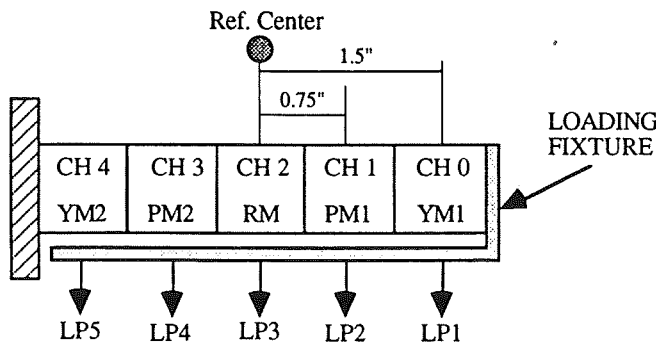
- GAUGES AND TERMINALS ARE WATER-PROOFED AND A RUBBER SLEEVE IS USED AS A SECONDARY PROTECTION

A key to accurately acquiring data from a force/moment balance is a precise and repeatable calibration. For a multi-component balance, it is important to determine the response of each section to a load in its primary plane of action (sensitivity) and also to loads in other planes (interactions). A simple calibration apparatus, shown in the photograph, was designed and built to calibrate the 5-component balance.

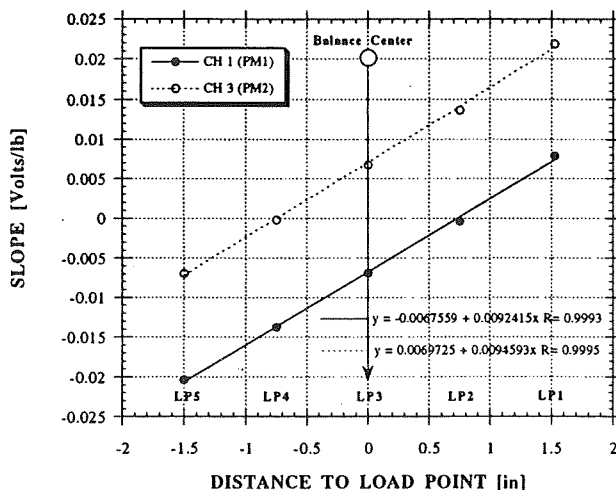
A full calibration was performed using the calibration rig and standard procedures typical of wind tunnel sting balances. The balance was loaded at five load points with positive and negative normal and side forces, and at the balance reference center (LP3) with positive and negative rolling moments. After all the loading cases were completed, the slopes of the output of each channel at the different load points were plotted versus the distance to said load points. The first plot shows the response of the pitching moment gages to an applied pitching moment. The slopes of the lines are the sensitivity to pitching moment, while the y-intercepts are the sensitivity of these channels to a normal force. Similarly, the sensitivity of the yawing moment gages to an applied yawing moment was obtained.

The rolling moment calibration is presented in the other plot. The output at the gages in Volts is plotted versus moment for the five channels. The response of the rolling moment component (CH 2) is linear, both for the positive and negative cases. The slope of this line represents the sensitivity of the section to rolling moment, and the interactions with the other gauges are negligible. In general, all the interactions were found to be very small.

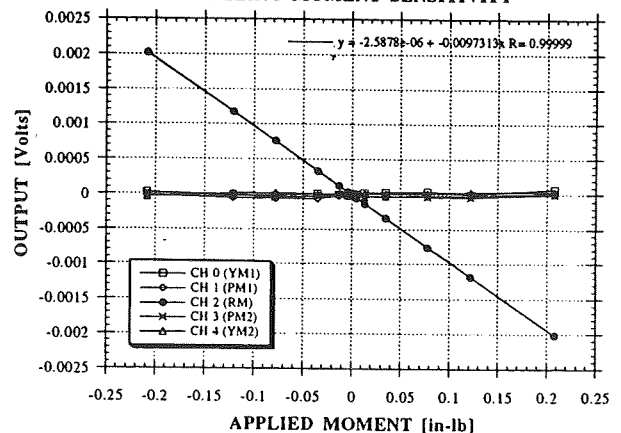
BALANCE CALIBRATION



PITCHING MOMENT SENSITIVITY



ROLLING MOMENT SENSITIVITY



All experiments were conducted in the Eidetics Model 2436 Flow Visualization Water Tunnel. The facility is a continuous horizontal flow tunnel with a test section 3 ft high x 2 ft wide x 6 ft long.

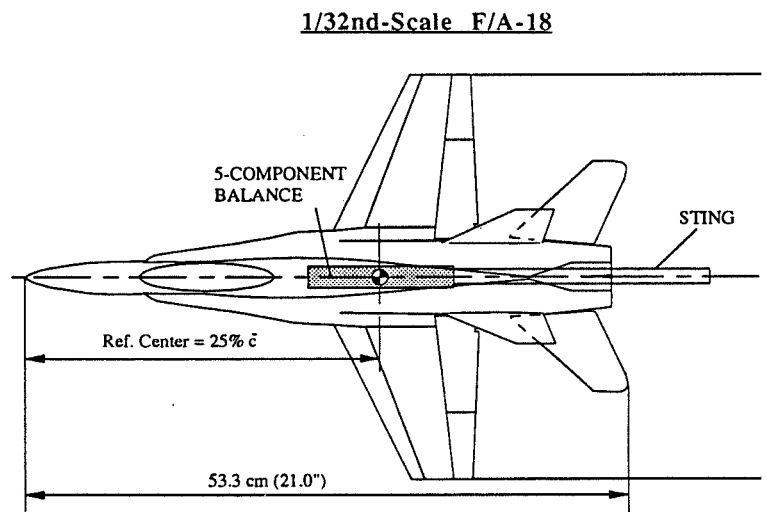
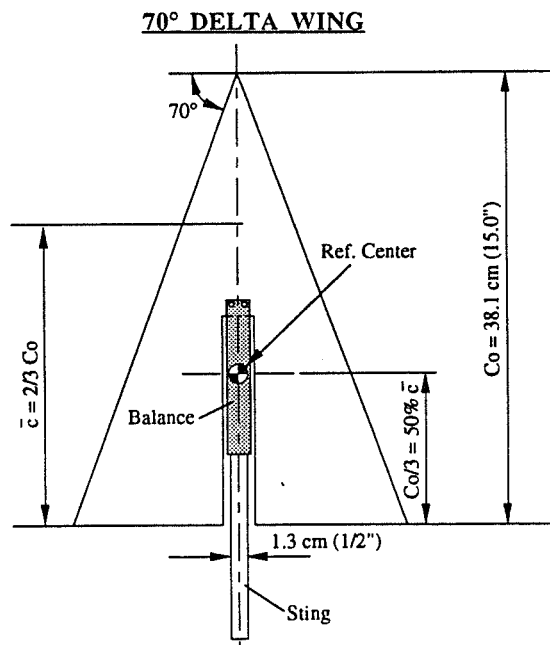
A 70° flat plate delta wing was used for these experiments. The extensive wind tunnel test data base on delta wings provided enough material for comparison. The aluminum delta wing has a root chord of 15 inches and a double-beveled leading edge. The balance is located at the model centerline and two fiberglass fairings (top and bottom) covered the entire balance.

Additional static and dynamic experiments were performed on a 1/32nd-scale F/A-18 model. The reason for choosing the F/A-18 was also the availability of data from several wind tunnel tests on this configuration that could be used for direct comparison to evaluate the performance of the balance. The plastic model is equipped with dye ports for flow visualization and the balance is attached to an internal aluminum plate. Control surfaces were fixed at 0° throughout the entire test (leading edge flaps were fixed at 34°).

The rotary balance experiments were performed on a 1/48th-scale F/A-18 due to size constraints in the water tunnel. The width of the test section (24 inches) did not allow the use of the 1/32nd-scale F/A-18 model utilized for the other dynamic experiments. The smaller plastic model has a span of 10 inches and a total length of 14 inches. Moments are referenced to the 50% \bar{c} on the delta wing and to the 25% \bar{c} on the F/A-18 models, except when indicated.

EXPERIMENTAL SETUP

- EIDETICS 2' x 3' WATER TUNNEL
- MODELS
 - 70° DELTA WING (STATIC AND DYNAMIC TESTS)
 - 1/32nd-SCALE F/A-18 (STATIC AND DYNAMIC TESTS)
 - 1/48th-SCALE F/A-18 (ROTARY BALANCE TESTS)



1/48th-Scale F/A-18
b = 10", L = 14"

The static tests were performed following standard "wind tunnel procedures". The gages were zeroed at the beginning of each run with the model at $\alpha = \beta = \phi = 0^\circ$. A static tare (or weight tare) was performed before the actual run. This consists of an angle of attack sweep with the tunnel off ($q_\infty = 0$) to account for gravity effects. After that, the model is always returned to $\alpha = 0^\circ$, a zero point is taken and the tunnel is started.

The water tunnel data were corrected only at high angles of attack. This correction is required as a result of a significant expansion of the wake when the wing stalls and it was developed by Cunningham (Ref. 1). It is a semi-empirical relationship based only on planform blockage and α .

The data acquisition/reduction software was developed specifically for this application using National Instrument's LabView, a graphical programming language. The basic methodology for the data reduction system, particularly the treatment of the balance equations, is based on the same approach used for typical wind tunnel data reduction schemes. The data acquisition/reduction software allows to perform a full balance calibration, as well as to acquire and reduce data during static and dynamic experiments. It allows the user to display "on-line" signals, acquire data at specified sampling rates and to reduce the data to coefficient form. Files with raw and coefficient data are created and saved to a disk for later plotting or reprocessing. Static data were acquired at 100 samples/sec for 25 seconds (500 samples/channel) and were not filtered. The large number of samples acquired permitted to obtain a mean value that closely represents the average gage reading at the particular loading condition. The force/moment measurements were conducted at velocities ranging of 0.42 to 0.58 ft/sec, that correspond to Reynolds numbers from 34,000 to 47,000 per foot.

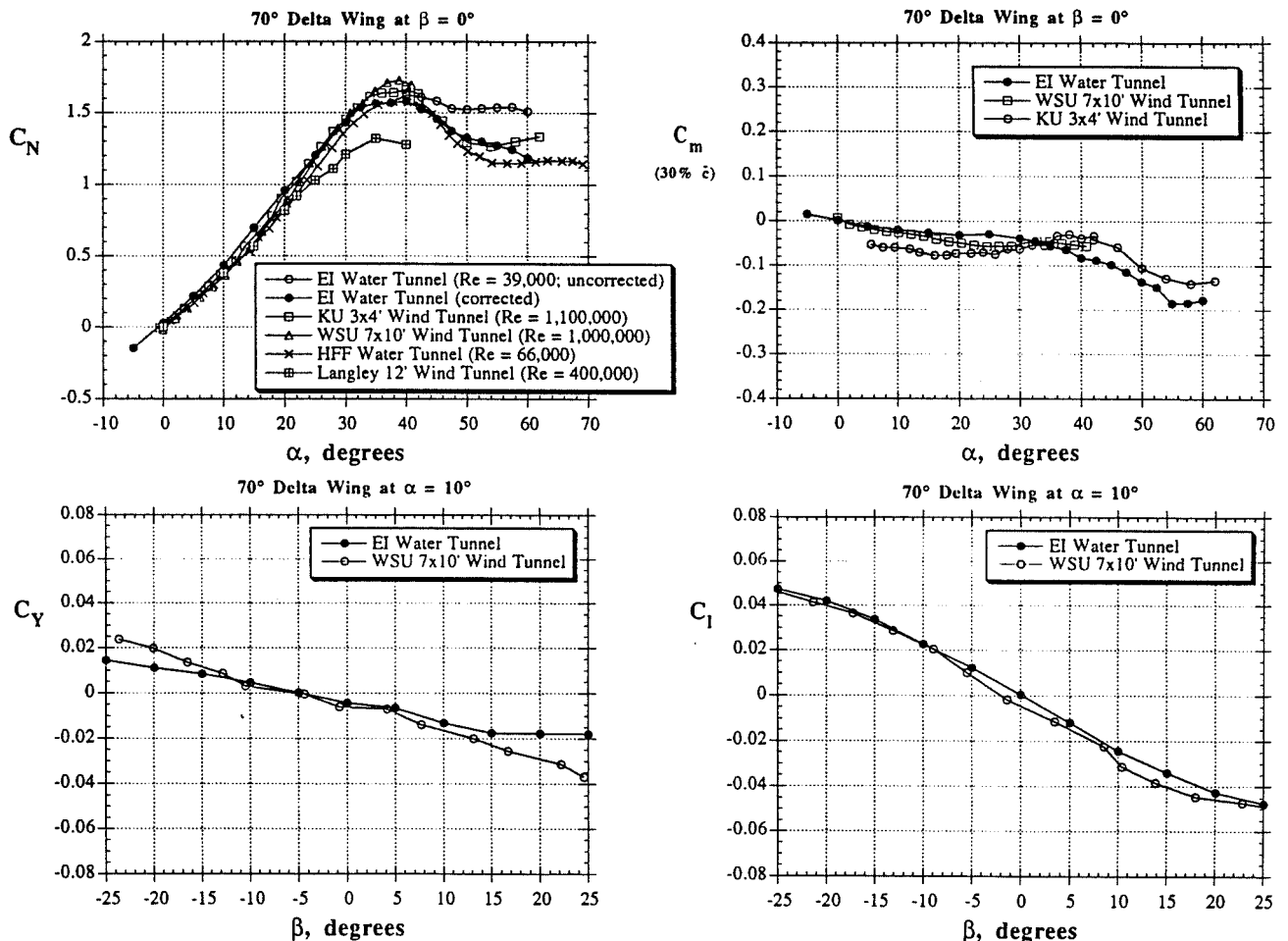
METHODOLOGY (STATIC TESTS)

- TESTS PERFORMED USING STANDARD WIND TUNNEL PROCEDURES
- A STATIC TARE ("WEIGHT" TARE) IS PERFORMED BEFORE RUNNING A NEW CONFIGURATION
- WATER TUNNEL DATA WERE CORRECTED ONLY AT HIGH ANGLES OF ATTACK. THE CORRECTION (REQUIRED AS A RESULT OF A SIGNIFICANT EXPANSION OF THE WAKE WHEN THE WING STALLS) IS SEMI-EMPIRICAL AND IS BASED ON PLANFORM BLOCKAGE AND ANGLE OF ATTACK
- CUSTOM DATA ACQUISITION/REDUCTION SYSTEM (LabView/MACINTOSH BASED)
- TEST PARAMETERS:
 - α RANGE = 0 to 60°
 - β RANGE = -20° to 20°
 - V_∞ = 0.42-0.58 ft/sec
 - Re = 34,000-47,000 per foot

The longitudinal characteristics of the 70° delta wing during static conditions are presented and compared to wind tunnel data in the top two plots. The water tunnel data (obtained at $V_\infty = 0.58$ ft/sec) are compared to similar data obtained in another water tunnel (Ref. 1), and in the KU 3x4' wind tunnel (Ref. 2), the WSU 7x10' wind tunnel (Ref. 3) and the Langley 12' wind tunnel (Ref. 4). The normal force coefficient agrees very well with most of the data, except for the Langley data. The differences between these data and the other wind tunnel data are quite significant and are probably due to the type of corrections applied, mounting system, flow quality, etc. Since the software provided the moments referenced to the 50% \bar{c} , the appropriate transformations had to be applied to obtain C_m at other locations. The pitching moment at 30% \bar{c} is compared to two sets of wind tunnel data and the agreement is satisfactory.

Side force changes were observed during sideslip sweeps at constant angles of attack. These changes are due, in part, to the large fiberglass fairings that cover the balance and act like a body. Results compare very well to wind tunnel data from Ref. 5 at $\alpha = 10^\circ$, where a delta wing with a similar fairing was tested. Changes in rolling moment with sideslip variations are as expected. The asymmetric vortices over the delta wing produce negative rolling moments with positive β and vice versa.

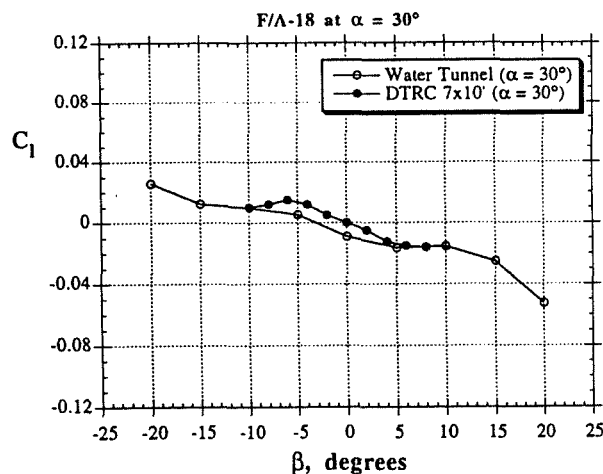
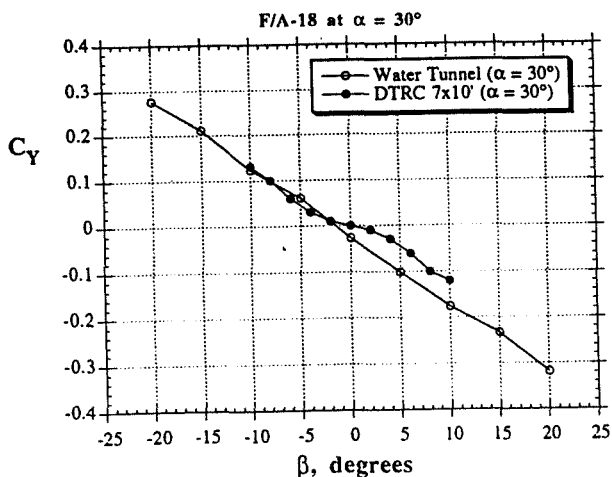
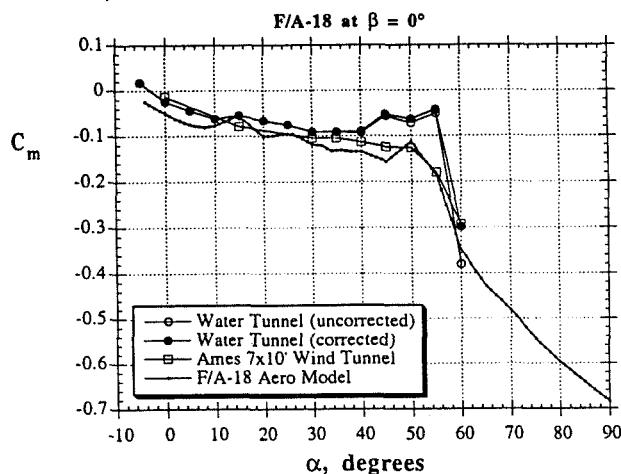
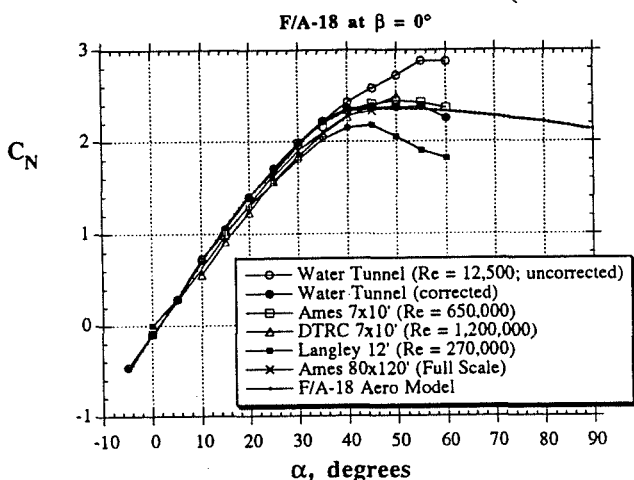
STATIC FORCE/MOMENT MEASUREMENTS (70° DELTA WING MODEL)



This figure shows a comparison between the water tunnel test and other wind tunnel tests for the baseline F/A-18. Angle of attack sweeps at $\beta = 0^\circ$ were performed and the agreement in C_N is very good, both in slope and absolute magnitude. The data obtained in the water tunnel match not only other small-scale wind tunnel tests (Refs. 6-7 and 9), but the full-scale test at the NASA Ames 80x120' (Ref. 8) and the F/A-18 Aero Model used in simulation as well. Only one data set (Langley 12', Ref. 10) has much lower values than those obtained in this test. The pitching moment measurements also agree well with other data; small differences are seen between 45° and 55° angle of attack, but trends and slopes are very similar.

Lateral/directional characteristics were compared to data from Ref. 9, as seen in the bottom two plots, and similarities in the C_Y and C_l curves during β sweeps at $\alpha = 30^\circ$ are evident. It should be noted that corrections due to wall proximity during sideslip sweeps were not introduced in the data reduction scheme, and therefore, small discrepancies can be expected. These comparisons show that the balance can be used effectively to measure five components of the forces and moments experienced by a "real" configuration (as opposed to "generic", as in the case of the delta wing) in this flow regime.

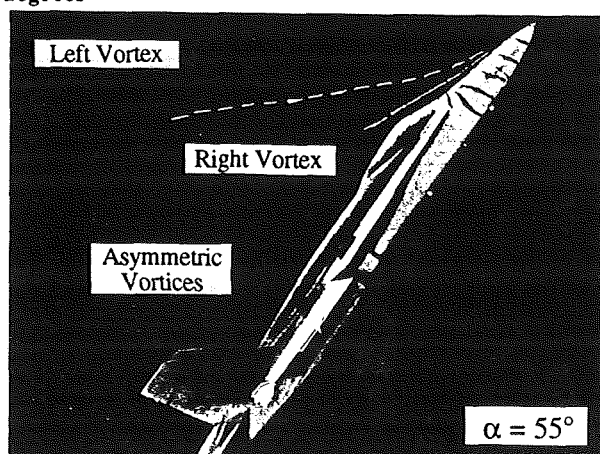
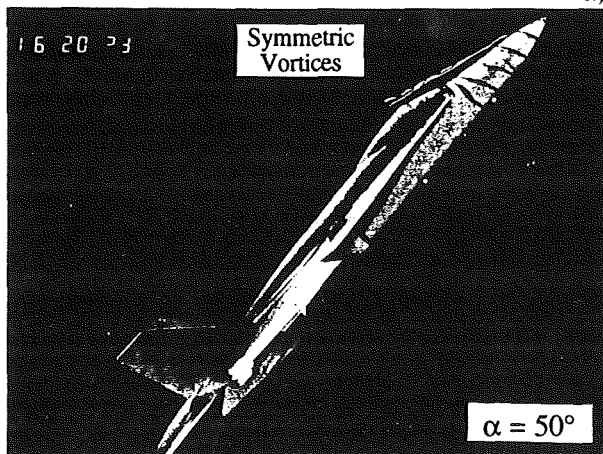
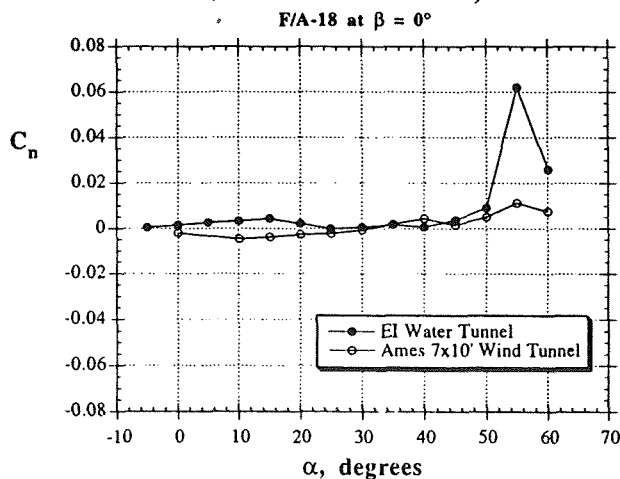
STATIC FORCE/MOMENT MEASUREMENTS (F/A-18 MODEL)



An example of the importance of having the capability of performing F/M measurements and flow visualization simultaneously is given by the particular flow field of the F/A-18 at high angles of attack. The yawing moment coefficient measured in the water tunnel agrees very well with wind tunnel data up to $\alpha = 50^\circ$; at higher angles of attack, the water tunnel data show a much larger C_n , which could be due to a large forebody vortex asymmetry. The presence of the asymmetry is confirmed by the flow visualization. As the photographs show, the forebody vortex flow field is symmetric for angles of attack up to $\alpha = 50^\circ$. At $\alpha = 55^\circ$, however, the flow presents a strong left-vortex-high asymmetry that will produce a large positive or "nose-right" yawing moment. Sideslip variations (positive and negative β) at $\alpha = 55^\circ$ indicated a significant hysteresis effect on the forebody asymmetry orientation and resulting yawing moments. The direction of the asymmetry at $\beta = 0^\circ$ depends on the direction of the sideslip variation, thus providing a "bi-stable" behavior of the forebody vortices. This behavior was also observed in Ref. 11. At $\alpha = 60^\circ$ the flow is still asymmetric, but the right forebody vortex has moved away from the body surface, therefore decreasing the asymmetry and the magnitude of the yawing moment.

The disagreement in the directional coefficients is not surprising considering that the forebody aerodynamics of this configuration is very sensitive to Reynolds number and to imperfections or perturbances (such as blowing ports) in the nose region.

STATIC F/M MEASUREMENTS AND FLOW VISUALIZATION (F/A-18 MODEL)



Some of the dynamic experiments conducted in this project, with the appropriate reduced rate parameter, are summarized in this table. The rates selected for experiments in the water tunnel should, of course, be scaled properly to represent the correct relationship between rotation rate, scale, and free stream velocity.

During the dynamic experiments, the data are corrected at high angles of attack with the same technique utilized during the static water tunnel experiments. The software handles the entire data acquisition and reduction processes, as well as the model motion. In order to correlate the F/M measurements with the model position, the software takes an encoder reading, then acquires the balance data, takes a second encoder reading and assigns the balance values to the average of the two encoder readings. The number of balance samples acquired between each encoder reading can be varied, and the final value for each channel is the arithmetic average of the samples taken. As expected, the larger the number of samples acquired, the better the quality of the data. It was found that by acquiring 800/1,000 per channel, the data obtained are very smooth and repeatable, requiring no post-processing or curve-fitting and clearly indicating the value of the force/moment at the particular model location. Since the A/D board used allows acquiring data very fast (10,000 samples per second), it was possible to take a large number of samples per channel and still obtain an adequate density of points (again, the low motion rates required in the water tunnel facilitate these experiments).

For the rotary balance tests, data were acquired and averaged over two revolutions to avoid excessive twisting of the cables (no slip-ring was used). A weight tare ($V_\infty = 0$), also averaged over exactly two revolutions, was performed at each angle of attack and subtracted from the "tunnel on" data.

METHODOLOGY (DYNAMIC TESTS)

• DYNAMIC TESTS INCLUDED:

Maneuver	Reduced Rate Parameter
PITCH-UP/PITCH-DOWN AND HOLD	$q_0 = \frac{q \bar{c}}{V_\infty}$
LARGE AMPLITUDE OSCILLATIONS IN PITCH, YAW AND ROLL	$k = \frac{\pi f \bar{c}}{V_\infty}$
ROTARY-BALANCE TESTS	$\Omega = \frac{\omega b}{2 V_\infty}$

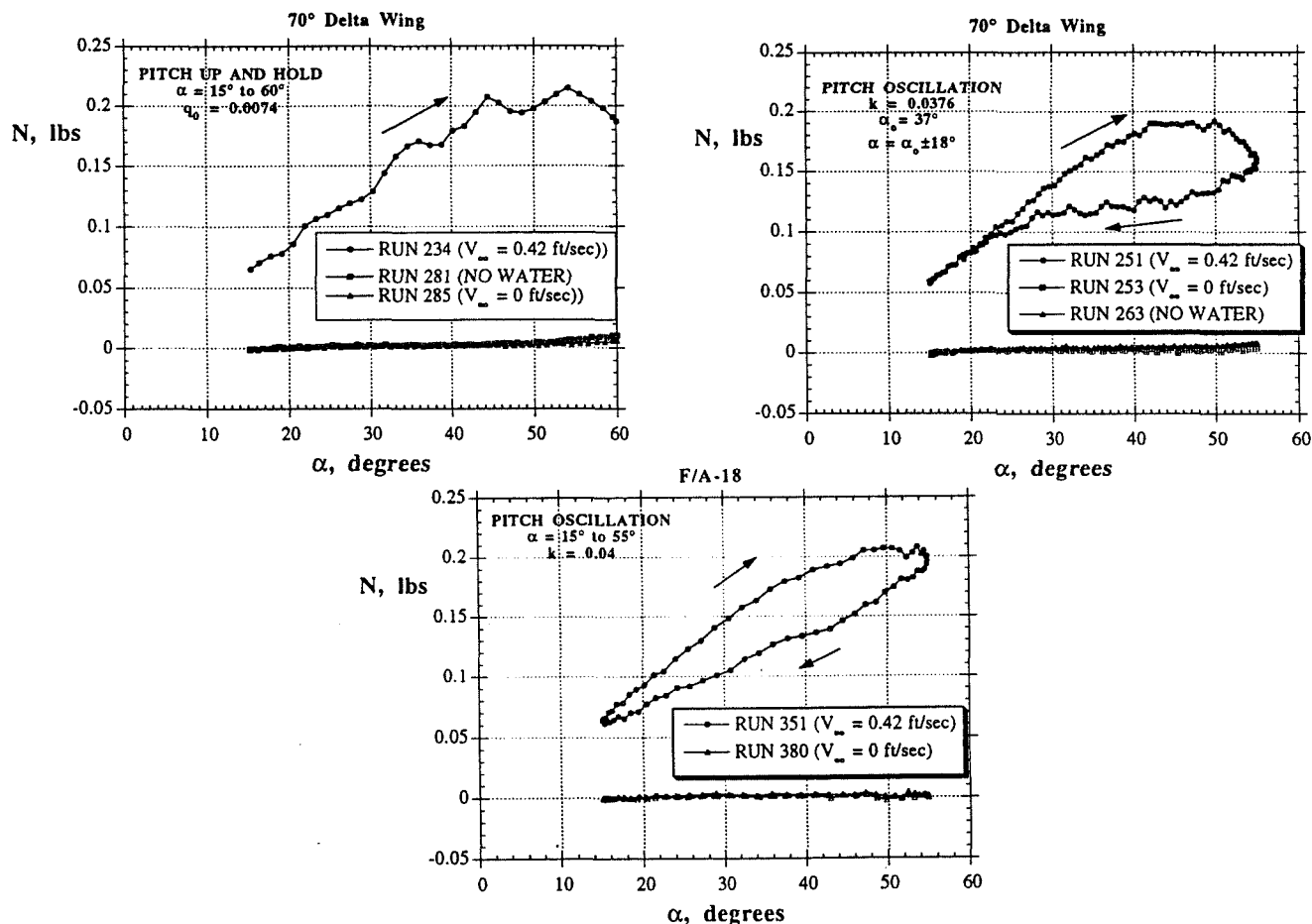
- DYNAMIC WATER TUNNEL DATA WERE CORRECTED USING THE SAME BOUNDARY CORRECTIONS AS IN THE STATIC TESTS
- A WEIGHT TARE IS PERFORMED BEFORE THE DYNAMIC MANEUVER
- FOR THE ROTARY BALANCE TESTS, DATA ARE AVERAGED OVER TWO REVOLUTIONS. A WEIGHT TARE ($V_\infty = 0$) IS PERFORMED AND DATA ARE ALSO AVERAGED OVER TWO REVOLUTIONS
- MOTION SOFTWARE IS ALSO LabView/MACINTOSH BASED

• DUE TO THE LOW ROTATION RATES, THE INERTIAL CONTRIBUTION TO FORCES AND MOMENTS WAS FOUND TO BE VERY SMALL, AS EXPECTED, AND DEPENDING ON THE ACCURACY OF THE DATA, THE INERTIAL TARES CAN BE NEGLECTED

One of the unknowns in dynamic water tunnel experiments was the model inertia effects on the data, i.e., the effect of the resistance to motion due to the model mass moment of inertia. Before actually performing the experiments, it was calculated that the inertia contribution to the aerodynamic values to be measured would be small, because of the low motion rates used in the water tunnel. The inertia effects are determined by measuring the time-variant moment recorded by the balance with the model in motion with the tunnel velocity at zero. This motion must be identical to the motion generated with the tunnel on ($V_\infty > 0$). The aerodynamic contribution is determined by subtracting the measured moment at $V_\infty = 0$ from the moment measured at $V_\infty > 0$.

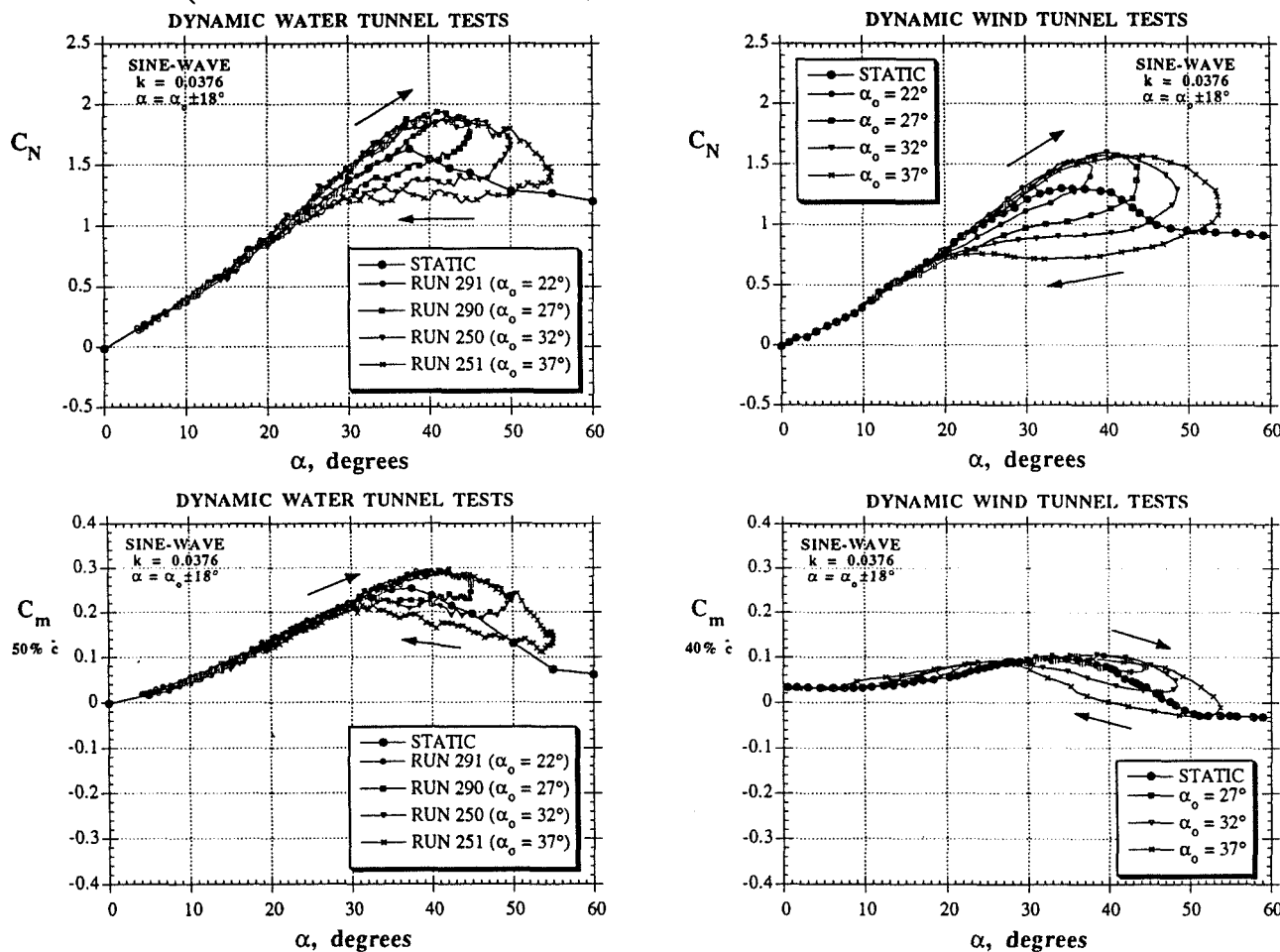
Results indicate that the inertial contribution is, indeed, very small. The first plot in this figure shows the measured normal force on the 70° delta wing during a ramp-hold maneuver from 15° to 60° angle of attack. The value of the normal force N (lbs) measured during the pitch-up motion when the water tunnel is off ($V_\infty = 0$) is almost negligible, approximately 1% of the value measured with tunnel speed. Also included in this plot is the value of the normal force measured during the specified motion with no water in the tunnel. The value of N throughout the dynamic maneuver under the "no water" condition is very similar to the $V_\infty = 0$ case, indicating that there are no major "virtual mass effects" (resistance of the surrounding water to being displaced by the moving model). Similar results were obtained during pitch oscillations, both for the 70° delta wing and the F/A-18 models, and during the other dynamic experiments (yaw and roll oscillations, rotary balance tests). Therefore, depending on the quality of the data required, the inertia effects can be ignored, facilitating the testing and the data reduction process.

EFFECT OF INERTIAL TARES ON DYNAMIC DATA



The first set of dynamic experiments consisted of large-amplitude pitch oscillations about a mean angle of attack α_0 . The purpose of these tests was to directly compare the water tunnel data to results from wind tunnel tests conducted at NASA Langley by Brandon and Shaw, where a 70° wing was investigated for forces and moments produced by these large-amplitude pitch motions (Ref. 4). This figure presents changes in the normal force and pitching moment coefficients produced by oscillating the delta wing $\pm 18^\circ$ about different α_0 's with a reduced frequency $k = 0.0376$. This k value corresponds to a maximum full-scale pitch rate of approximately 60 deg/sec for a typical fighter aircraft at altitude and at $V_\infty = 200$ ft/sec. The hysteresis loops are evident in the force measurements, with all the cases producing similar values of C_N overshoot. Results from the wind tunnel tests in Ref. 4 are shown in the plots at the right hand side and the similarities in the two data sets can be clearly identified. The level of C_N is slightly lower in the wind tunnel test, especially above 25° , but the shape of the dynamic loops and the relative increments are very similar in both tests. Even though the models in the two experiments rotated about a different reference point (50% \bar{c} for the present investigation and 40% \bar{c} for the wind tunnel test), the behavior of the pitching moment is very similar. As the angle of attack is increasing, the lag in the burst point of the vortex produces a destabilizing increment in C_m at high angles of attack. When the model reverses direction, a negative C_m increment is produced for the higher α_0 cases. This increment, produced by a lag in the flow reattachment, is very small for the $\alpha_0 = 22^\circ$ and 27° cases; the dynamic C_m curves follow the static curve very closely. As in the normal force case, the size of the hysteresis loops in pitching moment increases as the mean angle α_0 increases.

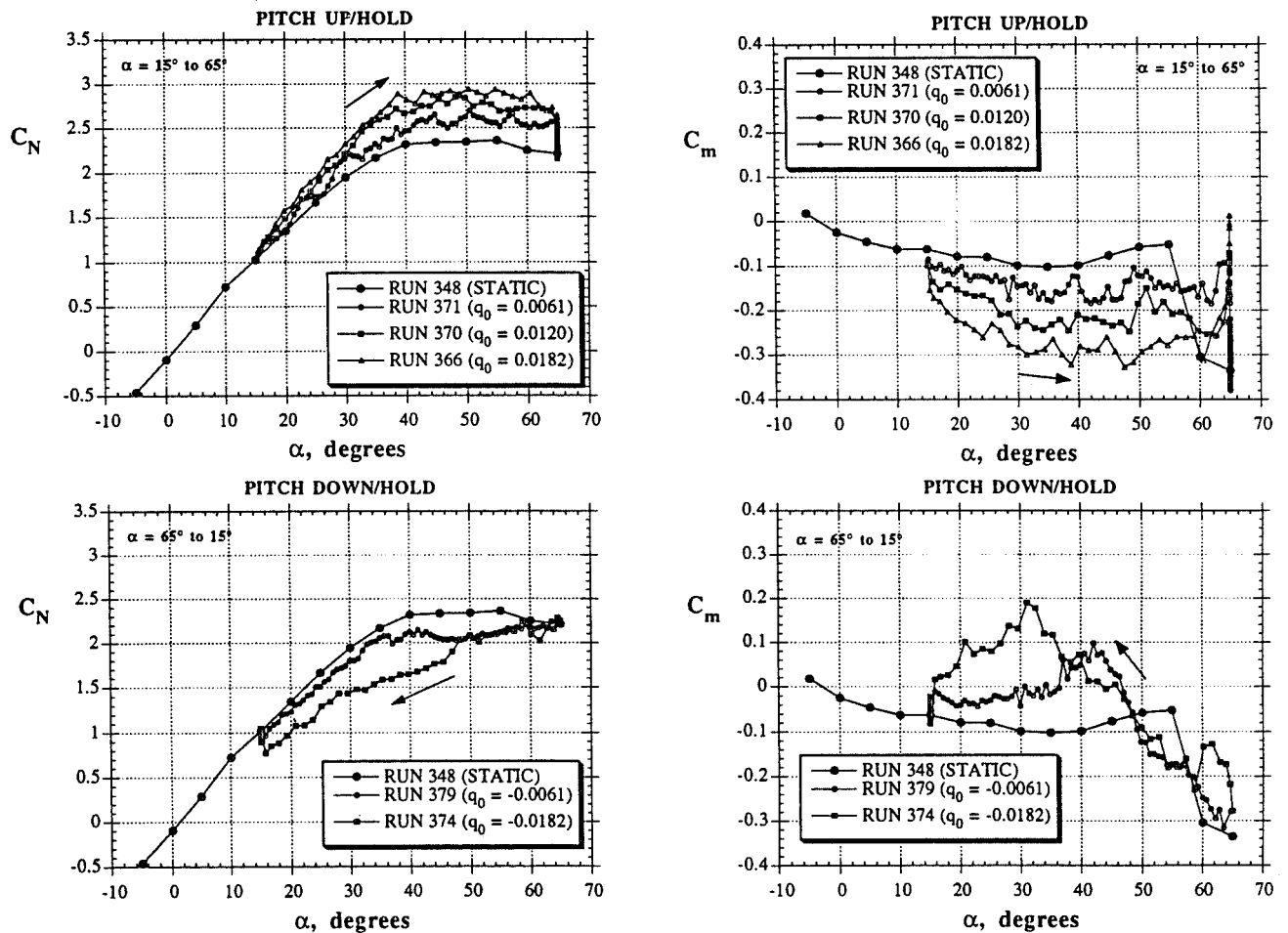
DYNAMIC FORCE/MOMENT MEASUREMENTS (PITCH OSCILLATIONS, 70° DELTA WING MODEL)



Experiments on the 1/32nd-scale F/A-18 model included pitch-up/down and hold maneuvers. The model rotates about the 25% \bar{c} , and the motions are basically constant rate ramps. The top plots present results for pitch-up and hold motions from 15° to 65° angle of attack for different non-dimensional pitch rates q_0 . The normal force and pitching moment data show a dependency on pitch rate, as reported by Brandon and Shaw in Ref. 10. In general, there is an increase in C_N and a decrease in C_m over the entire range of motion. As discussed in Ref. 10, the induced angle of attack in the horizontal tails and the lag in the separation and vortex formation are mainly responsible for the negative C_m increment at angles of attack lower than 55°. At higher angles of attack, the lag in the breakdown of the LEX vortex becomes dominant, generating a positive C_m increment.

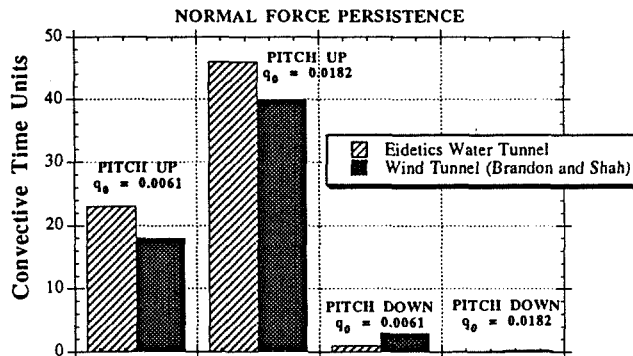
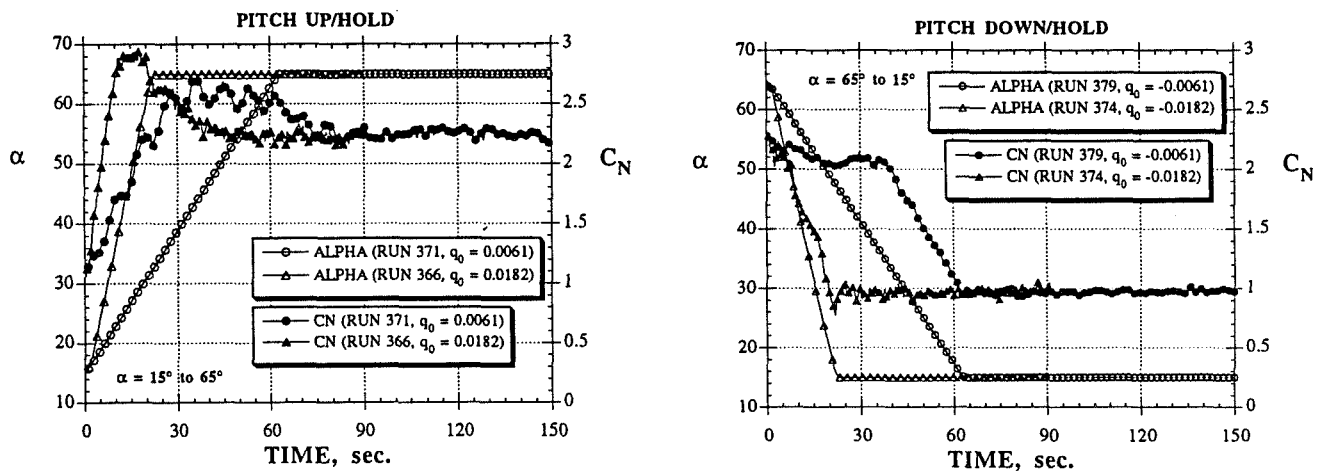
This set of experiments was completed with pitch-down and hold maneuvers at different rates. The maneuver consisted of pitching down the F/A-18 model from 65° to 15° angle of attack, and the responses of the normal force and the pitching moment are also revealed in this figure. The data show an undershoot in C_N that is independent of rate at the beginning of the motion (from 65° to 50° angle of attack). Between 50° and 15° angle of attack, the high rate motion generates a larger undershoot in C_N and a larger overshoot in C_m .

DYNAMIC FORCE/MOMENT MEASUREMENTS (PITCH UP/DOWN AND HOLD, F/A-18 MODEL)



The motion profiles for the maneuvers described in the previous page, along with the variation of the normal force coefficient with time, are illustrated in this figure. The "persistence" in normal force, defined as the time it takes the force to reach its steady or static value from the moment the motion stopped, is clearly observed in the first plot. The plot in the right hand side shows the motion profiles and the change in the normal force coefficient versus time for the pitch-down and hold maneuver. It is very interesting to notice that, contrary to the behavior observed during the pitch-up maneuvers in terms of persistence, by the time the model stops after the pitch-down, the value of the normal force is almost the same as the static value, denoting a very small or almost zero persistence. The persistence in C_N , in terms of convective time units, is compared to data from the wind tunnel experiments (Ref. 10) in the bar chart. A convective time unit is the time it takes one particle in the free stream to travel a distance equal to the mean aerodynamic chord on the model. The similarities between the results from the two experiments are quite evident, indicating similar flows and dynamic force/moment responses. The small discrepancies in the value of persistence observed in each test can be attributed to the difference in motions. While the pitch-up and pitch-down angles from the present test were between 15° and 65° angle of attack, those performed in Ref. 10 were between 0° and 75° . Results from the same investigation indicated that the persistence is a strong function of not only the non-dimensional pitch rate, as the water tunnel test indicates, but of the ending angle of attack as well. Limitations in the water tunnel model support did not allow for reproducing the same motion.

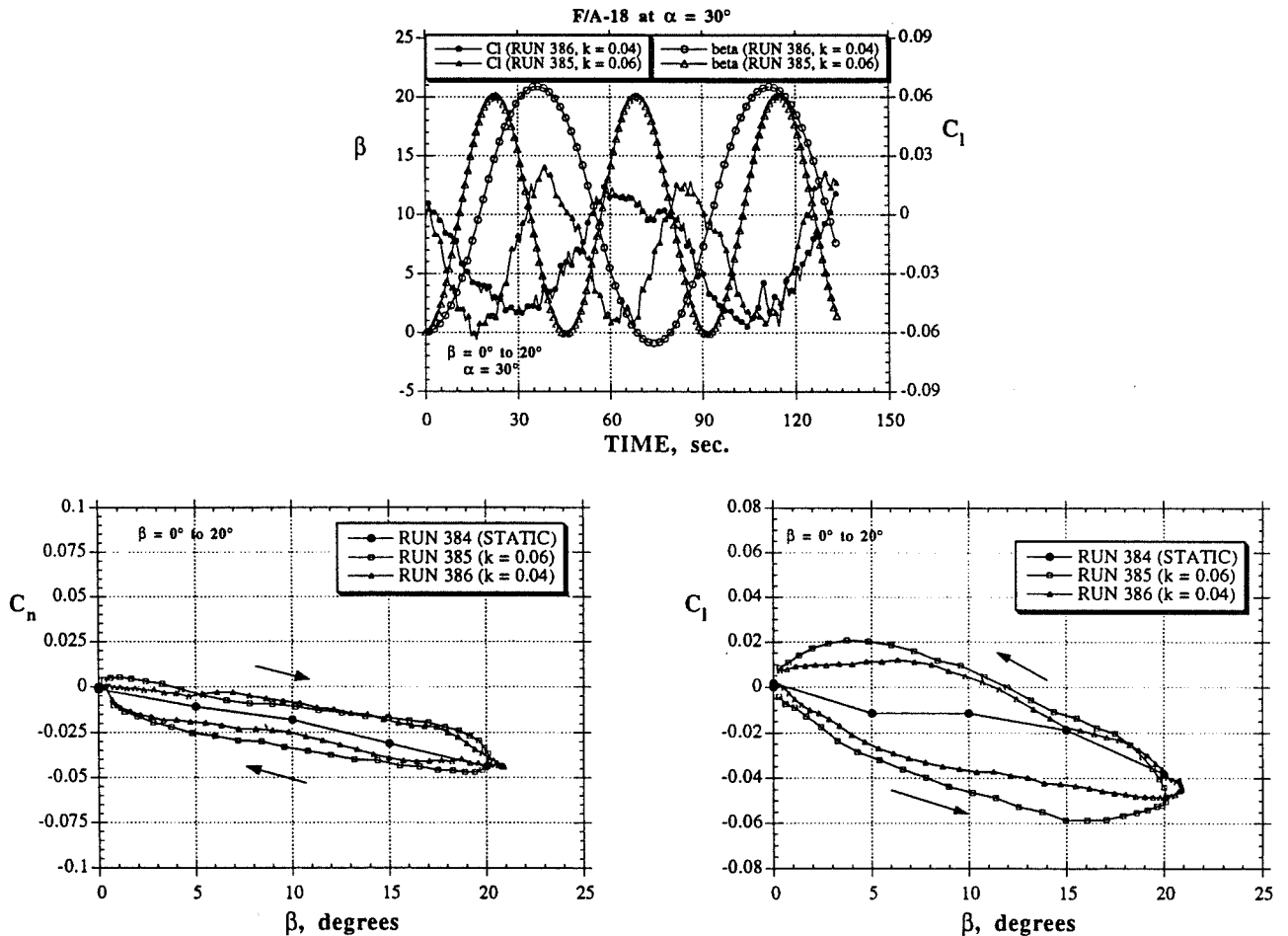
DYNAMIC FORCE/MOMENT MEASUREMENTS (PITCH UP/DOWN AND HOLD, F/A-18 MODEL)



The methodology and procedures for conducting the dynamic experiments in yaw are very similar to those utilized for the pitch experiments. Since the tests were performed in a horizontal tunnel, the weight component does not change with sideslip angle, and therefore, a weight tare is not needed.

The dynamic tests in the yaw axis were limited to oscillations between 0° and 20° sideslip angle, at $\alpha = 30^\circ$, and at two reduced frequencies k . The motion profiles and the response of the rolling moment coefficient with time are presented in the first plot in this figure. Results indicate that the hysteresis in the longitudinal characteristics is minimum; the values follow the static case very closely. The major changes are observed, as expected, in the lateral-directional characteristics. The yawing moment and rolling moment data present hysteresis loops with opposite directions. The loops for C_n are clockwise, while the loops for C_l are much larger and counter-clockwise. While the principal mechanism for the loops in yawing moment is probably the yaw damping produced by the vertical tails, the primary mechanism responsible for the loops in C_l is the lag in the LEX vortex burst and reformation.

DYNAMIC FORCE/MOMENT MEASUREMENTS (YAW OSCILLATIONS, F/A-18 MODEL)

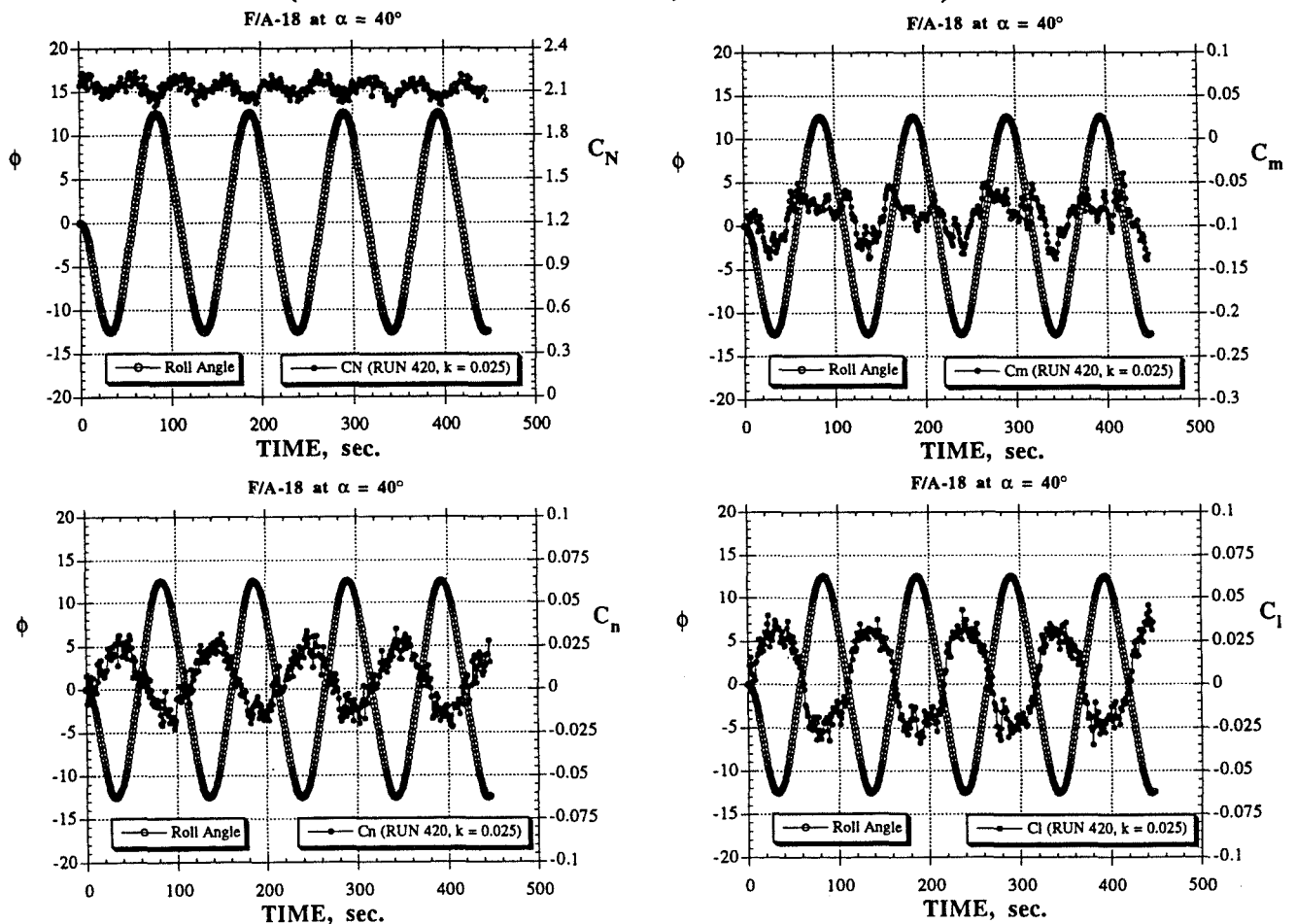


Roll oscillations were also conducted using the 1/32nd-scale F/A-18 model. For these particular dynamic experiments, the model is positioned at the desired angle of attack and a weight tare ($V_\infty = 0$) is performed throughout the entire roll angle range.

The approach for the set of experiments presented here was to match the free-to-roll motion obtained in the wind tunnel test performed in Ref. 12. In that investigation, a 2.5%-scale model of the F-18 presented a limit cycle oscillation or "wing rock motion" for angles of attack between 30° and 50°, with peak-to-peak amplitudes that could exceed 40° roll angle. At $Re = 20,000$ and $\alpha = 40^\circ$, the F-18 oscillated between -13° and 13° in the wind tunnel. This condition was explored in detail in the present water tunnel test. It should be noted that the motion utilized is a sine wave approximation, and therefore, small differences in some motion parameters, especially acceleration, and in the response of the forces and moments, can be expected.

Four components of the forces and moments measured with the balance during a body-axis roll (between -13° and 13°) at $k = 0.025$ (which matches exactly the wind tunnel reduced frequency) are presented in this figure. Variations in normal force are small, but the changes in C_m produced by the rolling motion are more noticeable. Changes in directional characteristics are significant and, in general, a positive roll angle ϕ is associated with positive side force and yawing moment coefficients and vice versa.

DYNAMIC FORCE/MOMENT MEASUREMENTS (ROLL OSCILLATIONS, F/A-18 MODEL)



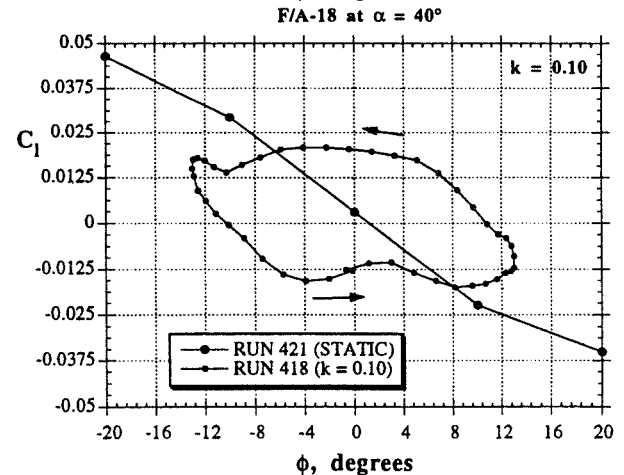
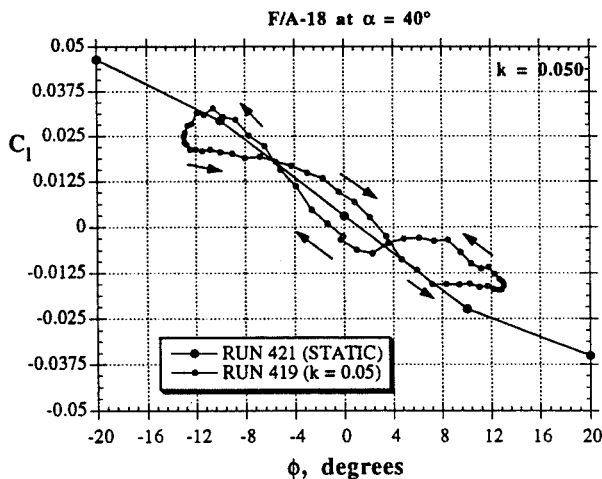
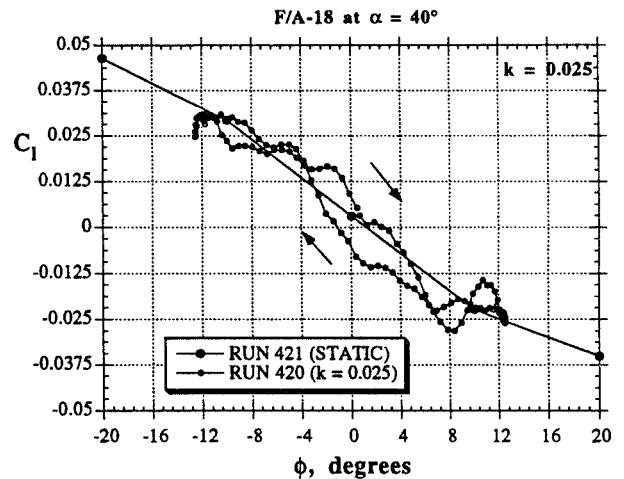
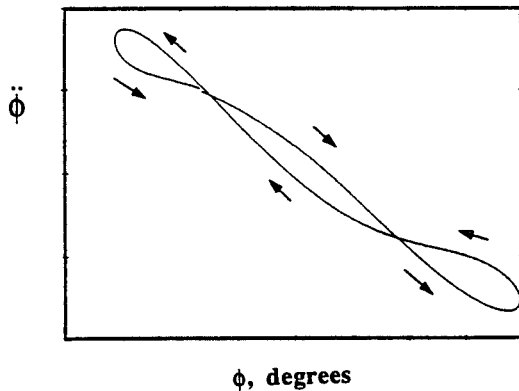
The rolling moment behaves as expected, with negative rolling moments occurring during positive roll angles and vice versa. In order to observe the hysteresis in rolling moment, C_l can be plotted versus roll angle. Typical "wing rock" or hysteresis phase plots are obtained by plotting $\ddot{\phi}$ versus ϕ . Since the acceleration $\ddot{\phi}$ is proportional to the total aerodynamic rolling moment coefficient, ($C_l = \frac{\ddot{\phi} I_{xx}}{q_\infty S b}$) then the shape of the C_l vs. ϕ plot should show similar characteristics. In a

phase plot, a clockwise loop denotes an area where energy is being added to the system, i.e., the oscillations are being driven (destabilizing). The counter-clockwise loops near the maximum roll angle represent areas where the system is consuming energy, and therefore the motion is being damped (stabilizing). The areas contained within the destabilizing and stabilizing loops are about equal, indicating an energy balance which is required to sustain the limit-cycle wing rock. The hysteresis plot seen in the top right corner of this figure ($k = 0.025$), shows a large central clockwise loop, but near the roll angles extremes, the typical counter-clockwise loops are not well organized. This could be due to the differences in accelerations between the real free-to-roll motion and the oscillation performed in the water tunnel.

This investigation also reveals that the shape of the hysteresis plots is strongly dependent on the frequency. The same "forced-to-roll" motion was performed at reduced frequencies of $k = 0.050$ and 0.10 , and it appears that by increasing the frequency, the central clockwise loop (destabilizing) starts decreasing, while the two counter-clockwise loops near the extremes become larger. The central loop disappears completely for the high frequency oscillation ($k = 0.10$); only a single counter-clockwise loops is observed in this particular case.

DYNAMIC FORCE/MOMENT MEASUREMENTS (ROLL OSCILLATIONS, F/A-18 MODEL)

Typical Wing Rock Phase Plot

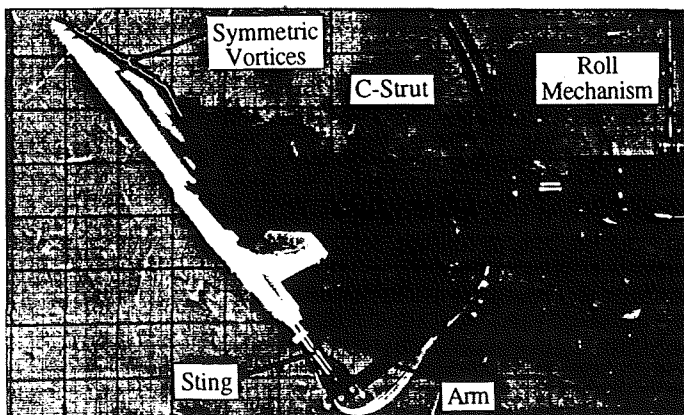


Another important maneuver for present and future aircraft is the "loaded roll" or rolling around the velocity vector at medium to high angles of attack. In the wind tunnel, rotary balances are used to acquire force and moment data from an internal balance with the model rotating around the velocity vector at varying rotation rates. With the balance, the water tunnel can provide a simplified version of the same type of test capability with the added benefit of being able to observe the behavior of the flow at the same time.

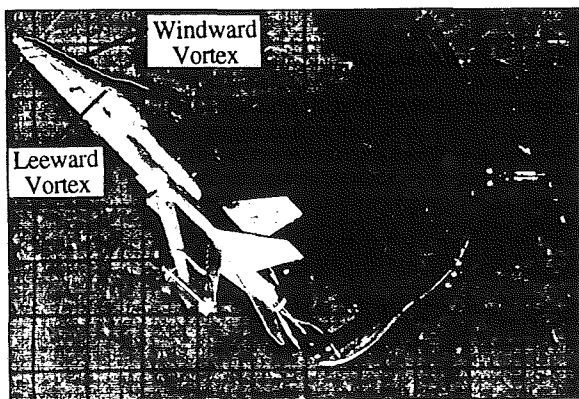
The rig consists of an aluminum C-strut that attaches to the roll mechanism and the water tunnel main C-strut. The angle of attack is changed manually by sliding the arm along the C-strut, allowing testing at angles of attack between 0° and 60° . Once the desired α is obtained, the arm is fixed in position. Sideslip can be varied by rotating the sting in the adapter located at the end of the arm.

This figure shows flow visualization performed on the 1/48th-scale F/A-18 model at $\alpha = 50^\circ$ and at three conditions: static, and positive and negative rotations ($\Omega = \pm 0.15$). For the static case, the forebody vortex flow field is symmetric, as observed during the static tests performed with the 1/32nd-scale F/A-18 model. The positive rotation (clockwise, pilot's view), causes that the windward (right/red) gets lifted up from the body. A "right-vortex-high" asymmetry is created, with the associated negative side force and yawing moment. The opposite occurs when the model is rotated at $\Omega = -0.15$, i.e., a "left-vortex-high" asymmetry is produced. The excellent flow visualization provides interesting information not only about the forebody vortex position, but also about the different vortex interactions.

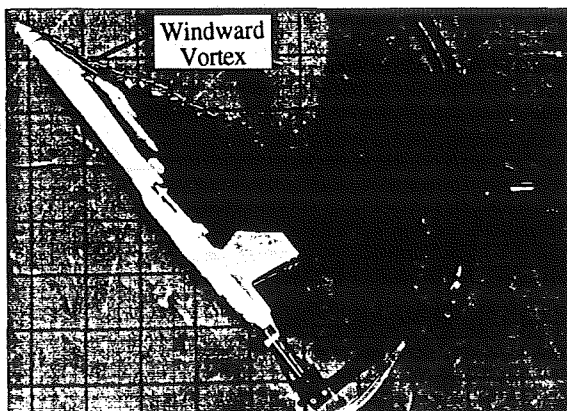
FLOW VISUALIZATION
(ROTARY BALANCE TESTS, F/A-18 MODEL)



Static
 $\alpha = 50^\circ$



Positive Rotation, $\Omega = 0.15$



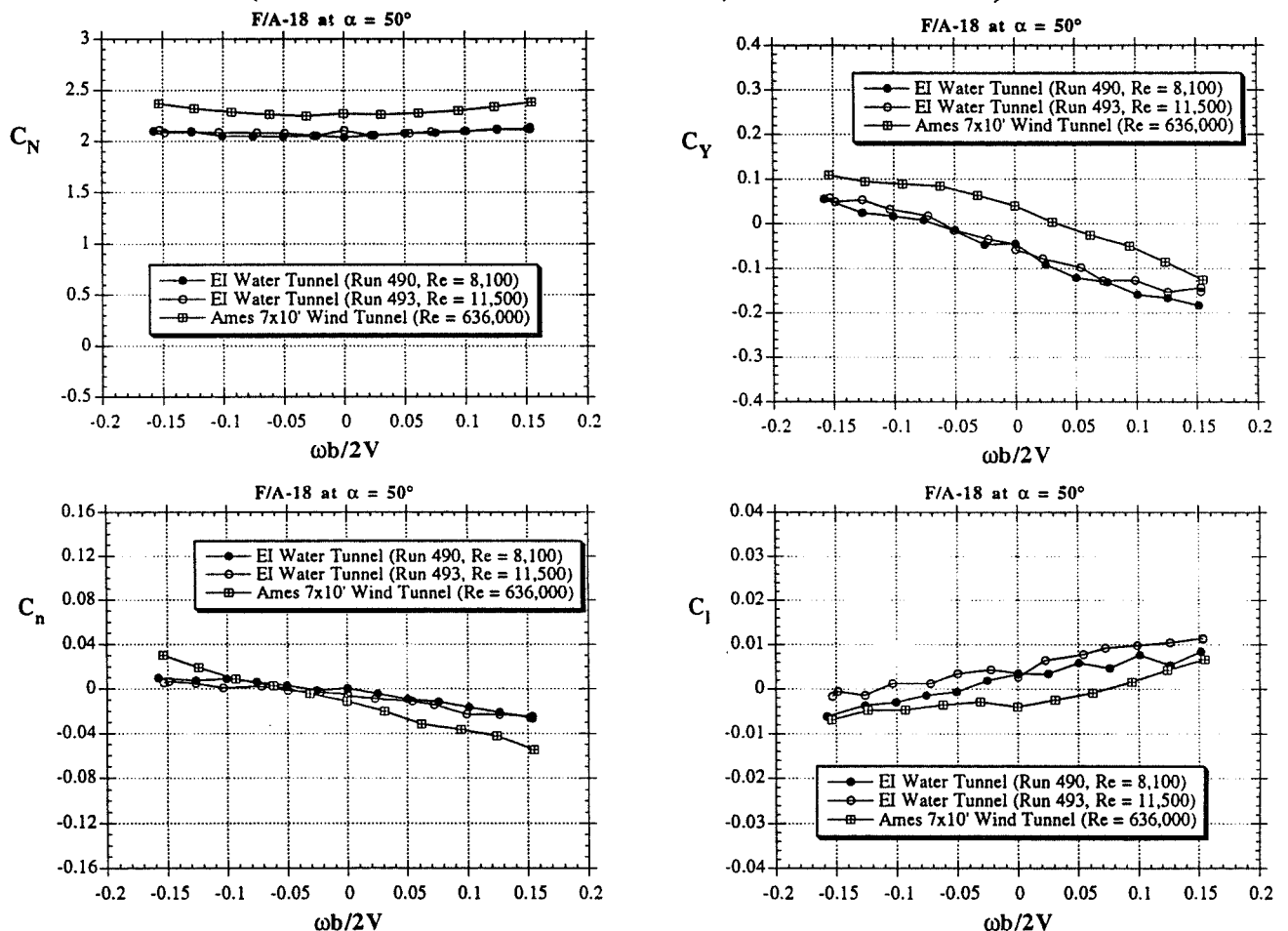
Negative Rotation, $\Omega = -0.15$

As mentioned before, and because of the complexity associated with a hydraulic slip-ring for the dye and with a electric (submersible) slip-ring for the balance, the number of revolutions are limited. Data were acquired and averaged over exactly 2 revolutions. Four components of the forces and moments at $\alpha = 50^\circ$ are presented in this figure. Data from the water tunnel rotary balance tests correspond to runs at 0.42 ft/sec and 0.58 ft/sec. These data are compared to results from a rotary balance test performed by Eidetics on a 6%-scale F/A-18 in the NASA Ames 7' x 10' wind tunnel (Ref. 13).

The normal force coefficient presents the same trends in both tests, i.e., a slight increase with rotation rate. There is a difference in the static value ($\omega b/2V_\infty = 0$) that could be due to boundary corrections, geometry differences, etc.

The agreement in the lateral/directional coefficients is quite acceptable. Evidently, the forebody vortex flow fields in the water and wind tunnel experiments present opposite asymmetries, as indicated by the side force value at $\omega b/2V_\infty = 0$, but the anti-spin slope is similar in both tests. The yawing moment coefficient obtained in the water tunnel presents a smaller slope than that revealed by the wind tunnel results, especially for negative rotations, denoting a possible slight shift in the center of pressure. The anti-spin behavior, however, is still present. The rolling moment shows positive slopes in both tests, and it is the component that shows the larger Reynolds number effects in the water tunnel tests. Results from these experiments can be considered quite encouraging, especially in terms of having the capability of performing flow visualization and F/M measurements to assess spin characteristics during the preliminary design phase.

DYNAMIC FORCE/MOMENT MEASUREMENTS (ROTARY BALANCE TESTS, F/A-18 MODEL)



A five-component balance was designed, built and tested in the Eidetics' water tunnel. The balance was calibrated and showed good linearity and low interactions. Results of static experiments were quite satisfactory, showing good correlation with wind tunnel data of similar configurations (delta wing and F/A-18 models).

This research project also explored the use of the balance to perform dynamic experiments in the water tunnel. The model support of the Eidetics' water tunnel was improved, and both a new roll mechanism and a rotary rig were designed and built to assess the performance of the balance under different types of dynamic situations. Among the advantages of conducting dynamic tests in a water tunnel are less demanding motion and data acquisition rates than in a wind tunnel test (because of the low-speed flow) and the capability of performing flow visualization and force/moment measurements simultaneously with relative simplicity. Of significant importance is the fact that this investigation showed that the values of the inertial tares (the effect of the resistance to motion due to the mass model of inertia) are very small due also to the low rotation rates required in the water tunnel. Depending on the accuracy of the data required, these tares can be ignored, and that facilitates the testing and data acquisition process. This investigation clearly showed all the different dynamic experiments that can be easily performed in a water tunnel, and the capability of simultaneous flow visualization and F/M measurements proved extremely useful to explain the results obtained during these dynamic tests.

In general, results obtained in this contract should encourage the use of water tunnels for a wider range of quantitative and qualitative experiments, especially during the preliminary phase of aircraft design.

CONCLUDING REMARKS

- FORCES AND MOMENTS WERE MEASURED IN A WATER TUNNEL USING A 5-COMPONENT BALANCE
- IN GENERAL, THE WATER TUNNEL DATA PRESENTED GOOD AGREEMENT WITH STATIC AND DYNAMIC WIND TUNNEL DATA
- RESULTS EMPHASIZE THE IMPORTANCE OF HAVING THE CAPABILITY OF PERFORMING SIMULTANEOUS FLOW VISUALIZATION AND FORCE/MOMENT MEASUREMENTS
- THE DEVELOPMENT OF THE CAPABILITY FOR PERFORMING DYNAMIC EXPERIMENTS IN THE WATER TUNNEL, INCLUDING ROTARY BALANCE TESTS, OFFERS A WIDE VARIETY OF NEW POSSIBILITIES FOR USING THE WATER TUNNEL AS A PRELIMINARY DESIGN TOOL

REFERENCES

1. Cunningham, A., "Steady and Unsteady Force Testing of Fighter Aircraft Models in a Water Tunnel," AIAA Paper 90-2815, presented at the AIAA 8th Applied Aerodynamics Conference, Portland, Oregon, Aug. 20-22, 1990.
2. Wentz, W. H. Jr., "Wind Tunnel Investigations of Vortex Breakdown on Slender Sharp-Edged Wings," Ph.D. Dissertation, University of Kansas, Lawrence, KS.
3. Phillis, D.L., "Force and Pressure Measurements Over a 70° Delta Wing at High Angles of Attack and Sideslip," Master Thesis, Aeronautical Engineering Department, The Wichita State University, 1991.
4. Brandon, J. M. and Shah, G. H., "Effect of Large Amplitude Pitching Motions on the Unsteady Aerodynamic Characteristics of Flat-Plate Wings," AIAA Paper 88-4331, presented at the Atmospheric Flight Mechanics Conference, August 15-17, 1988.
5. Sprage, R., "Wind Tunnel & Water Channel High Angle of Attack Delta Wing Study and Comparison with Particular Reference to Vortex Core & Burst Location," Master Thesis, Aeronautical Engineering Department, The Wichita State University, August 1989.
6. Kramer, B. R., Suárez, C. J., and Malcolm, G. N., "Forebody Vortex Control With Jet And Slot Blowing On An F/A-18," AIAA Paper 93-3449, presented at the 11th Applied Aerodynamics Conference, Monterey, California, Aug. 10-12, 1993.
7. Suárez, C. J., Kramer, B. R., and Malcolm, G. N., "Forebody Vortex Control On An F/A-18 Using Small, Rotatable Tip-Strakes," AIAA Paper 93-3450, presented at the 11th Applied Aerodynamics Conference, Monterey, California, Aug. 10-12, 1993.
8. Lanser, W. R. and Murri, D. G., "Wind Tunnel Measurements on a Full-Scale F/A-18 With Forebody Slot Blowing or Forebody Strakes," AIAA Paper 93-1018, presented at the AIAA/AHS/ASEE Aerospace Design Conference, Irvine, CA, 1993.
9. Erickson, G. E., Hall, R. M, et. al., "Experimental Investigation of the F/A-18 Vortex Flows at Subsonic Through Transonic Speeds," AIAA Paper 89-2222 (invited), presented at the AIAA 7th Applied Aerodynamics Conference, Seattle, WA, 1989.
10. Brandon, J. M. and Shah, G. H., "Unsteady Aerodynamic Characteristics of a Fighter Model Undergoing Large-Amplitude Pitching Motions at High Angles of Attack," AIAA Paper 90-0309, 28th Aerospace Sciences Meeting, January, 1990, Reno, Nevada.
11. Ng, T. T., Malcolm, G.N., "Aerodynamic Control of the F/A-18 Using Forebody Vortex Control," AIAA Paper 91-0618, presented at the 29th Aerospace Sciences Meeting, Reno, NV, 1991.
12. Quast, T., Nelson, R.C. and Fisher, D.F.; "A Study of High Alpha Dynamics and Flow Visualization for a 2.5% Model of the F-18 HARV Undergoing Wing Rock," AIAA Paper 91-3267, presented at the 9th Applied Aerodynamics Conference, Baltimore, MD, 1991.
13. Kramer, B. R., Suárez, C. J., Malcolm, G. N. and James, K. D., "Forebody Vortex Control on an F/A-18 in a Rotary Flow Field", AIAA Paper 94-0619, presented at the 32nd Aerospace Sciences Meeting, Reno, NV, 1994.

REPORT DOCUMENTATION PAGEForm Approved
OMB No. 0704-0188

Public reporting burden for this collection of information is estimated to average 1 hour per response, including the time for reviewing instructions, searching existing data sources, gathering and maintaining the data needed, and completing and reviewing the collection of information. Send comments regarding this burden estimate or any other aspect of this collection of information, including suggestions for reducing this burden, to Washington Headquarters Services, Directorate for Information Operations and Reports, 1215 Jefferson Davis Highway, Suite 1204, Arlington, VA 22202-4302, and to the Office of Management and Budget, Paperwork Reduction Project (0704-0188), Washington, DC 20503.

1. AGENCY USE ONLY (Leave blank)

2. REPORT DATE

July 1994

3. REPORT TYPE AND DATES COVERED

Conference Publication

4. TITLE AND SUBTITLE

Fourth NASA High Alpha Conference

5. FUNDING NUMBERS

WU 505-68-30

6. AUTHOR(S)

7. PERFORMING ORGANIZATION NAME(S) AND ADDRESS(ES)

NASA Dryden Flight Research Center
P.O. Box 273
Edwards, California 93523-02738. PERFORMING ORGANIZATION
REPORT NUMBER

H-2007

9. SPONSORING/MONITORING AGENCY NAME(S) AND ADDRESS(ES)

National Aeronautics and Space Administration
Washington, DC 20546-000110. SPONSORING/MONITORING
AGENCY REPORT NUMBERNASA CP-10143
Volume 1

11. SUPPLEMENTARY NOTES

This document is a preprint for a conference held at NASA Dryden Flight Research Center, July 12-14, 1994. Conference Chair Donald Gatlin; Technical Chair Victoria Regenie; Administrative Chair Everlyn Cruciani.

12a. DISTRIBUTION/AVAILABILITY STATEMENT

Unclassified—Unlimited
Subject Category 02

12b. DISTRIBUTION CODE

13. ABSTRACT (Maximum 200 words)

The goal of the Fourth High Alpha Conference, held at the NASA Dryden Flight Research Center on July 12-14, 1994, was to focus on the flight validation of high angle-of-attack technologies and provide an in-depth review of the latest high angle-of-attack activities. Areas that were covered include, high angle-of-attack aerodynamics, propulsion and inlet dynamics, thrust vectoring, control laws and handling qualities, tactical utility, and forebody controls.

14. SUBJECT TERMS

Aerodynamics; F-18 HARV; High angle of attack; X-31 aircraft

15. NUMBER OF PAGES

207

16. PRICE CODE

A10

17. SECURITY CLASSIFICATION
OF REPORT

Unclassified

18. SECURITY CLASSIFICATION
OF THIS PAGE

Unclassified

19. SECURITY CLASSIFICATION
OF ABSTRACT

Unclassified

20. LIMITATION OF ABSTRACT

Unlimited